ABSTRACT

Title of Document:	QUANTIFICATION OF PERMEABILITY-POROSITY RELATIONSHIPS IN SEAFLOOR VENT DEPOSITS: DEPENDENCE ON PORE EVOLUTION PROCESSES
	Jill Leann Gribbin Master of Science – 2011
Directed By:	Associate Professor Wenlu Zhu Department of Geology

Hydrothermal mineral deposits formed along seafloor spreading centers help regulate the transfer of heat and mass from Earth's interior to the oceans. Aqueous fluids circulate within the seafloor and are emitted through vent deposits, formed from interaction between vent fluids and seawater. These deposits evolve as they react physically and chemically with venting fluids and seawater, therefore changing transport properties, such as permeability and porosity. In this study, measurements of permeability (k) and porosity (ϕ) were used in conjunction with microstructural observations to identify evolution of permeability-porosity relationships (EPPRs) for vent deposits. EPPRs are power-law relationships relating permeability and porosity through an exponent, α, which is sensitive to changes in these properties. These relationships are important for understanding pore evolution processes and fluid distribution, in addition to their effects on environmental conditions within vent deposits.

QUANTIFICATION OF PERMEABILITY-POROSITY RELATIONSHIPS IN SEAFLOOR VENT DEPOSITS: DEPENDENCE ON PORE EVOLUTION PROCESSES

By

Jill Leann Gribbin

Thesis submitted to the Faculty of the Graduate School of the
University of Maryland, College Park, in partial fulfillment
of the requirements for the degree of
Master of Science
2011

Advisory Committee:
Associate Professor Wenlu Zhu, Chair
Professor Philip Candela
Assistant Professor Saswata Hier-Majumder

Acknowledgements

I want to thank my advisor, Wenlu Zhu, for her support and guidance while working on this project. I also want to thank Meg Tivey of Woods Hole Oceanographic Institution with whom we have collaborated on this project. I also want to acknowledge Sarah Penniston-Dorland (UMD) for access to and help in the microscope lab; Margaret Sulanowska (WHOI) for coring our deposit samples; my thesis committee for their valuable feedback on this project; and the UMD Geology Department. Additionally, I want to thank my family, especially my mom, for their continued love and support.

I also want to acknowledge NSF grants EAR-0741339 and OCE-0648337, both of which funded this project.

Table of Contents

List of Tables

List of Figures

Chapter 1: Introduction

Seafloor hydrothermal vents provide a gateway between the Earth's interior and the oceans, regulating the flow of heat and mass between them. Vents facilitate both conductive and convective heat transport, making them important for maintaining environmental conditions within the oceans [*Lowell*, 1991; *Wilcock and Delaney*, 1996]. Heat from magma chambers associated with seafloor spreading centers is easily conducted through seafloor rock [*Lowell et al.*, 1995]. The convective transfer of heat, however, is dependent on the flow of hydrothermal fluids and the circulation of seawater from the seafloor to deep within the crust. This process relies on the percolation of cold seawater down into the crust through broad recharge zones in forms of seafloor faults, dikes, fissures, and natural basaltic pore spaces [*Sleep*, 1991; *Tivey et al.*, 1995]. As the water travels downward possibly reaching Moho depths [*Lowell and Germanovich*, 2004], it becomes hotter and loses many of its original dissolved ions, such as Mg^{2+} and SO_4^{2-}, while gaining various sulfides and oxides (i.e. Fe and Mn oxides). This chemically altered fluid becomes increasingly hot and buoyant at which point it begins to ascend to the seafloor [*Von Damm et al.*, 1998; *Henderson et al.*, 2005]. As the fluid rises through the subsurface and then to the seafloor, interactions with cold seawater will lower fluid temperatures. Changes in temperature, in addition to a change in fluid pressure, result in mineral precipitation and the formation of hydrothermal vent deposits.

Vent fields are found on the seafloor along mid-ocean ridges and back-arc basins; however, environmental conditions present at vent fields can vary. Despite differences between many vent fields, they each generally have regions of both high-temperature and lower-temperature deposits [*Elderfield and Schultz*, 1996]. High-temperature areas (Figure 1.1a) are generally characterized by large black smoker chimneys, which form from the rapid ascension (1-5 m/s) of 350-400°C fluid emission [*Haymon*, 1983; *Delaney et al.*, 1992; *Tivey et al.*, 1995]. The extreme thermal gradient existing between this fluid and the 2°C seawater it enters causes the precipitation of sulfides, anhydrite, and amorphous silica that build upwards creating the chimney structure [*Haymon*, 1983; *Tivey and McDuff*, 1990]. Black smokers tend to be situated closer to the ridge axis [*German and Parson*, 1998], where fluids can be subjected to higher temperatures within the crust and also have greater channelization due to near axis faults, which can accommodate the fluid's high speed.

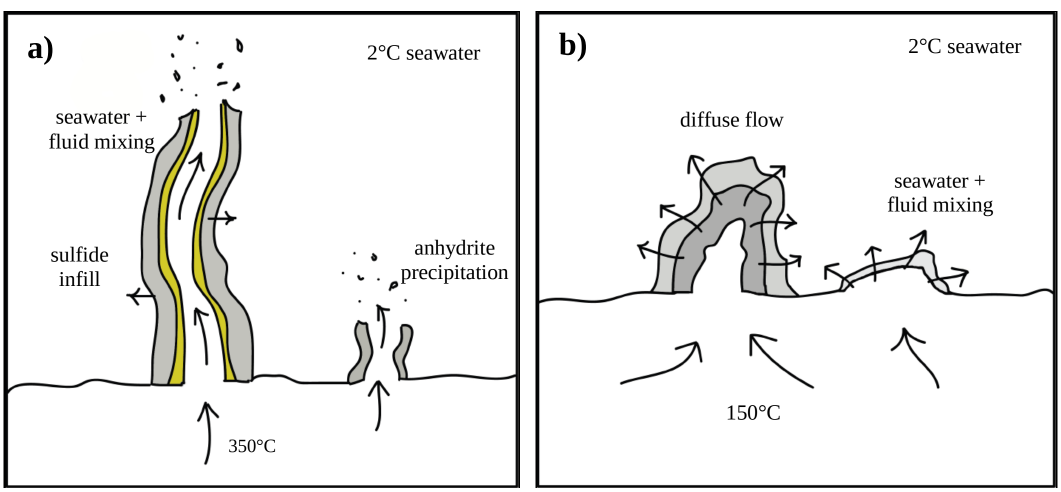

Figure 1.1: Schematic diagrams of seafloor vent deposits. **a)** Black smoker. High-temperature fluid emits through central chimney conduit with fluid diffusely transferred from structure sides; **b)** White smoker. Low-temperature fluid percolates through small branching channels. Vent deposits usually lack a well-defined central conduit.

Lower temperature diffuse vents (Figure 1.1b) are also very common at vent fields and possibly elsewhere throughout the seafloor [*Delaney et al.*, 1992;

Scheirer et al., 2006]. These deposits form in areas where fluid within the seafloor is only weakly channeled. Consequently, the hydrothermal fluid will entrain, and mix with colder seawater, resulting in precipitation of metal sulfides and anhydrite [*Tivey et al.*, 1995; *Mills et al.*, 1996]. Fluid that is diffusively expelled will generally have a temperature less than 150°C [*Pester et al.,* 2008]. Although the fluid temperature is lower than that of black smokers, diffuse deposits are believed to transfer several times more heat to the oceans than chimney deposits due to their expansiveness on the seafloor [*Rona et al.*, 1993; *Elderfield and Schultz*, 1996; *Juteau and Maury*, 1999]. The amount of flow exiting through these deposits, however, is poorly constrained, making it important to study parameters that impact this flow.

Physical properties that influence the evolution of both high- and low-temperature vent deposits include permeability and porosity. Permeability (k) is the ability of a material to transmit fluid, while porosity (ϕ) is the volume fraction of void space in a material (Figure 1.2) [*Norton and Knapp*, 1977]. Permeability is dependent upon porosity, as well as pore geometry and connectivity.

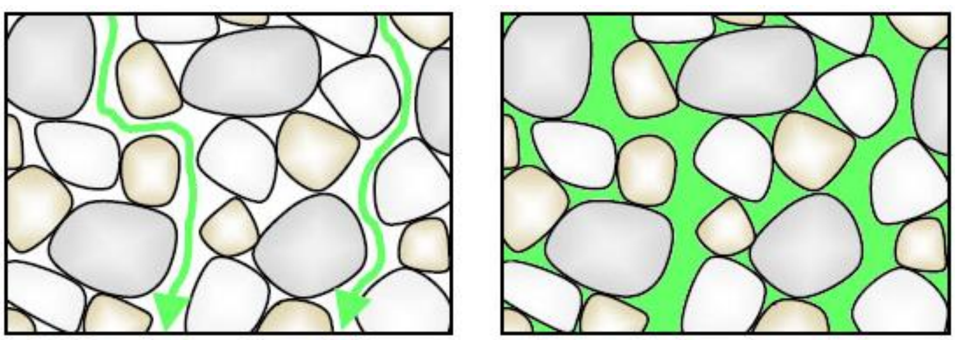

a) b)

Figure 1.2: Permeability and porosity are properties that vary in materials – differences between the two properties for the same medium are illustrated, **a)** permeability is indicated by green arrows representing available flow pathways through connected pores, **b)** the medium's porosity, shaded in green, includes all void space regardless of connectivity.

Depending on the location of a vent deposit and its exposure to hydrothermal fluids, permeability and porosity of a deposit will vary. Fluid interactions can lead to a number of processes, such as mineral dissolution, precipitation, and thermal cracking, which can significantly alter pore space and thus affect permeability. Conversely, changes in permeability and porosity will affect the mixing and distribution of vent fluids. The extent to which chemical processes resulting from fluid interactions alter permeability and porosity and thereby impact fluid flow within vent deposits is not fully understood.

In this project, permeability and porosity of vent deposit samples were measured to determine the relationships between permeability and porosity in vent deposits. Various types of vent deposits from many different vent sites were studied. Such data for the same type of vent deposits at different stages provide an evolution of permeability-porosity relationships (EPPRs) [*Zhu et al*., 2007]. Identified EPPRs can be used to constrain flow properties of vent deposits, which are crucial in modeling how vents evolve over time.

1.1 Samples Measured in Study

The seafloor vent deposits were divided into five groups based on sample type. The first sample group was composed of massive anhydrite deposits (Figure 1.3a). Anhydrite ($CaSO_4$) forms as a result of increasing seawater temperature. As the seawater is heated above ~150°C by hot rock and fluid, dissolved $CaSO_4$ becomes less soluble and begins to precipitate as anhydrite (at depths near 3000 m) [*Tivey et al*., 1995; *Kuhn et al*., 2003]. It commonly forms within seafloor cracks and on the seafloor where it forms as massive deposits or develops as the framework structure necessary for the development of metal-rich chimney structures [*Haymon*, 1983; *Tivey and McDuff*, 1990].

The second group of samples consists of portions of flanges, slabs, and crust. Flanges (Figure 1.3b) are deposits that form horizontally like tiers or ledges off the sides of larger vent structures from the precipitation of sulfides, sulfates, and possibly carbonates. Vent fluid that is emitted radially from a primary chimney structure [*Goldfarb*, 1988; *Tivey et al.*, 1999] will pool under the flange until it gradually flows out from under the flange or is diffused upwards through the flange [*Kerr*, 1997]. Conductive cooling of fluids flowing through flanges results in the precipitation of amorphous silica along grain edges [*Tivey et al.*, 1999]. Hydrothermal slabs (Figure 1.3c) are found at the Lucky Strike Vent Field along the Mid-Atlantic Ridge (MAR). They are layered silicified volcanic deposits (i.e. hydrothermally cemented breccias) rich in sulfides, barite, silica and basalt fragments [*Langmuir et al.*, 1997; *Rouxel et al*., 2004]. Fluid trapped beneath slabs will circulate and gradually diffuse through cracks in the slab. A crust deposit from the Trans-Atlantic Geotraverse (TAG) field active mound along the MAR will also be included in this group (Figure 1.3d). TAG crust is notable for its brecciation and incorporation of re-cemented vent debris [*Thompson et al*., 1985; Humphris *et al*., 1995].

The remaining three groups are composed of Zn-rich actively diffusing spires, black smoker chimneys and relict spires, respectively. The group of Zn-rich actively diffusing spires (Figure 1.3e), which includes white smoker chimneys, consists of spires that form from the emission of roughly 250-300°C fluid. This fluid is conductively cooled at depth where it will precipitate much of its sulfide components [*Hannington et al.*, 1995; *Humphris et al.*, 1995]. Fluids from these spires are depleted in sulfur, but enriched in zinc compared to fluids from higher temperature deposits. The zinc abundance is due to both the dissolution of sphalerite and remobilization of zinc at depth, which increases the fluid's zinc concentration. As the fluid is emitted the zinc is re-precipitated as sphalerite in the deposit [*Humphris et al.*, 1995]. These Zn-rich diffusing spires lack a central conduit, but instead contain numerous small channels through which fluid can be passed. In contrast, the black smoker chimneys, discussed earlier in the paper, (Figure 1.3f) rely on the precipitation of anhydrite, sulfides, and silica resulting from the interaction of high-temperature fluid (350-400°C) with seawater on the seafloor. For these structures to develop, an initial ring of anhydrite must first precipitate on the seafloor. As fluid is channeled through the anhydrite structure, sulfide minerals precipitate along the inner walls, forming a well-defined central conduit [*Haymon,* 1983; *Tivey and McDuff,* 1990]. Additionally, pore spaces within the outer anhydrite layers gradually infill due to this sulfide precipitation. Relict spires (Figure 1.3g) are spires that were not actively venting when they were recovered from the seafloor. Their inactivity presumably results from pathways becoming blocked by mineral precipitation over time. Because there are many different types of samples being measured in this study, a large range of both permeability and porosity values is expected.

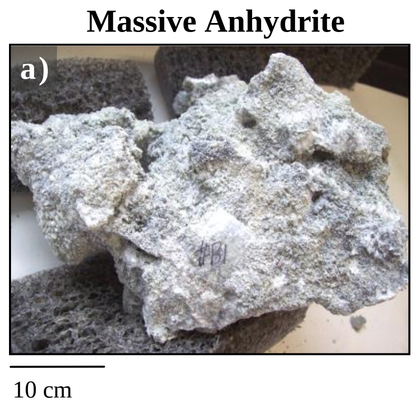

Figure 1.3: Pictures of vent deposits from each sample group. Each black scale bar represent 10 cm. **a)** Massive anhydrite [*ALV 2581-8, TAG*], **b)** Flange [*ALV 3521-R2, Guaymas*], **c)** Slab [*ALV 2608-4-1, Lucky Strike*], **d)** Crust [*ALV 2179-1-1, TAG*], **e)** Zn-rich actively diffusing spire [*ALV 2187-1-1, TAG*], **f)** Black smoker chimney [*J2-213-3-R1, Kilo Moana*], and **g)** Relict spire [*J2-136-6-R1, ABE*].

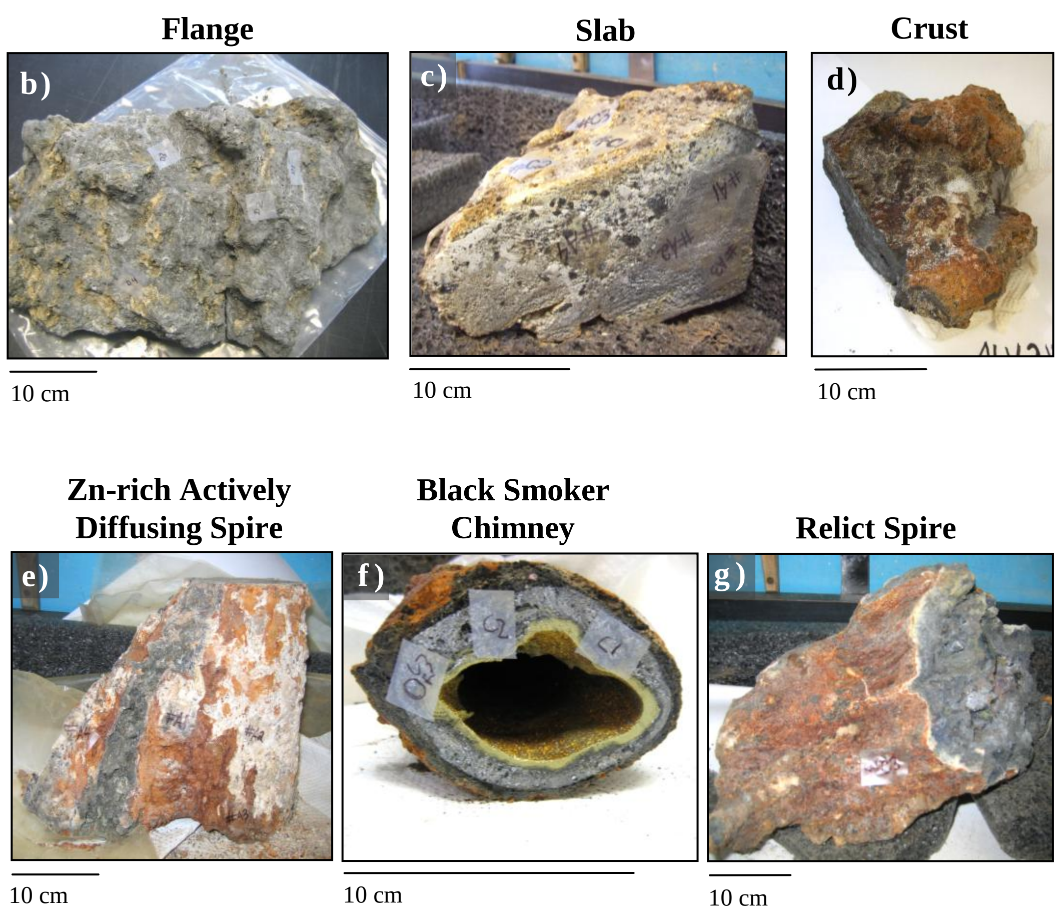

1.2 Geologic setting

In this study, permeability and porosity of vent samples recovered from ten different vent fields have been measured (Figure 1.4). Each location has variations in environmental conditions that are important to consider when linking the effects of pore evolution processes on the evolution of permeability and porosity within the deposits.

Figure 1.4: Vent field locations (red circles) from which deposit samples were recovered. From left to right: Fenway, Kilo Moana & ABE, Juan de Fuca (includes Main Endeavour Field and Cleft), Guaymas Basin, Trans-Atlantic Geotraverse (TAG), Lucky Strike, and Central Indian Ridge (CIR).

A few samples have been collected from the Fenway vent field in the Manus back-arc basin in the Bismarck Sea near Papua New Guinea. The vent field is dominated by a large two-tiered mound upon which several high-temperature black smoker chimneys have developed [*Craddock and Bach*, 2010]. Outer portions of the mound are covered in sulfide chimney debris, massive anhydrite outcrops, and hydrothermal sediment, which accommodate lower temperature diffuse flow [*Craddock and Bach*, 2010]. Recovered anhydrite from

Fenway tends to be coarse-grained, suggesting that the anhydrite likely precipitates within cavities accessible to fluid flow that are capped by a less permeable sulfide-rich layer. Over time, these sulfide layers collapse, exposing the anhydrite deposits [*Craddock and Bach*, 2010].

There is one sample that has been recovered from the Edmond vent field along the Central Indian Ridge (CIR) nearby the Rodriguez Triple Junction. The vent field is partially covered by lava flows, pillow basalts, and sediment and is believed to have experienced robust magmatism for about 2 Myr [*Kumagai et al*., 2008]. Vent fluids sampled from the Edmond field show low Na/Cl ratios (though fluid is enriched in both Na and Cl) and high Ca/Cl ratios, which can be explained by ongoing albitization of subseafloor rocks [*Gallant and Von Damm*, 2006]. Measured temperatures from spires show typical values, with high temperatures around 380°C [*Kumagai et al*., 2008].

Two carbonate-rich vent samples have been recovered from the Guaymas Basin vent field in the Gulf of California. Guaymas Basin is notable for its rapid rate of sediment deposition and high concentrations of dissolved carbon compounds that result from the interaction of fluids with organic-rich sediments [*Pearson et al.*, 2005]. Previous work has shown that both sulfides and calcite/barite are large constituents of hydrothermal deposits at Guaymas [*Koski et al*., 1985]. Sampled vent fluids are depleted in Zn, Cu, and Fe due to sediment and subsurface reactions, which is unusual for sulfide deposits [*Koski et al.*, 1985]. Fluid temperatures and alkalinity are largely consistent with other vent fields.

Four samples will be measured from the Lucky Strike hydrothermal field along the MAR. Lucky Strike is dominated by a large volcanic seamount that has deposited multiple lava flows across the area. Many different vent structures are present at Lucky Strike: high- and low-temperature chimneys, relict spires, flanges, anhydrite deposits, and slabs [*Langmuir et al.*, 1997]. Sampled vent fluids exhibit slightly lower silica concentrations than found in most mid-ocean ridge vent fields and also lower hydrogen sulfide contents [*Langmuir et al.*, 1997]. Fluid temperatures depend on location within the vent field and appear to change over time-scales as short as a few days, suggesting influences from seafloor eruptions.

Moving further south along the MAR, the TAG vent field has a large central mound constructed from the build-up and collapse of hydrothermal material situated atop an area of brecciated seafloor [*Humphris et al.*, 1995]. Strong mineralogical zoning is present on the TAG mound, with high-temperature, chalcopyrite-anhydrite rich chimneys clustered predominantly at the top of the mound. Lower-temperature Zn-rich diffusing spires are common lower down on the sides of the mound [*Humphris et al.*, 1995]. Extensive anhydrite veining is also present at TAG as a result of seafloor crack infill. The anhydrite abundance indicates that the TAG mound environment regularly maintains seawater temperatures >150°C to allow for retrograde anhydrite precipitation [*Humphris et al.*, 1995]. Multiple samples from the TAG field have been measured in this study.

Along the Juan de Fuca Ridge (JFR), several vent fields have been discovered from which vent samples have been included in this study. A few vent samples have been collected from the Main Endeavour Field (MEF) located along the northern portion of the JFR. The MEF is characterized by large sulfide chimneys, areas of diffuse flow, and many inactive spires and flanges [*Tivey et al.*, 1999]. Vent fluids from MEF are unusual in that they have a high pH (4.2-4.5), exhibit a strong temperature and chlorinity gradient across the field, and have high concentrations of methane and ammonia [*Tivey et al.*, 1999]. Samples from the Cleft segment of the southern JFR have also been measured. The Cleft segment is focused around an untectonized lava plain that houses three major areas of high temperature vents [*Embley and Chadwick*, 1994]. Both high-temperature and diffuse deposits have been detected along the segment, with most found along seafloor fissures. A large majority of the vents along the Cleft segment are not actively venting; it is believed that many of them vented in accordance with lava producing seafloor eruptions [*Embley and Chadwick*, 1994]. These older deposits have high silica content and pyritic mineralogy [*Embley and Chadwick*, 1994].

Samples have also been recovered from both the Kilo Moana and ABE vent fields located along the Eastern Lau Spreading Center, located near the islands of Fiji and Tonga. Seafloor bathymetry of Kilo Moana shows two broad low relief volcanic domes cross-cut by fissures where vent structures have formed [*Ferrini et al.*, 2008]. Both high-temperature and diffuse vent structures have been detected there. The ABE vent field is highly faulted with evidence for several lava flows and heavy sedimentation [*Ferrini et al.*, 2008]. Most venting spires are surrounded by diffusely venting structures. Flanges forming off the sides of spires and occasionally off of lava flows are common. Between the two vents fields, ABE is slightly shallower and less acidic (4.3-4.9) than Kilo Moana [*Ferrini et al.*, 2008].

Chapter 2: Pore Evolution Processes and Permeability Change

There exists no single relationship between permeability and porosity that is applicable to all materials. However, correlations can be made for materials under specific conditions. Permeability (k) can be related to porosity (ϕ) through a power-law relationship (Equation 2.1) whereby the exponent, α, is sensitive to changes in a material's pore structure [e.g., *Turcotte and Schubert*, 1982; *Zhu et al.*, 1999; 2007; *Bernabé et al.*, 2003]. The value k_0 is the permeability at a reference porosity ϕ_0 [*Zhu et al.*, 1995].

$$\left(\frac{k}{k_0}\right) \propto \left(\frac{\phi}{\phi_0}\right)^{\alpha} \tag{2.1}$$

This relationship can be depicted as a line in log(k) vs. log(ϕ) plot where α is the slope of this line [*Bernabé et al.*, 2003]. Higher α values (i.e., steeper slopes) represent greater changes in permeability with respect to changes in porosity.

A number of diagenetic processes (e.g. compaction, dissolution) can alter a materials pore structure; these processes define the evolution of permeability-porosity relationships (EPPRs). EPPRs can be used to provide a convenient description of how transport properties evolve during a specific diagenetic process.

A variety of theoretical [e.g., *Paterson*, 1983; *Walsh and Brace*, 1984], numerical [e.g., *Steefel and Lasaga*, 1994; *Quispe et al.*, 1995; *Zhu et al.*, 1995, 1999], and experimental studies [*Bernabé et al.*, 1982; *Bourbie and Zinszner*, 1985; *Zhang et al*., 1994] have examined permeability and porosity under different conditions and have found a range of EPPRs [*Guéguen and Palciauskas*, 1994; *Bernabé et al.*, 2003]. Deep sea hydrothermal vent deposits are products of the interaction between aqueous fluids and sea water. The vent structures, in turn, exert important control of fluid flow distribution. To understand this coupled system, it is important to quantitatively characterize EPPRs of vent deposits from various sites. Several physical and chemical processes that can significantly alter pore structures have been described in previous studies on sedimentary rocks. These processes are pertinent to vent formation and thus will be summarized here.

A simple analog of a porous material is a cubic matrix embedded with identical tubes (Figure 2.1). In this analog the tubes constitute all of the material's pore space. Assuming laminar flow conditions, permeability can be related to porosity with an α value of 2 [*Turcotte and Schubert*, 1982]. If the tubes are replaced by cracks where the apertures of the tubes differ from their diameters, then permeability and porosity can be related with an α value of 3 [*Guéguen and Palciauskas*, 1994]. While the isotropic and homogeneous tube model is idealized compared to those of true materials, it provides a good frame of reference from which permeability-porosity relationships of more complex pore networks can be estimated. Understanding these basic EPPRs provide a good foundation for exploring the effects of different pore evolution processes. Next, the effects of mechanical compaction, hot isostatic pressing, thermal

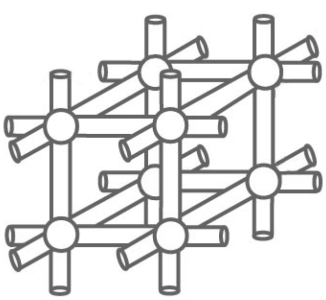

Figure 2.1: Diagram of a simple cubic matrix of circular tubes. This pore geometry yields a permeability-porosity relationship with an α value of 2. This relationship is a good reference for considering more complex EPPRs.

cracking, precipitation, and dissolution, all of which are processes pertinent to the formation of vent deposits, on pore structure are discussed, in addition to how they result in permeability-porosity relationships significantly deviating from the simple tube model (Table 2.1).

Processes	Materials	α
Plastic compaction	Synthetic aggregates	2.5–3 α increasing with decreasing ϕ if disconnection occurs
Sintering	Porous glass	4.5 for $\phi < 0.10$ disconnection at $\phi \approx 0.04$
Semi-brittle compaction	Salt aggregates	5–7
Elastic compaction	Sandstones	1–25 depending on microstructure
Cataclastic compaction (hydrostatic)	Sandstones $\phi > 0.30$	≈ 20
	$0.15 > \phi > 0.30$	10–20
	$\phi < 0.15$	≈ 10
Cataclastic compaction (triaxial)	Sandstones $\phi > 0.30$	5–10
	$0.15 > \phi > 0.30$	10–20
	$\phi < 0.15$	≈ 20
Dilatant microcracking	Dense rocks	7–8 α decreasing with increasing ϕ
Thermal microcracking	Dense rocks	5–7 $\alpha \approx 1$ at very low ϕ
Dissolution	Sedimentary rocks	>20
Precipitation	Sedimentary rocks	≈ 8
Chemical alteration (roughening)	Porous glass	>10
Diagenesis	Sedimentary rocks	α decreasing with decreasing ϕ $\alpha \approx 2$ at $\phi < 0.10$

Table 2.1: Chart listing compiled α values for multiple pore evolution processes obtained from experimental studies on a variety of natural and synthetic rock types. Chart taken from *Bernabé et al.* [2003].

2.1 Mechanical Compaction

If pressure is applied to a porous material, its granular structure and pore space will be compacted. This compaction will result in tighter grain packing, which will limit the amount of space available between grains (Figure 2.2). This reduction in pore space, in addition to the changes in pore geometry, will result in a permeability decrease within the material. The magnitude of the permeability reduction will depend on many factors, including the initial pore geometry of the material and the magnitude of the pressure applied.

Previous studies identified two different regimes of mechanical compaction on porous sandstones [e.g., *Zhang et al*., 1990; *Zhu and Wong*., 1996]. When the applied pressure is relatively low, resultant changes in pore space are mostly reversible. Many studies analyzed suites of elastically deformed sandstones and found a large range of observed EPPRs with α values spanning roughly 1-21 [*Bernabé et al.*, 1991; *Fredrich et al.*, 1993; *David et al.*, 1994]. However, when the pressure applied exceeds a given threshold, grain crushing and pore collapse occur, where resultant changes in pore space of previously pressure-insensitive pores are non-reversible (Figure 2.2c). The extent to which k will change as a result of changes in ϕ depends highly on the initial pore geometry of the sample. Samples having a high initial ϕ show a steeper trend as they move into the brittle regime, whereas samples with a low initial ϕ experience a decrease in trend during this transition [*Bernabé et al.*, 2003].

These correlations determined from porous sandstones may be applicable to vent deposits. Many vent deposits have structures consisting of interlocking crystals; however, some have a granular structure with pore space distributed somewhat similarly to that of sandstone. In deposits that exhibit this structure it is important to look for evidence of mechanical compaction. Larger isolated pores located at grain junctions may be indicative of elastic compaction, whereas crushed grains may provide evidence for brittle compaction.

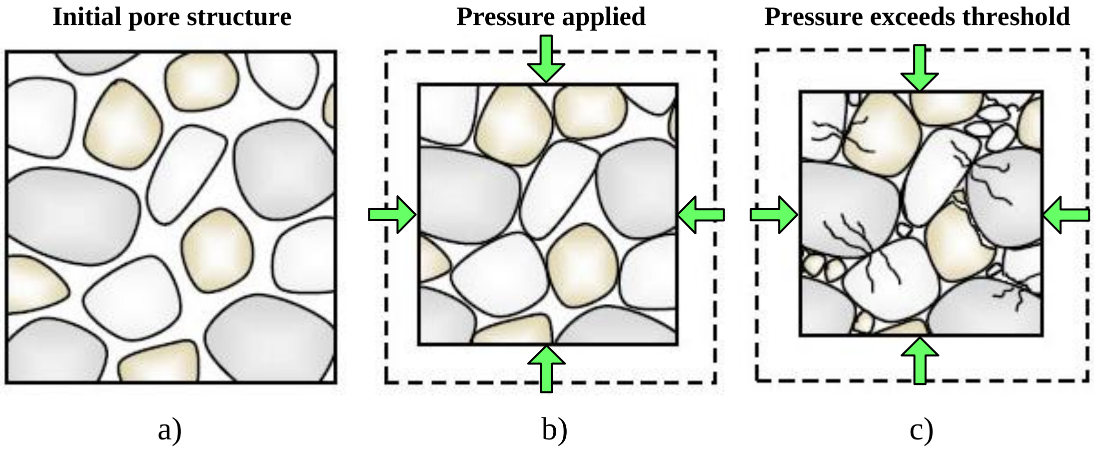

Figure 2.2: Diagrams illustrating the effects mechanical compaction on pore structure. **a)** Initial pore structure prior to compaction. **b)** Uniform application of pressure (green arrows) on pore structure from a) results in tighter grain packing and a reduction in *k* and ϕ. Dashed box represents initial sample size. **c)** When the applied pressure exceeds the threshold pressure, non-reversible grain crushing and pore collapse occur further decreasing *k* and ϕ.

2.2 Hot Isostatic Pressing (HIP)

A porous material subjected to high temperatures and pressures will densify during the process of hot isostatic pressing (HIP) (Figure 2.3). As a result of the high temperature conditions, HIP is a plastic pore evolution process. Experiments on synthetic rock aggregates are conducted under both dry and wet conditions [e.g., *Bernabé et al.*, 1982, 2003; *Zhang et al.*, 1994; *Wark and Watson*, 1998], similar to environmental conditions during diagenesis.

Previous studies show that there is a critical porosity during HIP of calcite aggregates and carbonate rocks. In rocks with porosity greater than the critical porosity, the exponent α value is approximately 3, whereas below the critical porosity higher α values are observed [*Bernabé et al.*, 1982, 2003; *Zhang et al.*, 1994]. *Zhu et al.* [1999] show that the interplay between pore space shrinking due to plastic deformation of grains and isolation of pores at grain junctions from the pinching off of connecting tubes is responsible for the change in EPPRs above and below the critical porosity.

Unlike in calcite, HIP of wet quartz does not produce major changes in EPPR, which suggests that pore disconnection through tube pinch off does not regularly occur within these rocks [*Wark and Watson*, 1998].

HIP experiments are good analogs to natural pore evolution processes and allow us to investigate the mechanisms that operative during plastic compaction and how they affect EPPRs. Although pressures and temperatures exerted on vent deposits are lower than those in most HIP experiments, seafloor hydrothermal deposits may experience deformation similar to that seen during HIP.

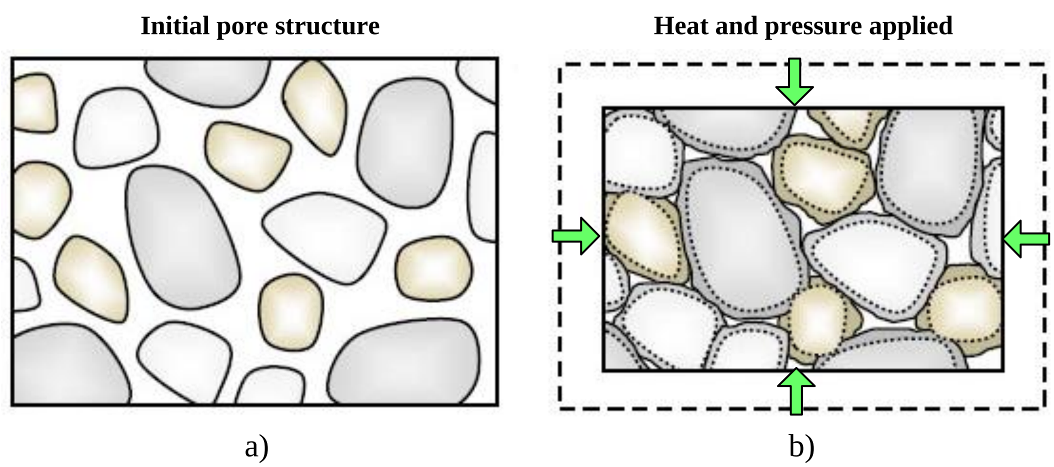

Figure 2.3: Diagrams illustrating the effects of hot isostatic pressing (HIP) on pore structure. **a)** Initial pore structure prior to HIP. **b)** Uniform application of pressure (green arrows) and heat on pore structure from a). Dashed box represents initial sample size. Pressure compacts the grains, reducing pore space, while the heat causes the grains to expand outward into pore space. Dotted lines show initial grain sizes and darker shaded areas around grains represent thermally expanded portions of the grains. Together the compaction and thermal expansion create a dense material with limited permeability and porosity.

2.3 Thermal Cracking

Stresses caused by large changes in temperature can produce isotropic microcracks throughout a porous material (Figure 2.4). Internal stresses are caused by the thermal expansion of grains, which can create grain size mismatches and anisotropy within a material [*LeRavalec et al.*, 1996]. Therefore, the magnitude of these stresses is controlled by the thermoelastic properties of the mineral grains within the material [*deMartin et al.*, 2004]. The development of thermal cracks can potentially have a significant impact on the permeability of a material.

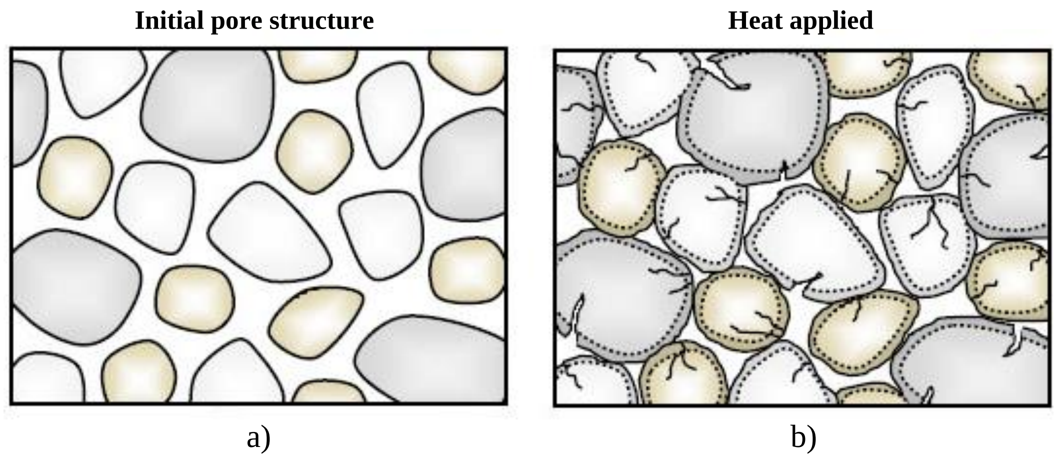

Figure 2.4: Diagrams illustrating the effects of thermal cracking on pore structure. **a)** Initial pore structure prior to heat application and cracking. **b)** Application of heat on pore structure from a) causing the grains to expand outward into pore space and develop isotropic cracks. Dotted lines show initial grain sizes with darker shaded areas around grains representing thermally expanded portions of the grains. Thermal cracks produced during grain expansion can potentially increase permeability despite pore space loss to grain expansion.

Studies investigating the effects of thermal cracking on permeability involve the controlled heating of rocks, in some instances via HIP, for extended periods of time followed by a period of controlled cooling. Depending on the techniques employed, the nature of thermal cracking varies within samples, which leads to some differences in how the cracks influence permeability. In mylonite samples that were exposed to a simple thermal treatment (no HIP), increasing temperatures resulted in increased porosity in the form of well-connected cracks [*LeRavalec et al.*, 1996]. The increased connectivity in these samples yielded higher permeability values; however, these permeabilities are sensitive to changes in pressure. A small increase in confining pressure on the samples would close the microcracks and decrease the permeability [*LeRavalec et al.*, 1996].

With experiments using HIP, samples are heated and pressurized to create a relatively impermeable sample with few cracks. A study with olivine aggregates used the HIP technique and then evaluated crack growth and permeability development during cooling and depressurization [*deMartin et al.*, 2004]. This study found that longer HIP durations inhibited the development of large crack networks, because pressing reduced the number of potential initiation sites. Also, larger grains were more prone to developing cracks because of increased stresses [*deMartin et al.*, 2004]. As a result porosity would somewhat increase in these samples due to crack formation without significantly enhancing permeability. On average, *Bernabé et al.* [2003] notes α values ranging from 5-7 for samples having experienced thermal cracking (Table 2.1).

The contrasting temperatures of hot hydrothermal fluids and cold seawater present at seafloor vent fields may make vent deposits susceptible to pore structure changes resulting from thermal cracking. Cracking, if present, may increase deposit permeability and potentially channel fluids moving through the deposits. Most vent deposits are initially quite porous, so the effects of thermal cracking may be expected to be more similar to those obtained without HIP.

2.4 Precipitation

Although the processes discussed thus far have been physical processes, chemical processes can also produce large changes in permeability. Precipitation occurs as fluids saturated in various ions pass through a material and react to produce solid mineral phases. Because the fluids must pass through pore space, precipitates formed during the chemical reactions will be deposited within the pore space. This precipitation can lead to a narrowing of channels and pores, thereby decreasing permeability and restricting the overall flow of fluid.

A good example on how precipitation affects EPPRs is Fontainebleau sandstone from Paris basin. This well-sorted sandstone is monomineralic (99.9% quartz) with a wide range of porosity due to different degrees of cementation resulted from groundwater oversaturated with quartz. *Bourbie and Zinszner* [1985] conducted permeability measurements on a suite of Fontainebleau sandstone samples with initial porosity from 3-28%. They found that for samples with porosity greater than 7%, the exponent α value is approximately 3, whereas below the 7%, α value increases to ~7 (Table 2.1). *Zhu et al.* [1995] show that the increase in the α value can be explained by pore connectivity loss in low porosity samples.

Experiments transmitting fluids through sandstones [*Reis and Acock*, 1994; *Todd and Yuan*, 1992] have shown that mineral precipitation, as expected, produces a loss of both permeability and porosity. These studies found that precipitation within pore space produces roughness along pore walls (Figure 2.5). Roughness creates irregularities along pore walls with small pockets that cannot effectively transmit flow [*Bernabé et al.*, 2003]. Although the precipitated roughness may contain pores, lessening the net loss of porosity, permeability is greatly restricted by the roughness, particularly because the pore wall topography will narrow or even pinch off pore channels limited connectivity. Because of this large decrease in permeability with respect to minor reductions in porosity, samples experiencing precipitation will have high α values, averaging about 8 (Table 2.1) [*Bernabé et al.*, 2003].

Seafloor vent deposits regularly transmit fluids rich in a range of ions, many of which begin to precipitate upon emission to the seafloor. It has been previously shown [*Zhu et al.*, 2007] that precipitation can dramatically impact the permeability and porosity of vent deposits, such as relict spires. High degrees of precipitation with spires lead to a loss of connectivity and an inability to continue transmitting fluids. Therefore, it is important to identify occurrences of late-stage precipitation within the deposits included in this study.

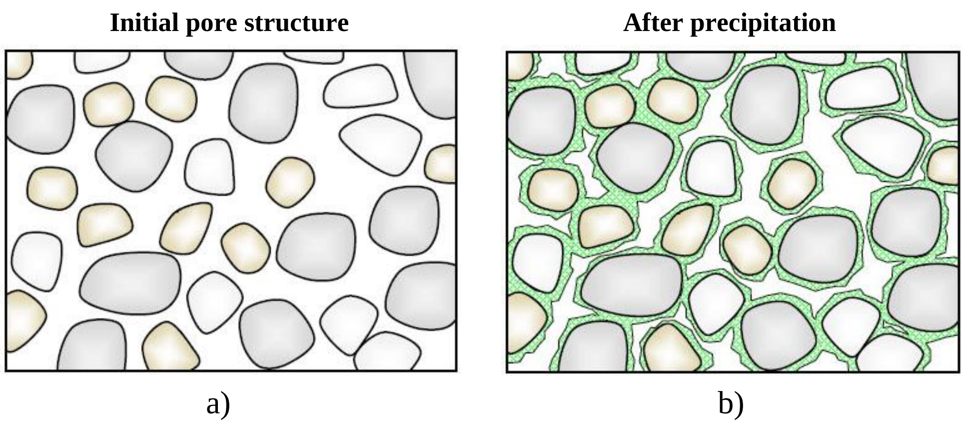

Figure 2.5: Diagrams illustrating the effects of precipitation on pore structure. **a)** Initial pore structure prior to precipitation. **b)** Late-stage mineral precipitation (green areas) within the pore structure of a) creating roughness along pore walls. Roughness narrows pore channels and in some cases pinches off channels. These effects decrease the porosity and restrict the permeability of the material.

2.5 Dissolution

Much like precipitation, dissolution is a chemical process that can produce large changes in a material's pore structure. Dissolution occurs when the chemical components of a fluid react with and breakdown the surrounding grain/crystal host structure. The dissolved components of the material become entrained in the fluid and get carried away or potentially re-precipitated as the fluid passes through the host structure. As a result, mineral dissolution increases the porosity of a material, while typically also enhancing the permeability.

The extent of dissolution a material experiences depends highly on the chemical composition of the fluid, particularly its acidity, and the composition of the host material. For example, studies have been conducted on sandstones and carbonate rocks whereby acidic fluid is passed through the rocks and changes in k and ϕ are then observed [*McCune et al.*, 1979; *Luquot and Gouze*, 2009]. Dissolution was shown to enhance permeability in both cases; however, the increase in permeability in the carbonate rocks was several orders of magnitude higher than the increase seen in the sandstones. The dissolution along grain edges helps create wider and more connected flow channels, particularly in areas of the pore network that were initially well-conducting pores (Figure 2.6) [*Bernabé et al.*, 2003]. The differences in the extent of dissolution between the two rock types is confirmed by their respective α values, with the sandstones have α values from 8-10 and the carbonate rocks having much higher α values ~ 20 (Table 2.1) [*Bernabé et al.*, 2003].

The majority of analyzed hydrothermal fluids have been found to be acidic, making dissolution reactions common during fluid migration. Certain vent deposits that contain higher abundances of carbonate minerals may be more susceptible to dissolution. Given the large impact dissolution can have on the pore structure and permeability of any material, it is important to identify whether dissolution has occurred within the vent deposit samples.

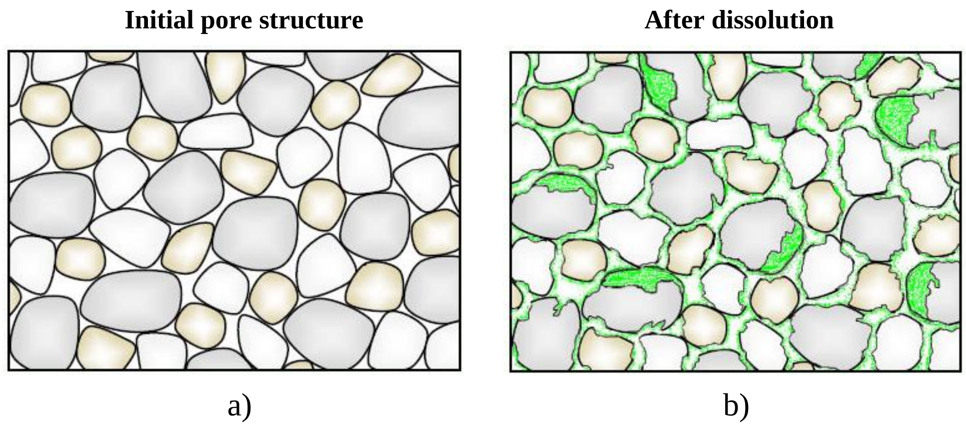

Figure 2.6: Diagrams illustrating the effects of dissolution on pore structure. **a)** Initial pore structure prior to dissolution. **b)** Fluid reacts with and dissolves grains, removing material (green regions) and decreasing grain size, thereby increasing pore space and significantly enhancing permeability.

Chapter 3: Experimental Methods

3.1 Probe permeability

Vent deposits are heterogeneous. The permeability of vent deposits is generally heterogeneous and anisotropic. To assess the heterogeneity and anisotropy of the various deposits, permeability measurements were taken at multiple sites from multiple facets of each deposit sample using a probe permeameter. Variations in probe permeability values provide a measure of sample heterogeneity [*Zhu et al.*, 2007].

Permeability measurements on vent deposits were conducted by using a portable probe permeameter, the NER TinyPerm II™ (Figure 3.1a). The probe permeameter measurements provide a quantitative measurement of permeability heterogeneity within the samples. Comparison of permeability values obtained from different facets of a vent sample can be used to identify existing anisotropy.

The probe permeameter is a syringe-like device that pulls air out of a sample through a compressible rubber tip (Figure 3.1b). The compressible tip is held firmly against the sample surface to reduce the possibility of leaked air (Figure 3.1c). A micro-controller unit within the permeameter monitors the syringe volume as air is pulled from the sample. While air is pumped from the vicinity of the sample surface, transient vacuum pulses are created. Air is pulled from the near-surface region around the measurement site, where it is not directionally restricted. A signal processing algorithm determines the permeability using the vacuum pulses and syringe volume.

To assess the permeability anisotropy of each sample, permeability values along different orientations were compared by conducting measurements on multiple facets of the sample. Along each facet, permeability was measured at several different sites. At each measurement site, five permeability measurements were collected (Figure 3.1c). Permeability values provided for each site are given by the geometrical mean of the 5 measurements.

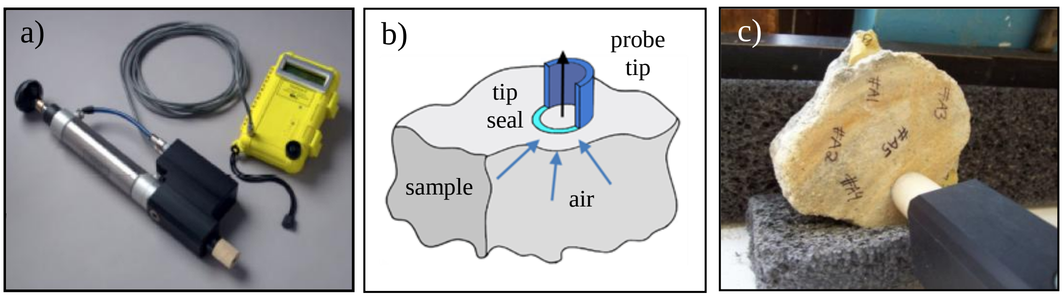

Figure 3.1: **a)** NER TinyPerm II^{TM} probe permeameter. **b)** Operation of a probe permeameter—the probe tip seal against a sample surface and air being pumped from the sample. **c)** A probe permeameter in use—multiple measurement sites along the sample surface are shown by the black labels. At each site, 5 measurements were conducted.

3.2 Core permeability

Because the flow pattern around the probe tip is unknown (Figure 3.1b), the probe permeability are not unidirectional. Furthermore, there are no porosity data available for the vent samples. To quantify the permeability–porosity relationships in vent deposits, right-cylindrical cores were then taken near the selected probe permeameter measurement sites so that core permeability data can be compared to the probe permeability data obtained. The cores are 2.54 cm (1 inch) in diameter and their lengths vary from ~1-6 cm.

Using these cylindrical cores, permeability was measured along the axial direction with a nitrogen permeameter, the UltraPerm^{TM}400. The permeameter uses Darcy's law, whereby fluid flow is proportional to a differential pressure over a given length, to determine sample permeability. This relationship can be rearranged to solve for permeability, assuming a number of flow properties are known (Equation 3.1). This expression requires a well constrained flow of nitrogen through the sample that can then be used in conjunction with recorded upstream and downstream pressures to determine the permeability of the core. The sample length (L) and cross-sectional area (A) are input for each core, while the nitrogen flow rate (Q), upstream pressure (P_1), downstream pressure (P_2), and flow viscosity (μ) are measured by the permeameter. Since the permeameter uses Darcy's law, it is critical that the flow rate is low (~ 3 cm^3/min), because Darcy's law only holds true for linear laminar fluid flow.

$$k = \frac{Q\,L\mu}{\left(P_1 - P_2\right)A} \tag{3.1}$$

Unlike with the probe permeameter, fluid flow through the sample is restricted along the axial direction by the application of impermeable jackets against the cylindrical surface. To circumvent problems caused by surface roughness, such as large voids positioned along the sample surface, plastic wrap was also applied around the sample. To prevent by-flow between the sample and the impermeable jacket, higher confining pressure was applied. Additionally, to account for gas slippage within pore space that can occur during measurement, a Klinkenberg correction has been applied to the permeability data.

Higher confinement could cause mechanical compaction of the sample and consequently alter sample porosity and permeability. To address this problem, permeability measurements were taken at multiple confining pressures, increasing incrementally from 0.5-2.7 MPa (~ 70-400 psi). After completing measurements taken at each incremental confining pressure (loading cycle), measurements were then taken with confining pressure decreasing from the peak pressure (unloading cycle) to 0.5 MPa. The permeability data obtained during the loading and unloading cycles can be used to gauge the effect of confining pressure on the core's permeability. Five permeability measurements were made at each confining pressure. Geometrical mean and the standard deviation of these values were determined.

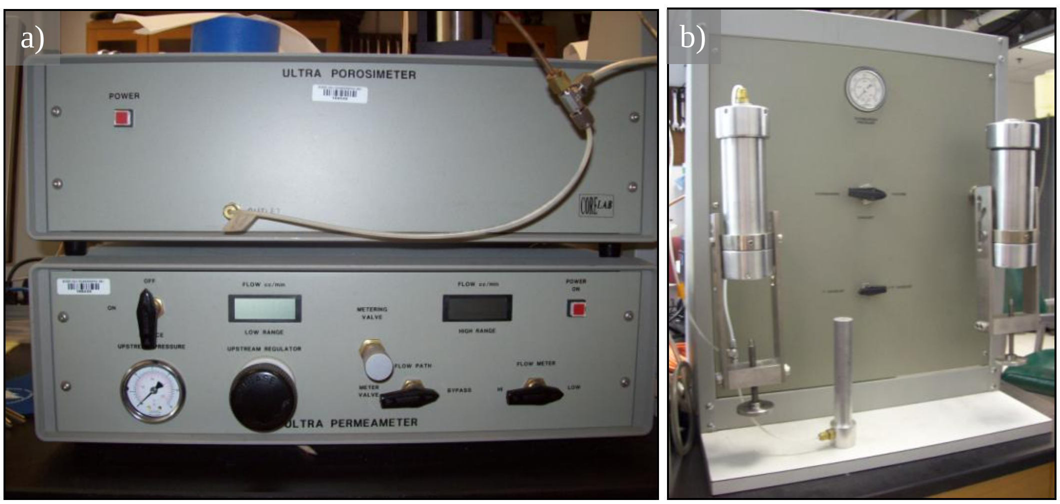

Figure 3.2: **a)** UltraPerm™400 nitrogen permeameter (bottom) and UltraPore™300 helium porosimeter (top). **b)** Pressure chamber used with the nitrogen permeameter and helium porosimeter. 2.54 cm diameter cores were measured in the left chamber.

3.3 Porosity

Porosity measurements have been made on the sample cores using a helium porosimeter, the UltraPore™300. The operation principal of the porosimeter is based on Boyle's law (Equation 3.2), where pressure and volume are inversely proportional at a constant temperature.

To obtain the porosity, it is first necessary to measure the sample pore volume. Measuring the pore volume requires the porosimeter to use a reference volume. In this case, a known volume of helium is held in a reference cell under a known pressure of 1.4 MPa. These values will serve as the initial conditions V_1 and P_1, respectively. As measurement begins, helium from the reference tank is directed into the sample core resulting in a pressure drop within the reference tank. Once the helium fills the sample's available pore space, the decreased pressure in the reference tank is recorded as P_2. The remaining volume of helium within the tank is recorded as the dead volume (V_{dead}), with V_2 equaling the sum of the sample's pore volume (V_{pore}) and V_{dead} (Equation 3.3). Using these values, V_{pore} can be solved for (Equation 3.4).

$$\frac{P_1 V_1}{T_1} = \frac{P_2 V_2}{T_2} \quad where\ T_1 = T_2 \tag{3.2}$$

$$P_1 V_1 = P_2 (V_{dead} + V_{pore}) \tag{3.3}$$

$$V_{pore} = \frac{P_1}{P_2}\left(V_1 - V_{dead}\right) \tag{3.4}$$

To determine the sample porosity, the core's bulk volume (V_{bulk}) is needed, which can be found using measured values of the core's length (l) and diameter (d) (Equation 3.5). The porosity is then calculated by dividing the pore volume by the bulk volume (Equation 3.6).

$$V_{bulk} = \left(\frac{d}{2}\right)^2 l\pi \tag{3.5}$$

$$\phi = \frac{V_{pore}}{V_{bulk}} \times 100 \tag{3.6}$$

The procedure for sample preparation is similar to that described for permeability measurements. Because using helium makes the experimental setup more susceptible to by-flow, higher confinements are applied for porosity measurements. Five pore volume measurements are made at confining pressures of 2.1-3.1 MPa. Cores having a length ≤ 2.54 cm were measured with a steel core (with a known volume of 14.8 cm^3) so that the measurement is conducted on a more substantial bulk volume that yielded more accurate pore volume measurements. In these cases, the total calculated pore volume for the combined cores was accepted as the pore volume for the vent core, assuming negligible pore volume for the steel core. The porosities were then determined using this calculated pore volume and the bulk volume of the sample core.

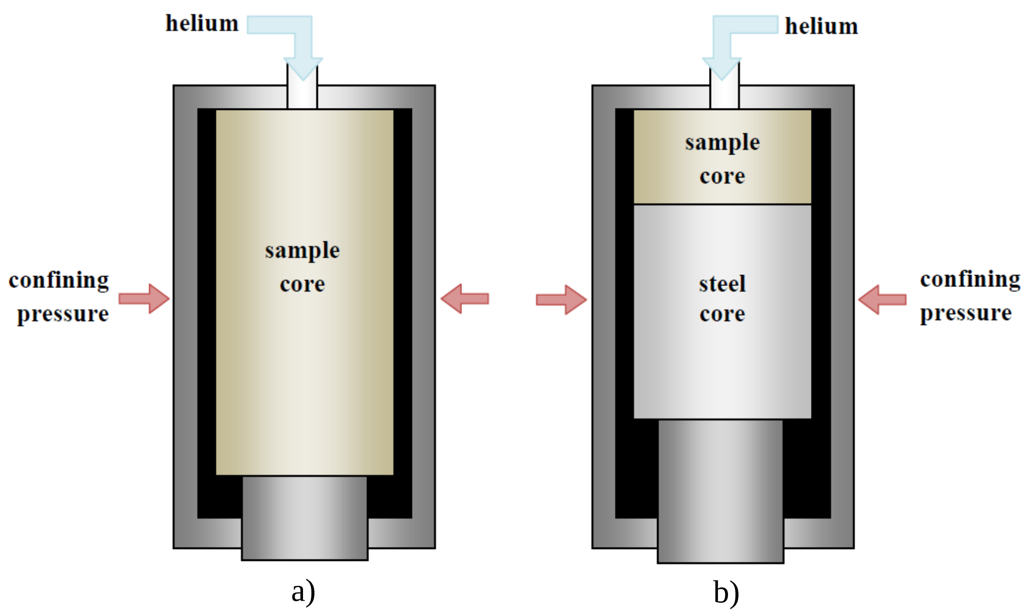

Figure 3.3: Experimental setup for porosity measurements using a helium porosimeter. **a)** A core sample with plastic wrap along its side is placed within the pressure chamber. **b)** Core shorter than 2.54 cm together with a steel core within the pressure chamber. The steel core helps to create a better seal around the sample thus increasing the accuracy of the porosity measurements. In both cases a confining pressure is applied along the radial directions, while helium is flowing through the core along the axial direction.

Permeability-porosity relationships of vent deposits can be obtained. Compiling the porosity and permeability values collected on vent samples at different formation stages provides the evolution of permeability and porosity of seafloor hydrothermal vents.

3.4 Petrography

After completing the permeability and porosity measurements, thin sections were made from a large subset of the cores. Thin sections were 30 μm thick and were impregnated with epoxy. Sections were cut both radially (Figure 3.4a) and axially (Figure 3.4b) through the cores. Microstructural analyses using reflected and refracted light petrography were then conducted on thin sections to identify pore evolution processes. These analyses are necessary in order to interpret the EPPRs observed for the different samples. Evidence for processes, such as mineral dissolution or precipitation, were recorded in addition to other sample characteristics, including grain size, sorting, and packing. The overall mineralogy of the samples was also noted. While these sections only represent a 2-D cross-section through the sample, in many cases, different orientations of sections from the same sample could be compared and used to make inferences regarding the 3-D structure of the sample (Figure 3.4c).

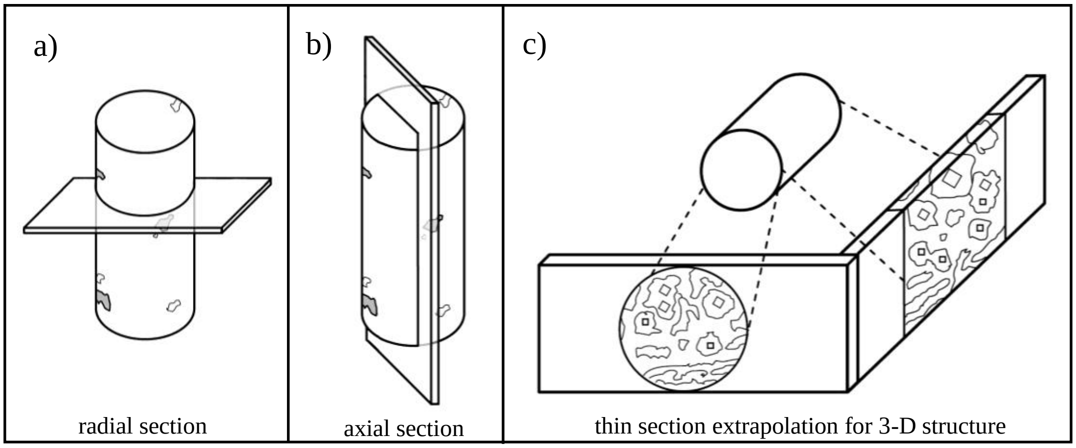

Figure 3.4: Diagrams showing orientation of thin sections cut from cores and their relation to the 3-D structure of the sample. **a)** A radial cut through a core. **b)** An axial cut through a core. **c)** How radial and axial thin sections for the same sample can be used to make inferences about the 3-D structure.

Chapter 4: Massive Anhydrite

Measured anhydrite samples were recovered from three different vent fields: the Fenway vent field within the Manus Basin, the Edmond vent field along the Central Indian Ridge (CIR), and the Trans-Atlantic Geotraverse (TAG) along the Mid-Atlantic Ridge. For this study, there were a total of 8 samples measured: 3 from Fenway, 1 from CIR, and 4 from TAG.

4.1 Permeability and Porosity

Probe permeability measurements were made along the surface of each of the samples; these data are plotted in Figure 4.1. The permeability data ranged from ~ 1×10^{-14} to 6×10^{-12} m^2. These data represent permeability measurements made along the various sides of the samples, and no systematic difference in permeability values was observed. This suggests that there is not significant permeability anisotropy within these samples. In a few samples, such as J2-216-5-R1, the degree of the surface roughness varies considerably (Figure 4.2). For these samples, permeability

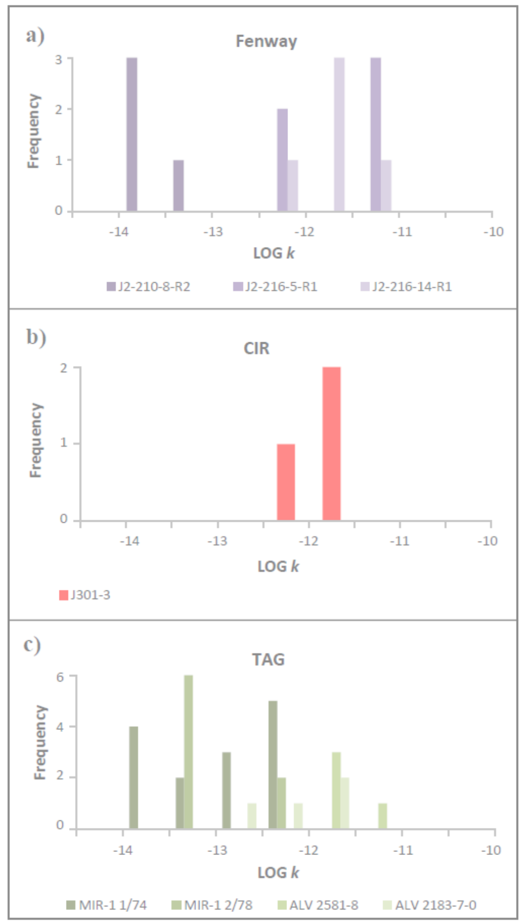

Figure 4.1: Histograms showing probe permeability data for massive anhydrite samples. Plots show frequency of measurements at a given permeability. Colors indicate sample locations: Fenway = purple, CIR = red, and TAG = green. **a)** Data for three Fenway samples. **b)** Data for one CIR sample. **c)** Data for four TAG samples.

values obtained along the cut surfaces (Figure 4.2) are generally smaller than the ones obtained along the rough surfaces. Greater permeability values are likely consequences of the imperfect seal between the probe tip and the rough surfaces, thus does not represent actual anisotropy.

Figure 4.2: Anhydrite sample J2-216-5-R1 with one cut side (highlighted in green). A cut surface has significantly reduced surface roughness. Measurements along this surface would have lower permeability values, since the probe permeameter is able to form a tighter seal against the sample.

Cylindrical cores were taken from selected sites where probe permeability measurements were taken. Permeability and porosity along axial direction of a total of 17 anhydrite cores were measured using the nitrogen permeameter and helium porosimeter, respectively.

During permeability measurements, cores were subjected to different confining pressures of ~0.5-2.7 MPa. The incremental application and removal of confining pressure allowed us to gauge the effects of pressure on anhydrite permeability. Permeability data of all the cores is compiled in Table 4.1. As confining pressure increases, a slight reduction in permeability is observed (Figure 4.3). This permeability reduction is more pronounced at relatively low confining pressures, which is generally attributed to crack closure [*Walsh, 1965*]. Data during the removal of confining pressure (unloading) show that this crack closure is predominantly reversible and therefore has little effect on the permeability of the cores.

Permeability values for the cores range from ~10^{-16} - 6×10^{-13} m^2, while porosity values range from 2-15%. Permeability vs. porosity obtained at a confining pressure of 2.1 MPa is plotted in Figure 4.4. The EPPR best fitting the data has a trend with an α value of 4. From this plot, it is clear that the data fall into roughly two groups: one with high k and ϕ values and another with low k and ϕ. To understand the differences between the two groups and the variation within the data, it is necessary to identify the elements of the pore structure and evidence for pore evolution processes controlling k and ϕ.

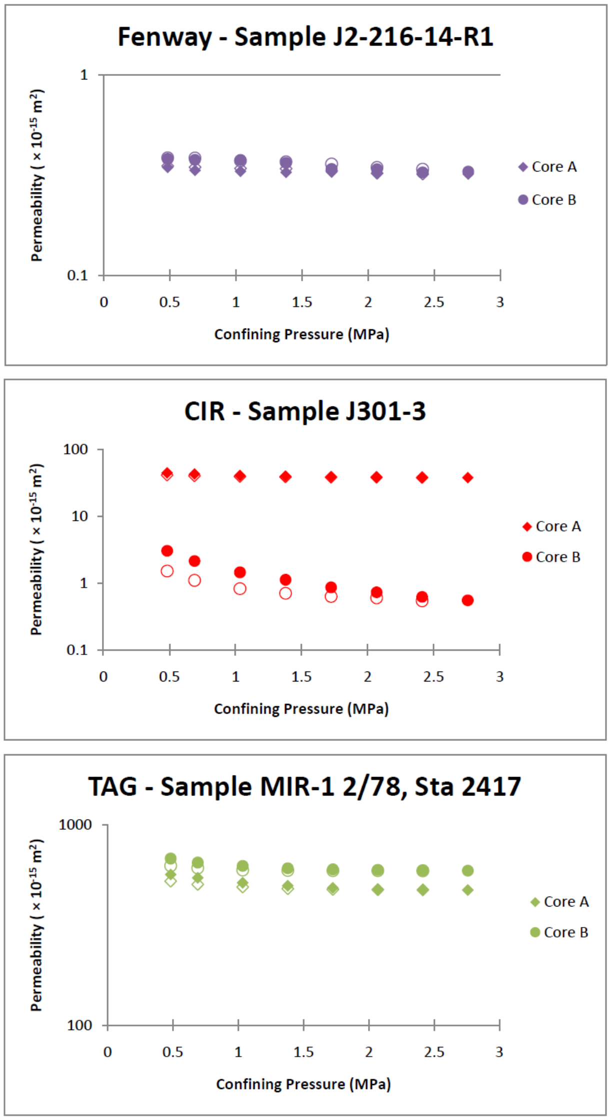

Figure 4.3: Plots showing pressure profiles for select samples during permeability measurement. Colors indicate sample location: Fenway = purple, CIR = red and TAG = green. Symbol shapes represent different sample cores. Solid symbols for pressure loading and empty symbols for unloading cycles. Generally minor changes in permeability with pressure. **a)** Pressure profiles for Fenway sample J2-216-14-R1 cores. **b)** Pressure profiles for CIR sample J301-3 cores. **c)** Pressure profiles for TAG sample MIR-1 2/78, Sta 2417 cores.

Sample	Core	Probe *k* ($\times 10^{-15}$ m^2)		Core *k* ($\times 10^{-15}$ m^2)						Core ϕ (%)			
				1.4 MPa		2.1 MPa		2.7 MPa		2.1 MPa		2.7 MPa	
		k	2σ	*k*	2σ	*k*	2σ	*k*	2σ	ϕ	2σ	ϕ	2σ
Fenway:													
J2-210-8-R2	A-1	39.0	±0.4	0.3	±0.02	0.3	±0.01	0.3	±0.01	2.3	±1.1	2.7	±1.7
	A-2	--		0.1	±0.01	0.1	±0.01	0.1	±0.01	1.9	±2.7	2.0	±2.2
	A-3	--		0.2	±0.01	0.1	±0.01	0.1	±0.01	2.8	±4.6	2.1	±4.6
J2-216-5-R1	A2	402.8	±1.9	237.9	±0.7	230.4	±0.5	225.2	±0.2	11.5	±4.8	11.8	±4.0
J2-216-14-R1	A	2268.4	±2.9	0.3	±0.02	0.3	±0.01	0.3	±0.01	2.1	±2.2	3.1	±1.1
	B	2144.6	±3.2	0.4	±0.04	0.3	±0.01	0.3	±0.01	5.6	±0.1	5.5	±0.1
***CIR*:**													
J301-3	A	1938.5	±1.1	39.8	±0.3	38.5	±0.4	38.0	±0.3	14.8	±0.1	14.7	±0.1
	B	1694.3	±1.3	1.1	±0.04	0.7	±0.04	0.6	±0.05	7.9	±0.1	7.8	±0.1
***TAG*:**													
ALV 2581-8	A	1713.4	±1.6	357.8	±2.0	352.6	±2.1	349.2	±1.8	12.7	±0.1	12.6	±0.1
MIR 1 1/74	A-1	29.0	±0.4	125.3	±0.7	123.2	±0.9	121.4	±0.4	10.9	±0.2	10.8	±0.1
Sta 2403	A-2	--		340.4	±2.2	336.7	±1.9	335.1	±2.1	12.2	±0.2	12.0	±0.2
	B	509.8	±2.2	79.3	±0.6	77.1	±0.7	75.7	±0.3	9.0	±0.1	8.9	±0.1
MIR 1 2/78	A	106.5	±3.0	497.3	±1.2	477.9	±1.0	473.0	±1.1	15.0	±0.1	14.8	±0.1
Sta 2417	B	1043.7	±3.9	607.4	±1.5	595.9	±0.7	590.9	±0.4	13.5	±0.2	13.3	±0.1
ALV 21837-0	2	--		1.0	± ---	0.4	± ---	0.1	± ---	5.0	± ---	3.6	± ---
	3	--		0.4	± ---	0.4	± ---	0.3	± ---	6.1	± ---	2.4	± ---
	B	674.9	±3.9	0.6	± ---	0.3	± ---	0.2	± ---	6.6	± ---	4.0	± ---

Table 4.1: Permeability and porosity data for anhydrite cores.

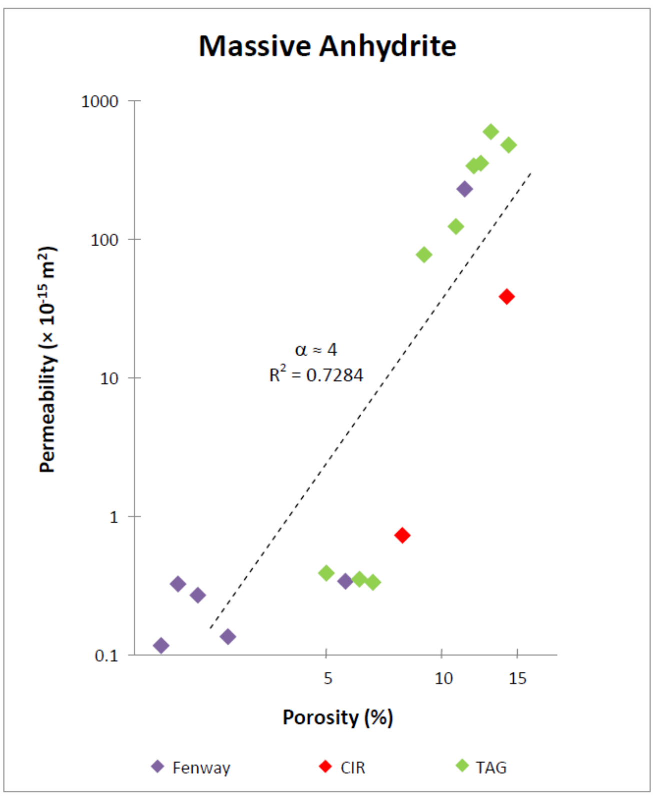

Figure 4.4: Permeability and porosity data plotted for each of the anhydrite cores. Symbol colors consistent with Figure 4.3. Dashed line indicates trend of EPPR with $\alpha \sim 4$. Data are divided into roughly two groups high k and ϕ and low k and ϕ.

4.2 Microstructural Analyses

Twelve thin sections were made from a subset of the measured anhydrite cores. Permeability and porosity data of cores from which thin sections were taken are plotted in Figure 4.5. Thin section descriptions have been organized into two groups, high k and ϕ and low k and ϕ, consistent with the permeability and porosity data.

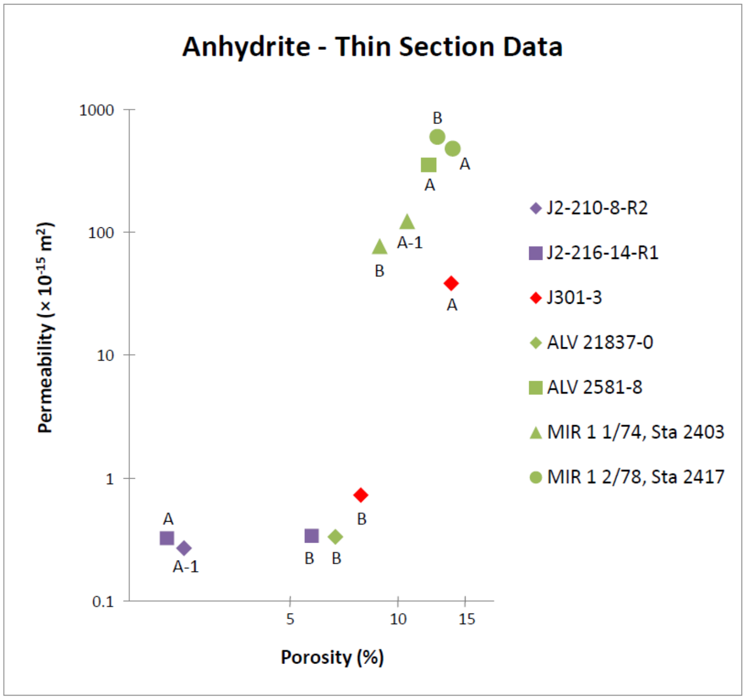

Figure 4.5: Permeability and porosity data plotted for each of the anhydrite cores from which thin sections were made. Symbol colors consistent with Figure 4.3. Symbol shape represents sample and symbol labels indicate respective core. Data are divided into roughly two groups: high k and ϕ and low k and ϕ.

4.2.1 High k and ϕ cores

There were six thin sections taken from the high k and ϕ cores: MIR 1 2/78, Sta 2417 (Cores A and B), ALV 2581-8 (Core A), MIR 1 1/74, Sta 2403 (Cores A-1 and B), and J301-3 (Core A). Each section predominantly contains anhydrite with minor amounts of sulfides (i.e. chalcopyrite, pyrite, and sphalerite). Anhydrite crystals are typically tabular with well defined cleavage planes. They initially form in a tightly interlocked grain structure with little space between crystals. All of the thin sections in this group have, however, experienced dissolution, which has created pore space and channels between crystals (Figures 2.6 and 4.6). Dissolution has weathered crystal edges causing many of the crystals to lose their tabular shape and also develop cracks. Pore spaces are irregularly shaped and well-connected likely due to dissolution. This can account for the higher permeability and porosity values measured for these samples.

The thin sections for the cores (A and B) from the MIR 1 2/78, Sta 2417 sample are very similar. They both show blocky anhydrite crystals, ranging in size from about 40-1200 μm, with smaller crystals generally appearing to be broken portions of larger crystals (Figure 4.6a). Most crystals adjacent to larger pores and channels have rough edges indicative of crystal breakdown via dissolution. Additionally, dissolution has produced narrow cracks along anhydrite cleavage planes, which in some cases appears to have lead to the division and eventual breakdown of large crystals into several smaller crystals. Very small amounts of chalcopyrite have begun to precipitate within some of the newly created pore space, though these crystals do not sufficiently block any pore space between the anhydrite crystals.

The thin section for ALV 2581-8, Core A is also very similar to those of MIR 1 2/78, Sta 2417. The section contains anhydrite crystals that have been dissolved along crystal edges and internally along cleavages. The dissolution has also created broad channels between crystals, in some cases as wide as 100 μm

(Figure 4.6b). This section does exhibit a greater abundance of chalcopyrite that has precipitated within the pore space. The chalcopyrite crystals are typically small (10-40 μm) and do not appear to effectively block much of the pore space.

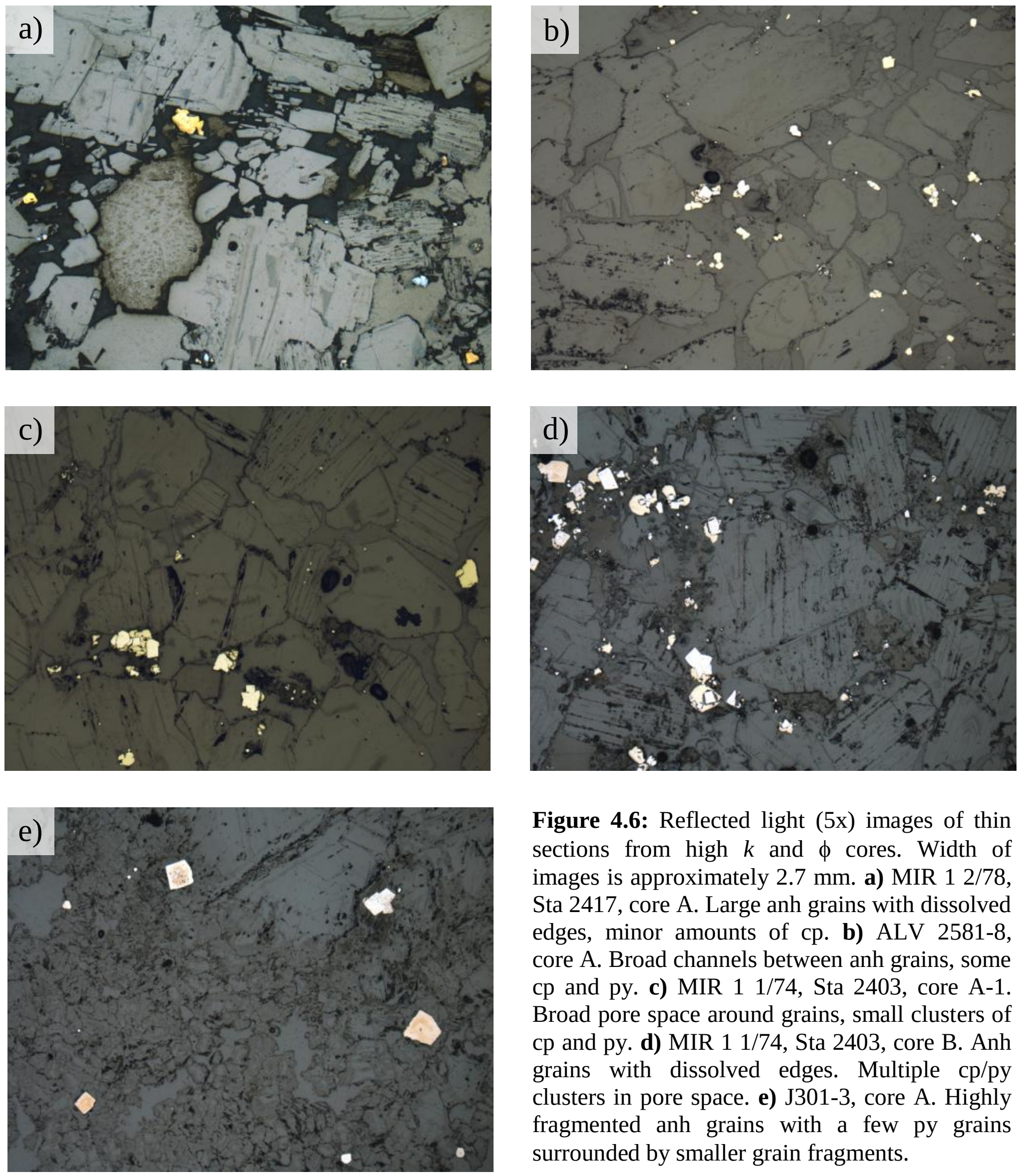

Figure 4.6: Reflected light (5x) images of thin sections from high k and ϕ cores. Width of images is approximately 2.7 mm. **a)** MIR 1 2/78, Sta 2417, core A. Large anh grains with dissolved edges, minor amounts of cp. **b)** ALV 2581-8, core A. Broad channels between anh grains, some cp and py. **c)** MIR 1 1/74, Sta 2403, core A-1. Broad pore space around grains, small clusters of cp and py. **d)** MIR 1 1/74, Sta 2403, core B. Anh grains with dissolved edges. Multiple cp/py clusters in pore space. **e)** J301-3, core A. Highly fragmented anh grains with a few py grains surrounded by smaller grain fragments.

Thin sections for cores A-1 and B of sample MIR 1 1/74, Sta 2403 are consistent with those discussed above. Both cores have clearly experienced a significant about of dissolution, which has created significant pore space within the initially close-packed anhydrite structure (Figures 4.6c, d). These sections differ slightly from those previously discussed in that they both show precipitation of chalcopyrite and some pyrite, which appear to cluster within larger pores. While this precipitation does not fully block most of the pore channels between crystals, it is clearly restrictive. The greater proportion of sulfides within these two cores can likely account for the somewhat lower permeability and porosity values measured compared to those of the previous cores discussed.

Lastly, core A from sample J301-3 also plots within the high *k* and ϕ group of samples, though it plots slightly off from the EPPR trend. The thin section for this core is structurally quite different from those of the previously discussed cores (Figure 4.6e). There is evidence for extensive anhydrite dissolution, perhaps multiple dissolution events, that have severely cracked and broken down many of the crystals (Figure 4.7a). Large anhydrite crystals that have remained intact are heavily weathered. The dissolution has created more pore space around and within crystals, though the development of broad channels as seen in the previous thin sections appears inhibited by the packing of many of the small, anhydrite

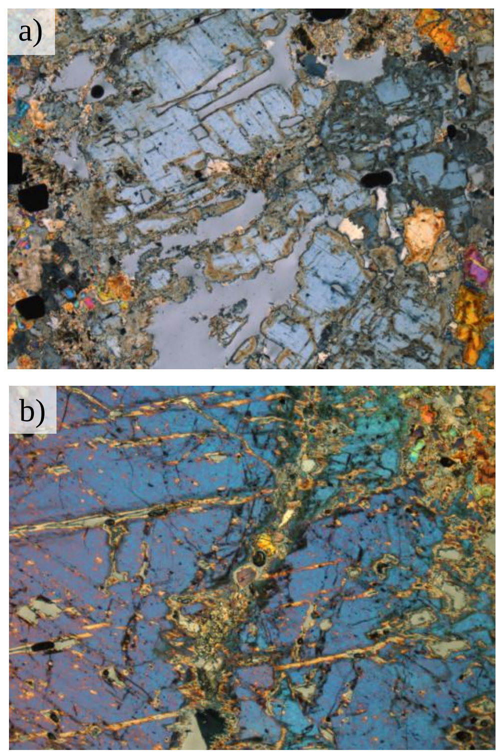

Figure 4.7: Cross-polarized images (5x) of sample J301-3. Sample has experienced severe dissolution, which has cracked and broken anh grains. Pore space has been created within and around grains. Width of images is ~ 2.7 mm. **a)** Core A. **b)** Core B.

crystal fragments. The tight packing of these anhydrite fragments likely somewhat limits the permeability of the core, which is why this core plots below the high *k*/high ϕ trend. Late-stage sulfide precipitation is less pronounced within this thin section. A few pyrite crystals have developed within the section and are surrounded by anhydrite fragments. It is possible that the pyrite precipitated in pore space created by early dissolution, and that further precipitation was impeded by the infill of anhydrite fragments within the pore space during subsequent dissolution events.

4.2.2 Low *k* and ϕ cores

Six thin sections were made from cores that plotted in the low *k*/low ϕ group: J301-3 (Core B), ALV 21837-0 (Core B), J2-216-14-R1 (Cores A and B) and J2-210-8-R2 (Core A-1). Similar to the previous cores, these all show evidence for having experienced anhydrite dissolution. Anhydrite edges are weathered and rough, while the crystals themselves are heavily cracked. These cores, however, appear to have undergone secondary processes that reduced the pore space created by dissolution.

Much like sample J301-3 core A, J301-3 core B exhibits evidence for extensive amounts of anhydrite dissolution. Anhydrite crystals have been thoroughly cracked and fragmented with few large crystals remaining (Figure 4.7b). The majority of the anhydrite is present as small crystal fragments that have been tightly packed. The close packing of these crystals has clearly limited the availability of pore space between the crystals, more so than in core A. Core B also contains more pyrite crystals than core A, which probably helped fill pore spaces created during an early dissolution event (Figure 4.8a). These pyrite crystals have also been tightly packed with the anhydrite fragments, suggesting that they precipitated prior to some of the more intense dissolution events. The

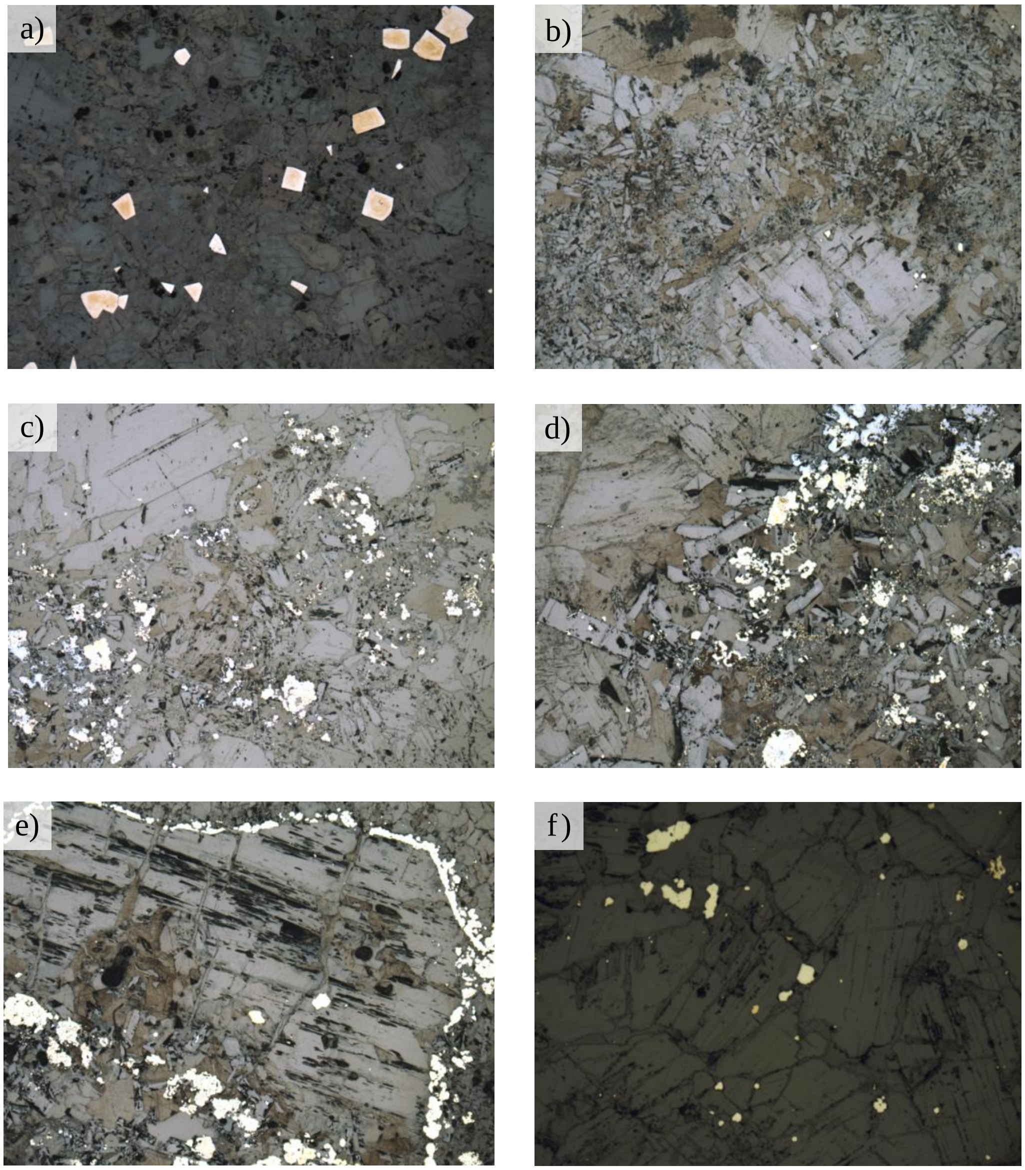

Figure 4.8: Reflected light (5x) images of thin sections from low *k* and ϕ cores. Width of images is approximately 2.7 mm. **a)** J301-3, core B. Tightly packed anh grain fragments surrounding py grains. **b)** ALV 21837-0, core B. Vugs created from dissolution have been infilled by newly precipitated smaller anh grains. **c)** J2-216-14-R1, core B. Precipitation of sulfides and anh fill in pore space. **d)** J2-216-14-R1, core A. Precipitation of sulfides and anh fill pore space created during dissolution. Precipitated anh grains are large and add significant surface roughness along pore walls. **e)** J2-216-14-R1, core A. Fragmented anh grain surrounded by cp. Cp precipitated later and will prevent further dissolution of the anh grain. **f)** J2-210-18-R2, core A-1. Dissolution to a lesser extent produces narrow channels between grains that can be easily restricted or blocked by sulfide precipitation.

tightly packed structure and greater abundance of pyrite within core B likely accounts for the variation observed between the two J301-3 cores.

Core B from sample ALV 21837-0 has also experienced considerable dissolution which has created broad channels between anhydrite crystals and cracks within crystals. Some crystals have been fragmented following severe cracking, though not nearly to the extent as seen in sample J301-3. Small amounts of both chalcopyrite and pyrite have precipitated in the pore space without creating much restriction. These sulfide crystals are dispersed widely and seldom form clusters. This core does, however, contain large patches of more recently precipitated interlocking anhydrite crystals. These crystals are well-formed, but much smaller (5-30 μm) than the original crystals. They appear to have precipitated within vugs (large pore spaces), where they protrude outwards into remaining pore space, creating significant roughness along the pore channels (Figure 4.8b). Permeability and porosity enhancements resulting from anhydrite dissolution are reduced due to this late-stage precipitation of smaller anhydrite crystals.

Sample J2-216-14-R1 has three thin sections, two for core B and one for core A. The core B thin sections show that pore space created by dissolution has been restricted by the precipitation of sulfides and small anhydrite crystals (Figure 4.8c). These new crystals block pore space between crystals and created added roughness along channel walls, which decrease the permeability of the core. Core A shows evidence for similar precipitation of sulfides and newer anhydrite. The precipitated anhydrite crystals in core A are well-formed and larger (30-400 μm) than those seen in core B (Figure 4.8d). These crystals extend into pore spaces, often blocking flow channels. Sulfide precipitation is also more pronounced in core A with chalcopyrite and pyrite filling pore space around crystal edges (Figure 4.8e).

Lastly, core A-1 from sample J2-210-8-R2 also plots in the low *k*/low ϕ group. While this core shows signs of dissolution, the extent of dissolution is less than in the other samples. Pore space has been created around crystals, but is narrower than as seen in other sample thin sections (Figure 4.8f). Small amounts of chalcopyrite and pyrite have precipitated within some of the pore space, and in most cases because the pore space is narrow, it blocks flow channels. The lesser amounts of initial anhydrite dissolution in conjunction with the sulfide precipitation restrict the permeability of the core.

4.3 Discussion

Seafloor massive anhydrite deposits form by the mixing of hot fluids with seawater, and likely behave similarly to subsurface deposits. Although anhydrite precipitation is recognized as being a key constraint on the flow of hydrothermal fluids, effects of anhydrite precipitation on transport properties of the seafloor and its subsurface structures are not well quantified [*Mills and Tivey*, 1999; *Lowell et al.*, 2003].

Microstructural analyses show that the pore geometry of anhydrite deposits is controlled by both dissolution and precipitation. As fluids pass through the deposits, environmental conditions such as temperature and pH are altered, which may cause anhydrite deposits to become unstable and dissolution to occur. In general, dissolution creates pore space and enhances permeability. The anhydrite samples investigated in this study all show evidence for dissolution.

Precipitation is sensitive to environmental conditions and pore size [*Aquilano et al.*, 1992; *Pape et al.*, 2005]. In a study of anhydrite cementation in sandstones, *Pape et al.* [2005] found that anhydrite preferentially precipitates in larger pore spaces, such as in wide flow channels, as opposed to smaller spaces that could be more easily infilled. It is observed that anhydrite precipitation in smaller pores quickly becomes unstable with drops in the calcium sulfate concentration [*Pape et al.*, 2005]. Anhydrite crystal growth is shown to begin with the nucleation of a single crystal within a large pore, not through growth along the edges of pre-existing crystals as is common with other minerals such as quartz. Thus anhydrite precipitation creates highly efficient blockages that impede fluid transmission, and as such results in large permeability reduction.

This mode of crystal growth may explain the difference between the two observed sample groups. In high k and ϕ samples, pore space consists primarily of channels along crystal edges. In low k and ϕ samples, abundant vugs are observed. The vugs are ideal for the growth of secondary anhydrite that results in low permeability. In contrast, channels are less conducive to anhydrite growth.

The precipitation of sulfides, such as chalcopyrite and pyrite, is also observed within many of the anhydrite samples. Precipitation of such minerals requires higher temperatures [*Fontaine et al.*, 2001]. Sulfides preferentially precipitate within constrictive spaces making them more likely to restrict pore spaces and decrease permeability [*Fontaine et al.*, 2001].

The effects of both dissolution and precipitation of secondary anhydrite or sulfides within the anhydrite deposits depend highly on their initial crystal structures and environmental conditions. Vugs within the anhydrite pore structure are not necessarily caused by dissolution and can be original to the grain structure. Vug-rich anhydrite deposits are predisposed to secondary anhydrite precipitation. Additionally, late-stage precipitation can occur at any time, regardless of the timing of dissolution events. Precipitation can occur within pore space original to the grain structure, as well as in pores created through dissolution. The extent and timing of these processes is controlled by the chemistry of the vent fluids.

The $\alpha \sim 4$ trend identified for the anhydrite deposits reflects this interplay between dissolution and precipitation. As previously discussed, dissolution, a permeability and porosity enhancing process, has been shown to produce α values as high as 20 [*Bernabé et al.*, 2003]. Precipitation, which results in lower permeability and porosity, generally has α values around 8 [*Bernabé et al.*, 2003]. Because both of these processes occur in anhydrite deposits, the α value will reflect a balance of their effects on pore structure (Figure 4.9). By selecting a starting k and ϕ and then imposing either process, the pore structure of the material will change. If this altered composition then experiences the opposing process, the trend from the starting structure to the final structure will be similar to that of $\alpha \sim 4$.

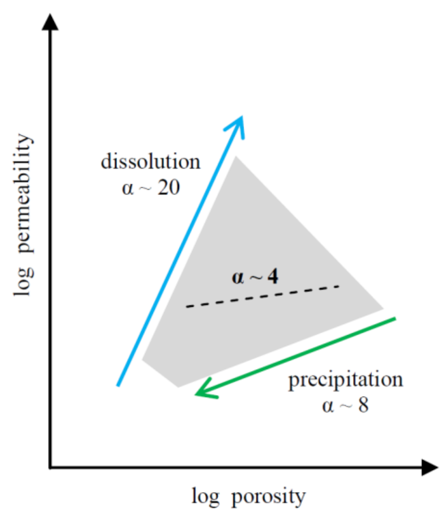

Figure 4.9: $\alpha \sim 4$ trend reflects interplay between dissolution and precipitation.

Chapter 5: Flanges, Slabs, and Crust

Flanges, slabs and crust are diffusive vent deposits that facilitate fluid transport laterally as well as upwards through deposit cracks, which results in a layered structure (Figure 5.1). This structural characteristic indicates that the processes controlling the formation of their layers, such as mineral precipitation or dissolution, may be similar in these vents [*Delaney et al.,* 1992*; Tivey et al.,* 1995*; Cooper et al.,* 2000]. Ten deposit samples were included in this group: 5 flanges, 4 slabs, and 1 crust. Prior to discussing the results, it is first necessary to understand variations between the deposits, such as how and where they develop.

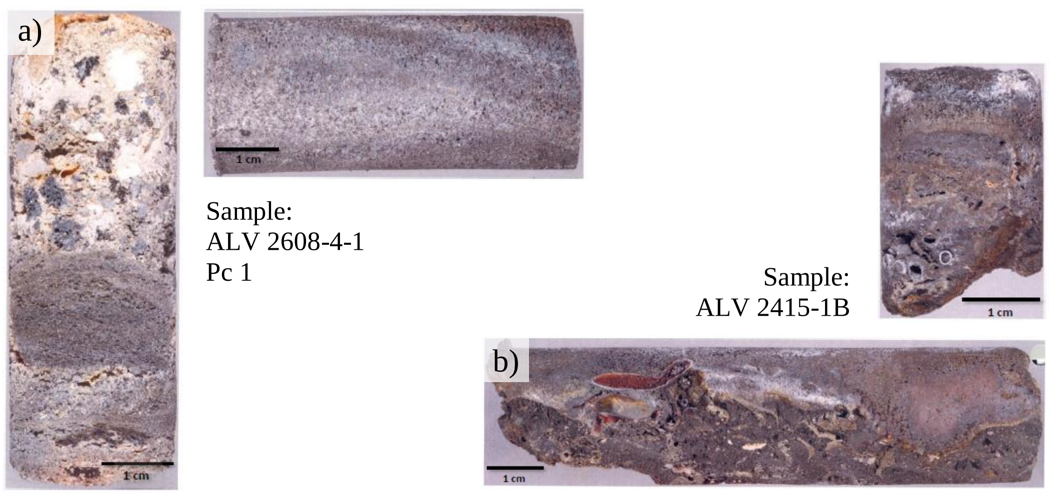

Figure 5.1: Two sets of cores illustrating the prominent structural layering throughout the samples. **a)** Slab sample ALV 2608-4-1, Pc 1. Left core was taken perpendicular to layering and right core was taken parallel to layering. **b)** Flange sample ALV 2415-1B. Top core was cut perpendicular to layering, while the bottom core was taken parallel to layering.

5.1 Geologic Descriptions

The most widespread of these sample types are the flanges (Figure 5.2a), which have been identified at multiple vent sites. Flanges are deposits that extrude horizontally from the sides of larger chimney structures, like a ledge or tier, where fluid will pool and form layers within the flange parallel to the surface of the fluid [*Delaney et al.,* 1992*; Woods and Delaney,* 1992]. Fluids pooled beneath a flange will percolate upwards through the flange, or in the case where the fluid flux from the adjacent chimney structure exceeds the maximum amount able to percolate, the fluid will overflow around the edge of the flange [*Kerr*, 1997; *Tivey et al.,* 1999]. As fluid overflows, mineral precipitation along the flange edge occurs. This precipitation, particularly that of silica, results in the lateral growth of the flange [*Turner*, 1995; *Kerr*, 1997; *Tivey et al.*, 1999]. In general, flanges are compositionally abundant in sulfides, sulfates, and silica ± carbonates [*Lonsdale and Becker,* 1985; *Delaney et al.*, 1992; *Tivey et al.,* 1999]. Flange samples for this study are from the Guaymas Basin in the Gulf of California and also the Main Endeavour Field (MEF) located along the northern portion of the Juan de Fuca Ridge. Guaymas Basin is notable for its rapid rate of sediment deposition and hydrothermal

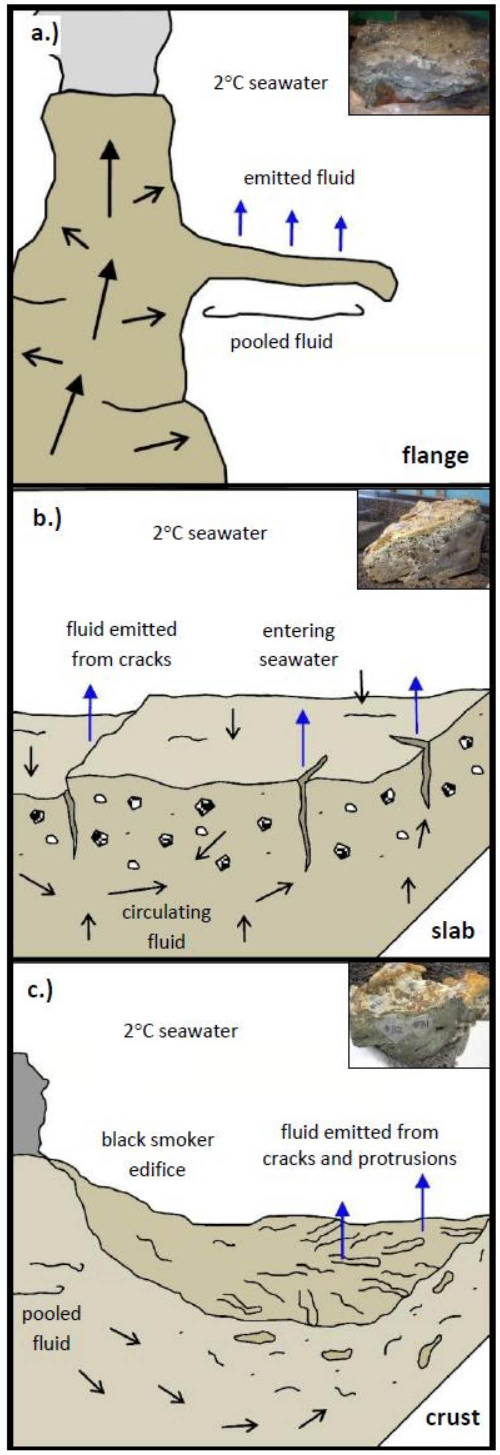

Figure 5.2: Diagrams illustrating the general structure and flow pathways within flanges, slabs, and crust with insets showing samples used in this study. **a)** Flange extending from the side of a larger chimney structure. Fluid emitted from the side of the chimney will pool under the flange and percolate upwards through the flange. **b)** Slab with circulating fluids. **c)** Crust with fingerlike protrusions at the base of the TAG black smoker edifice.

reactions between fluids and organic-rich sediments [*Pearson et al., 2005*]. As a result, calcite and barite are common constituents of vent deposits from this region [*Koski et al.,* 1985]. The MEF is atypical in that it has unusually high fluid pH and high concentrations of methane and ammonia, which likely influence vent fluid reactions [*Tivey et al.*, 1999].

Hydrothermal slabs (Figure 5.2b) are found at the Lucky Strike vent field along the Mid-Atlantic Ridge (MAR). The Lucky Strike vent field is unique in that it is situated adjacent to a large seamount that periodically produced lava flows that extend across the vent field [*Langmuir et al.,* 1997]. Fluid temperature and chemistry at the vent field are highly controlled by the frequent volcanic eruptions, which have been found to change environmental conditions as often as every few days [*Langmuir et al.*, 1997]. Slabs from Lucky Strike are hydrothermally silicified breccias composed of amorphous silica rimmed volcanic fragments (basaltic glass and plagioclase), barite, and sulfides [*Cooper et al.*, 2000*; Rouxel et al.*, 2004]. Slabs also exhibit layering parallel to the slab surface, likely developed in part to the ongoing volcanic activity. Research on the composition of fluid emitted from slabs suggests that seawater enters and circulates within the slab [*Cooper et al.,* 2000*; Rouxel et al.*, 2004]. This fluid will convect through the slab and eventually exit diffusely from cracks within the slab.

Crust samples (Figure 5.2c) are from the TAG vent field, also located along the MAR. This vent field is focused around a large central mound consisting of collapsed vent fragments [*Thompson et al.,* 1985*; Humphris et al.,* 1995]. Situated atop the center of the mound is a high-temperature black smoker edifice. Hydrothermal crust forms a platelike, massive-sulfide layered surface that surrounds the TAG active mound upon which the black smoker edifice sits [*Humphris et al.*, 1995; *Tivey et al.*, 1995]. The crust is formed through the gradual deposition and re-cementation of older vent debris and because of this, crust is highly cracked [*Humphris et al.*, 1995; *Tivey et al.*, 1995]. Crust also characteristically forms fingerlike protrusions [*Tivey et al.*, 1995]. Fluid that has pulled within the black smoker edifice will seep out from these cracks and protrusions and rise, where it will become entrained within the black smoker plume [*Tivey et al.*, 1995].

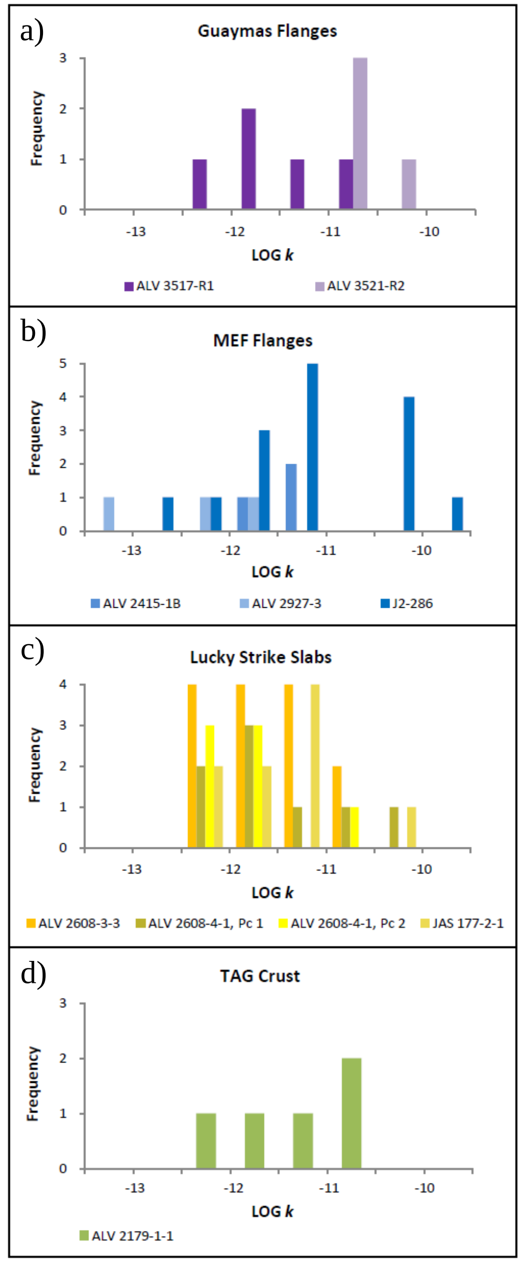

Figure 5.3: Histograms of probe permeability data for flange, slab, and crust samples. Plots show frequency of measurements at a given permeability. Colors indicate sample locations: Guaymas = purple, MEF = blue, Lucky Strike = gold and TAG = green. **a)** Data for two Guaymas samples. **b)** Data for three MEF samples. **c)** Data for four Lucky Strike samples. **d)** Data for one TAG sample.

5.2 Permeability and Porosity

Probe permeability data provide a quantitative measure of permeability heterogeneity within the samples (Figure 5.3). Comparison of permeability values obtained from different sides of each sample show that measurements oriented parallel to the layering within the samples were predominantly on the order of 10^{-12} m^2. Measurements taken perpendicular to the layering yielded a much broader range of values.

Cores were taken both parallel and perpendicular to layering from each of the samples in order to better quantify permeability anisotropy using the nitrogen permeameter. In total, 40 cores were obtained with 9 cores oriented parallel and 31 cores perpendicular to layering.

Pressure profiles from select cores showing the effects of confining pressure on permeability are shown in Figure 5.4. In general, the permeability decreased slightly with increases in confining pressure – likely due to crack

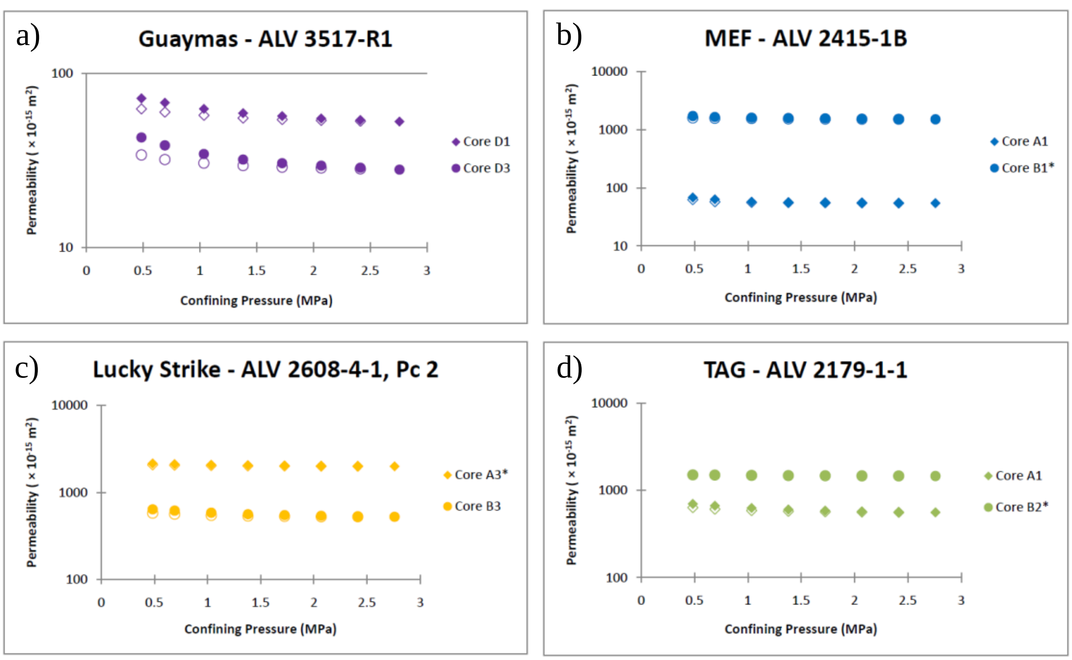

Figure 5.4: Plots showing pressure profiles for select samples during permeability measurement. Colors consistent with Fig. 4.3. Symbol shapes represent different sample cores (solid = pressure loading, empty = unloading) and asterisk indicates parallel-to-layering core. Generally negligible changes in permeability with pressure. **a)** Guaymas flange sample ALV 3517-R1 cores. **b)** MEF flange sample ALV 2415-1B cores. **c)** Lucky Strike slab sample ALV 2608-4-1, Pc 1cores. **d)** TAG crust sample ALV 2179-1-1 cores.

closure [e.g., *Walsh*, 1965]. Permeability values obtained during unloading agree well with the values obtained during loading, indicating that the pressure effect is mostly reversible with no permanent damage introduced during pressurization.

Sample	Core	Probe k ($\times 10^{-15}$ m^2)	Core k ($\times 10^{-15}$ m^2)			Core ϕ (%)	
			1.4 MPa	2.1 MPa	2.7 MPa	2.1 MPa	2.7 MPa
		k 2σ	k 2σ	k 2σ	k 2σ	ϕ 2σ	ϕ 2σ
Guaymas Flange:							
ALV 3517-R1	D1	3230.4 ±3.6	59.1 ±0.3	55.1 ±0.3	52.9 ±0.4	2.3 ±3.3	21.6 ±3.1
	D3	1884.9 ±4.5	32.0 ±0.3	29.5 ±0.2	28.0 ±0.2	2.8 ±4.4	19.8 ±4.0
ALV 3521-R2	A2	29981.0 ±4.5	1425.8 ±3.2	1420.6 ±3.3	1414.2 ±13.0	11.5 ±0.1	40.5 ±0.2
	Ex 1	--	1311.7 ±3.3	1243.4 ±3.8	1213.1 ±8.5	2.1 ±0.4	44.8 ±0.2
	Ex 2	--	969.7 ±4.2	954.7 ±5.4	953.8 ±2.0	5.6 ±0.4	44.7 ±0.3
MEF Flange:							
ALV 2415-1B	A1	1694.3 ±3.8	56.5 ±0.3	55.4 ±0.4	54.7 ±0.5	20.2 ±1.2	20.5 ±0.4
	B1	9704.2 ±3.3	1594.6 ±4.8	1552.3 ±3.4	1514.3 ±4.7	31.2 ±0.3	30.9 ±0.4
	1	--	46.1 ± ---	40.5 ± ---	36.5 ± ---	17.1 ± ---	15.3 ± ---
	2	--	5.3 ± ---	3.5 ± ---	2.6 ± ---	19.2 ± ---	17.2 ± ---
ALV 2927-3	B1	2193.3 ±2.5	1930.6 ±10.8	1889.1 ±12.7	1863.5 ±6.2	38.2 ±0.1	37.9 ±0.1
	1	--	1950.2 ± ---	1717.7 ± ---	1595.6 ± ---	41.8 ± ---	39.6 ± ---
	2	--	155.6 ± ---	148.7 ± ---	145.0 ± ---	32.7 ± ---	29.5 ± ---
	3	--	994.2 ± ---	967.3 ± ---	948.7 ± ---	40.7 ± ---	38.2 ± ---
J2-286	A1	2062.0 ±3.7	1.3 ±0.1	0.5 ±0.02	0.2 ±0.02	20.7 ±0.1	20.5 ±0.3
	A3	4181.9 ±4.3	279.4 ±1.3	233.1 ±1.3	196.0 ±1.6	25.3 ±1.6	25.3 ±0.9
	C2-1	46446.3 ±3.8	0.8 ±0.04	0.8 ±0.02	0.7 ±0.03	27.2 ±0.5	27.3 ±0.3
	C2-2	--	1.3 ±0.04	1.2 ±0.02	1.2 ±0.1	24.1 ±0.2	24.2 ±0.4
	C3-1	79602.4 ±3.2	162.9 ±0.4	146.0 ±1.3	138.3 ±1.4	27.6 ±4.5	27.8 ±3.4
	C3-2	--	49.9 ±0.5	48.7 ±0.2	48.3 ±0.3	21.2 ±1.1	20.7 ±1.5
	C4	94066.3 ±2.8	18.7 ±0.1	17.7 ±0.2	17.0 ±0.1	17.7 ±2.4	19.9 ±2.1
Lucky Strike Slab:							
ALV 2608-3-3	B2	1960.4 ±4.4	2744.7 ±13.5	2737.1 ±11.9	2746.1 ±5.6	42.9 ±0.4	42.5 ±0.3
	C1	1051.5 ±4.5	1445.3 ±5.9	1447.1 ±3.1	1436.6 ±3.5	29.2 ±0.3	28.8 ±0.3
ALV 2608-4-1	A1	816.8 ±3.9	787.8 ±2.7	740.6 ±3.4	706.5 ±1.1	34.9 ±0.2	34.8 ±0.3
Pc 1	C1-1	428.4 ±3.9	530.0 ±1.9	486.7 ±0.4	461.0 ±2.3	37.2 ±1.0	36.5 ±1.3
	C1-2	--	757.9 ±8.2	655.1 ±5.1	604.9 ±4.0	46.4 ±0.8	46.3 ±0.4
	C3-1	1196.4 ±3.8	28.1 ±0.2	24.1 ±0.2	22.2 ±0.2	35.0 ±0.9	34.8 ±0.3
	C3-2	--	120.3 ±1.2	111.7 ±1.1	106.9 ±0.8	37.2 ±0.8	37.1 ±0.6
ALV 2608-4-1	A3	2319.9 ±4.6	2056.1 ±4.5	2016.9 ±6.5	1994.5 ±5.5	39.8 ±0.3	39.6 ±0.1
Pc 2	B3	1176.4 ±4.0	561.6 ±2.2	538.3 ±2.8	523.0 ±0.9	43.1 ±0.1	42.8 ±0.2
	1	--	5475.2 ± ---	5023.6 ± ---	4885.3 ± ---	45.6 ± ---	44.1 ± ---
	2	--	661.4 ± ---	574.6 ± ---	534.1 ± ---	48.0 ± ---	46.3 ± ---
	4	--	962.2 ± ---	695.1 ± ---	528.8 ± ---	44.0 ± ---	42.4 ± ---
JAS 177-2-1	A2	3975.9 ±4.1	198.5 ±1.8	170.4 ±2.1	152.1 ±1.5	46.1 ±0.4	45.7 ±0.4
	B1	2729.9 ±3.5	1827.7 ±3.8	1774.8 ±2.9	1745.9 ±4.5	38.8 ±1.5	38.9 ±1.2
	B2	9435.7 ±3.2	2998.6 ±13.7	2954.2 ±11.8	2898.5 ±4.1	41.2 ±1.8	41.0 ±1.7
	C2	69963.2 ±3.9	194.1 ±0.5	192.1 ±0.6	191.9 ±0.2	41.2 ±3.7	39.5 ±3.4
TAG Crust:							
ALV 2179-1-1	A1	13897.7 ±3.0	605.0 ±2.8	575.9 ±0.7	560.7 ±1.2	36.9 ±3.1	35.3 ±4.3
	A2	5234.4 ±3.6	1106.7 ±6.9	1079.1 ±5.5	1062.7 ±2.9	37.9 ±5.0	37.8 ±3.2
	A3	23030.1 ±1.4	927.9 ±4.4	887.3 ±4.7	863.2 ±4.7	38.4 ±4.5	37.2 ±2.5
	B2	1464.2 ±3.4	1487.5 ±5.0	1476.5 ±9.7	1462.7 ±4.6	43.2 ±0.2	42.4 ±0.4

Table 5.1: Average probe permeability, core permeability, and porosity and 2σ values for flange, slab, and crust samples. Additional data for analyses was taken from cores without corresponding probe permeability measurements. Text in blue represents data for measurements taken parallel to layering.

The permeability reduction in all cores became negligible as the applied confining pressure increased from 2.1 MPa to 3.1 MPa. Thus, the measurements taken at 2.1 MPa were used for analyses. Table 5.1 shows the average permeability and porosity values at 2.1 MPa alongside the respective average probe permeability measurements. The majority of the cores measured had corresponding probe measurements, but additional measurements were also conducted on several cores taken where no probe permeameter measurements were made. Comparison between the permeability values obtained by the probe permeameter and those obtained by the nitrogen permeameter indicate that for the same sample, probe permeability is consistently higher. Part of the difference is due to the application of the confining pressure during core permeability measurements. Another reason is that flow measured by the probe permeameter is not directionally restricted, so the values obtained are a representation of a near surface volume average, whereas the nitrogen permeameter gives an axial permeability of a cylindrical core [*Zhu et al.*, 2007]. In addition, probe measurements were sometimes made on surfaces that were trimmed off of cores (because the core measurements need to be made on cylindrical cores with parallel upper and lower surfaces). Notwithstanding these differences, data of the core samples reinforce the observation that within each sample, the parallel-to-layering permeability values do not show a lot of variability and are high, on the order of 10^{-12} m^2, compared to the perpendicular-to-layering permeability values, which range over several orders of magnitude.

Permeability and porosity values obtained from these cylindrical cores can be divided into two groups: cores with axes oriented parallel-to-layering and cores with axes oriented perpendicular-to-layering (Figure 5.5). The parallel-to-layering cores all had relatively high permeabilities on the order of 10^{-12} m^2 and porosities ranging from ~30-40%. For the perpendicular-to-layering cores, permeability values ranged from 10^{-16}-10^{-12} m^2 and porosities ranged from ~20-40%, indicating larger variabilities compared to the parallel-to-layering cores.

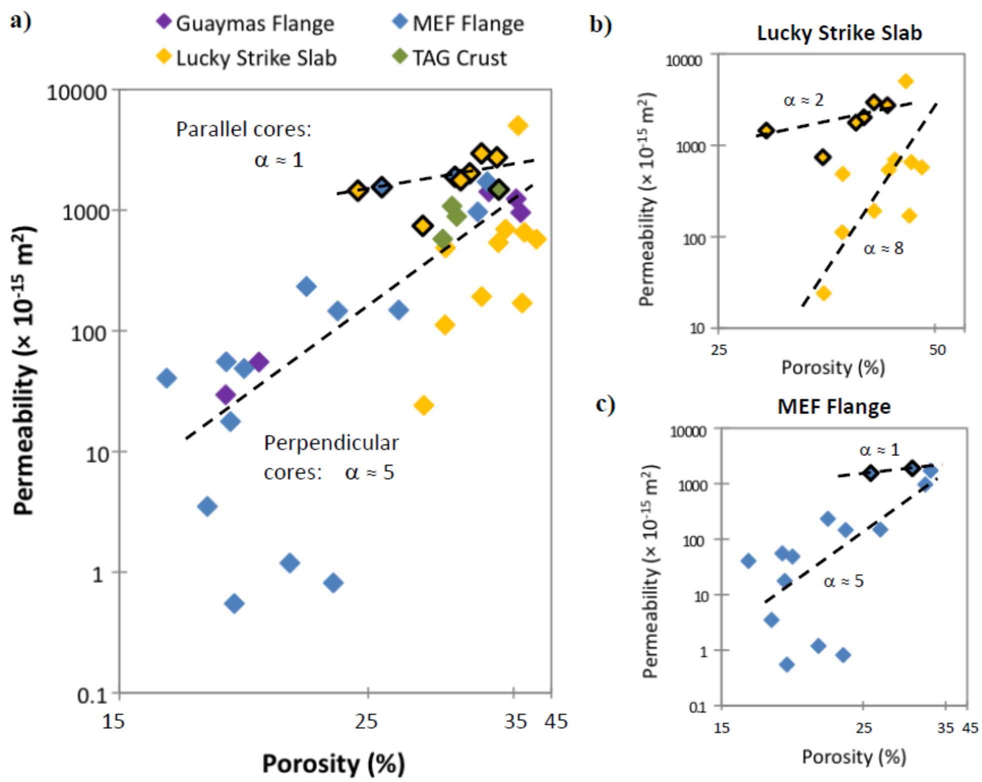

Figure 5.5: a) Permeability versus porosity data for all of the cores. In general, permeability values for cores taken parallel-to-layering, symbols outlined in black, are higher (~ 10^{-12} m^2) than for cores taken perpendicular-to-layering (10^{-16}-10^{-12} m^2). Differences in permeability as a function of porosity can be best fit by power-law relationships (black dashed lines), with a power-law exponent of $\alpha \sim 1$ (or 2) for the parallel-to-layering cores and $\alpha \sim 5$ (or 8) for the perpendicular-to-layering cores. Symbol color denotes location of sample origin: purple = Guaymas Basin, blue = MEF, yellow = Lucky Strike, and green = TAG. **b)** Permeability versus porosity for only Lucky Strike cores with power-law relationships identified. **c)** Permeability versus porosity for MEF cores with power-law relationships labeled.

From Figure 5.5, two distinct trends of EPPRs are evident for the parallel-to-layering and perpendicular-to-layering cores. The exponent $\alpha \sim 1$ is for the parallel-to-layering cores, whereas for the perpendicular-to-layering cores $\alpha \sim 5$. To correctly interpret the observed EPPRs, it is critical to relate the power-law relationships to the actual pore evolution processes using sample thin sections. Thin sections were made from a large subset of the cores, both parallel and perpendicular to the layers within the samples.

5.3. Microstructural Analyses

Microstructural analyses using reflected and transmitted light petrography were conducted on thin sections to identify pore evolution processes. Permeability-porosity data for samples from which thin sections were obtained are plotted in Figure 5.6. Data are grouped according to vent field and sample type: Guaymas flanges, MEF flanges, Lucky Strike slabs, and TAG crust. A summary of observations for each thin section is provided in Table 5.2.

5.3.1 Guaymas Flanges

The flanges have been separated into two groups, carbonate-dominated samples from the Guaymas, and sulfide-dominated samples from the MEF. The permeability and porosity values of two flange samples from Guaymas, ALV 3517-R1 and ALV 3521-R2, differ considerably (Figure 5.6a). For each sample, one thin section was cut axially through one core, and a second was cut transversely through another core (Table 5.2). For sample ALV 3517-R1, the axial cut (core D1) exposes a moderately layered structure with large calcite crystals (~250 μm) at the base of the core, adjacent to where hot fluid was pooled. Smaller calcite crystals (~50 μm) are present above these larger crystals, and

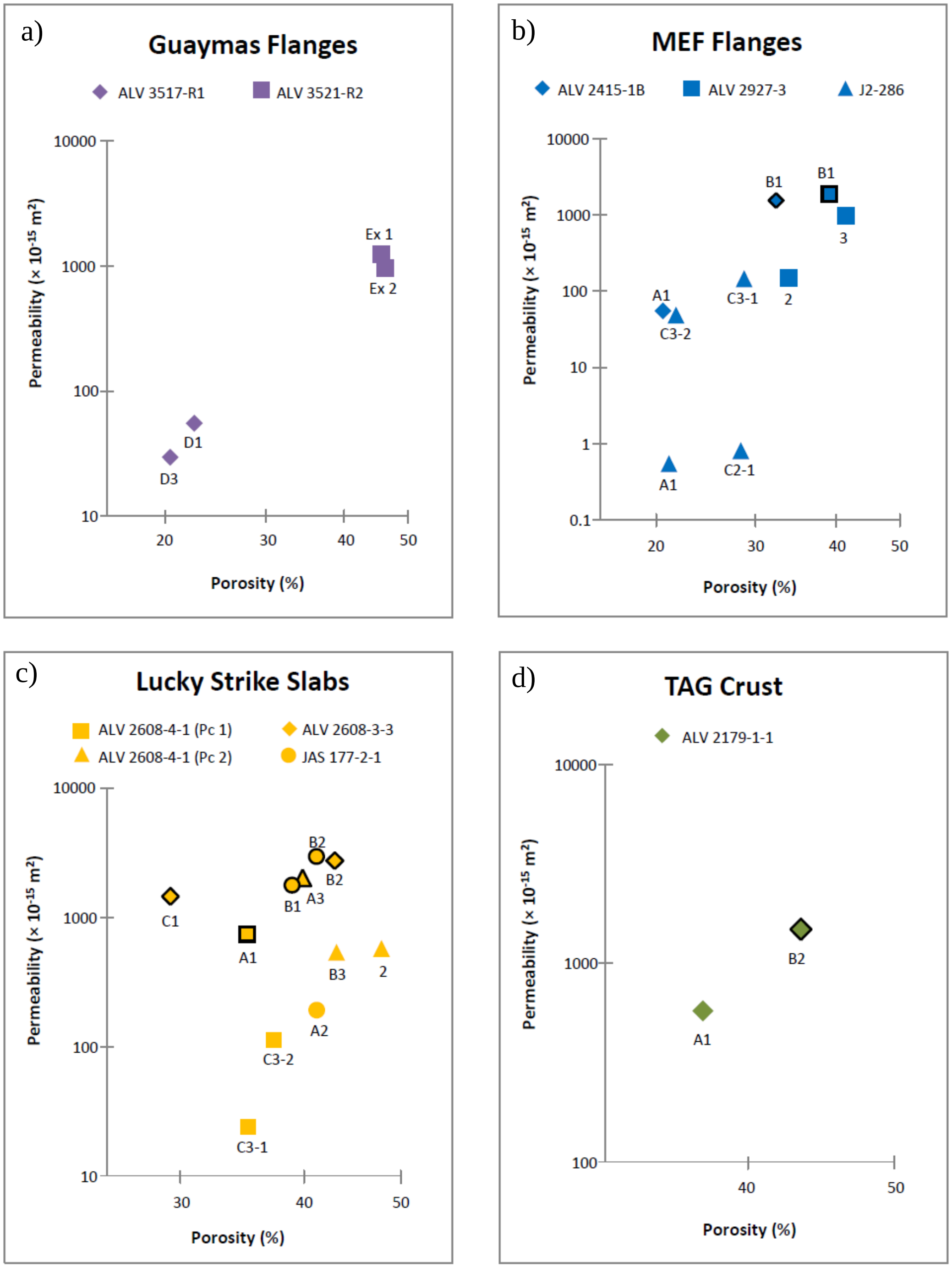

Figure 5.6: Permeability and porosity data for cores from which thin sections were obtained for microstructural analyses. Symbol colors are consistent with Figure 2 and are indicative of sample location: purple = Guaymas Basin, blue = MEF, yellow = Lucky Strike, and green = TAG. Different samples from each group are marked by differently shaped symbols, with black-rimmed symbols denoting parallel-to-layering cores. **a)** Guaymas flange data, **b)** MEF flange data, **c)** Lucky Strike slab data, and **d)** TAG crust data.

Sample / Section	Mineral Present	Grain Packing	Grain Size (μm)	Pore Size (μm)	Pore Connectivity	Channel Width (μm)	Section Orientation
ALV 3517-R1							
D1	ca, st (cp, sp)	tight	250; 50	350; 60	low	10	(2)
D3	ca, st (cp, sp)	tight	250; 50	350; 60	low	10	(3)
ALV 3521-R2							
Ex 1	ca, st (brt, cp, sp)	tight	100; 50	300; 70	moderate	10	(2)
Ex 2	ca, st (brt, cp, sp)	tight	100; 50	300; 70	moderate	10	(3)
ALV 2927-3							
2	py, wz (po, cp, am Si)	tight	45	50	moderate	20	(2)
3	py, wz (po, cp, am Si)	moderate	50	80	high	40	(3)
B1	py, wz (po, cp, am Si)	loose	50	30	high	20	(1)
J2-286							
A1	py, po, am Si (wz)	moderate	50	50	low	20	(2)
C2-1	py, wz (po)	moderate	35	75	moderate	20	(3)
C3-1	py, wz, po (am Si)	tight	30; 150	20	low	20	(2)
C3-2	py, am Si (wz, cp)	tight	50	20	low	20	(2)
ALV 2415-1B							
A1	py, po, am Si (cp, wz)	tight-mod	75	75	low	20	(2)
B1	py, po, am Si (cp, wz)	moderate	75	50	moderate	20	(1)
ALV 2608-3-3							
B2	gl (pl, am Si, py)	loose	300	175	high	40	(1)
C1	gl, am Si (pl, py)	moderate	200	150	moderate	10	(1)
ALV 2608-4-1, Pc 1							
A1	gl, am Si, cl (pl)	tight	80	30	low	15	(1)
C3 (top)	gl, am Si, cl (pl)	moderate	100	100	moderate	50	(2)
C3 (bottom)	gl, am Si, cl (pl)	tight	80	60	moderate	20	(2)
ALV 2608-4-1, Pc 2							
A3	gl (am Si, cl, pl)	moderate	200	175	high	40	(1)
B3	gl (am Si, cl, pl)	tight	100	175	high	40	(2)
2	gl (am Si, cl, pl)	tight	100	175	high	40	(2)
JAS 177-2-1							
A2	gl, pl (am Si, cl)	loose	140	150	high	40	(2)
B1	gl (am Si, cl, pl)	loose	200	175	high	50	(1)
B2	gl (am Si, cl, pl)	loose	200	175	high	50	(1)
ALV 2179-1-1							
A1	cp, py, sp	moderate	30	60	high	10	(3)
B2	cp, py, sp	moderate	50	60	high	60	(1)

(1) parallel-to-layering core

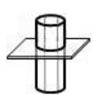

thin section cut radially transects different layers

(2) perpendicular-to-layering core

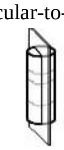

thin section cut axially transects different layers

(3) perpendicular-to-layering core

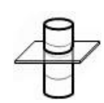

thin section cut radially consists of a single layer

am Si = amorphous silica; brt = barite; ca = calcite; cp = chalcopyrite; cl = clay; gl = palagonitized glass; pl = plagioclase; po = pyrrhotite; py = pyrite; sp = sphalerite; st = stevensite; wu = wurtzite

Table 5.2: Summary of microstructural observations for each thin section.

filling pore space between the larger crystals. Pore space is limited, occurring between clusters of calcite crystals, and there is little to no pore connectivity. The transverse section (core D3), taken through a region of the core near the transition from larger to smaller crystals, also reveals limited pore space and a lack of pore connectivity (Figure 5.7a). Tight packing of calcite crystals limits pore space, pore connectivity, and likely inhibits flow and accounts for the low permeability values measured.

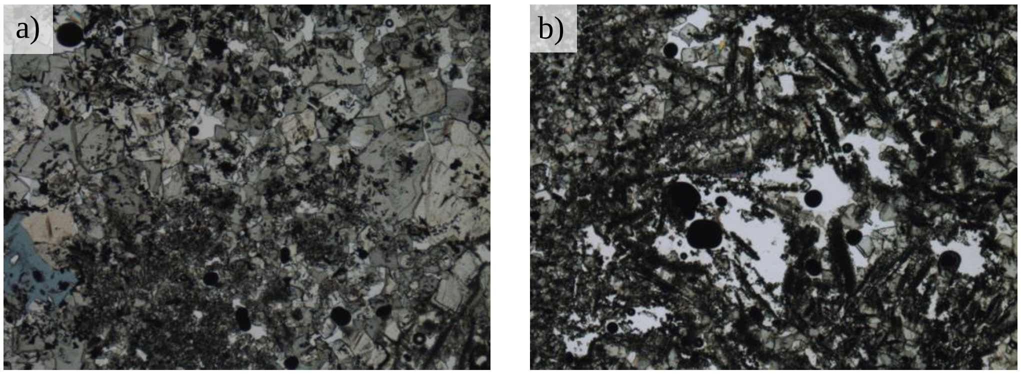

Figure 5.7: Cross polarized images of Guaymas flange cores. Width of each image ~2.7 mm. Larger blocky grains are calcite crystals; dark, elongated and grungy looking crystals are stevensite; white space is pore space. **a)** Section D3 is from sample ALV 3517-R1. Calcite crystals are very tightly packed. **b)** Section Ex 2 from sample ALV 3521-R2. Crystals structure contains larger pores.

For sample ALV 3521-R2, which has much higher permeability and porosity values, the axial cut (core Ex 1) is composed of large calcite crystals at the base of the core, adjacent to where hot fluid was pooled, and there are also patches of large crystals throughout the core. Calcite crystal size and packing is more variable in this sample, and there is more pore space (Figure 5.7b), than in sample ALV 3517-R1. Greater pore connectivity is observed in addition to greater porosity.

The distribution of calcite crystals observed in the Guaymas samples suggests that as CO_2-rich fluids pool under the flange large calcite crystals precipitate along this surface under relatively constant conditions and high temperatures. Fluid that percolates upwards across a steep thermal gradient cools, and more variable conditions result in precipitation of smaller calcite crystals, stevensite, and sulfide minerals within pore space of upper parts of the flange.

5.3.2 MEF Flanges

The MEF flange samples are composed dominantly of sulfide minerals, not carbonate. Nine thin sections were made from three samples: ALV 2927-3 (3 thin sections), ALV 2415-1B (2 thin sections), and J2-286 (4 thin sections) (Figure 5.6b). Seven of the nine thin sections are from cores oriented perpendicular to layering, with five of these sections cut vertically to cross the different layers, and two cut horizontally, parallel to layering; the other two thin sections are from cores oriented parallel to layering, and were cut horizontally to cross the different layers. The thin sections oriented perpendicular-to-layering exhibit the full range of textures in each sample.

The thin section from the highest permeability core, ALV 2927-3 core B1, reveals layers composed of small to moderate sized crystals of wurtzite and pyrite (20 to 125 μm, average 40 μm), with minor amounts of similarly sized chalcopyrite and pyrrhotite and trace clay. Differences in crystal size and packing distinguish one layer from another, with different crystal packing resulting in a range of pore connectivity throughout the sample. For instance, one layer is particularly porous and well connected with channels averaging ~80-100 μm in width; pore connectivity in other layers is not as high, though crystal packing is still loose. The thin section from core 3 of the same sample, a core with lower permeability but higher porosity, reveals only one layer (because it was cut parallel to layering), and thus likely is not representative of the entire core. The layer is similar in mineral content, texture, crystal size, packing, and pore connectivity to the layer of core B1 that exhibits the highest pore connectivity, though in patches a very thin layer of amorphous silica is present (Figure 5.8a). The thin section from ALV 2927-3 core 2 reveals layers and textures very similar to those in the thin section from core 3, B1 of the same sample. Pore connectivity in some layers of core 2 is very low, with sulfide crystals more tightly packed, and some pore connectivity decreased and channels blocked by small amounts of late amorphous silica, particularly at the top of the core, nearest the upper flange surface.

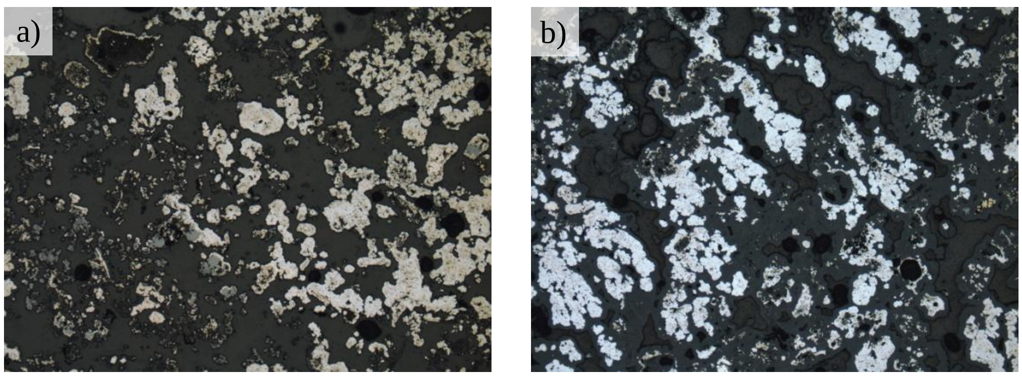

Figure 5.8: Reflected light images. **a)** Section 3 is from sample ALV 2927-3. The grains are loosely packed. Large well-connected, equant void space is observed, which is usually an indication of high-connectivity and high permeability. **b)** Section A1 from sample ALV 2415-1B. Precipitation of amorphous silica causes void space reduction and likely causes a loss of pore connectivity, thus reducing permeability.

Thin sections from sample ALV 2415-1B cores B1 and A1 similarly reveal textures of several layers. The thin section from core A1 is composed of pyrite, with minor wurtzite, marcasite, trace pyrrhotite and chalcopyrite, and variable amounts of amorphous silica (Figure 5.8b). Fossil worm tube casts and clasts of outermost marcasite-rich upper flange layers that collected on the upper flange surface as debris are present near the top of the core, coated with a layer of late amorphous silica. Large isolated pores are present in this uppermost layer. Amounts of amorphous silica are least at the base of the core, closest to where hot fluid was pooled, and greatest near the top of the flange. Pore connectivity is only present in layers where the sulfide crystals were initially widely spaced (loosely packed). The thin section from ALV 2415-1B core B1 also shows variable amounts of late stage amorphous silica, with greater amounts nearer the top of the flange. Due to the broad spacing of the initial sulfide crystals, pore connectivity and channel width have been retained in some of the layers. As with ALV 2927-3 core B1, the highest permeability layer of ALV 2415-1B core B1 should exert the greatest control on the overall permeability of the core.

For sample J2-286, four thin sections were made from cores oriented perpendicular to layering. The thin section from core C3-1 reveals layers of different mineral composition, crystal shape and size, porosity, and packing. The layer at the base of the core is composed of large pyrrhotite (blades ~550 μm long) and cubanite, with large pore spaces adjacent to large crystals. Mid-layers of the core are composed of finer-grained resorbed pyrrhotite, pyrite and wurtzite, with the uppermost layer composed of mixed pyrite and wurtzite (crystals 10-50 μm in size). Cracks are present, with textures consistent with the cracks having been conduits for fluid in the past: one crack is lined with pyrite, and another filled with amorphous silica, and amorphous silica fills pore spaces adjacent to the crack. The thin section from core also reveals a large range in crystal sizes through the layers. The layers are composed primarily of pyrite crystals with minor amounts of wurtzite and marcasite, and nearly all crystals are heavily coated with amorphous silica. The precipitation of amorphous silica in many of the layers appears to have severely restricted and in some cases blocked flow channels between crystals. Although, in one of the layers the crystals were initially widely spaced, so that even with the later precipitation of the amorphous silica coating there was still ample space between crystals to accommodate flow. Fossil tube worm casts are present in one layer, with the tubes 50% filled by later precipitated pyrite and amorphous silica spherules. The thin section from core A1 is similar compositionally to that from core C3-2, with the exception that abundant amorphous silica is present coating crystals and filling what was pore space in the majority of the layers in core A1, resulting in little to no pore connectivity. There are layers present that do still contain pore space, but these pores are isolated. The thin section from core C2-1 is different from the other thin sections in that it was taken through one of the core's layers rather than through the whole core. The layer exhibits narrow channels that are moderately well connected. Amorphous silica is absent, some Fe-oxide is present at crystal boundaries, and the fossil worm tube casts present are much smaller in size than in other parts of this sample. It is likely that the low permeability measured for this core may be indicative of the presence of substantial amorphous silica elsewhere in the core, in a layer that was not transected by the thin section.

Flange growth can be closely linked to the microstructures observed in the thin sections, as was true for the Guaymas flanges. Larger sulfide crystals develop along the base of the flange overlying the pooled fluid, under relatively constant conditions. Pore space between these large sulfide crystals accommodates the upward migration of hot fluids. As the fluids cool, smaller sulfide crystals precipitate throughout the flange under more variable conditions. Conductive cooling of vent fluid or vent fluid/seawater mixtures result in saturation and deposition of amorphous silica on existing surfaces as a thin layer. Over time the precipitation of angular sulfide crystals and coatings of silica will block flow pathways and limit the permeability through the flange.

5.3.3 Lucky Strike Slabs

The slab samples are composed of shards of palagonitized glass ± plagioclase shards and later stage amorphous silica and clay. Eleven thin sections were made from four slab samples: ALV 2608-3-3 (2 sections), ALV 2608-4-1, Pc 1 (3 sections), ALV 2608-4-1, Pc 2 (3 sections), and JAS-177-2-1 (3 sections) (Figure 5.6c), all cut through the cores such that the samples' layers were present in each section. Layers were delineated by changes in grain packing and often grain size. Thin sections from five perpendicular-to-layering cores were examined to identify microstructural features that might explain the relatively steep ($\alpha \sim 8$) permeability-porosity trend for these cores. The thin section from the most permeable core (ALV 2608-4-1, Pc 2 core 2) reveals moderately sorted, highly fragmented shards of palagonitized glass (~100 μm), in each of its layers, and amorphous silica and clay coat many of the glass grains; however, pore connectivity remains intact through each of the layers. The thin section from core B3 of the same sample is very similar and contains layers of highly fragmented glass shards, although within this section greater variability in the structure of the layers is apparent. There are two layers visible within this section that can account for the somewhat lower measured permeability and porosity values: a layer of slightly smaller and more tightly packed grains, and a layer where pore space between grains has been almost entirely filled with amorphous silica and clay.

These restrictive features were not observed in the thin section from core 2. The thin section from sample JAS 177-2-1 core A2 is also composed of palagonitized glass shards, though shard size varies considerably through the different layers. There is a greater abundance of plagioclase shards than in the previously described thin sections, although they too vary in size and shape. The shards are widely spaced, but in several of the layers there is a thick amorphous silica and clay coating that fills previous pore space and blocks flow channels between shards. The lower permeability values can be attributed to this high degree of channel restriction. Thin sections from cores C3-1 and C3-2 of sample ALV 2608-4-1, Pc 1 exhibit similar textures – a mixture of large and small palagonitized glass shards coated in amorphous silica. Much of the space between shards has been infilled with clay that blocks channels and isolates many of the pores. Microstructural observations are consistent with core C3-1 being least permeable because it includes a layer that has been severely infilled by clay and amorphous silica precipitation.

Thin sections from parallel-to-layering slab cores reinforce the observations from the previously described slab thin sections. The most and least permeable of these cores are from sample ALV 2608-3-3. Thin sections from both cores B2 and C1 reveal poorly sorted palagonitized glass shards (and a few plagioclase shards) coated with amorphous silica and minor clay. In the thin section from core B2, grains are loosely packed, and the coating of amorphous silica narrows, but seldom blocks channels (Figure 5.9a, b). In the thin section from core C1, glass shards are more densely packed than in core B1, and coatings

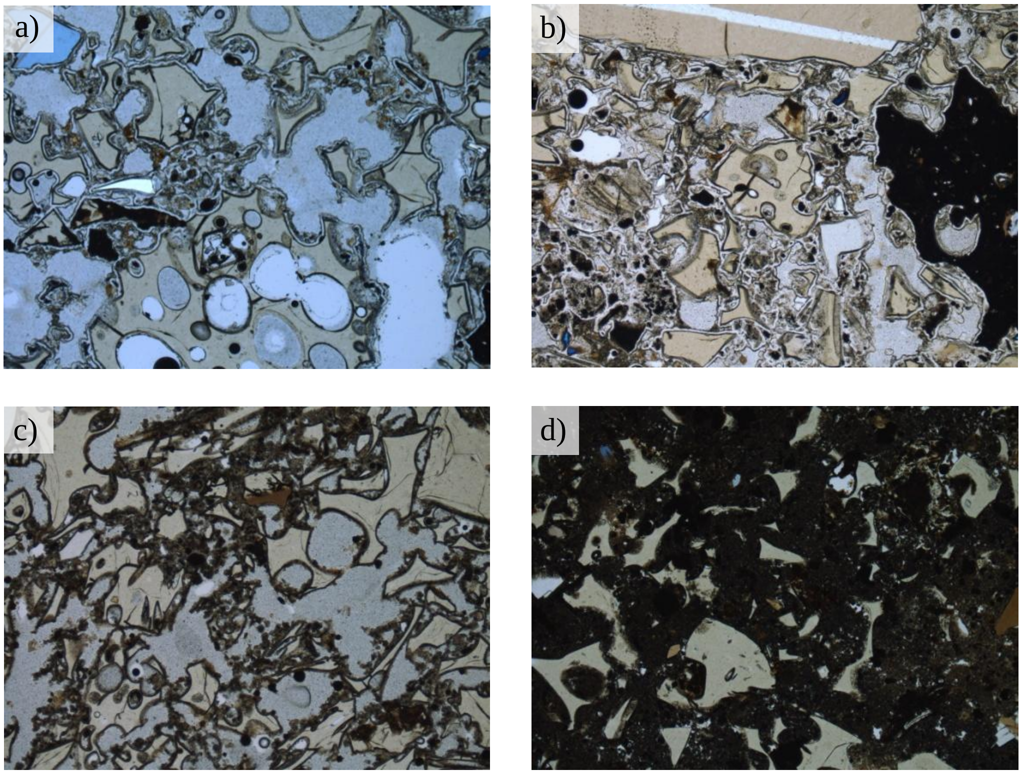

Figure 5.9: Cross polarized slab images showing variation in grain packing and precipitation between sample layers. Width of images is 2.7mm. **a and b)** Section B2 from sample ALV 2608-3-3. A layer with large, broadly spaced glass shards is shown in a), while a more tightly packed layer with highly fragmented grains is shown in b). Close packing of angular grains can cause pinch-offs in void space around grains that can typically lead to limited pore connectivity and a lower permeability. **c and d)** Section B2 from sample JAS 177-2-1. A well connected, high permeability layer is shown in c), whereas a layer with pore space that had been densely infilled by the precipitation of amorphous silica and clay is shown in d). The precipitation of amorphous silica and clay results in void space reduction, which generally leads to a loss of pore connectivity, thereby reducing permeability.

of amorphous silica and clay are thicker, resulting in less pore connectivity. However grain packing is less dense, and pore connectivity greater, in the layer of core C1 nearest the top of the slab; this layer likely explains why the permeability of this core (made parallel to layering) has a high permeability despite a low porosity. Textures observed in the thin section from sample JAS 177-2-1 cores B2 and B1 are very similar to those from core A2 from that sample. As with core A2, there is considerable variability between the structure and packing, with both highly porous and well connected layers alternating with a layer that has been heavily coated with amorphous silica and clay (Figure 5.9c, d). Permeability of the cores oriented parallel to layering is likely controlled by the layer with the highest pore connectivity. The thin section from sample ALV 2608-4-1, Pc 2 core A3 reveals both amorphous silica and clay precipitated throughout the various layers, but pore space and pore connectivity are still both high, as in this sample's core 2. The core with the lowest permeability of the parallel-to-layering cores is ALV 2608-4-1, Pc 1 core A1. The thin section from this core exhibits abundant amorphous silica and clay, and pore connectivity appears lower than in the other parallel-to-layering cores.

From a mineralogical and textural perspective, seafloor hydrothermal slabs can be classified as hyaloclastites that form from the interaction of hot magma with seawater. Hyaloclastites contain glass shards, as seen in the slab thin sections, which form as thermal stresses break apart large pieces of volcanic glass. The orientation of the slab layers and the grain size within each layer suggests that smaller shards settle to the bottom of the slab while larger fresher grains are found predominantly along the slab surface. Layers are delineated by differences in shard size, initial packing density, and late stage amorphous silica and clay deposition. The presence of amorphous silica indicates that silica-rich vent fluids, or mixtures of vent fluids and seawater, have percolated through the slabs with cooling of the fluids resulting in amorphous silica and clay saturations [e.g., *Tivey et al*., 1999) and deposition along grain edges, resulting in cementation of some slab layers.

The slab samples are notable in that the perpendicular-to-layering cores plot at a slightly steeper trend than the other vent deposit sample groups (Figure 5.5b), which may be due to the high angularity of the glass grains. Angular grains create roughness along flow pathways that can significantly impact the deposit's permeability. Any changes in grain shape over time can have a large effect on permeability while not producing major changes in the overall porosity, resulting in a steeper trend.

5.3.4 TAG Crust

Measurements were made on only one crust sample, ALV 2179-1-1. Thin sections were made form core A1 (from a perpendicular-to-layering core) and core B2 (from a parallel-to-layering core) (Figure 5.6d). The thin section from core A1 was cut horizontally through just one of the sample's layers. The layer is composed dominantly of fine-grained chalcopyrite and pyrite (~30 μm) with pore space (~60 μm) along crystal edges. Pore connectivity in this layer is high, but through narrow (~10 μm) channels. Unfortunately no information on pore connectivity in other layers of this sample is available. The thin section from core B2 was cut across the layering (Figure 5.10). Textures and mineral contents are similar to

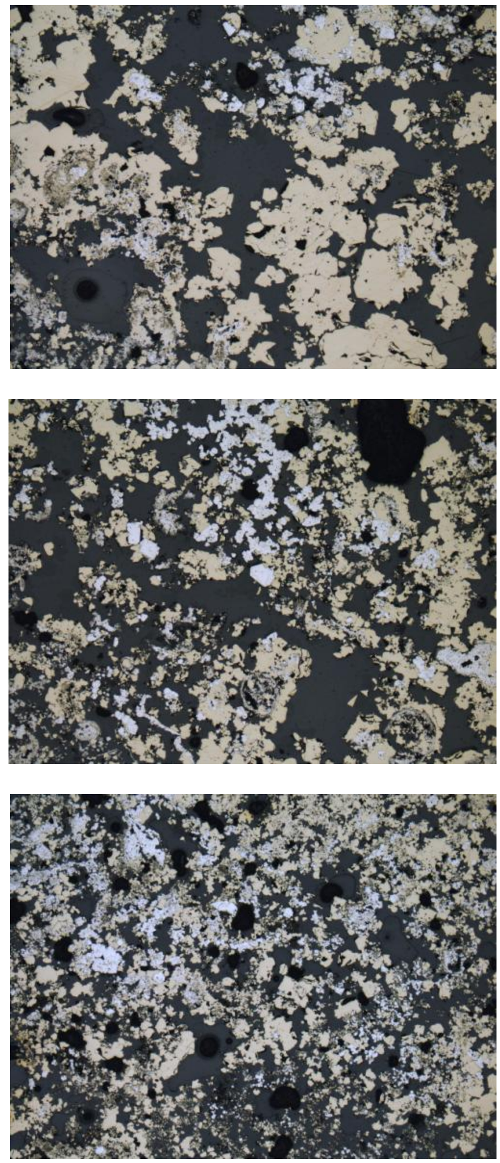

Figure 5.10: Reflected light images of layering through crust sample ALV 2179-1-1, core B2. Sulfide-rich layers grade from loosely packed crystals (high connectivity) to more closely packed crystals (lower connectivity). Images are each ~2.7 mm wide.

those in core A1. Layering was apparent only through changes in crystal size. High pore connectivity is consistent through most of the layers and can explain the high permeability value.

Because crust deposits on the TAG active mound are situated adjacent to high-temperature black smokers, fluids beneath the crust are likely hot (around 300°C). The crust sample appears to have developed much like sulfide flange deposits, with hot fluid percolating upwards from the base of the sample [*Tivey et al.*, 1995]. Textures are consistent with this, with large sulfide crystals at the bottom of the crust where conditions are likely relatively constant. Packing of the crystals is loose, providing space at crystal boundaries to accommodate fluids moving up through the deposit. As the fluid travels upwards it cools, resulting in precipitation of smaller more closely packed crystals under more variable conditions.

5.4. Discussion

In this study, permeability and porosity measurements were conducted on flange, slab, and crust samples, each of which exhibit layering that parallels upper and lower surfaces of the deposits. The data document that permeability values in the direction parallel to layering are considerably less variable and higher than permeability values in the direction perpendicular to layering. These differences in permeability suggest different flow behaviors caused by layering, and have broad implications for the overall fluid flux accommodated by flange, slab, and crust seafloor deposits. Given observed permeabilities, fluid will travel horizontally through these deposits, within prominent highest permeability deposit layers. This layer will be able to continually facilitate the lateral flow of fluid through the deposits, because permeability decreases little as porosity decreases (trend of $\alpha \sim 1$).

The difference in magnitude as well as in variation of permeability values of cores taken parallel-to-layering versus perpendicular-to-layering in all samples can be quantified using an effective permeability model. Because the total volume flux parallel to layering is equal to the sum of the volume flux through each layer, the effective permeability (k_{pal}) in this case is the sum of each layer's permeability (k_i) multiplied by the fraction of the total thickness that layer constitutes (h_i/H) (5.1), where h_i and H are the thickness of each layer and the total thickness of the sample, respectively (e.g., *Freeze and Cherry*, 1978):

$$k_{pal} = \sum_{i=1}^{n} k_i \frac{h_i}{H} \tag{5.1}$$

In comparison, the fluid flux perpendicular to layering must obey mass conservation while crossing several layers of varying permeabilities. The effective permeability (k_{pep}) perpendicular-to-layering equals the total deposit thickness (H) divided by the sum of the ratios between layer thicknesses (h_i) to their respective permeabilities (k_i):

$$k_{pep} = H \Big/ \sum_{i=1}^{n} \frac{h_i}{k_i} \tag{5.2}$$

From eqn. (5.1) and (5.2), it is easy to see that permeability of a layered vent deposit is generally anisotropic, with the parallel-to-layering effective permeability k_{pal} greater than the perpendicular-to-layering effective permeability k_{pep}.

The parallel versus serial flow patterns within the deposit cores are supported by microstructural observations from sample thin sections. Petrographic examination shows that the flange, slab, and crust deposits generally consist of layers with large contrasts in crystal packing, void space, and pore connectivity (Figures 5.8-5.10). Low-permeability layers, resulting from initial differences in crystal packing, and/or subsequent deposition of crystals in pore space, and/or late stage precipitation of amorphous silica ± clay, are observed in both the parallel- and perpendicular-to-layering cores. These low permeability layers restrict the overall flux perpendicular to layering thus exerting primary control on k_{pep}, whereas the flux parallel to layering and thus k_{pal} is affected primarily by the highest permeability layer. This explains why the permeability values in the parallel-to-layering cores are consistently higher than those in the perpendicular-to-layering cores and why the perpendicular-to-layering cores exhibit much greater permeability variations.

This difference in parallel flow and serial flow is best seen by comparing textures observed in thin sections from cores B1 and 2 of sample ALV 2927-3. Both of these thin sections clearly show the same sequence of sample layering with some layers of relatively high pore connectivity, and thus likely permeability, and some with lower pore connectivity and thus likely permeability. Although they are similar, core B1, oriented parallel-to-layering, has a measured permeability over an order of magnitude greater than that of core 2, which was oriented perpendicular-to-layering.

The microstructural observations provide explanations for the two EPPRs identified for these deposits. For the parallel-to-layering cores, with an EPPR with an exponent of $\alpha \sim 1$, the change in the effective permeability of the samples are relatively small, even for large changes in porosity. The thin sections taken from all of the cores show that the layers within these cores have undergone pore evolution processes, such as late-stage precipitation of amorphous silica or clays or thermal cracking of crystals. Textures resulting from these processes have been observed in the sample thin sections to significantly change the porosity of the layers. With late-stage amorphous silica precipitation, precipitation can initially result in smoothing of crystal edges, but after larger amounts of precipitation these mineral coatings can pinch-off, block, or completely infill pore space and channels along crystal edges. The parallel-to-layering cores have experienced a loss of porosity as a result of these processes; however, layers of high permeability which were retained during these processes will still allow the deposit to accommodate a high flux of fluid.

Data from the perpendicular-to-layering cores reveal an EPPR with an exponent of $\alpha \sim 5$, and pore evolution processes that are significantly more effective in changing the overall permeability. Flow through these samples, perpendicular to layering, is serial. Changes in pore space of least permeable layers will restrict this serial flow and lower the effective permeability of the sample. These effects of pore evolution processes on the sample layers and the effective permeability of the deposits are important for modeling their fluid fluxes.

Chapter 6: Spire Deposits

Hydrothermal spires are tower-like deposits that grow vertically upwards from the seafloor. Zn-rich actively diffusing spires, black smoker chimneys, and relict spires are all spires deposits. These deposits were grouped together following data collection and analyses, because they have similar structural features and likely experience similar evolution processes. In total the spire sample set includes 9 actively diffusing spires, 6 black smoker chimneys, and 8 relict spires. These spires come from several different vent fields: ABE, MEF, TAG, Cleft, and Kilo Moana.

6.1 Permeability and Porosity

Probe permeability measurements for the Zn-rich actively diffusing spires, black smoker chimneys and relict spires are plotted in Figures 6.1, 6.2, and 6.3 respectively. The Zn-rich actively diffusing spires were the most permeable with values ranging from ~6×10^{-13} - 8×10^{-10} m^2. Permeability anisotropy is observed in most of these samples. In general, permeability measurements made near the center of the spire are lower than those made along the outer rim of the sample. The black

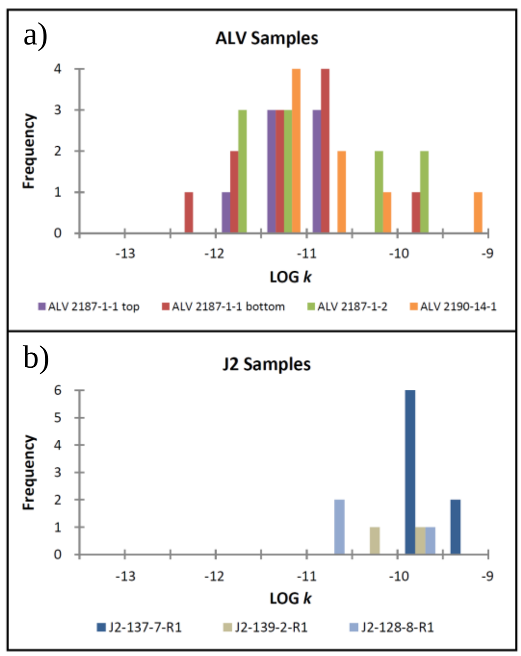

Figure 6.1: Histograms showing probe permeability data for Zn-rich diffusing spire samples. Plots show frequency of measurements at a given permeability. Colors represent individual samples. **b)** Data for four ALV samples. **b)** Data for three J2 samples.

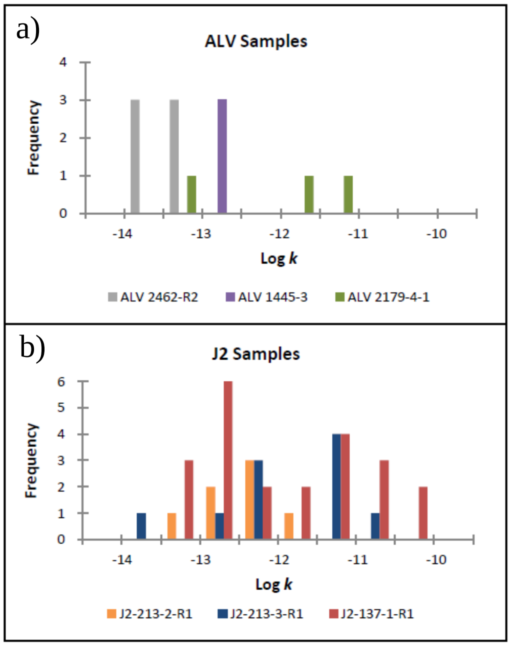

Figure 6.2 (*above*): Histograms showing probe permeability data for black smoker chimney samples. Plots show frequency of measurements at a given permeability. Colors represent individual samples. **a)** Data for three ALV samples. **b)** Data for three J2 samples.

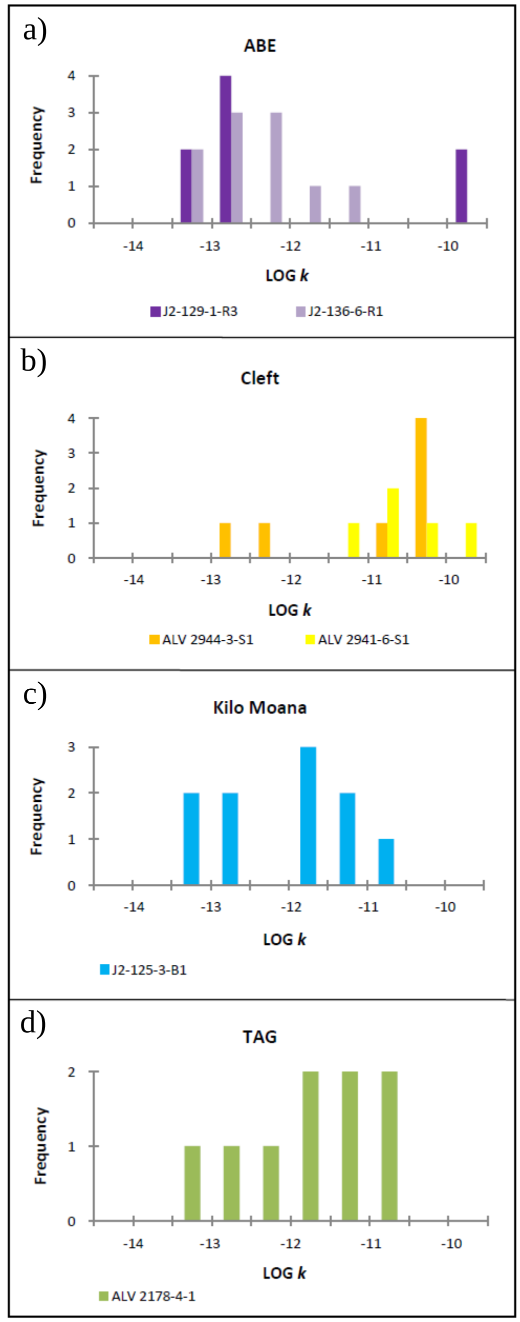

Figure 6.3 (*right*): Histograms showing probe permeability data for relict spire samples. Plots show frequency of measurements at a given permeability. Colors represent sample locations: ABE = purple, Cleft = gold, Kilo Moana = blue and TAG = green. **a)** Data for two ABE samples. **b)** Data for two Cleft samples. **c)** Data for one Kilo Moana sample. **d)** Data for one TAG sample.

smoker chimneys, which had permeability values ranging from ~2×10^{-14} - 8×10^{-11} m^2, also showed permeability variations within samples. Permeability measurements made along the inner chalcopyrite lining were lower than those made along the outer, more anhydrite-rich layers. For the relict spires, probe permeability values ranged between ~4×10^{-14} - 2×10^{-10} m^2. The relict spires had more pronounced variability in measurements made along the same direction, suggesting that these samples may have a higher degree of surface roughness than the other spire samples. The few measurements that were obtained axially along spires have slightly lower permeability values than those made radially for the same sample.

Similar to the other discussed sample types, varying degrees of surface roughness can account for some of the observed variability in the probe permeability data. High degrees of surface roughness can lead to an insufficient permeameter seal against the sample surface, which can increase the potential for air to be leaked during measurement. An improper seal can lead to variations in the data that are not representative of the samples' true permeability anisotropy.

After completing probe permeability measurements, cylindrical cores were taken from select probe measurement sites for axial permeability and porosity measurement. In total, 22 Zn-rich diffusing spire cores, 11 black smoker chimney cores, and 34 relict spire cores were made taken from the deposit samples. Permeability and porosity data for the Zn-rich diffusing spires, black smoker chimneys and relict spires are listed in Tables 6.1, 6.2, and 6.3, respectively. Confining pressure from approximately 0.5-2.7 MPa was incrementally applied to the cores during measurement. Pressure profiles for the Zn-rich diffusing spires, black smoker chimneys and relict spires are shown in Figures 6.4, 6.5, and 6.6, respectively.

Sample	Core	Probe k ($\times 10^{-15}$ m^2)		Core k ($\times 10^{-15}$ m^2)						Core ϕ (%)			
				1.4 MPa		2.1 MPa		2.7 MPa		2.1 MPa		2.7 MPa	
		k	2σ	k	2σ	k	2σ	k	2σ	ϕ	2σ	ϕ	2σ
ALV 2187-1-1	A2	8339.8	±3.6	6111.0	±42.5	5462.3	±35.7	4847.3	±30.4	45.5	±0.3	44.1	±0.2
(top)	A4	8386.7	±4.1	4013.4	±17.4	3433.7	±24.3	3038.1	±14.8	36.5	±0.2	35.8	±0.2
	B1	27560.5	±4.1	613.1	±1.1	596.3	±2.5	578.6	±1.1	45.5	±0.6	44.2	±0.7
ALV 2187-1-1	A2	25910.6	±2.0	340.2	±1.2	332.9	±1.1	322.6	±0.9	38.9	±0.5	38.4	±0.3
(bottom)	B1	31357.7	±3.3	590.4	±1.3	581.7	±4.5	557.6	±2.1	42.1	±0.2	41.8	±0.3
	C2	1137.5	±3.9	618.9	±2.8	551.0	±2.3	523.8	±1.3	41.0	±0.2	40.5	±0.3
	C3	641.7	±4.1	1709.6	±10.0	1467.9	±6.7	1306.2	±5.4	40.6	±0.4	40.0	±0.4
ALV 2187-1-2	B2-2	--		1817.8	±5.7	1748.7	±2.8	1704.0	±5.3	41.8	±0.2	41.3	±0.2
	C1/C2	216149.9	±1.4	1813.7	±17.6	1619.4	±14.4	1476.5	±9.0	39.4	±0.1	38.7	±0.2
	C3-1	2372.5	±3.3	2657.3	±11.0	2602.0	±11.2	2534.5	±3.6	41.3	±0.3	40.9	±0.2
	C3-2	--		2809.0	±15.5	2670.0	±7.1	2501.7	±9.2	42.4	±0.3	41.5	±0.5
	C5	7580.9	±4.0	1460.9	±5.5	1426.3	±3.3	1400.6	±5.4	42.9	±0.2	42.2	±0.1
ALV 2190-14-1	A1	4066.2	±4.5	2802.2	±25.4	2726.3	±9.8	2661.7	±7.4	47.5	±0.2	46.7	±0.2
	B1	12847.6	±3.1	1195.5	±3.1	1140.0	±2.6	1073.3	±6.1	47.6	±0.6	46.1	±0.6
	B2	8541.1	±3.7	797.7	±3.2	775.1	±3.0	761.1	±1.9	41.3	±0.5	41.0	±0.5
J2-128-8-R1	Ex	--		29.0	±0.5	22.2	±0.3	18.2	±0.1	28.0	±0.2	27.4	±0.5
J2-137-7-R1	B1	239125.2	±2.5	1181.7	±6.0	1068.4	±5.8	994.2	±3.2	47.8	±1.0	44.3	±0.7
J2-222-1-R1	A1	--		367.8	±2.6	327.3	±1.0	305.8	±1.2	35.0	±0.3	34.1	±0.3
	A2	--		231.3	±0.3	227.7	±0.5	225.9	±0.6	36.0	±0.5	35.6	±0.7
	Ex	--		220.8	±1.6	202.9	±1.0	190.8	±0.8	29.8	±0.8	29.4	±0.5
J2-127-1-R2	B2	--		379.2	±0.4	371.1	±0.6	366.1	±1.1	37.4	±0.5	37.1	±0.5
	B3	--		444.1	±1.2	438.2	±1.0	432.3	±1.2	36.2	±0.2	35.7	±0.3

Table 6.1: Average probe permeability, core permeability, and porosity and 2σ values for Zn-rich actively diffusing spires.

Sample	Core	Probe k ($\times 10^{-15}$ m^2)		Core k ($\times 10^{-15}$ m^2)						Core ϕ (%)			
				1.4 MPa		2.1 MPa		2.7 MPa		2.1 MPa		2.7 MPa	
		k	2σ	k	2σ	k	2σ	k	2σ	ϕ	2σ	ϕ	2σ
ALV 1445-3	C1	129.6	±1.7	21.5	±0.3	16.1	±0.2	13.5	±0.2	24.9	±0.3	24.0	±0.8
ALV 2179-4-1	A1	1230.4	±2.9	167.6	±0.6	135.6	±0.4	113.7	±0.5	42.7	±1.0	41.4	±0.7
	B1	309.4	±2.4	27.0	±0.7	17.7	±0.4	12.9	±0.2	36.6	±0.4	35.0	±0.6
	C1	3675.5	±2.4	132.1	±0.8	124.1	±0.3	122.1	±0.2	42.2	±0.4	41.4	±0.5
J2-137-1-R1	D1	111.6	±0.1	0.7	±0.02	0.6	±0.03	0.6	±0.02	16.9	±0.5	16.7	±0.5
	D2	61.3	±0.2	0.4	±0.03	0.4	±0.02	0.4	±0.02	13.9	±0.4	13.8	±0.5
	D3	223.0	±0.1	0.8	±0.1	0.7	±0.02	0.7	±0.02	18.0	±0.4	17.8	±0.3
	D4	90.0	±0.3	0.6	±0.02	0.6	±0.01	0.6	±0.02	17.7	±0.3	17.4	±0.5
J2-213-3-R1	A1	12146.5	±2.9	20.3	±0.1	18.4	±0.1	17.5	±0.2	28.9	±0.5	28.6	±0.8
	B1	309.4	±3.2	40.5	±0.4	37.7	±0.3	34.9	±0.3	30.6	±0.1	30.1	±0.4
	D1	3675.5	±3.7	115.2	±0.6	99.5	±1.4	86.6	±0.6	39.0	±0.6	38.6	±0.8

Table 6.2: Average probe permeability, core permeability, and porosity and 2σ values for black smoker chimneys.

Sample	Core	Probe k ($\times 10^{-15}$ m^2)		Core k ($\times 10^{-15}$ m^2)						Core ϕ (%)			
				1.4 MPa		2.1 MPa		2.7 MPa		2.1 MPa		2.7 MPa	
		k	2σ	k	2σ	k	2σ	k	2σ	ϕ	2σ	ϕ	2σ
ABE:													
J2-129-1-R3	B2	88.0	±2.9	751.8	±5.9	740.4	±3.0	731.8	±2.7	41.0	±0.2	40.2	±0.1
J2-136-6-R1	A1-1	152.5	±3.7	155.0	±1.3	140.1	±1.0	133.5	±1.0	31.3	±7.8	30.0	±4.7
	A1-2	--		194.5	±1.2	190.8	±1.4	188.8	±1.6	30.2	±1.1	29.8	±1.3
	C2	448.1	±2.3	22.6	±0.4	19.4	±0.3	17.5	±0.2	25.4	±2.4	24.8	±2.0
Cleft:													
ALV 2944-3-S1	A1	51095.7	±3.8	633.1	±3.4	626.4	±4.8	624.2	±3.1	37.6	±10.0	36.3	±6.2
Pc 1	A3	41748.7	±3.6	43.0	±0.3	40.9	±0.3	39.7	±0.2	30.9	±5.7	31.2	±4.5
	B1	27100.4	±4.2	859.4	±5.9	825.7	±8.8	712.9	±7.1	36.0	±8.5	34.6	±5.0
ALV 2944-3-S1	A1	--		331.4	±0.7	327.2	±1.1	325.6	±0.4	33.5	±5.8	31.1	±10.1
Pc 2	A2	--		651.9	±1.3	645.8	±2.5	639.6	±1.4	42.6	±4.5	42.1	±3.3
	A3	--		566.8	±3.2	562.9	±1.1	560.7	±1.0	40.6	±6.5	41.9	±6.2
	A4	--		426.5	±1.5	404.5	±1.0	392.7	±0.8	31.6	±4.7	29.8	±5.9
ALV 2941-6-S1	A1	126826.6	±2.5	194.5	±0.4	140.6	±0.3	117.4	±0.1	32.5	±4.4	32.6	±5.1
Kilo Moana:													
J2-125-3-B1	B2-1	3953.7	±3.3	440.7	±1.5	356.3	±1.6	312.2	±1.4	34.7	±3.5	34.9	±2.3
	B2-2	--		156.6	±0.7	149.4	±0.3	146.6	±0.4	35.4	±5.1	32.7	±5.7
	B3-1	1189.7	±4.1	98.6	±0.7	97.0	±0.6	96.3	±0.9	32.6	±4.0	32.5	±3.3
	B3-2	--		235.4	±0.6	227.5	±0.6	221.9	±0.8	34.6	±2.7	32.1	±4.7
	Ex B2	--		509.6	±2.5	502.5	±2.6	499.5	±1.8	37.8	±2.7	37.1	±3.4
TAG:													
ALV 2178-4-1	4	--		2306.0	±4.6	2224.3	±8.5	2127.5	±10.0	49.3	±0.5	47.5	±0.2
	5	--		1595.5	±10.9	1556.6	±4.7	1525.6	±7.9	45.6	±0.1	44.8	±0.2
	A4	7207.5	±4.0	628.8	±1.6	592.8	±4.5	581.5	±2.2	39.6	±0.4	38.9	±0.4
	A5	30661.6	±3.1	784.3	±3.1	766.9	±2.5	754.7	±4.3	44.9	±0.5	44.2	±0.3
MEF:													
ALV 2461-R13	1-1	--		837.4	±2.9	822.4	±2.4	813.7	±1.7	26.7	±0.1	26.6	±0.1
	1-2	--		1168.1	±3.1	1142.5	±0.7	1118.2	±3.0	22.2	±0.1	22.1	±0.1
	2	--		740.3	±2.3	733.8	±2.0	731.1	±2.3	28.9	±0.2	28.7	±0.3
	3-1	--		0.8	±0.01	0.8	±0.03	0.8	±0.02	17.3	±0.4	16.9	±0.3
	3-2(1-1)	--		0.2	±0.04	0.2	±0.01	0.2	±0.01	5.0	±2.5	8.1	±5.7
	3-2(1-2)	--		0.3	±0.01	0.3	±0.02	0.3	±0.03	10.4	±3.4	10.4	±3.3
	3-2(2)	--		7.7	±0.01	6.4	±0.1	5.9	±0.03	12.2	±0.6	11.0	±2.5
	4-1	--		9.7	±0.1	6.6	±0.1	4.1	±0.2	18.7	±1.6	18.5	±1.8
	4-2	--		5.9	±0.1	4.4	±0.1	3.6	±1.0	22.0	±1.8	21.4	±2.3
	6	--		1.8	±0.01	1.4	±0.02	1.1	±0.04	17.5	±0.2	17.3	±0.2
	7	--		49.7	±0.3	48.3	±0.4	46.8	±0.4	24.4	±1.2	24.7	±0.1
	8-1	--		118.8	±0.7	115.2	±0.4	113.3	±0.3	20.7	±0.2	20.6	±0.1
	8-2	--		119.9	±0.5	112.6	±0.6	107.6	±0.3	20.7	±0.1	20.5	±0.04

Table 6.3: Average probe permeability, core permeability, and porosity and 2σ values for the relict spires.

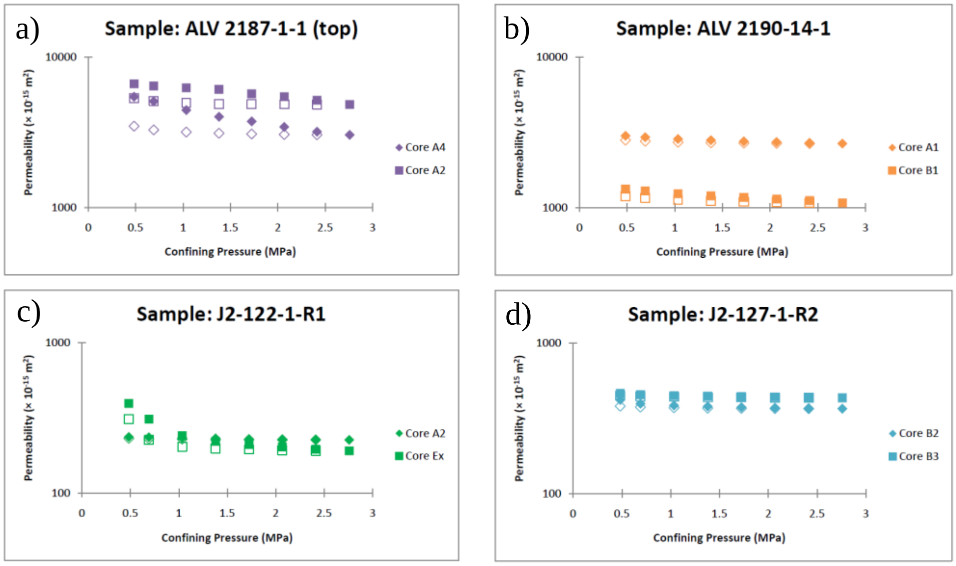

Figure 6.4: Plots showing pressure profiles for select Zn-rich diffusing spire samples during permeability measurement. Colors represent sample: ALV 2187-1-1 (top) = purple, ALV 2190-14-1 = orange, J2-122-1-R1 = green and J2-127-1-R2 = blue. Symbol shapes represent different sample cores (solid = pressure loading, empty = unloading). Changes in permeability with pressure are minor. **a)** ALV 2187-1-1 (top) cores. **b)** ALV 2190-14-1 cores. **c)** J2-122-1-R1 cores **d)** J2-127-1-R2 cores.

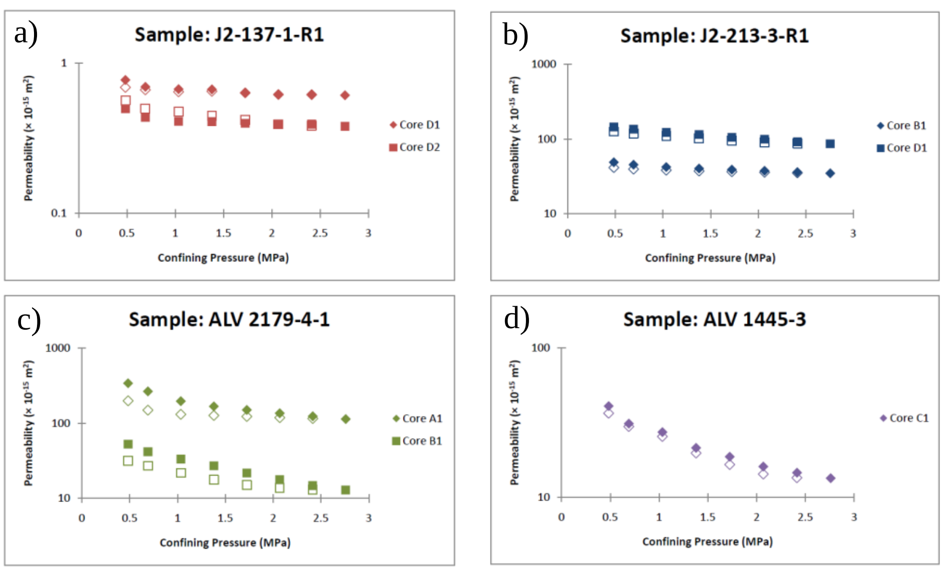

Figure 6.5: Plots showing pressure profiles for select black smoker chimneys during permeability measurement. Colors represent sample: J2-137-1-R1 = red, J2-213-3-R1 = navy, ALV 2179-4-1 = green and ALV 1445-3 = purple. Symbol shapes represent different sample cores (solid = pressure loading, empty = unloading). Changes in permeability with pressure are minor. **a)** J2-137-1-R1 cores. **b)** J2-213-3-R1 cores. **c)** ALV 2179-4-1 cores **d)** ALV 1445-3 core.

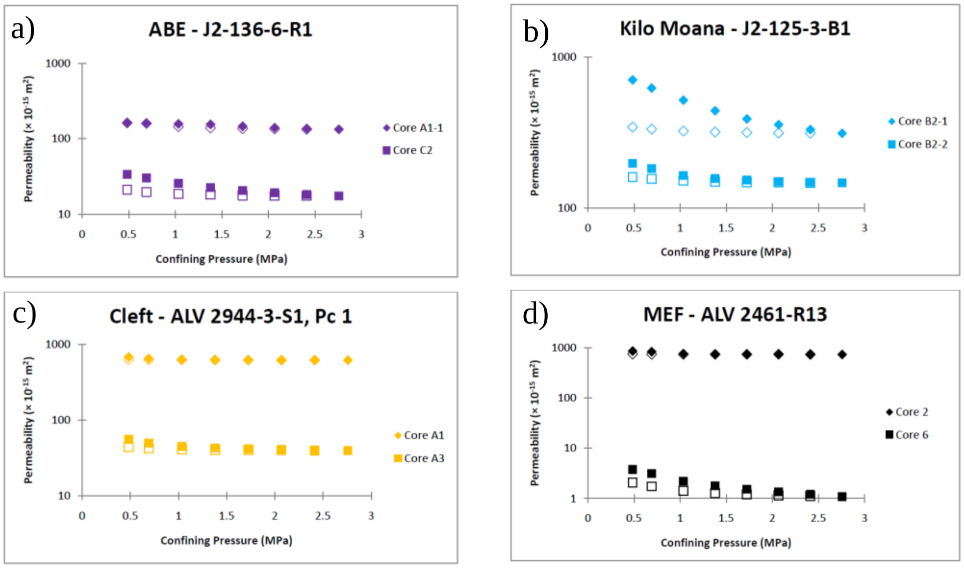

Figure 6.6: Plots showing pressure profiles for select relict spires during permeability measurement. Colors are consistent with Figure 6.3. Symbol shapes represent different sample cores (solid = pressure loading, empty = unloading). Changes in permeability with pressure are minor. **a)** J2-136-6-R1 cores. **b)** J2-125-3-B1 cores. **c)** ALV 2944-3-S1, Pc 1 cores **d)** ALV 2461-R13 core.

During the initial application of pressure, many of the samples experienced a reversible decrease in permeability that can be attributed to the closure of microcracks within the cores [*Walsh*, 1965]. This permeability decrease may be reversible, because lowering the confining pressure would allow the cracks to re-open, therefore increasing permeability. Overall, permeability values measured during pressure unloading are consistent with the values measured during pressure loading. A few cores had permeability values from the unloading cycle that were lower than those of the loading cycle. In these cases the confining pressure may have slightly compacted the structure of the cores, thereby resulting in slightly lower permeability values during the unloading cycle.

Permeability and porosity for the Zn-rich diffusing spires, black smoker chimneys and relict spires are plotted in Figures 6.7, 6.8, and 6.9. Permeability values for the Zn-rich diffusing spires range from ~2×10^{-14} - 5×10^{-12} m^2 and porosity values are between approximately 30-45%. An EPPR trend of α ~ 6 best fits the data for these spires. The black smoker chimneys have permeability values between ~3×10^{-16} - 3×10^{-13} m^2 with porosity values around 15-40%. These data plot along an EPPR trending α ~ 5. Lastly, the relict spires have permeability values from ~7×10^{-16} - 2×10^{-12} m^2 and porosity values from 5-45%. The EPPR trend for the relict spires is α ~ 5. Characteristics of the cores' pore structure identified through microstructural analyses helps explain the determined EPPRs, therefore providing a better understanding of how these spires evolve.

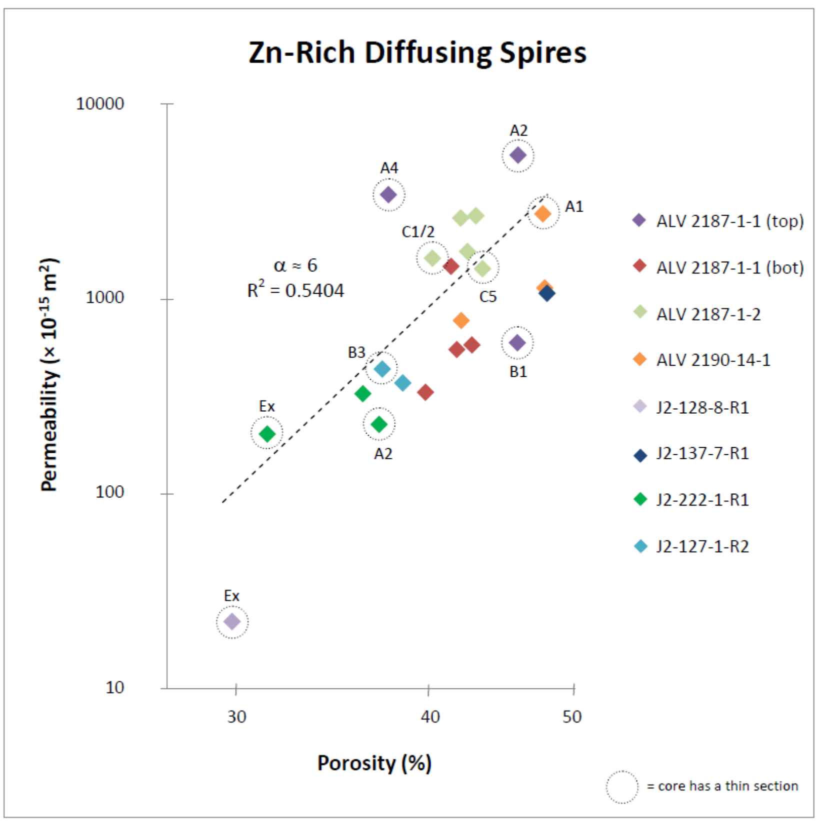

Figure 6.7: Permeability versus porosity data for the Zn-rich actively diffusing spires. Differences in permeability as a function of porosity can be best fit by power-law relationships (black dashed line), with a power-law exponent of α ~ 6. Symbol color denotes sample. Circles around symbols indicate that a thin section was taken from that core. All circled cores are labeled with the core number.

Figure 6.8: Permeability versus porosity data for the black smoker chimneys. Trend of EPPR (black dashed line), is α ~ 5. Symbol color denotes sample. Circles around symbols indicate that a thin section was taken from that core. All circled cores are labeled with the core number.

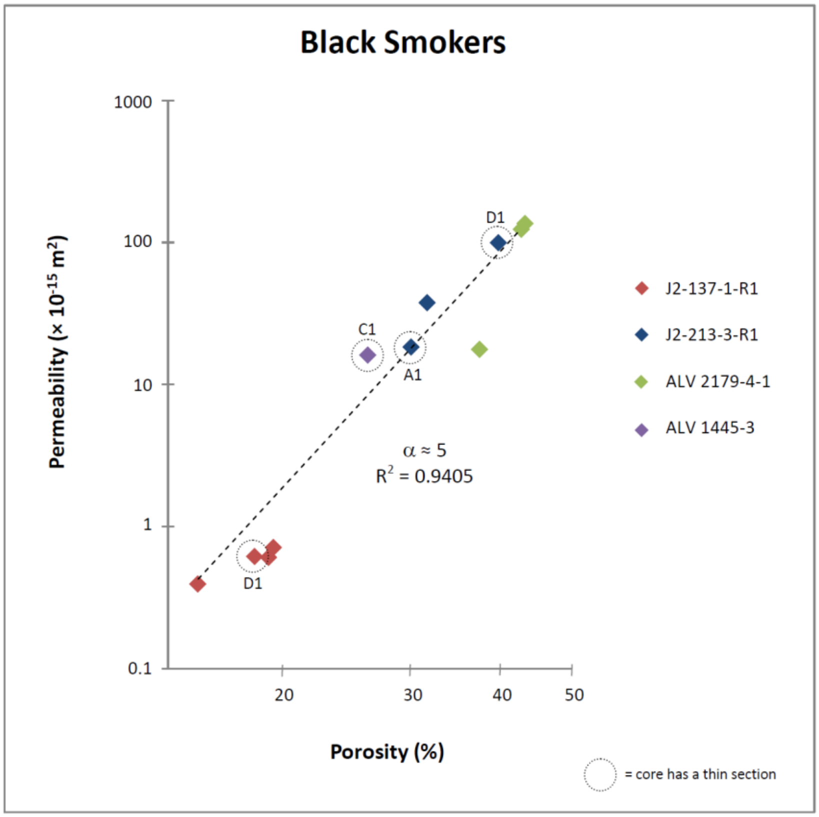

Figure 6.9: Permeability versus porosity data for the relict spires. Trend of EPPR (black dashed line), is α ~ 5. Symbol color/ shape denotes sample. Circles around symbols indicate that a thin section was taken from that core. All circled cores are labeled with the core number.

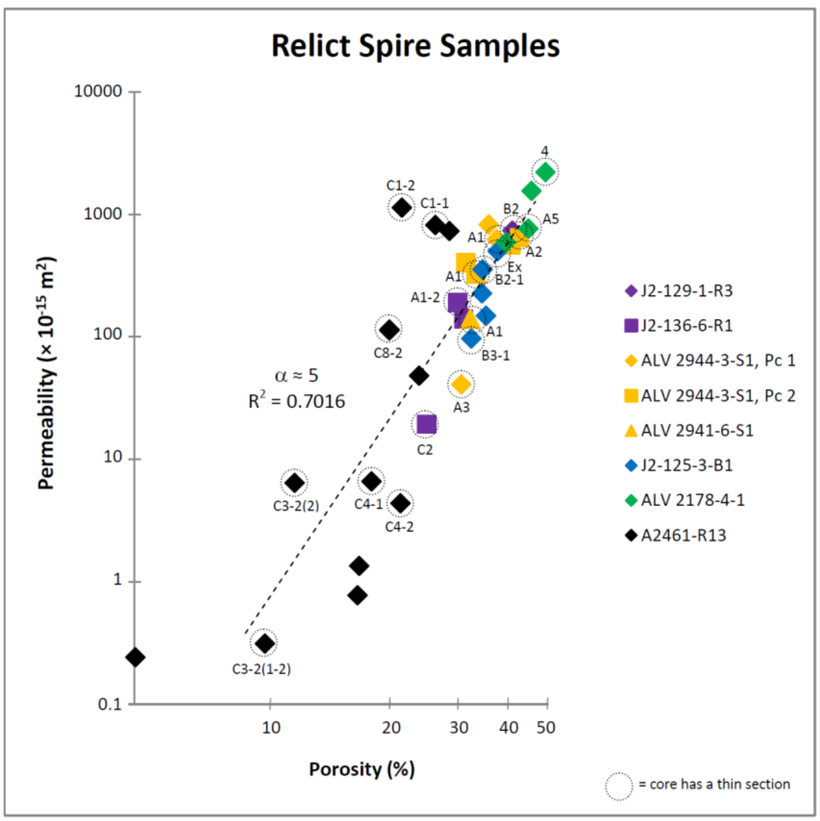

6.2 Microstructural Analyses

Thin sections were taken from select spire deposits: 10 sections from the Zn-rich actively diffusing spires, 4 from the black smoker chimneys and 20 from the relict spires. Figures 6.7-6-9 show the cores from which these sections were taken.

6.2.1 Actively Diffusing Spires

The Zn-rich actively diffusing spires, which included white smoker chimneys, were the most permeable of the spires. The group of white smoker chimneys consisted of thin sections from sample ALV 2187-1-1 (top) cores A2, A4, and B1 and sample ALV 2187-1-2 cores C1/2 and C5. The remaining thin sections were taken from Zn-rich diffusing spire samples ALV 2190-14-1 core A1, J2-137-7-R1 core B3, J2-222-1-R1 cores A2 and Ex, and J2-128-8-R1 core Ex.

Thin sections from the white smoker sample ALV 2187-1-1 (top) are compositionally similar, being composed almost entirely of sphalerite with only trace amounts of chalcopyrite. Core A2, taken axially from the deposit sample, has the highest permeability and has a thin section characterized by broadly spaced sphalerite crystals (Figure 10a). Crystals are small to moderate sized (30-100 μm) and are surrounded by wide, well-connected pore channels (70-150 μm). Core A4, also taken axially from the sample, has a similar permeability to that of A2, but with a lower porosity. Sphalerite crystals are similar in size to that of core A2 with crystals ranging from 30-100 μm. Pore channels are well-connected, but narrower (30-60 μm) than in A2 due to a tighter packing of crystals. Core B1 has a similar porosity to A2, but a lower permeability and was made radially from the deposit sample. The section for core B1 reveals layering through a prominent change in crystal size and packing. The layer oriented towards the original center of the spire deposit contains small sphalerite crystals (10-40 μm) that are widely spaced. This layer grades into an outer layer consisting of larger (50-100 μm), more closely packed crystals. Pore space within this layer appears predominantly connected through narrow channels and, in some of the more tightly packed areas, pore spaces are isolated by larger sphalerite crystals.

The thin sections from sample ALV 2187-1-2 are similar to those of ALV 2187-1-1 (top). Both ALV 2187-1-2 sections are primarily composed of sphalerite crystals with minor amounts of chalcopyrite and pyrite. The two cores have comparable permeabilities, though core C5 has a higher porosity. Core C5 has small to moderately sized (30-100 μm) sphalerite crystals that are loosely packed (Figure 10b). Pore space between crystals appears well-connected throughout the section. For core C1/2 the crystal size is similar to that of C5; however, C1/2 has some patches of tightly packed crystals. There are no areas of very broadly spaced crystals, though there are a few prominent flow channels through the section. The tighter packing in core C1/2 is likely why it has a lower porosity than core C5.

The remaining Zn-rich diffusing spire cores have structures similar to those of the white smokers. Core A1 of sample ALV 2190-14-1 has the highest permeability of the remaining cores. It comprises small to moderate sized (30-100 μm) sphalerite crystals with trace amounts of both chalcopyrite and

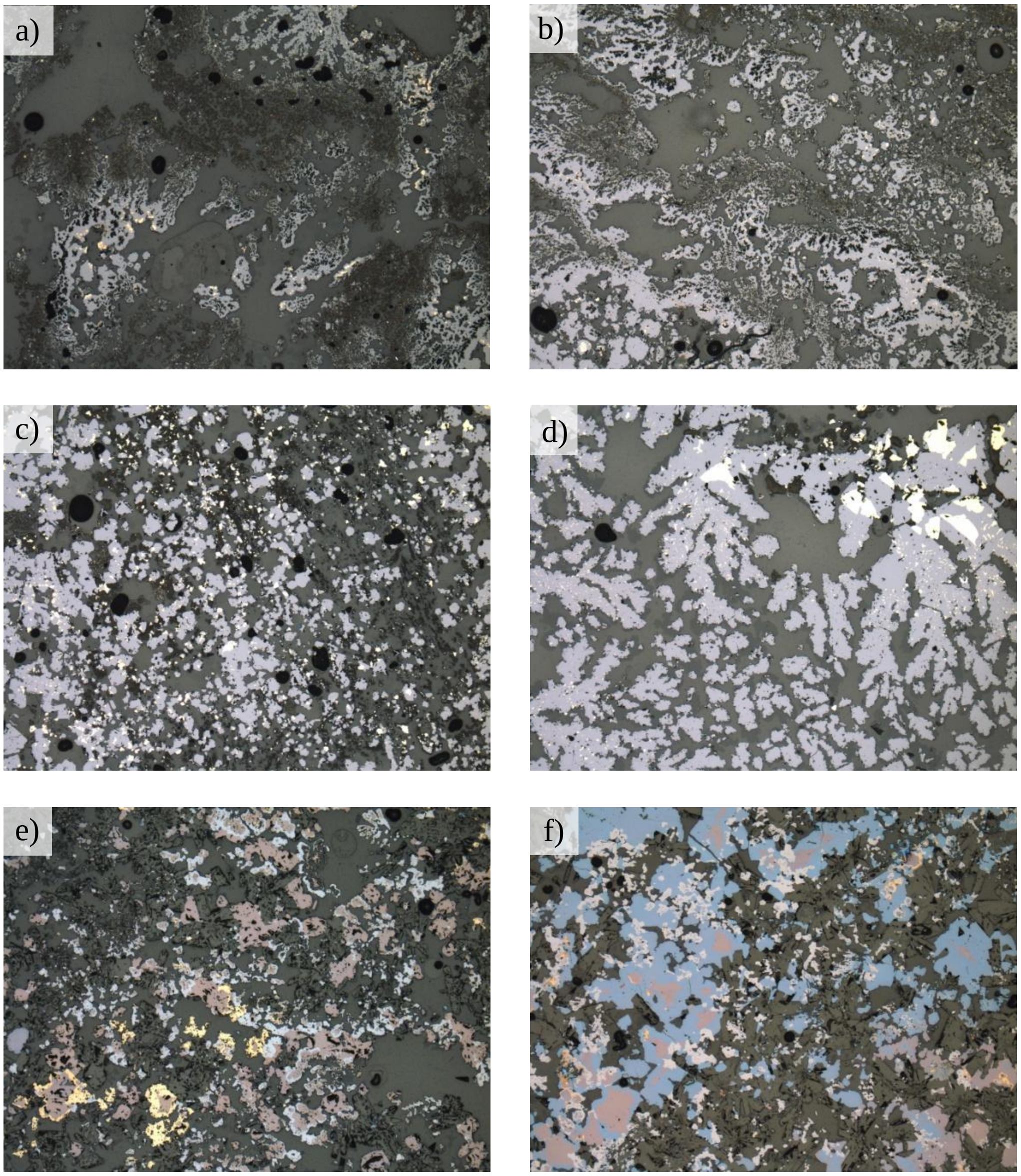

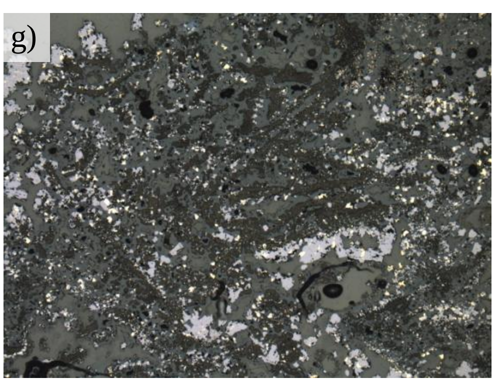

Figure 6.10: Reflected light (5x) images of Zn-rich actively diffusing spires. Width of images is ~ 2.7 mm. **a)** ALV 2187-1-1 (top), core A2. Broadly space sphalerite crystals. **b)** ALV 2187-1-2, core C5. Loosely packed, moderate sized crystals. **c)** J2-127-1-R2, core B3. Small crystals with well-connected pore space. **d)** J2-127-1-R2, core B3. Crystals with weathered edges, likely from dissolution. **e)** J2-222-1-R2, core A2. Moderately packed sulfides + anhydrite. **f)** J2-222-1-R2, core Ex. Tightly packed sulfides + anhydrite. **g)** J2-128-8-R2, core Ex. Clusters of sulfide crystals have been coated in am Si.

pyrite. Sphalerite crystals are moderately packed and surrounded by well-connected pore space. Channel width varies through different portions of the section but on average is ~70-100 μm. This section is similar to ALV 2187-1-1 (top) core A2, but its slightly tighter crystal packing likely makes it a little less permeable.

Core B3 from sample J2-127-1-R2 has a lower permeability and porosity than that of ALV 2190-14-1, core A1. Core B3 is dominated by wurtzite crystals ranging in size from 20-200 μm and lesser amounts of pyrite. The wurtzite crystals are well-formed and equant (Figure 10c). There are clear well-sorted areas of small crystals and of large crystals likely indicating somewhat variable environmental conditions. Wurtzite crystals are moderately to tightly packed, though pore connectivity is maintained through many narrow channels (10-40 μm). A few areas within the thin section appear to have experienced some dissolution. Crystals in these areas are more irregularly shaped with rough, weathered edges (Figure 10d). Pore connectivity appears enhanced in these regions by the presence of slightly broader pore channels. The tighter crystal packing observed may account for the decrease in porosity observed between this core and ALV 2190-14-1 core A1.

While core A2 of sample J2-222-1-R2 plots very close to J2-127-1-R2 core B3, the two cores are compositionally and structurally quite different. Core A2 contains an assortment of sulfide minerals including wurtzite, pyrite, chalcopyrite, pyrrhotite, and chalcocite. The core also contains many small, tabular anhydrite crystals (50-150 μm). The section reveals layering within the core whereby a layer containing broadly packed crystals transitions into a more tightly packed layer. Sulfide crystal sizes vary from 40-180 μm and are moderately sorted throughout the core (Figure 10e). In both the layers the anhydrite crystals create considerable roughness along the pore space edges. In the more closely packed layer these crystals restrict pore channel width. The layer of tight crystals will limit the core's permeability and porosity. Core Ex of the same sample is compositionally and texturally consistent with core A2, but has significantly tighter crystal packing within the core (Figure 10f).

Sample J2-128-8-R1 core Ex is composed primarily of wurtzite with lesser amounts of pyrite. This core shows a large range in wurtzite crystal sizes (10-300 μm), with similarly sized crystals clustered together. Both large and small crystals are closely packed throughout the core, limiting pore connectivity. Additionally, most clusters of small crystals have been coated in amorphous silica, further restricting connectivity (Figure 10g). As with J2-127-1-R2 there are a few areas of moderate sized crystals that appear to have experienced dissolution. These crystals have weathered edges with no amorphous silica and are surrounded by highly connected pore space. This core has the lowest permeability and porosity of the Zn-rich diffusing spires and likely because of the close packed grain structure and abundance of amorphous silica clogging pore space.

6.2.2 Black Smoker Chimneys

Four thin sections were made from the black smoker chimney cores: J2-213-3-R1, cores A1 and D1; ALV 1445-3 core C1; and J2-137-1-R1 core D1. Both thin sections for sample J2-213-3-R1 reveal a layered structure that consists

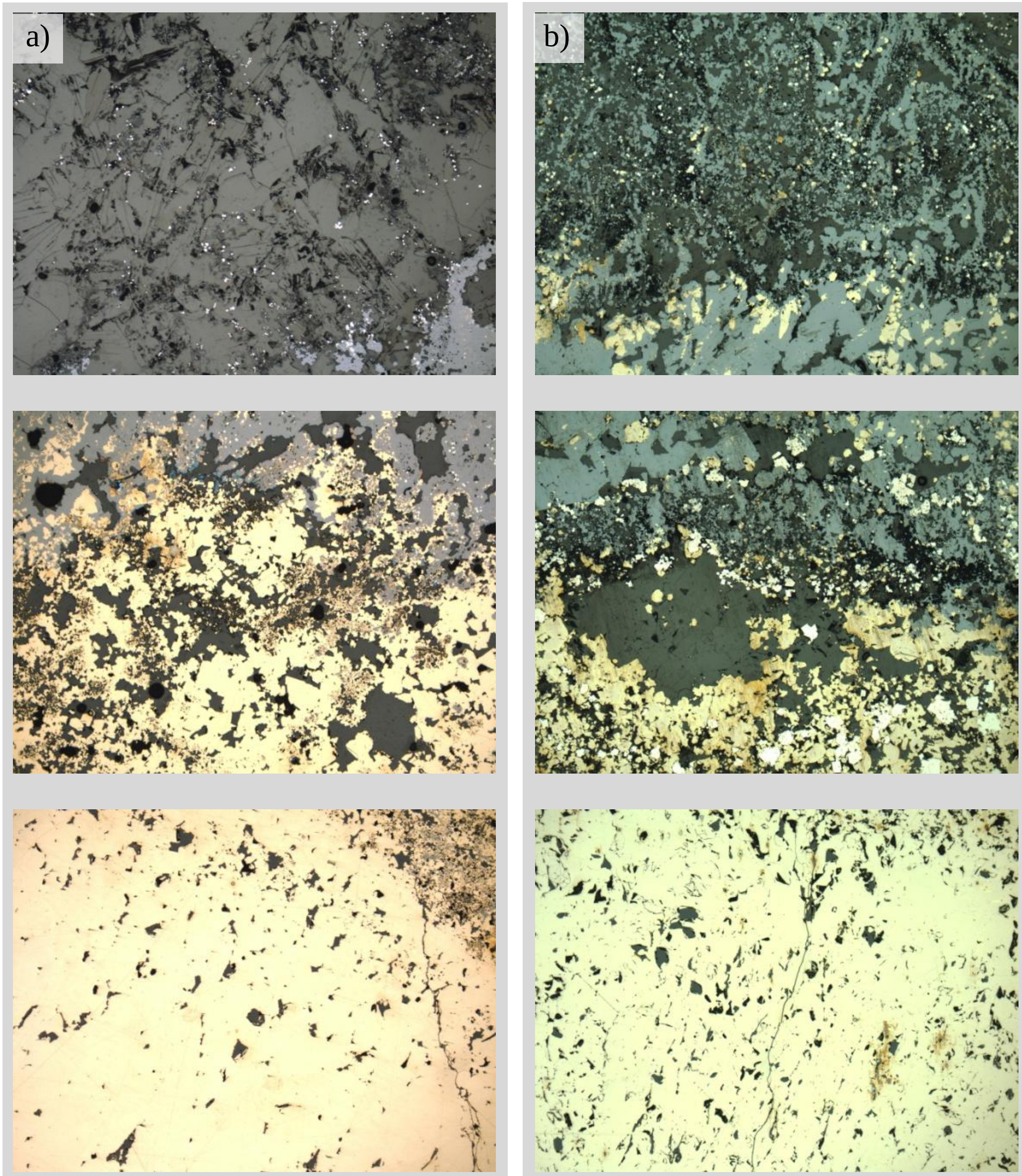

Figure 6.11: Reflected light (5x) images of black smoker chimneys. Image width ~ 2.7 mm. Images show prominent layering within the samples. Densely packed chalcopyrite layers (lower images) grade into an anhydrite-rich layer (upper images) that has experienced some pore space infill by assorted sulfide crystals. **a)** J2-213-3-R1, core D1. **b)** J2-137-1-R1, core D1.

of a chalcopyrite-rich layer that gradually transitions to a more anhydrite dominated layer (Figure 11a). Core D1, the more permeable of the two, contains a layer of moderately packed chalcopyrite crystals that range in size between 40-100 μm. This layer is followed by a layer consisting on an assortment of sulfide minerals including wurtzite, pyrrhotite, marcasite, and covellite, which are sized similarly to the chalcopyrite crystals. The crystals in this layer are slightly more broadly spaced than in the chalcopyrite layer. This sulfide layer grades into the anhydrite-rich layer, where anhydrite crystals are large (200-350 μm) and interspersed with smaller sulfide crystals. Pore space is connected through narrow channels (5-20 μm) within the different layers; however, in areas where the sulfide crystal packing is somewhat dense, pores tend to be more isolated. These observations are consistent with core A1. Core A1 has a lower permeability and porosity – a difference that can be attributed to A1 having a tighter grain structure.

Core C1 for sample ALV 1445-3 also exhibits a layered structure. Densely packed chalcopyrite crystals form a chalcopyrite layer similar to that observed in J2-213-3-R1. This layer contains small (10-20 μm), isolated pores and also a few thin cracks that likely formed as a result of pressure application during the measurements. The chalcopyrite layer is bordered by a slightly more porous layer of both pyrite and chalcopyrite, in addition to some anhydrite with crystals between 60-120 μm. This layer then transitions into an anhydrite-rich layer characterized by 100-200 μm anhydrite crystals with traces of sulfides. The anhydrite layer is also densely packed with crystals, though narrow channels between crystals are present. Like J2-213-3-R1 core A1, the tight packing of the grain structure likely controls the permeability and porosity of ALV 1445-3 core C1.

As with the previously discussed black smoker chimney cores, J2-137-1-R1 core D1 also has a layered structure consisting of a chalcopyrite-rich layer, an intermediate sulfide and anhydrite layer, and a layer that is mostly anhydrite crystals. Most of the pore space within these layers is isolated due to close crystal packing or is simply poorly connected through narrow channels between crystals. Unlike with the other cores the anhydrite layer here is relatively thin, such that the bulk of the core contains sulfides (Figure 11b). Because sulfides tend to form in clusters, crystals become close-packed, therefore restricting pore connectivity. It is the prominence of tightly packed sulfide crystals within this core which causes it to have a significantly lower permeability and porosity.

6.2.3 Relict Spires

The relict spire samples represent a large range of permeability and porosity values. Because of this, variations in pore structure across the different samples are to be expected. Twenty thin sections have been made from the relict spire cores in order to provide a better understanding of the processes influencing their EPPR.

The most permeable and porous of the relict spire samples is ALV 2178-4-1 from which two thin sections were made. The first thin section, core 4, is the more permeable of the two and is composed primarily of pyrite and chalcopyrite. Pyrite crystals range in size between 50-120 μm, while the chalcopyrite crystals are a bit smaller 30-70 μm. The crystals are fairly equally distributed throughout the core; however, the crystals are very widely spaced with pore channel width averaging around 100 μm (Figure 12a). The loose crystal packing within this core allows for high pore connectivity and thus high permeability. The second section, core A5, is composed of almost all chalcopyrite with small amounts of pyrite present. Chalcopyrite crystal size varies considerably from about 20-200 μm. These crystals are poorly sorted with spacing between crystals highly variable. Pore connectivity appears high in most areas with the exception of a few tightly packed crystal clusters. The permeability is clearly high due to this pore connectivity, although not quite as high as seen in core 4.

Sample ALV 2944-3-S1, Pc 2 also has two thin sections: core A1 and A2. Both cores are compositionally similar and are constituted largely of wurtzite and chalcopyrite with minor amounts of pyrite. Small to moderate (20-100 μm) sized chalcopyrite and wurtzite crystals are present and range from loosely packed to more moderately packed grain structure in both cores (Figure 12b). Pore connectivity appears high in both cores with abundant narrow channels (~20 μm) and several wider channels (80-100 μm) surrounding the sulfide crystals. Core A1 has a few large patches of small, tightly packed crystals that lack well-connected channels and are therefore likely restrictive to flow. This may explain why core A1 has a lower permeability and porosity than core A2.

The one thin section from sample J2-129-1-R3 comes from core B2. This core is compositionally comparable to the two ALV 2944-3-S1, Pc 2 cores. It is composed of mostly wurtzite and chalcopyrite crystals with similar size and crystal packing as ALV 2944-3-S1, Pc 2 core A2. The availability of pore space is not consistent throughout the section. There are areas that have broadly spaced crystals, some of which may have been enhanced by dissolution, since crystals appear irregularly shaped and with tattered edges. The core also has areas where the widely spaced crystals have been heavily coated in amorphous silica, blocking pore space around the crystals. It is possible that both dissolution and precipitation of amorphous silica have been occurring concurrently within the core. There are also a few patches of crystals that appear dissolved and then coated in amorphous silica, suggesting that in some cases dissolution may have preceded the silica precipitation (Figure 12c). Despite the crystal patches that are heavily coated in amorphous silica, the well-connected areas of crystals, including some areas of apparent dissolution, give the core a high permeability.

Sample ALV 2944-3-S1, Pc 1 has thin sections for core A1 and core A3. Core A1 is very similar to ALV 2944-3-S1, Pc 2 core A2. It is abundant in wurtzite and chalcopyrite with both small and moderate sized crystals (30-120 μm) throughout the core. There are areas of very loosely packed crystals and also of moderately packed crystals. The more tightly packed crystals have narrower pore channels (~10-20 μm), though the pore space still appears well connected. Core A3 has a lower permeability and porosity than core A1 and is structurally quite different. This core was the only core to have its thin section made axially, which may explain some of the variation between it and core A1. Core A3 appears to have a layered structure with a sulfide-rich layer of mainly wurtzite and chalcopyrite adjacent to a layer of anhydrite, similar to what was observed in the black smoker chimney cores (Figure 12d). The sulfide-rich layer is structurally analogous to core A1, but with more tightly packed crystals. Interestingly, the transition between the two layers has many small sulfide crystals that have been coated with amorphous silica. This coating appears to greatly restrict pore space between the sulfide crystals and limit pore connectivity. Within the anhydrite layer, anhydrite crystals (50-100 μm) are closely packed with pore space seemingly filled by late stage sulfide crystals. This core clearly has a tightly packed grain structure due to sulfide infill and amorphous silica precipitation that are consistent with it having a lower permeability and porosity than core A1.

Three sections were made from the J2-125-3-B1 sample: core Ex, core B2-1, and core B3-1. Cores Ex and B3-1 are principally composed of wurtzite and chalcopyrite, whereas core B2-1 is nearly all chalcopyrite. Core Ex has the higher permeability of the three cores and has both large and small crystals (40-250 μm). It has patches of very tightly packed crystals and also areas with very broad spaces between crystals. The high connectivity areas of this core are likely enhancing its permeability compared with the other J2-125-3-B1 cores. Core B2-1 mainly has small to moderate sized chalcopyrite crystals that are very rounded. The crystals are closely packed, but many narrow channels are present between crystals to accommodate flow. Core B3-1 is very similar to core A1 from ALV 2944-3-S1, Pc 2 with permeability and porosity only being limited by the tightly packed wurtzite and chalcopyrite grain structure. Sample ALV 2941-6-S1 core A1, which plots adjacent to the J2-125-3-B1 cores, is compositionally and structurally consistent with core B3-1.

Core A1-2 and C2 of sample J2-136-6-R1 are both largely made of wurtzite and chalcopyrite, similar to many of the other relict spire cores. Having a higher permeability, core A1-2 is characterized by small to moderately sized

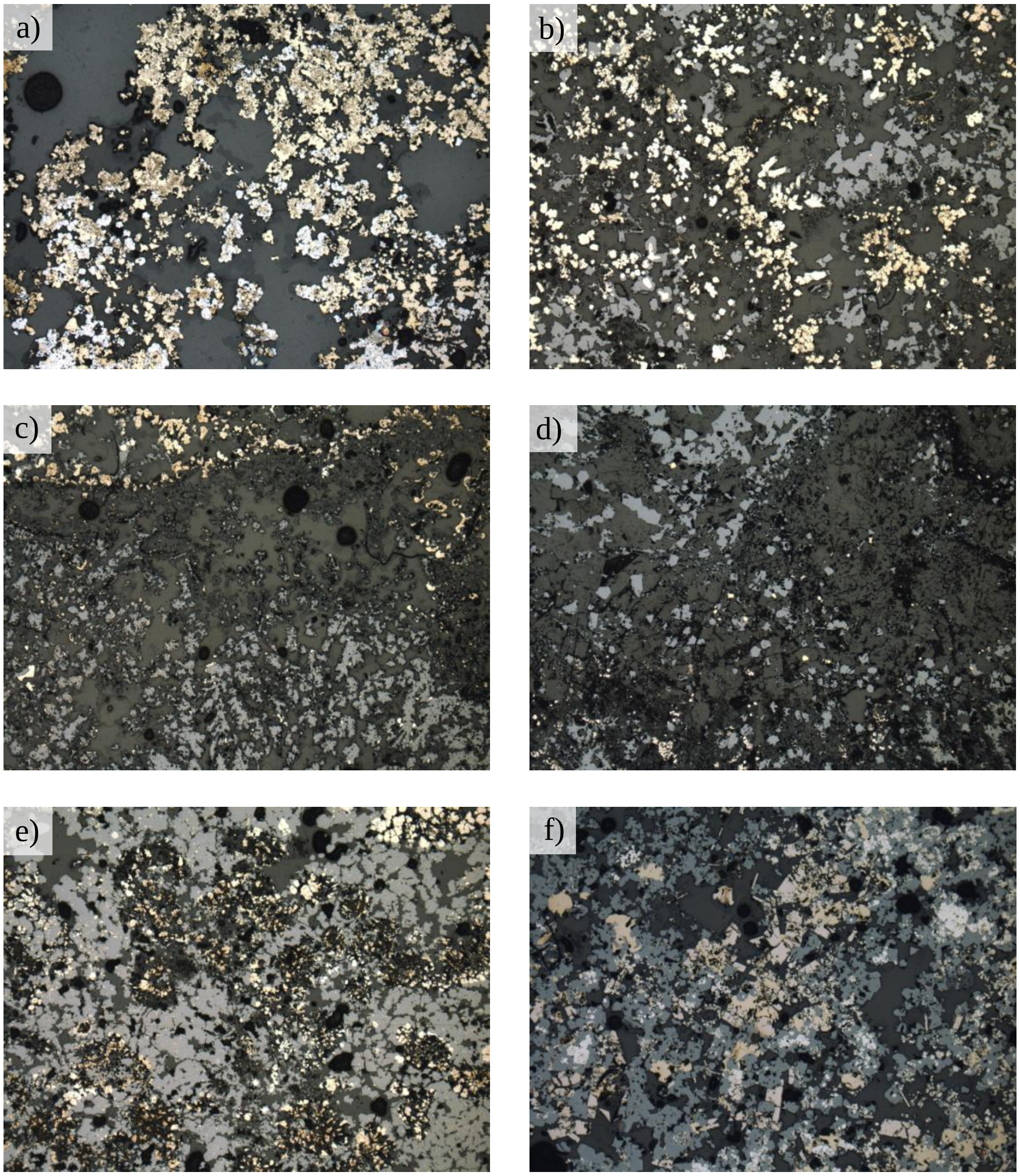

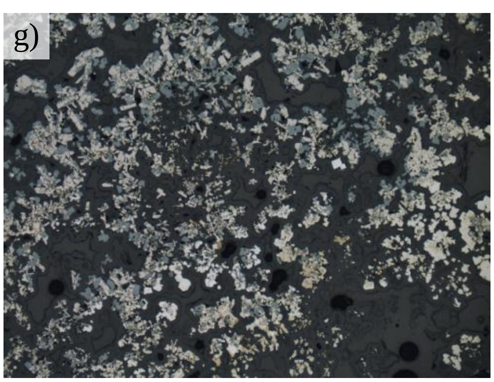

Figure 6.12: Reflected light (5x) images of thin sections from relict spire cores. Width of images is ~ 2.7 mm. **a)** ALV 2178-4-1, core 4. Loose crystal packing. **b)** ALV 2944-3-S1, Pc 2, core A2. Moderate crystal packing. **c)** J2-129-1-R3, core B2. Dissolved crystals with am Si coating. **d)** ALV 2944-3-S1, Pc 1, core A3. Anhydrite-rich layer adjacent to sulfide-rich layer. **e)** J2-136-6-R1, core C2. Patchy distribution of am Si. **f)** ALV 2461-R13, core C1-2. Sulfide grain structure with minimal am Si. **g)** ALV 2461-R13, core C4-2. Thick am Si coating along sulfide crystals.

crystals (30-100 μm) that range in crystal packing. Pore space around these crystals appears generally well connected, except in more densely packed areas. Core C2 is very similar to A1-2, but it has a more tightly packed grain structure and also patches of amorphous silica that block pore space (Figure 12e). These features can explain why core C2 has a lower permeability and porosity than core A1-2.

The seven thin sections made from the ALV 2461-R13 illustrate a clear progression from a high permeability and porosity structure to one that is heavily restricted by the precipitation of amorphous silica. Core C1-1, C1-2, and C8-2 have high permeability values for this sample. They have moderately packed crystal structures abundant in wurtzite and chalcopyrite with lesser amounts of pyrrhotite (Figure 12f). Pore space exists as narrow channels along crystal edges and as larger isolated pores; however, in some small patches channel connectivity is lost from amorphous silica precipitation (more so in C1-2). Cores C4-1 and C4-2 have initial crystal structures much more broadly spaced than the previous three cores. Small to moderate sized crystals of chalcopyrite, wurtzite, pyrite and pyrrhotite are present, although a high degree of amorphous silica precipitation has occurred. Amorphous silica forms a thick coating around most of the crystals, yet because the initial grain structure was loosely packed, pore channels and still intact (Figure 12g). Core C3-2(2) is very similar to these two cores, but has a slightly denser initial grain structure and a thicker amorphous silica coating. Lastly, C3-2(1-2), which has a very low permeability and porosity, appears to have had a more tightly packed grain structure than the previous cores that has since been densely coated with amorphous silica. Pore space between crystals has been blocked by amorphous silica resulting in minimal pore connectivity. The combined abundance of both sulfide crystals and amorphous silica can account for the low permeability and porosity of this core.

6.3 Discussion

Each of the spire samples is dominated by a sulfide crystals. As observed through deposit microstructures, the tightness or packing of this grain structure strongly influences permeability and porosity. The initial mineral assemblage and grain structure of the spires will depend on the chemistry and temperature of emitted vent fluids. As fluid flow progresses, pore evolution processes will occur and change the initial grain structure. From the microstructural observations, spire deposits appear to commonly experience late stage precipitation of additional sulfides or amorphous silica, both of which can decrease the permeability and porosity of the spires. In some of the spire cores, weathered crystals with rough edges indicate that dissolution has also occurred.

The pronounced effects of both the precipitation of sulfides and also of amorphous silica on hydrothermal spires were recognized [*Zhu et al.*, 2007]. Using techniques synonymous to those employed in this study, *Zhu et al.* [2007] identified two EPPRs for spire deposits having experienced precipitation. For deposits that primarily exhibited the precipitation of late stage sulfide crystals they found an $\alpha \sim 9$. Deposits having crystals that had been largely coated by amorphous silica were found to have an EPPR trend of $\alpha \sim 3$. The α value associated with sulfide precipitation is higher, because sulfide crystals are naturally quite angular making them effective at blocking pore space. Conversely, amorphous silica has a lower α value because it precipitates as a thin, rounded coating along crystal edges that builds up over time gradually decreasing permeability.

Correlating the trends determined by *Zhu et al.* [2007] to the Zn-rich diffusing spire data is simply not feasible, because there is not clear evidence for either precipitation process having occurred in the cores. Only one of the cores showed precipitation of amorphous silica. Comparing data for this core with measurements from *Zhu et al*. [2007] places it at the high k and ϕ end of the $\alpha \sim 3$ trend, suggesting that it may evolve along this trend. In general, cores measured in the *Zhu et al.* [2007] study showed a greater range in both permeability and porosity values from which interpretations of pore evolution could be made.

The black smoker chimneys did not show precipitation of amorphous silica (consistent with black smoker observations from *Zhu et al.* [2007]), but had a close-packed sulfide grain structure. From this grain structure and observations of sulfide infill within anhydrite dominated layers, it can be inferred that late stage precipitation of sulfides had occurred. The data clearly plot along a trend of $\alpha \sim 5$, whereas the cores from *Zhu et al.* [2007], which are similar compositionally, plot along the $\alpha \sim 9$ trend. The data for the lower k and ϕ cores are comparable to those of the lower k and ϕ cores from *Zhu et al.* [2007]; however, the same is not true for the high k and ϕ cores. *Zhu et al.* [2007] do not detail the structure of their black smoker samples, but do state that the cores, of which there were only four, cracked during the coring process. It is possible that these cracks may have enhanced the permeability values without significantly affecting their porosity, which is consistent with the samples.

The α value of 5 to some extent likely reflects the precipitation of sulfides. Black smoker chimneys should not, however, necessarily follow the $\alpha \sim 9$ trend observed by *Zhu et al.* [2007] in actively diffusing spires and relict spires. Black smoker chimneys have a distinct layered structure with a high abundance of anhydrite that the other spire types generally lack. The presence of significant anhydrite within black smokers should influence how the pore structure evolves. Anhydrite naturally has a close-packed grain structure, which a sulfide-rich layer does not necessarily have initially. Sulfides will infill pore spaces within the anhydrite, but the effects of this precipitation will be less pronounced compared to sulfide precipitation within an initially widely-spaced, sulfide-rich grain structure. Because of this, anhydrite should dilute or lessen the effects of sulfide precipitation on black smoker chimneys, potentially explaining why the data have an EPPR of $\alpha \sim 5$, as opposed to $\alpha \sim 9$.

For the relict spire samples, both late stage precipitation of sulfides and amorphous silica precipitation were observed in several of the cores – consistent with relict spires observations from *Zhu et al*. [2007]. As with the Zn-rich diffusing spires correlating the set of relict spires data to theirs is challenging, because many of the cores had permeability and porosity values higher than those of *Zhu et al.* [2007]. For the cores with porosities higher than ~30%, it is difficult to evaluate the effects of precipitation. Many of the high porosity samples did not have amorphous silica, but some samples did have tightly packed crystal structures, which can be an indicator of later sulfide precipitation. However, given the generally high permeability values for these samples, it seems unlikely that their initial crystal structures have experienced sulfide precipitation, seeing as they exhibit well-connected pore networks.

The relict spire samples with amorphous silica present compare well with the $\alpha \sim 3$ data of *Zhu et al.* [2007]. It seems likely that with continued precipitation of amorphous silica these samples would evolve along the $\alpha \sim 3$ trend. Sample ALV 2461-R13 is interesting because it has a large range of permeability and porosity values. Microstructural observations from this sample suggest that precipitation of both sulfides and amorphous silica contributed to the reduction in permeability. At some point sulfide crystal packing became denser and amorphous silica coatings became thicker. This may explain why these cores plot more steeply than the others. The overall $\alpha \sim 5$ trend determined for the relict spires is probably best applicable to samples which have not experienced large amounts of change to their initial pore structures.

The group of spire deposits as a whole follows a trend whereby as the deposits change over time, they lose pore space and connectivity. Spire samples initially have high k and ϕ, but gradually evolve to lower k and ϕ primarily as a result of precipitation. Spires will continue to evolve in this manner until they 'pinch-off'; a point at which precipitation has sufficiently clogged pore channels causing significant permeability reduction. This pinch-off is exemplified by the relict spire sample ALV 2461-R13 (Figure 13).

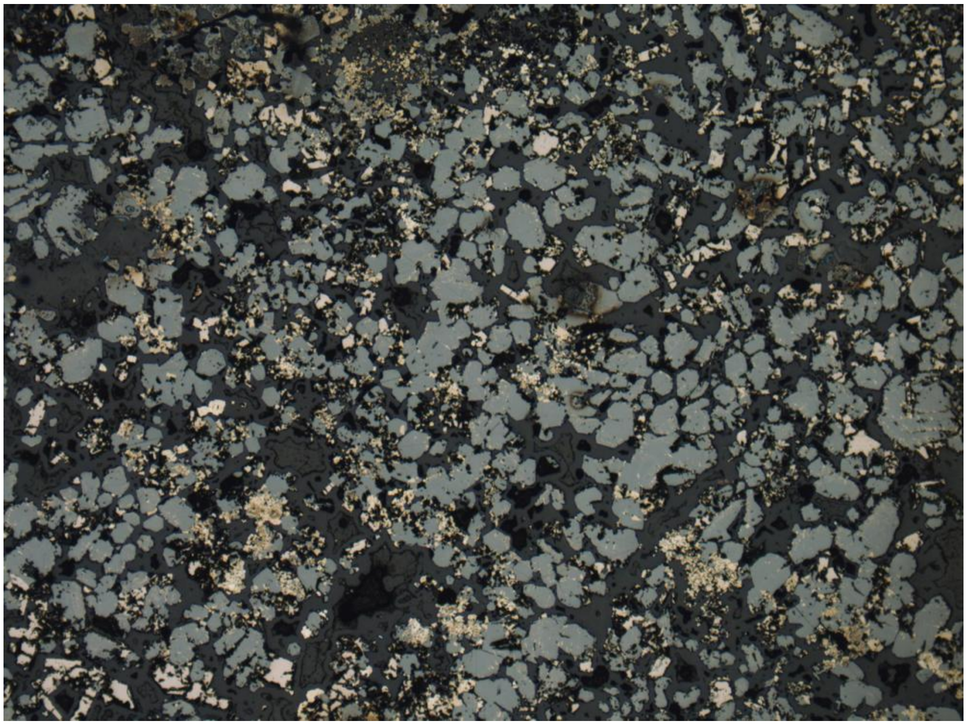

Figure 6.13 Reflected light (5x) images of relict spire ALV 2461-R13 core C3-2(1-2). Width of images is ~ 2.7 mm. Core has experience heavy precipitation of amorphous silica (dark gray, rounded coating) along sulfide crystal edges. Most of the pore space between crystals has been blocked by the amorphous silica, thus the precipitation is causing the ‘pinch-off’ of pore space and a large reduction in permeability.

Chapter 7: Conclusions

The interaction of hot hydrothermal fluids with seawater controls both chemical and physical processes that can change the structure of various seafloor vents. Much work has been done to identify the composition, structure, and evolution of hydrothermal vents from a range of vent fields. Early studies conducted on deposits from the East Pacific Rise, such as those by *Haymon* [1983] and *Goldfarb et al.* [1983], analyzed the most prominent of these vent structures, the black smoker chimneys. The rapid, high-temperature focused fluid emission of these chimneys is in stark contrast to the majority of vent structures through which fluid diffuses out to the seafloor. Diffuse hydrothermal vents accommodate much of the ongoing transfer of fluids between the subsurface and seafloor, yet little information is known about the feedback between the fluid, the vent structures, and the surrounding environmental conditions [*Delaney et al*., 1992; *Lowell et al.,* 1995].

The formation and evolution of all vent structures, both focused and diffuse, are closely dependent upon their physical and chemical environment. Changes in environmental conditions, such as temperature, flow rate, and the degree of mixing, can significantly impact how vents evolve over time [*Tivey and McDuff*, 1990; *Tivey*, 1995]. Conversely, changes in vent structures affect the ability of vents to transfer fluids. Many studies have collected data from vent fluids and deposit samples, and through models have been able to better understand how the fluid feedback within vents works and contributes to vent growth [*Lowell et al.*, 1995]. However, well-constrained transport property data, such as vent deposit permeability and porosity, are needed to improve these models. Despite its importance, systematic characterization of evolution permeability and porosity relationships (EPPRs) of vent deposits is scarce, with the exception of *Zhu et al*. [2007].

This study has provided the first set of systematic permeability and porosity data for many different vent deposit types from a large range of vent field locations. From these data and microstructural observations vent deposit permeability-porosity relationships and anisotropy have been identified. Deposit evolution is reflected by the different α values determined for each permeability-porosity power law relationship. Evidence for pore alteration processes was observed through quantitative microstructural analyses. Some deposits show interplay between these processes, which is reflected in the α values determined. These results can be used to accurately evaluate vent fluid distribution in order to gain a better understanding of mineralogical and biological processes.

The results of this study show that different deposits undergo similar evolutionary processes. Microstructural observations indicate that precipitation is dominant within each of the deposit types, and that other processes, such as dissolution or compaction, are common as well. Precipitation of minerals within the initial grain structure of a deposit has large implications on the pore structure of deposits. Precipitation limits pore space and connectivity, therefore lowering a deposit's permeability. The rate and degree to which precipitation reduces permeability will depend highly on the mineral precipitating, as different minerals have varying effects on permeability. It is important to understand that the pore structure observed in the deposits is not simply the product of one pore altering process, but rather a result of the interplay between multiple processes, whose timing or sequence is difficult to determine.

Measurements of vent deposit permeability and porosity conducted in this study can be used to identify permeability-porosity relationships and deposit characteristics, such as anisotropy. Microstructural observations provide evidence for pore evolution processes that can be used to explain the permeability-porosity relationships. Pore evolution processes are fundamental to the development of vent deposits, and recognizing key processes in this evolution reinforces the valuable role these deposits play in mass transport between the Earth’s subsurface and oceans. Identified anisotropy or a susceptibility of a deposit to a given pore evolution process are characteristics that have important implications for future efforts to model and constrain fluid fluxes from these vent structures. Ongoing modeling efforts emphasize the need for detailing factors that control the evolution of vent deposits. It is clear that the growth of these deposits is dependent on the interplay between fluids and the vent deposits themselves. These interactions influence local flow rates, temperatures, and chemistry, and affect heat and mass flux through different parts of the vent deposits, and the availability of nutrients to organisms living on deposit interiors and exteriors. As such, having flow property data for vent samples is imperative for refining our understanding of hydrothermal processes.

Appendix 1: Probe Permeability Data

A1.1 Massive Anhydrite Data

Sample	Site	Permeability (mD) 1	2	3	4	5		Mean (mD)	Mean (m^2)
J301-3	A1	2332.9	4325.1	1331.0	678.7	3003.2		1938.5	1.94E-12
	A2	624.0	589.9	512.7	336.6	717.9		539.2	5.39E-13
	B1	2610.0	542.3	2205.6	2839.3	1575.1		1694.3	1.69E-12
J2-210-8-R2	A1	78.2	10.1	181.5	47.2	13.4		39.0	3.90E-14
	A2	11.9	7.6	54.3	29.3	15.8		18.7	1.87E-14
	B1	34.7	26.9	23.4	3.3	20.3		17.1	1.71E-14
	C1	35.7	13.0	30.1	45.9	26.2		27.9	2.79E-14
J2-216-5-R1	A1	542.3	1189.7	606.7	433.2	557.7		624.0	6.24E-13
	A2	387.2	717.9	247.2	589.9	261.4		402.8	4.03E-13
	B1	4205.4	4838.9	4089.1	3759.0	3088.6		3953.7	3.95E-12
	B2	6776.1	5413.6	4838.9	6406.3	4705.0		5567.7	5.57E-12
	C1	5263.8	4574.8	3654.9	3553.8	3865.9		4135.2	4.14E-12
J2-216-14-R1	A1	624.0	826.1	573.6	826.1	678.7		698.1	6.98E-13
	A2	3003.2	1489.1	2332.9	2610.0	2205.6		2268.4	2.27E-12
	B1	2332.9	2205.6	1971.4	2839.3	1575.1		2144.6	2.14E-12
	B2	3003.2	2399.3	2399.3	2839.3	3865.9		2855.2	2.86E-12
	C1	6776.1	6776.1	5567.7	6776.1	6056.7		6370.4	6.37E-12
ALV 2581-8	A1	3088.6	2760.7	1156.8	849.6	1762.1		1713.4	1.71E-12
	A2	3759.0	5567.7	5413.6	6229.0	4574.8		5032.7	5.03E-12
	B1	1407.8	2144.6	2610.0	1713.4	924.2		1656.6	1.66E-12
	C1	2920.1	2684.3	3455.5	3865.9	3759.0		3303.8	3.30E-12
MIR 1, 1/74 Sta 2403	A1	85.1	80.5	57.5	71.9	74.0		73.1	7.31E-14
	A2	31.9	44.6	39.9	44.6	48.6		41.5	4.15E-14
	A3	115.9	13.7	6.6	106.5	18.2		29.0	2.90E-14
	A4	14.9	19.8	26.2	7.4	9.8		14.1	1.41E-14
	A5	33.7	112.7	16.7	17.7	48.6		35.3	3.53E-14
	A6	137.1	5.8	55.9	10.1	8.8		20.8	2.08E-14
	B1	240.3	309.4	181.5	186.7	227.2		224.7	2.25E-13
	B2	849.6	356.0	498.5	678.7	336.6		509.8	5.10E-13
	B3	678.7	781.0	641.7	781.0	950.5		759.4	7.59E-13
	B4	387.2	300.8	292.5	433.2	276.5		332.8	3.33E-13
	B5	557.7	624.0	557.7	484.7	433.2		527.3	5.27E-13
	B6	527.3	458.2	398.3	318.2	398.3		414.2	4.14E-13
	C1	376.5	318.2	346.1	589.9	214.8		350.0	3.50E-13
	C2	898.6	1331.0	924.2	1005.3	1124.8		1045.6	1.05E-12
MIR 1, 2/78 Sta 2417	A1	145.0	122.6	233.7	103.6	60.8	68.0	145.0	1.10E-13
	A2	106.5	62.5	51.4	42.2	34.7	32.8	106.5	5.04E-14
	A3	126.0	95.2	71.9	119.2	141.0	100.7	126.0	1.07E-13
	A4	133.3	112.7	95.2	82.7	122.6	141.0	133.3	1.13E-13
	A5	85.1	119.2	100.7	122.6	126.0	47.2	85.1	9.52E-14
	A6	103.6	97.9	166.9	112.7	133.3	106.5	103.6	1.18E-13
	B1	1223.5	1575.1	346.1	409.6	717.9	849.6	741.8	7.42E-13
	B2	1189.7	1093.6	1093.6	873.7	977.5	1063.4	1043.7	1.04E-12
ALV 2183-7-0	A1	2467.6	1916.9	924.2	950.5	1034.0		1338.5	1.34E-12
	A2	1666.0	2332.9	1666.0	2399.3	2839.3		2132.6	2.13E-12
	B1	606.7	803.2	606.7	698.1	678.7		674.9	6.75E-13
	B2	1971.4	1916.9	950.5	1368.9	1531.5		1497.5	1.50E-12

A1.2 Flange, Slab and Crust Data

Sample	Site	Permeability (mD) 1	2	3	4	5	Mean (mD)	Mean (m^2)
ALV 3517-R1	A1	15288.9	12562.4	15724.0	19136.7	7580.9	13437.6	1.34E-11
	D1	4705.0	2537.8	3865.9	3455.5	2205.6	3230.4	3.23E-12
	D2	20241.3	17105.0	12562.4	20241.3	18607.2	17493.3	1.75E-11
	D3	1863.9	1762.1	1762.1	1916.9	2144.6	1884.9	1.88E-12
	D4	2027.5	1223.5	1531.5	1331.0	1971.4	1583.9	1.58E-12
ALV 3521-R2	A1	65774.9	46970.5	87080.7	92107.4	108996.3	76966.7	7.70E-11
	A2	29981.0	26797.9	29981.0	32614.1	30834.2	29981.0	3.00E-11
	B1	10615.9	9226.3	12214.8	19136.7	18607.2	13362.4	1.34E-11
	B2	28344.8	41983.7	34496.7	22019.0	23290.0	29151.4	2.92E-11
ALV 2415-1B	A1	1863.9	1619.9	2205.6	1156.8	1812.3	1694.3	1.69E-12
	B1	8018.5	14865.9	10322.2	5413.6	12919.9	9704.2	9.70E-12
	C1	3266.9	10322.2	5263.8	8018.5	10918.0	6891.1	6.89E-12
ALV 2927-3	A1	1294.2	1156.8	1368.9	2332.9	606.7	1237.4	1.24E-12
	A2	37.7	42.2	109.5	82.7	71.9	63.6	6.36E-14
	B1	1005.3	1258.4	2684.3	5567.7	2684.3	2193.3	2.19E-12
J2-286	A1	1294.2	2205.6	2760.7	2268.4	2085.2	2062.0	2.06E-12
	A2	2684.3	2610.0	4976.6	2610.0	2027.5	2839.3	2.84E-12
	A3	3975.9	5118.2	3654.9	4325.1	3975.9	4181.9	4.18E-12
	A4	7796.7	7371.2	8722.7	4574.8	6406.3	6814.2	6.81E-12
	A5	8722.7	8018.5	7167.2	8246.7	7796.7	7973.7	7.97E-12
	A6	5413.6	4838.9	3759.0	5118.2	4448.2	4678.6	4.68E-12
	B1	1368.9	119.2	421.3	366.1	445.6	407.3	4.07E-13
	B2	458.2	327.2	37.7	356.0	433.2	244.4	2.44E-13
	B3	2144.6	738.4	1368.9	1619.9	1575.1	1407.8	1.41E-12
	C1	6588.6	7167.2	6776.1	8246.7	6968.9	7127.1	7.13E-12
	C2	43178.4	33542.2	40822.0	62185.3	58791.6	46446.3	4.64E-11
	C3	128981.9	80050.4	115288.0	52549.7	51095.7	79602.4	7.96E-11
	C4	87080.7	103047.9	67646.6	128981.9	152632.2	103627.8	1.04E-10
	C5	82328.4	75681.7	144302.4	54045.1	57164.8	77399.8	7.74E-11
	C6	202072.9	275141.7	180619.0	148408.9	213737.4	199817.6	2.00E-10
J2-286	A1	3088.6	2760.7	1156.8	849.6	1762.1	1713.4	1.71E-12
	A2	3759.0	5567.7	5413.6	6229.0	4574.8	5032.7	5.03E-12
	B1	1407.8	2144.6	2610.0	1713.4	924.2	1656.6	1.66E-12
	C1	2920.1	2684.3	3455.5	3865.9	3759.0	3303.8	3.30E-12
ALV 2608-3-3	A1	18092.3	22019.0	23290.0	19136.7	15288.9	19352.7	1.94E-11
	A2	1916.9	2205.6	2027.5	1713.4	1971.4	1960.4	1.96E-12
	A3	4205.4	4705.0	4976.6	4205.4	4574.8	4523.7	4.52E-12
	B1	8018.5	11876.9	13287.6	18607.2	17105.0	13213.2	1.32E-11
	B2	4705.0	10322.2	7796.7	6776.1	8722.7	7412.6	7.41E-12
	B3	3088.6	2537.8	1762.1	1575.1	2027.5	2132.6	2.13E-12
	C1	1124.8	1124.8	1034.0	950.5	1034.0	1051.5	1.05E-12
	C2	12919.9	9758.8	6056.7	8971.0	4705.0	7973.7	7.97E-12
	C3	4205.4	4574.8	4574.8	4448.2	3003.2	4112.1	4.11E-12
	C4	409.6	336.6	409.6	318.2	376.5	368.2	3.68E-13
	D1	1916.9	2144.6	2027.5	1575.1	1489.1	1812.3	1.81E-12
	D2	1713.4	2467.6	924.2	803.2	873.7	1223.5	1.22E-12
	D3	717.9	589.9	458.2	346.1	606.7	527.3	5.27E-13
	D4	2144.6	2144.6	--	--	--	2144.6	2.14E-12

ALV 2608-4-1 Pc 1	A1	1063.4	698.1	803.2	624.0	977.5	816.8	8.17E-13
	A2	10615.9	10322.2	9758.8	11876.9	12562.4	10979.4	1.10E-11
	A3	17591.7	14865.9	19136.7	18092.3	15288.9	16914.1	1.69E-11
	A4	3553.8	2085.2	3455.5	3359.9	3553.8	3141.1	3.14E-12
	B1	33542.2	52549.7	44407.2	31711.6	25335.5	36283.8	3.63E-11
	C1	512.7	458.2	484.7	433.2	292.5	428.4	4.28E-13
	C2	2332.9	2144.6	1971.4	2205.6	1812.3	2085.2	2.09E-12
	C3	1034.0	1093.6	924.2	1531.5	1531.5	1196.4	1.20E-12
ALV 2608-4-1 Pc 2	A1	8722.7	26056.4	32614.1	5726.1	12919.9	14054.6	1.41E-11
	A2	292.5	641.7	498.5	421.3	717.9	490.2	4.90E-13
	A3	2205.6	2332.9	2399.3	2467.6	2205.6	2319.9	2.32E-12
	B1	717.9	873.7	803.2	803.2	781.0	794.2	7.94E-13
	B2	3003.2	1093.6	1407.8	1368.9	977.5	1439.8	1.44E-12
	B3	1156.8	1489.1	1407.8	924.2	1005.3	1176.4	1.18E-12
JAS 177-2-1	A1	512.7	471.3	458.2	398.3	573.6	479.3	4.79E-13
	A2	3176.5	3759.0	3865.9	4448.2	4838.9	3975.9	3.98E-12
	A3	1575.1	1863.9	1331.0	950.5	1407.8	1392.1	1.39E-12
	B1	2144.6	3865.9	1916.9	2537.8	3759.0	2729.9	2.73E-12
	B2	14454.6	5118.2	7796.7	12919.9	10036.5	9435.7	9.44E-12
	B3	6229.0	22645.6	11228.7	5726.1	8481.4	9488.8	9.49E-12
	C1	4574.8	6968.9	4325.1	6588.6	8246.7	5955.5	5.96E-12
	C2	54045.1	89558.8	60464.6	87080.7	65774.9	69963.2	7.00E-11
	C3	4574.8	4574.8	6406.3	5263.8	6056.7	5323.2	5.32E-12
ALV 2179-1-1	A1	15288.9	23952.8	16631.7	6588.6	12919.9	13897.7	1.39E-11
	A2	4838.9	5118.2	8481.4	3975.9	4705.0	5234.4	5.23E-12
	A3	18607.2	11228.7	12214.8	11876.9	213737.4	23030.1	2.30E-11
	B1	738.4	458.2	924.2	376.5	542.3	576.8	5.77E-13
	B2	1156.8	1575.1	1005.3	2467.6	1489.1	1464.2	1.46E-12

A1.3 Zn-Rich Actively Diffusing Spire Data

Sample	Site	Permeability (mD)					Mean (mD)	Mean (m^2)
		1	2	3	4	5		
ALV 2187-1-1 top	A1	2920.1	2839.3	3003.2	2268.4	2537.8	2699.4	2.70E-12
	A2	8971.0	8246.7	10322.2	7167.2	7371.2	8339.8	8.34E-12
	A3	6968.9	8246.7	10036.5	6776.1	5118.2	7248.1	7.25E-12
	A4	7796.7	8971.0	8722.7	8971.0	7580.9	8386.7	8.39E-12
	B1	24634.4	28344.8	28344.8	26056.4	30834.2	27560.5	2.76E-11
	B2	22019.0	22019.0	19136.7	29151.4	23952.8	23030.1	2.30E-11
	B3	12562.4	22019.0	5118.2	23952.8	18607.2	14454.6	1.45E-11
ALV 2187-1-1 bottom	A1	180619.0	202072.9	121942.9	69571.7	180619.0	141099.3	1.41E-10
	A2	28344.8	28344.8	23952.8	26797.9	22645.6	25910.6	2.59E-11
	A3	10322.2	12919.9	8018.5	8018.5	6968.9	9021.5	9.02E-12
	A4	7580.9	3759.0	2920.1	3359.9	4574.8	4181.9	4.18E-12
	B1	25335.5	39692.5	26056.4	32614.1	35478.4	31357.7	3.14E-11
	B2	14454.6	16631.7	11876.9	8481.4	17591.7	13362.4	1.34E-11
	B3	3176.5	6968.9	4976.6	7167.2	7580.9	5694.1	5.69E-12
	C1	3553.8	2760.7	2684.3	2839.3	2399.3	2823.4	2.82E-12
	C2	1063.4	1093.6	1223.5	1005.3	1331.0	1137.5	1.14E-12
	C3	738.4	641.7	606.7	624.0	606.7	641.7	6.42E-13
	C4	18092.3	23952.8	25335.5	20817.4	16631.7	20700.9	2.07E-11

ALV 2187-1-2	A1	77835.4	48307.2	80050.4	28344.8	20817.4	44657.1	4.47E-11
	A2	19136.7	21409.8	57164.8	60464.6	35478.4	34690.8	3.47E-11
	B1	4838.9	4574.8	5118.2	4448.2	15288.9	5989.1	5.99E-12
	B2	4838.9	7167.2	7580.9	5263.8	2332.9	5032.7	5.03E-12
	B3	2268.4	1971.4	2537.8	2399.3	2399.3	2306.9	2.31E-12
	C1	291024.0	291024.0	232508.7	245930.1	307823.1	272070.8	2.72E-10
	C2	213737.4	84671.2	495982.9	219819.8	239125.2	216149.9	2.16E-10
	C3	2537.8	2205.6	1916.9	3176.5	2205.6	2372.5	2.37E-12
	C4	2610.0	2537.8	2920.1	3088.6	3455.5	2903.7	2.90E-12
	C5	8018.5	6776.1	8246.7	8246.7	6776.1	7580.9	7.58E-12
ALV 2190-14-1	A1	3975.9	4205.4	3865.9	4205.4	4089.1	4066.2	4.07E-12
	A2	10322.2	10615.9	13287.6	8246.7	7580.9	9813.8	9.81E-12
	A3	4089.1	3865.9	4574.8	3359.9	3654.9	3887.7	3.89E-12
	A4	9758.8	14054.6	14454.6	15288.9	14454.6	13437.6	1.34E-11
	A5	39692.5	49681.9	100196.6	73587.6	316582.9	85626.9	8.56E-11
	A6	919524.4	1704746.3	539542.1	799157.2	364265.9	755544.1	7.56E-10
	B1	11876.9	11548.2	10918.0	12214.8	19136.7	12847.6	1.28E-11
	B2	8722.7	7796.7	7580.9	10322.2	--	8541.1	8.54E-12
J2-137-7-R1 Pc 1	A1	275141.7	495982.9	156975.7	385292.8	232508.7	286165.4	2.86E-10
	A2	374631.8	694546.3	354186.7	603629.1	570686.7	501581.2	5.02E-10
	B1	170761.9	325591.9	354186.7	219819.8	180619.0	239125.2	2.39E-10
	B2	374631.8	226075.2	316582.9	275141.7	191045.0	269034.2	2.69E-10
	C1	65774.9	144302.4	92107.4	161442.7	191045.0	121942.9	1.22E-10
	C2	919524.4	972603.1	468915.2	734638.4	419130.7	664053.8	6.64E-10
	D1	226075.2	291024.0	175621.3	455940.4	307823.1	276690.1	2.77E-10
	E1	156975.7	275141.7	374631.8	334857.4	115288.0	228627.0	2.29E-10
J2-139-2-R1	A1	140309.6	63954.9	175621.3	87080.7	58791.6	95797.7	9.58E-11
	B1	115288.0	115288.0	132652.4	191045.0	121942.9	132652.4	1.33E-10
J2-128-8-R1	A1	11228.7	11876.9	29151.4	46970.5	67646.6	26203.1	2.62E-11
	A2	20241.3	12562.4	11228.7	9758.8	16631.7	13589.2	1.36E-11
	B1	125413.0	175621.3	396257.1	144302.4	170761.9	184719.3	1.85E-10

A1.4 Black Smoker Chimney Data

Sample	Site	Permeability (mD) 1	2	3	4	5	Mean (mD)	Mean (m^2)
ALV 2462-R2	A1	122.6	82.7	85.1	71.9	27.7	70.3	7.03E-14
	A2	69.9	47.2	14.1	19.8	20.3	28.5	2.85E-14
	A3	141.0	33.7	25.5	82.7	55.9	56.2	5.62E-14
	A4	103.6	103.6	71.9	100.7	64.3	87.0	8.70E-14
	B1	24.1	16.3	16.3	15.8	15.4	17.3	1.73E-14
	B2	25.5	17.7	38.8	15.8	27.7	23.8	2.38E-14
ALV 1445-3	A1	109.5	186.7	254.2	292.5	292.5	213.6	2.14E-13
	B1	346.1	318.2	327.2	214.8	153.4	260.0	2.60E-13
	C1	192.0	119.2	60.8	109.5	240.3	129.6	1.30E-13
ALV 2179-4-1	A1	1447.9	950.5	1063.4	1063.4	1812.3	1230.4	1.23E-12
	B1	398.3	376.5	421.3	208.9	214.8	309.4	3.09E-13
	C1	2085.2	3759.0	3975.9	3975.9	5413.6	3675.5	3.68E-12

J2-213-2-R1	A1	803.2	1005.3	698.1	678.7	898.6	807.7	8.08E-13
	B1	80.5	176.5	62.5	162.3	186.7	121.9	1.22E-13
	B2	458.2	458.2	318.2	512.7	--	430.2	4.30E-13
	B3	327.2	300.8	261.4	--	--	295.2	2.95E-13
	C1	27.7	34.7	35.7	--	--	32.5	3.25E-14
	D1	1407.8	1713.4	3553.8	1916.9	1063.4	1772.1	1.77E-12
	D2	3759.0	4976.6	4205.4	3088.6	2760.7	3675.5	3.68E-12
J2-213-3-R1	A1	13665.7	10322.2	18092.3	10036.5	10322.2	12146.5	1.21E-11
	B1	4705.0	4089.1	5726.1	4838.9	7167.2	5205.1	5.21E-12
	B2	3553.8	4838.9	4574.8	4705.0	4838.9	4473.2	4.47E-12
	B3	5726.1	4838.9	4205.4	5567.7	4574.8	4948.7	4.95E-12
	C1	471.3	433.2	387.2	421.3	356.0	411.9	4.12E-13
	C2	781.0	950.5	898.6	1063.4	1189.7	966.6	9.67E-13
	C3	112.7	149.2	137.1	--	--	132.1	1.32E-13
	D1	22.8	27.7	--	--	--	25.1	2.51E-14
	E1	5889.1	5413.6	7167.2	4089.1	--	5528.8	5.53E-12
	F1	624.0	1124.8	803.2	366.1	527.3	641.7	6.42E-13
J2-137-3-R1	A1	13665.7	8722.7	9758.8	6229.0	5726.1	8386.7	8.39E-12
	A2	13287.6	9758.8	5118.2	5413.6	5118.2	7127.1	7.13E-12
	A3	44407.2	108996.3	87080.7	71551.5	118568.8	81409.5	8.14E-11
	A4	22645.6	21409.8	15724.0	--	--	19681.3	1.97E-11
	B1	387.2	214.8	197.5	--	--	254.2	2.54E-13
	C1	7371.2	3266.9	6229.0	4325.1	4205.4	4866.1	4.87E-12
	C2	3759.0	3975.9	4205.4	4205.4	3266.9	3865.9	3.87E-12
	D1	115.9	100.7	119.2	--	--	111.6	1.12E-13
	D2	48.6	87.5	54.3	--	--	61.3	6.13E-14
	D3	268.9	203.1	203.1	--	--	223.0	2.23E-13
	D4	126.0	62.5	92.6	--	--	90.0	9.00E-14
	E1	45670.9	36488.0	48307.2	--	--	43178.4	4.32E-11
	E2	2839.3	2610.0	2467.6	--	--	2634.6	2.63E-12
	E3	115.9	171.6	112.7	106.5	103.6	119.8	1.20E-13
	E4	8971.0	11228.7	10322.2	--	--	10130.9	1.01E-11
	F1	2144.6	1863.9	2268.4	--	--	2085.2	2.09E-12
	F2	192.0	171.6	220.9	--	--	193.8	1.94E-13
	G1	300.8	336.6	233.7	--	--	287.1	2.87E-13
	G2	57.5	41.0	51.4	--	--	49.5	4.95E-14
	H1	327.2	387.2	366.1	--	--	359.3	3.59E-13
	H2	1971.4	803.2	398.3	484.7	--	743.6	7.44E-13

A1.5 Relict Spire Data

Sample	Site	Permeability (mD) 1	2	3	4	5	Mean (mD)	Mean (m^2)
J2-129-1-R3	A1	292.5	122.6	376.5	32.8	129.6	141.8	1.42E-13
	A2	157.8	233.7	203.1	214.8	192.0	198.6	1.99E-13
	A3	268.9	186.7	227.2	149.2	220.9	206.5	2.07E-13
	B1	276.5	157.8	284.4	284.4	186.7	231.1	2.31E-13
	B2	137.1	74.0	103.6	74.0	68.0	88.0	8.80E-14
	B3	51.4	68.0	47.2	38.8	25.5	43.9	4.39E-14
	C1	144302.4	112098.0	239125.2	170761.9	267528.6	177603.5	1.78E-10
	C2	121942.9	92107.4	166036.9	89558.8	100196.6	110846.9	1.11E-10
J2-136-6-R1	A1	181.5	171.6	133.3	129.6	153.4	152.5	1.53E-13
	A2	122.6	95.2	92.6	106.5	80.5	98.5	9.85E-14
	A3	2085.2	3088.6	1916.9	1971.4	1156.8	1949.4	1.95E-12
	A4	1005.3	498.5	233.7	409.6	660.0	501.3	5.01E-13
	B1	162.3	126.0	133.3	57.5	74.0	103.0	1.03E-13
	B2	247.2	300.8	261.4	220.9	318.2	267.4	2.67E-13
	B3	6776.1	4205.4	5889.1	8018.5	7167.2	6264.1	6.26E-12
	C1	387.2	421.3	606.7	471.3	542.3	479.3	4.79E-13
	C2	589.9	220.9	498.5	641.7	433.2	448.1	4.48E-13
	C3	119.2	62.5	74.0	64.3	69.9	75.6	7.56E-14
ALV 2944-3-S1 Pc 1	A1	63954.9	49681.9	43178.4	48307.2	52549.7	51095.7	5.11E-11
	A2	44407.2	57164.8	49681.9	45670.9	54045.1	49961.5	5.00E-11
	A3	44407.2	43178.4	36488.0	52549.7	34496.7	41748.7	4.17E-11
	A4	37526.3	57164.8	46970.5	25335.5	46970.5	41282.8	4.13E-11
	B1	292.5	214.8	176.5	247.2	227.2	228.5	2.28E-13
	B2	781.0	268.9	1156.8	898.6	387.2	610.1	6.10E-13
	B3	29151.4	25335.5	24634.4	29151.4	27560.5	27100.4	2.71E-11
ALV 2941-6-S1	A1	144302.4	191045.0	75681.7	152632.2	103047.9	126828.6	1.27E-10
	A2	38594.2	22019.0	63954.9	29981.0	34496.7	35478.4	3.55E-11
	B1	21409.8	16171.5	41983.7	15724.0	21409.8	21773.3	2.18E-11
	B2	25335.5	26797.9	18607.2	19681.3	27560.5	23290.0	2.33E-11
	C1	11228.7	12919.9	4574.8	5726.1	5726.1	7371.2	7.37E-12
J2-125-3-B1	A1	4325.1	6229.0	5889.1	3266.9	6776.1	5118.2	5.12E-12
	A2	220.9	284.4	309.4	261.4	149.2	237.7	2.38E-13
	A3	1223.5	1575.1	1447.9	1863.9	1124.8	1423.7	1.42E-12
	A4	1812.3	1863.9	1812.3	717.9	1447.9	1447.9	1.45E-12
	B1	18607.2	18092.3	11228.7	8018.5	14865.9	13513.2	1.35E-11
	B2	3003.2	4838.9	3654.9	5118.2	3553.8	3953.7	3.95E-12
	B3	1223.5	1368.9	1189.7	1034.0	1156.8	1189.7	1.19E-12
	C1	115.9	145.0	97.9	176.5	90.0	121.2	1.21E-13
	C2	87.5	55.9	28.5	45.9	35.7	46.9	4.69E-14
	C3	87.5	49.9	64.3	71.9	49.9	63.2	6.32E-14
ALV 2178-4-1	A1	14.9	15.8	119.2	122.6	78.2	48.6	4.86E-14
	A2	1619.9	1368.9	1005.3	1034.0	1093.6	1203.1	1.20E-12
	A3	557.7	1005.3	826.1	898.6	977.5	835.4	8.35E-13
	A4	7580.9	8018.5	6056.7	7796.7	6776.1	7207.5	7.21E-12
	A5	30834.2	20817.4	39692.5	29151.4	36488.0	30661.6	3.07E-11
	B1	18607.2	11228.7	15724.0	17591.7	21409.8	16538.6	1.65E-11
	B2	3654.9	3865.9	3654.9	2839.3	3553.8	3494.5	3.49E-12
	B3	498.5	356.0	247.2	268.9	247.2	311.1	3.11E-13
	B4	2027.5	1447.9	924.2	1531.5	1189.7	1376.6	1.38E-12

Appendix 2: Core Permeability Data

A2.1 Massive Anhydrite Data

Sample	Confining Pressure (psi)	Permeability (× 10^{-15} m^2) 1	2	3	4	5	Mean *k* (× 10^{-15} m^2)
	70	0.291	0.298	0.285	0.287	0.293	0.29
J2-210-8-R2	100	0.294	0.281	0.266	0.272	0.286	0.28
Core A-1	150	0.280	0.286	0.255	0.274	0.267	0.27
	200	0.282	0.294	0.267	0.281	0.276	0.28
	250	0.282	0.268	0.287	0.281	0.267	0.28
	300	0.267	0.262	0.267	0.266	0.281	0.27
	350	0.258	0.273	0.260	0.266	0.266	0.27
	400	0.272	0.266	0.260	0.265	0.259	0.26
	350	0.273	0.247	0.272	0.273	0.267	0.27
	300	0.267	0.280	0.283	0.275	0.276	0.28
	250	0.280	0.273	0.281	0.276	0.277	0.28
	200	0.279	0.285	0.280	0.257	0.294	0.28
	150	0.284	0.263	0.278	0.270	0.283	0.28
length: 1.551 cm	100	0.278	0.291	0.285	0.285	0.272	0.28
width: 2.522 cm	70	0.291	0.291	0.284	0.286	0.285	0.29
	70	0.180	0.172	0.178	0.178	0.173	0.18
J2-210-8-R2	100	0.161	0.168	0.146	0.157	0.157	0.16
Core A-2	150	0.135	0.14	0.137	0.137	0.134	0.14
	200	0.129	0.129	0.131	0.133	0.126	0.13
	250	0.124	0.123	0.118	0.126	0.122	0.12
	300	0.114	0.114	0.116	0.122	0.114	0.12
	350	0.111	0.115	0.114	0.117	0.114	0.11
	400	0.114	0.115	0.114	0.114	0.113	0.11
	350	0.102	0.110	0.116	0.117	0.111	0.11
	300	0.111	0.120	0.117	0.112	0.111	0.11
	250	0.123	0.125	0.123	0.114	0.120	0.12
	200	0.118	0.118	0.121	0.117	0.127	0.12
	150	0.124	0.124	0.124	0.123	0.126	0.12
length: 0.640 cm	100	0.137	0.134	0.133	0.130	0.128	0.13
width: 2.539 cm	70	0.132	0.133	0.135	0.135	0.132	0.13
	70	0.245	0.242	0.243	0.233	0.241	0.24
J2-210-8-R2	100	0.199	0.205	0.193	0.183	0.203	0.20
Core A-3	150	0.167	0.173	0.169	0.166	0.170	0.17
	200	0.158	0.154	0.150	0.147	0.151	0.15
	250	0.159	0.153	0.155	0.145	0.147	0.15
	300	0.132	0.141	0.131	0.138	0.134	0.14
	350	0.135	0.131	0.128	0.134	0.134	0.13
	400	0.129	0.131	0.128	0.131	0.133	0.13
	350	0.128	0.125	0.124	0.131	0.131	0.13
	300	0.135	0.138	0.138	0.131	0.138	0.14
	250	0.135	0.144	0.142	0.140	0.135	0.14
	200	0.136	0.138	0.138	0.139	0.147	0.14
	150	0.147	0.142	0.141	0.144	0.144	0.14
length: 0.714 cm	100	0.152	0.149	0.156	0.152	0.148	0.15
width: 2.540 cm	70	0.165	0.173	0.165	0.165	0.161	0.17
	70	267.995	267.835	267.235	267.199	266.897	267.43
J2-216-5-R1	100	256.373	256.285	255.569	255.047	255.080	255.67
Core A2	150	244.886	244.721	243.900	243.904	243.097	244.10
	200	237.992	238.129	238.062	238.039	237.304	237.91
	250	233.748	233.856	234.876	234.120	233.957	234.11
	300	230.644	230.369	230.221	230.047	230.580	230.37
	350	228.403	228.082	228.014	228.269	228.144	228.18
	400	225.150	225.074	225.095	225.220	225.254	225.16
	350	226.236	225.710	225.992	225.736	225.754	225.89
	300	226.563	226.393	226.728	226.656	226.423	226.55

	250	227.757	227.715	227.538	228.202	227.604	227.76
	200	230.622	230.223	230.201	230.386	230.315	230.35
	150	233.764	233.847	234.236	234.051	233.975	233.97
length: 1.142 cm	100	239.299	239.613	239.999	240.511	240.297	239.94
width: 2.533 cm	70	246.349	246.666	247.122	247.279	247.447	246.97
	70	0.365	0.324	0.343	0.349	0.352	0.35
J2-216-14-R1	100	0.329	0.334	0.336	0.340	0.333	0.33
Core A	150	0.334	0.326	0.325	0.344	0.326	0.33
	200	0.310	0.333	0.333	0.334	0.325	0.33
	250	0.332	0.338	0.331	0.315	0.324	0.33
	300	0.331	0.323	0.316	0.323	0.329	0.32
	350	0.329	0.330	0.322	0.330	0.323	0.33
	400	0.323	0.321	0.322	0.315	0.322	0.32
	350	0.306	0.323	0.323	0.324	0.324	0.32
	300	0.314	0.323	0.333	0.322	0.324	0.32
	250	0.332	0.341	0.333	0.324	0.332	0.33
	200	0.349	0.340	0.331	0.350	0.335	0.34
	150	0.332	0.342	0.350	0.335	0.350	0.34
length: 1.841 cm	100	0.341	0.351	0.349	0.351	0.342	0.35
width: 2.530 cm	70	0.343	0.351	0.353	0.359	0.353	0.35
	70	0.380	0.392	0.371	0.390	0.376	0.38
J2-216-14-R1	100	0.389	0.378	0.388	0.361	0.373	0.38
Core B	150	0.371	0.377	0.386	0.386	0.364	0.38
	200	0.365	0.391	0.371	0.355	0.344	0.37
	250	0.331	0.347	0.330	0.354	0.336	0.34
	300	0.343	0.342	0.336	0.341	0.333	0.34
	350	0.324	0.324	0.316	0.332	0.336	0.33
	400	0.328	0.335	0.329	0.326	0.330	0.33
	350	0.342	0.335	0.326	0.345	0.347	0.34
	300	0.341	0.348	0.348	0.348	0.345	0.35
	250	0.365	0.355	0.363	0.363	0.355	0.36
	200	0.374	0.365	0.367	0.375	0.366	0.37
	150	0.373	0.362	0.384	0.374	0.375	0.37
length: 2.243 cm	100	0.386	0.386	0.396	0.380	0.380	0.39
width: 2.536 cm	70	0.398	0.388	0.370	0.389	0.388	0.39
	70	44.519	44.719	44.820	44.789	44.714	44.71
J301-3	100	43.244	42.910	42.915	42.990	42.865	42.99
Core A	150	40.907	40.837	40.942	40.751	40.928	40.87
	200	39.711	39.921	39.959	39.651	39.784	39.81
	250	38.926	38.955	39.029	38.942	38.913	38.95
	300	38.632	38.308	38.730	38.592	38.377	38.53
	350	38.093	38.303	37.967	38.138	37.996	38.10
	400	37.959	37.832	37.962	38.224	37.860	37.97
	350	37.888	37.916	38.050	37.933	37.989	37.96
	300	38.558	38.089	38.118	38.249	38.469	38.30
	250	38.303	38.524	38.362	38.304	38.361	38.37
	200	38.765	38.720	38.765	38.939	39.177	38.87
	150	39.377	39.376	39.497	39.450	39.254	39.39
length: 3.205 cm	100	40.232	40.297	40.411	40.267	40.207	40.28
width: 2.546 cm	70	41.201	41.325	41.416	41.435	41.547	41.39
	70	3.089	3.066	3.026	3.024	2.968	3.03
J301-3	100	2.150	2.146	2.135	2.109	2.115	2.13
Core B	150	1.455	1.449	1.430	1.458	1.424	1.44
	200	1.136	1.110	1.139	1.101	1.106	1.12
	250	0.896	0.865	0.861	0.831	0.844	0.86
	300	0.749	0.744	0.702	0.730	0.710	0.73
	350	0.647	0.614	0.630	0.598	0.613	0.62
	400	0.585	0.540	0.519	0.570	0.543	0.55
	350	0.536	0.545	0.545	0.526	0.552	0.54
	300	0.603	0.581	0.617	0.594	0.609	0.60
	250	0.616	0.639	0.619	0.639	0.620	0.63
	200	0.711	0.710	0.694	0.700	0.699	0.70
	150	0.785	0.830	0.843	0.815	0.839	0.82
length: 5.196 cm	100	1.090	1.078	1.113	1.089	1.113	1.10
width: 2.530 cm	70	1.503	1.495	1.531	1.506	1.520	1.51

ALV 2581-8 Core A	70	385.778	384.319	385.783	384.144	383.108	384.63
	100	374.542	371.234	372.748	371.396	372.332	372.45
	150	362.374	361.987	362.167	363.945	363.416	362.78
	200	357.285	356.242	358.376	358.436	358.500	357.77
	250	356.364	354.978	354.431	354.002	357.723	355.50
	300	351.712	352.298	351.648	353.377	353.968	352.60
	350	352.045	350.767	351.025	349.991	352.317	351.23
	400	348.820	349.987	350.331	348.535	348.358	349.21
	350	348.225	350.087	352.225	349.879	350.863	350.25
	300	350.128	351.000	350.836	349.445	351.289	350.54
	250	353.742	352.350	351.312	352.930	352.921	352.65
	200	352.815	352.397	353.182	355.053	354.727	353.63
	150	354.993	357.216	356.021	357.617	354.069	355.98
length: 4.438 cm	100	360.272	360.339	357.751	359.583	359.185	359.43
width: 2.528 cm	70	362.774	363.853	362.634	361.279	362.299	362.57
MIR 1 1/74 Sta 2403 Core A-1	70	135.771	136.271	135.784	136.702	136.388	136.18
	100	131.260	131.457	131.069	131.908	131.009	131.34
	150	127.532	127.636	127.371	127.072	127.154	127.35
	200	125.868	124.886	125.383	125.161	125.198	125.30
	250	124.119	124.734	124.165	123.651	123.813	124.10
	300	123.370	123.450	122.803	122.660	123.694	123.20
	350	121.650	122.313	121.862	121.975	122.058	121.97
	400	121.260	121.522	121.195	121.720	121.248	121.39
	350	122.782	121.967	122.664	121.476	121.576	122.09
	300	122.833	122.256	121.581	122.061	122.088	122.16
	250	122.363	122.535	122.409	122.873	122.051	122.45
	200	123.295	123.105	122.979	123.350	123.529	123.25
	150	123.983	124.000	124.916	124.065	124.273	124.25
length: 4.080 cm	100	125.344	124.935	125.422	125.452	125.637	125.36
width: 2.520 cm	70	127.342	127.799	127.236	128.125	127.296	127.56
MIR 1 1/74 Sta 2403 Core A-2	70	357.041	356.924	355.229	356.338	357.554	356.62
	100	350.290	351.167	349.277	349.815	350.009	350.11
	150	346.193	343.608	346.194	344.498	345.392	345.18
	200	340.481	341.295	341.624	339.100	339.459	340.39
	250	340.261	339.332	338.326	338.670	338.652	339.05
	300	335.709	336.357	337.967	337.275	335.983	336.66
	350	335.851	336.011	334.411	335.670	334.360	335.26
	400	333.827	336.329	335.811	334.138	335.304	335.08
	350	335.426	334.711	334.827	335.333	335.196	335.10
	300	336.528	333.855	336.582	336.918	335.792	335.93
	250	335.845	336.931	336.698	337.289	335.492	336.45
	200	338.839	338.392	340.869	339.559	338.494	339.23
	150	341.243	341.277	340.400	342.486	343.831	341.85
length: 3.877 cm	100	341.921	342.633	343.197	342.419	342.093	342.45
width: 2.529 cm	70	345.162	345.266	346.373	345.499	346.322	345.72
MIR 1 1/74 Sta 2403 Core B	70	86.833	85.839	86.324	86.657	86.212	86.37
	100	84.007	84.256	84.087	83.734	83.397	83.90
	150	81.437	81.045	81.600	81.417	81.217	81.34
	200	79.590	79.354	79.035	79.640	79.045	79.33
	250	78.097	78.285	78.335	78.035	78.176	78.19
	300	77.708	76.980	77.103	77.085	76.782	77.13
	350	76.151	76.316	76.309	76.303	76.053	76.23
	400	75.776	75.629	75.852	75.820	75.503	75.72
	350	75.747	75.949	75.938	75.634	75.722	75.80
	300	75.965	75.651	75.906	75.994	75.842	75.87
	250	76.275	76.458	76.165	76.090	76.327	76.26
	200	77.304	77.092	77.322	77.582	77.255	77.31
	150	78.187	78.207	78.412	78.789	78.267	78.37
length: 4.356 cm	100	80.134	79.754	80.008	79.955	80.429	80.06
width: 2.508 cm	70	81.089	81.219	81.179	81.305	81.319	81.22
MIR 1 2/78 Sta 2417 Core A	70	565.306	566.096	564.979	565.900	566.007	565.67
	100	544.609	544.723	544.195	544.468	544.754	544.55
	150	515.184	515.581	514.383	513.178	514.121	514.49
	200	497.879	498.050	497.085	497.058	496.599	497.33
	250	485.011	485.151	485.553	485.245	484.821	485.16
	300	478.147	478.037	477.992	477.013	478.106	477.86

	350	474.495	474.649	473.589	473.699	474.462	474.18
	400	473.657	472.722	472.364	473.590	472.916	473.05
	350	474.642	473.263	473.368	472.481	473.760	473.50
	300	474.334	473.837	474.064	474.164	474.416	474.16
	250	475.323	475.484	475.883	475.993	475.989	475.73
	200	478.983	479.242	480.187	479.864	480.441	479.74
	150	488.561	489.244	488.237	489.682	490.677	489.28
length: 4.298 cm	100	502.721	504.234	504.597	505.237	503.814	504.12
width: 2.513 cm	70	520.387	522.875	524.750	524.661	523.826	523.30
	70	681.645	681.853	678.793	676.887	677.152	679.27
MIR 1 2/78	100	651.131	649.723	648.576	647.284	647.463	648.84
Sta 2417	150	624.709	622.992	625.431	623.076	623.382	623.92
Core B	200	607.457	608.314	608.026	606.649	606.720	607.43
	250	600.058	599.980	599.837	600.318	598.928	599.82
	300	596.260	596.248	595.899	595.687	595.395	595.90
	350	593.906	593.905	593.706	592.511	594.022	593.61
	400	591.232	591.019	590.889	590.801	590.648	590.92
	350	590.377	590.179	590.226	590.142	590.364	590.26
	300	590.700	590.492	590.282	590.984	590.493	590.59
	250	591.335	591.691	591.068	590.580	591.189	591.17
	200	592.121	593.435	592.129	594.559	592.129	592.88
	150	595.642	595.707	594.393	596.614	595.254	595.52
length: 5.405 cm	100	608.309	609.071	609.444	610.170	609.128	609.22
width: 2.532 cm	70	623.684	625.737	625.578	625.398	625.045	625.09
	70	3.38	--	--	--	--	3.38
ALV 21837-0	100	2.37	--	--	--	--	2.37
Core 2	150	1.38	--	--	--	--	1.38
	200	0.96	--	--	--	--	0.96
	250	0.56	--	--	--	--	0.56
	300	0.38	--	--	--	--	0.38
	350	0.28	--	--	--	--	0.28
	400	0.15	--	--	--	--	0.15
	70	0.57	--	--	--	--	0.57
ALV 21837-0	100	0.48	--	--	--	--	0.48
Core 3	150	0.43	--	--	--	--	0.43
	200	0.41	--	--	--	--	0.41
	250	0.40	--	--	--	--	0.40
	300	0.35	--	--	--	--	0.35
	350	0.31	--	--	--	--	0.31
	400	0.31	--	--	--	--	0.31
	70	1.84	--	--	--	--	1.84
ALV 21837-0	100	1.39	--	--	--	--	1.39
Core B	150	0.91	--	--	--	--	0.91
	200	0.63	--	--	--	--	0.63
	250	0.43	--	--	--	--	0.43
	300	0.32	--	--	--	--	0.32
	350	0.25	--	--	--	--	0.25
	400	0.18	--	--	--	--	0.18

A2.2 Flange, Slab and Crust Data

Sample	Confining Pressure (psi)	Permeability ($\times 10^{-15}$ m^2) 1	2	3	4	5	Mean *k* ($\times 10^{-15}$ m^2)
ALV 3517-R1 Core D1	70	70.805	71.677	72.375	72.667	72.521	72.01
	100	67.892	68.285	68.184	67.776	67.699	67.97
	150	62.624	62.911	62.409	62.601	62.509	62.61
	200	59.040	59.111	59.040	59.122	59.383	59.14
	250	56.880	56.684	57.275	56.854	56.860	56.91
	300	55.102	55.352	55.159	54.941	55.129	55.14
	350	54.297	53.894	53.808	53.863	54.247	54.02
	400	53.103	52.562	52.859	52.925	53.031	52.90
	350	53.019	53.307	53.273	52.958	53.289	53.17
	300	53.447	53.695	53.872	54.147	53.425	53.72
	250	54.397	54.672	54.122	54.208	54.403	54.36
	200	55.279	55.686	55.364	55.254	55.448	55.41
	150	57.220	57.541	57.758	57.788	57.316	57.52
length: 1.196 cm	100	59.625	60.020	59.875	59.971	60.437	59.99
width: 2.466 cm	70	62.444	62.399	62.590	62.511	62.827	62.55
ALV 3517-R1 Core D3	70	42.394	43.024	42.979	43.222	42.797	42.88
	100	38.946	38.571	38.503	38.473	38.708	38.64
	150	34.605	34.770	34.412	34.364	34.155	34.46
	200	32.177	32.063	32.013	31.799	32.022	32.01
	250	30.661	30.457	30.391	30.660	30.437	30.52
	300	29.404	29.651	29.493	29.603	29.467	29.52
	350	28.892	28.732	28.516	28.824	28.760	28.74
	400	28.122	27.926	28.084	28.076	27.878	28.02
	350	28.342	28.234	28.232	28.307	28.231	28.27
	300	28.510	28.607	28.543	28.600	28.810	28.61
	250	28.890	28.947	28.897	29.050	29.005	28.96
	200	29.576	29.519	29.538	29.540	29.613	29.56
	150	30.559	30.519	30.574	30.344	30.660	30.53
length: 1.162 cm	100	32.034	31.898	32.058	31.975	32.105	32.01
width: 2.478 cm	70	33.750	34.175	34.014	34.163	34.116	34.04
ALV 3521-R2 Core A2	70	1422.323	1432.011	1429.505	1445.900	1430.926	1432.11
	100	1439.282	1433.864	1438.254	1430.905	1428.842	1434.22
	150	1425.212	1426.640	1430.618	1418.309	1428.974	1425.94
	200	1427.109	1426.700	1426.908	1423.637	1424.397	1425.75
	250	1425.486	1427.395	1428.837	1422.022	1428.646	1426.47
	300	1419.542	1420.056	1423.414	1420.600	1419.476	1420.62
	350	1418.238	1417.933	1416.070	1417.482	1410.995	1416.14
	400	1421.449	1418.553	1405.410	1410.019	1415.608	1414.20
	350	1412.030	1417.276	1415.924	1417.663	1414.897	1415.56
	300	1419.043	1410.887	1418.774	1417.031	1412.395	1415.62
	250	1416.467	1420.862	1415.722	1426.463	1416.719	1419.24
	200	1426.614	1429.301	1417.698	1429.803	1428.223	1426.32
	150	1430.473	1422.260	1437.298	1423.172	1428.742	1428.38
length: 1.480 cm	100	1433.816	1435.671	1429.821	1431.754	1432.303	1432.67
width: 2.532 cm	70	1435.617	1428.755	1432.076	1430.764	1433.378	1432.12
ALV 3521-R2 Core Ex 1	70	1353.598	1364.733	1371.937	1367.487	1360.415	1363.62
	100	1358.823	1360.463	1364.393	1361.455	1361.677	1361.36
	150	1346.417	1347.489	1347.749	1344.863	1345.314	1346.37
	200	1311.957	1313.285	1312.571	1308.962	1311.605	1311.68
	250	1264.914	1268.423	1270.390	1264.302	1269.735	1267.55
	300	1243.826	1245.147	1242.611	1240.430	1244.946	1243.39
	350	1226.449	1225.160	1220.550	1223.529	1224.535	1224.04
	400	1218.592	1214.403	1212.955	1206.820	1212.597	1213.07
	350	1217.010	1217.070	1218.116	1225.262	1218.163	1219.12
	300	1225.640	1223.960	1222.842	1226.517	1224.837	1224.76
	250	1226.037	1224.133	1227.264	1228.886	1220.633	1225.39
	200	1243.490	1237.553	1241.162	1239.066	1241.635	1240.58
	150	1269.815	1272.410	1270.950	1275.712	1269.935	1271.76

length: 1.549 cm	100	1302.646	1303.591	1304.986	1316.100	1312.943	1308.04
width: 2.506 cm	70	1338.587	1341.667	1335.947	1336.308	1335.224	1337.54
	70	1013.176	1012.378	1022.284	1011.949	1017.531	1015.46
ALV 3521-R2	100	1006.855	1004.269	1001.139	1004.820	1000.574	1003.53
Core Ex 2	150	974.762	981.290	981.475	979.969	984.304	980.35
	200	971.354	969.261	966.181	971.116	970.228	969.63
	250	958.035	958.814	960.185	961.126	960.605	959.75
	300	954.072	957.787	956.848	950.985	953.788	954.69
	350	953.184	954.635	952.004	954.165	954.336	953.66
	400	954.974	952.534	953.422	954.716	953.275	953.78
	350	952.618	955.944	952.412	955.546	956.446	954.59
	300	950.459	949.099	954.063	954.352	956.801	952.95
	250	954.661	955.023	955.972	952.357	956.625	954.93
	200	955.066	955.984	956.841	954.333	956.917	955.83
	150	971.874	970.979	963.867	967.613	968.145	968.49
length: 1.014 cm	100	974.243	972.702	977.035	979.075	979.594	976.53
width: 2.517 cm	70	984.051	984.049	988.846	984.498	989.657	986.22
	70	68.571	68.423	68.871	68.180	68.119	68.43
ALV 2415-1B	100	63.621	63.567	63.575	63.585	63.501	63.57
Core A1	150	57.862	58.024	57.944	57.796	57.926	57.91
	200	56.608	56.730	56.434	56.485	56.399	56.53
	250	55.865	55.821	55.957	55.731	55.799	55.83
	300	55.432	55.202	55.374	55.306	55.675	55.40
	350	55.240	55.095	55.064	54.881	54.913	55.04
	400	54.756	54.597	54.604	54.411	55.120	54.70
	350	54.742	54.755	54.877	54.928	54.797	54.82
	300	54.926	55.479	55.094	55.313	55.169	55.20
	250	55.701	55.558	55.400	55.541	55.690	55.58
	200	55.686	55.673	55.728	55.755	55.872	55.74
	150	56.401	56.215	56.317	56.300	56.195	56.29
length: 2.084 cm	100	57.992	57.659	57.656	57.678	57.699	57.74
width: 2.480 cm	70	62.883	62.735	62.855	62.786	62.703	62.79
	70	1731.305	1727.945	1726.755	1720.326	1726.610	1726.58
ALV 2415-1B	100	1661.130	1662.277	1659.746	1656.780	1661.611	1660.31
Core B1	150	1621.342	1621.304	1620.372	1619.277	1617.850	1620.03
	200	1598.285	1593.126	1595.238	1594.572	1591.969	1594.64
	250	1572.853	1573.635	1570.254	1570.673	1573.056	1572.09
	300	1551.429	1555.157	1550.990	1551.450	1552.245	1552.25
	350	1534.874	1533.078	1535.014	1534.458	1533.041	1534.09
	400	1517.890	1513.684	1512.048	1515.330	1512.577	1514.30
	350	1517.067	1519.251	1517.333	1518.957	1517.523	1518.03
	300	1522.546	1525.321	1525.635	1525.267	1521.020	1523.96
	250	1531.960	1532.006	1533.799	1531.695	1527.531	1531.40
	200	1545.121	1547.289	1545.072	1547.390	1545.990	1546.17
	150	1559.269	1561.854	1562.734	1562.881	1562.708	1561.89
length: 5.838 cm	100	1577.023	1576.552	1580.638	1578.798	1580.188	1578.64
width: 2.490 cm	70	1595.937	1593.497	1596.318	1592.738	1598.929	1595.48
	70	66.8	--	--	--	--	66.8
ALV 2415-1B	100	59.3	--	--	--	--	59.3
Core 1	150	52.0	--	--	--	--	52.0
	200	46.1	--	--	--	--	46.1
	250	41.6	--	--	--	--	41.6
	300	39.2	--	--	--	--	39.2
	350	37.3	--	--	--	--	37.3
	400	36.0	--	--	--	--	36.0
	70	11.8	--	--	--	--	11.8
ALV 2415-1B	100	9.8	--	--	--	--	9.8
Core 2	150	7.1	--	--	--	--	7.1
	200	5.3	--	--	--	--	5.3
	250	4.5	--	--	--	--	4.5
	300	3.5	--	--	--	--	3.5
	350	2.9	--	--	--	--	2.9
	400	2.5	--	--	--	--	2.5
	70	1998.995	1995.040	1989.075	1994.736	1993.444	1994.26
ALV 2727-3	100	1973.888	1979.961	1979.924	1981.849	1977.613	1978.65
Core B1	150	1956.234	1955.954	1948.347	1956.622	1958.593	1955.15

	200	1931.790	1935.533	1928.452	1934.961	1922.350	1930.61
	250	1902.452	1904.822	1902.014	1898.109	1906.368	1902.75
	300	1887.248	1894.701	1896.360	1881.084	1885.969	1889.06
	350	1872.134	1874.619	1871.287	1872.729	1875.124	1873.18
	400	1862.190	1866.476	1866.930	1862.102	1859.724	1863.48
	350	1860.102	1877.249	1860.662	1863.453	1867.762	1865.83
	300	1867.857	1867.034	1863.636	1870.709	1873.502	1868.54
	250	1874.716	1876.572	1878.228	1883.035	1881.153	1878.74
	200	1892.253	1893.593	1895.523	1897.051	1887.724	1893.23
	150	1905.288	1906.861	1908.943	1906.681	1905.719	1906.70
length: 2.658 cm	100	1929.958	1920.503	1927.836	1929.570	1932.740	1928.12
width: 2.485 cm	70	1951.330	1943.875	1939.239	1947.789	1950.196	1946.48
	70	2631.6	--	--	--	--	2631.6
ALV 2927-3	100	2601.1	--	--	--	--	2601.1
Core 1	150	2295.1	--	--	--	--	2295.1
	200	1950.2	--	--	--	--	1950.2
	250	1816.9	--	--	--	--	1816.9
	300	1715.5	--	--	--	--	1715.5
	350	1653.1	--	--	--	--	1653.1
	400	1613.7	--	--	--	--	1613.7
	70	182.4	--	--	--	--	182.4
ALV 2927-3	100	172.8	--	--	--	--	172.8
Core 2	150	161.8	--	--	--	--	161.8
	200	155.6	--	--	--	--	155.6
	250	151.5	--	--	--	--	151.5
	300	148.7	--	--	--	--	148.7
	350	146.1	--	--	--	--	146.1
	400	145.3	--	--	--	--	145.3
	70	1081.4	--	--	--	--	1081.4
ALV 2927-3	100	1062.7	--	--	--	--	1062.7
Core 3	150	1010.0	--	--	--	--	1010.0
	200	994.2	--	--	--	--	994.2
	250	966.1	--	--	--	--	966.1
	300	968.9	--	--	--	--	968.9
	350	955.6	--	--	--	--	955.6
	400	948.7	--	--	--	--	948.7
	70	5.003	4.930	4.920	4.856	4.852	4.91
J2-286	100	3.726	3.716	3.686	3.681	3.696	3.70
Core A1	150	2.215	2.204	2.183	2.145	2.144	2.18
	200	1.375	1.346	1.322	1.295	1.274	1.32
	250	0.879	0.845	0.839	0.824	0.811	0.84
	300	0.573	0.553	0.545	0.543	0.532	0.55
	350	0.372	0.364	0.363	0.347	0.347	0.36
	400	0.230	0.205	0.222	0.211	0.228	0.22
	350	0.251	0.243	0.252	0.245	0.242	0.25
	300	0.309	0.313	0.318	0.317	0.314	0.31
	250	0.373	0.386	0.390	0.388	0.384	0.38
	200	0.505	0.502	0.526	0.525	0.530	0.52
	150	0.770	0.795	0.799	0.808	0.816	0.80
length: 2.868 cm	100	1.432	1.469	1.459	1.493	1.504	1.47
width: 2.533 cm	70	2.059	2.117	2.142	2.152	2.197	2.13
	70	439.838	438.832	438.354	438.718	437.868	438.72
J2-286	100	368.859	368.805	370.881	371.413	369.797	369.95
Core A3	150	322.158	322.574	317.979	319.613	319.194	320.30
	200	279.324	280.227	279.470	279.646	278.441	279.42
	250	255.609	254.216	251.834	254.330	251.736	253.54
	300	233.886	233.420	232.187	233.161	232.871	233.10
	350	213.140	211.920	212.417	211.869	214.545	212.78
	400	196.954	196.538	195.662	195.956	194.888	196.00
	350	203.158	203.336	202.614	202.411	203.359	202.98
	300	215.031	215.563	214.968	215.484	214.721	215.15
	250	230.742	232.038	230.680	231.189	230.912	231.11
	200	249.850	248.087	249.670	249.983	250.200	249.56
	150	274.082	272.449	273.810	273.139	274.139	273.52
length: 5.280 cm	100	302.767	302.318	304.170	307.748	303.678	304.13
width: 2.525 cm	70	325.777	326.183	326.831	328.068	331.561	327.68

J2-286 Core C2-1	70	0.917	0.896	0.865	0.862	0.916	0.89
	100	0.910	0.906	0.869	0.864	0.882	0.89
	150	0.853	0.808	0.839	0.882	0.889	0.85
	200	0.807	0.858	0.851	0.834	0.818	0.83
	250	0.880	0.827	0.859	0.839	0.811	0.84
	300	0.814	0.820	0.829	0.793	0.817	0.81
	350	0.783	0.778	0.754	0.786	0.791	0.78
	400	0.766	0.769	0.789	0.774	0.743	0.77
	350	0.786	0.753	0.797	0.785	0.761	0.78
	300	0.789	0.819	0.793	0.803	0.822	0.81
	250	0.781	0.773	0.824	0.811	0.836	0.80
	200	0.823	0.777	0.789	0.810	0.825	0.80
	150	0.855	0.847	0.833	0.783	0.852	0.83
length: 1.960 cm	100	0.878	0.828	0.826	0.844	0.830	0.84
width: 2.520 cm	70	0.915	0.863	0.865	0.902	0.890	0.89
J2-286 Core C2-2	70	1.376	1.316	1.320	1.341	1.398	1.35
	100	1.385	1.308	1.357	1.322	1.335	1.34
	150	1.258	1.268	1.254	1.228	1.278	1.26
	200	1.243	1.280	1.242	1.282	1.250	1.26
	250	1.211	1.218	1.202	1.209	1.227	1.21
	300	1.198	1.172	1.216	1.178	1.198	1.19
	350	1.215	1.167	1.222	1.170	1.189	1.19
	400	1.140	1.179	1.218	1.139	1.199	1.17
	350	1.236	1.204	1.220	1.244	1.222	1.23
	300	1.252	1.228	1.224	1.254	1.258	1.24
	250	1.355	1.308	1.356	1.335	1.368	1.34
	200	1.326	1.353	1.358	1.366	1.389	1.36
	150	1.394	1.360	1.357	1.342	1.356	1.36
length: 3.137 cm	100	1.372	1.391	1.390	1.341	1.354	1.37
width: 2.530 cm	70	1.391	1.372	1.392	1.380	1.396	1.39
J2-286 Core C3-1	70	185.271	185.176	184.815	184.534	185.821	185.12
	100	175.694	176.695	177.123	177.993	177.633	177.03
	150	170.851	170.930	171.989	171.571	171.891	171.45
	200	163.143	162.622	162.664	162.877	163.017	162.86
	250	152.794	153.467	153.257	152.485	152.454	152.89
	300	145.672	145.911	145.358	147.131	145.947	146.00
	350	141.506	142.266	141.051	140.182	141.250	141.25
	400	139.136	138.557	138.575	137.348	137.831	138.29
	350	139.164	138.605	138.142	139.521	138.503	138.79
	300	140.467	141.136	140.875	139.761	141.474	140.74
	250	143.716	142.803	142.978	143.609	143.316	143.28
	200	148.219	147.587	149.246	148.690	148.001	148.35
	150	157.364	157.677	158.338	156.804	157.850	157.61
length: 1.320 cm	100	172.424	173.504	171.991	174.596	173.699	173.24
width: 2.517 cm	70	179.532	180.064	178.833	179.368	179.895	179.54
J2-286 Core C3-2	70	57.872	58.003	58.184	57.857	58.008	57.98
	100	54.417	54.526	54.147	54.344	54.146	54.32
	150	51.471	51.068	51.131	51.274	51.009	51.19
	200	49.982	49.641	50.102	50.041	49.565	49.87
	250	48.993	49.000	49.006	48.933	48.843	48.95
	300	48.733	48.869	48.828	48.586	48.664	48.74
	350	48.353	48.706	48.272	48.409	48.049	48.36
	400	48.325	48.453	48.062	48.091	48.338	48.25
	350	48.485	48.209	48.405	48.261	48.379	48.35
	300	48.409	48.490	48.171	48.187	48.509	48.35
	250	48.651	48.433	48.269	48.533	48.379	48.45
	200	48.541	48.464	48.362	48.587	48.740	48.54
	150	48.790	48.988	48.960	48.943	48.764	48.89
length: 2.166 cm	100	49.496	49.097	49.544	49.443	49.586	49.43
width: 2.530 cm	70	50.230	50.391	50.858	50.457	50.515	50.49
J2-286 Core C4	70	22.544	22.713	22.845	22.920	22.557	22.72
	100	21.136	21.159	21.172	21.031	21.045	21.11
	150	19.479	19.738	19.524	19.533	19.430	19.54
	200	18.737	18.829	18.635	18.738	18.771	18.74
	250	18.234	18.215	18.267	18.179	18.180	18.21
	300	17.665	17.724	17.912	17.633	17.797	17.75

	350	17.335	17.286	17.239	17.272	17.215	17.27
	400	16.973	16.987	16.979	17.125	17.064	17.03
	350	17.282	17.309	17.257	17.237	17.223	17.26
	300	17.364	17.347	17.315	17.350	17.350	17.35
	250	17.551	17.581	17.392	17.502	17.455	17.50
	200	17.513	17.635	17.770	17.751	17.659	17.67
	150	18.164	18.117	18.011	18.113	18.096	18.10
length: 2.242 cm	100	18.457	18.419	18.517	18.750	18.636	18.56
width: 2.534 cm	70	19.155	19.191	19.282	19.340	19.185	19.23
	70	2775.457	2753.390	2750.327	2750.043	2751.290	2756.08
ALV 2608-3-3	100	2731.965	2741.756	2748.601	2744.529	2743.458	2742.06
Core B2	150	2737.428	2746.376	2745.481	2743.131	2740.446	2742.57
	200	2739.747	2742.163	2747.917	2754.997	2738.889	2744.74
	250	2738.028	2745.671	2739.575	2742.961	2739.434	2741.13
	300	2731.569	2730.212	2744.337	2739.639	2739.495	2737.05
	350	2742.793	2747.108	2741.122	2746.627	2745.311	2744.59
	400	2743.230	2749.732	2743.436	2747.952	2746.149	2746.10
	350	2751.994	2753.703	2750.475	2750.154	2745.641	2750.39
	300	2748.038	2748.589	2752.861	2748.051	2753.687	2750.24
	250	2752.909	2757.370	2756.729	2754.918	2752.377	2754.86
	200	2752.351	2752.451	2759.157	2759.967	2753.436	2755.47
	150	2760.591	2762.581	2754.112	2754.220	2762.390	2758.78
length: 3.127 cm	100	2765.729	2766.051	2765.017	2764.154	2768.542	2765.90
width: 2.500 cm	70	2774.483	2772.973	2767.481	2773.497	2771.457	2771.98
	70	1463.134	1458.002	1452.060	1453.063	1455.805	1456.41
ALV 2608-3-3	100	1445.711	1447.873	1450.619	1446.636	1448.560	1447.88
Core C1	150	1442.011	1447.001	1448.876	1445.477	1447.688	1446.21
	200	1441.697	1444.850	1449.962	1444.873	1444.956	1445.27
	250	1443.511	1446.972	1446.920	1447.800	1446.114	1446.26
	300	1447.954	1446.510	1446.235	1445.371	1449.270	1447.07
	350	1438.684	1433.104	1441.381	1435.182	1436.227	1436.91
	400	1435.555	1439.549	1436.163	1435.085	1436.500	1436.57
	350	1438.654	1441.551	1435.478	1439.569	1440.906	1439.23
	300	1443.227	1443.663	1441.331	1439.345	1443.221	1442.16
	250	1444.857	1444.730	1445.591	1448.387	1446.511	1446.01
	200	1442.243	1451.638	1451.012	1449.685	1446.193	1448.15
	150	1450.345	1443.050	1448.496	1450.353	1455.514	1449.55
length: 2.092 cm	100	1457.652	1456.714	1456.325	1456.357	1454.295	1456.27
width: 2.496 cm	70	1456.331	1458.631	1458.978	1453.156	1459.316	1457.28
	70	896.556	896.976	898.147	898.717	899.208	897.92
ALV 2608-4-1	100	867.383	866.905	866.397	865.442	865.227	866.27
Pc 1	150	817.947	818.801	817.289	816.501	817.137	817.53
Core A1	200	789.223	789.364	786.787	787.071	786.689	787.83
	250	764.867	763.899	762.535	761.835	761.444	762.91
	300	742.977	741.256	740.065	740.453	738.363	740.62
	350	724.113	723.107	722.998	722.381	720.703	722.66
	400	707.246	706.542	705.728	706.282	706.539	706.47
	350	727.239	726.888	727.994	726.880	727.698	727.34
	300	729.733	728.912	729.021	728.698	729.093	729.09
	250	731.548	732.563	731.056	731.892	732.966	732.00
	200	738.577	738.613	741.350	740.166	741.369	740.01
	150	753.186	755.743	754.947	756.566	756.635	755.41
length: 5.837 cm	100	775.990	778.436	779.024	780.261	782.365	779.21
width: 2.525 cm	70	806.146	805.729	806.593	807.904	806.143	806.59
	70	688.516	687.165	687.920	687.060	687.454	687.62
ALV 2608-4-1	100	626.401	625.620	626.065	625.729	626.057	625.97
Pc 1	150	565.271	563.772	564.854	564.410	563.430	564.35
Core C1-1	200	531.547	529.972	529.863	529.831	528.912	530.02
	250	507.096	505.348	505.012	504.579	505.245	505.46
	300	486.959	486.771	486.493	486.415	486.727	486.67
	350	472.222	472.311	471.721	471.045	471.964	471.85
	400	462.210	461.304	461.877	459.981	459.623	461.00
	350	461.322	462.435	460.961	461.092	461.560	461.47
	300	465.128	464.707	465.331	464.802	465.701	465.13
	250	471.508	471.021	471.629	472.336	471.264	471.55
	200	482.808	483.077	482.236	483.054	482.665	482.77

	150	499.925	500.524	500.881	502.33	501.495	501.03
length: 3.065 cm	100	521.467	524.551	524.605	525.327	526.720	524.53
width: 2.509 cm	70	561.461	561.304	562.272	563.991	563.512	562.51
	70	1216.045	1215.732	1213.889	1216.707	1215.771	1215.63
ALV 2608-4-1	100	1120.904	1123.993	1121.756	1119.734	1121.623	1121.60
Pc 1	150	906.933	906.388	901.331	899.625	895.604	901.97
Core C1-2	200	764.156	759.042	757.380	756.200	753.009	757.95
	250	699.274	696.941	696.618	693.279	691.497	695.52
	300	658.984	655.809	655.071	652.304	653.557	655.14
	350	631.545	628.861	626.538	625.844	625.439	627.64
	400	608.057	604.984	604.253	604.479	602.626	604.88
	350	605.383	606.724	606.127	607.145	607.159	606.51
	300	611.158	611.741	612.523	612.120	612.056	611.92
	250	622.744	623.083	623.475	624.587	623.818	623.54
	200	643.272	642.737	644.052	645.296	643.215	643.71
	150	689.997	691.249	691.977	694.575	694.760	692.51
length: 2.290 cm	100	891.962	895.011	894.468	898.358	897.427	895.44
width: 2.507 cm	70	1029.031	1030.583	1037.165	1038.347	1041.383	1035.29
	70	65.612	65.701	66.047	66.003	66.088	65.89
ALV 2608-4-1	100	50.870	50.897	50.050	49.872	49.925	50.32
Pc 1	150	33.167	32.813	32.663	32.342	32.540	32.70
Core C3-1	200	28.195	28.094	28.046	27.989	28.271	28.12
	250	25.814	25.792	25.413	25.565	25.531	25.62
	300	24.232	24.100	24.129	23.964	24.043	24.09
	350	23.103	23.010	23.035	22.902	22.738	22.96
	400	22.234	22.279	22.225	22.048	22.126	22.18
	350	22.072	22.228	22.090	22.058	22.045	22.10
	300	22.305	22.412	22.233	22.292	22.361	22.32
	250	22.753	22.720	22.656	22.723	22.659	22.70
	200	23.241	23.474	23.517	23.434	23.487	23.43
	150	24.424	24.281	24.413	24.304	24.365	24.36
length: 2.418 cm	100	26.602	26.715	26.771	27.041	27.067	26.84
width: 2.527 cm	70	31.478	31.649	31.923	32.216	32.175	31.89
	70	152.548	153.826	153.471	152.733	152.695	153.05
ALV 2608-4-1	100	143.532	143.134	142.886	143.198	143.432	143.24
Pc 1	150	129.816	129.970	128.495	129.211	129.192	129.34
Core C3-2	200	121.013	120.525	119.597	119.728	120.566	120.28
	250	116.661	116.270	115.177	115.239	115.594	115.79
	300	112.540	111.717	111.127	111.282	111.681	111.67
	350	109.451	109.660	109.507	108.238	108.776	109.13
	400	107.546	106.507	106.784	106.999	106.847	106.94
	350	106.965	106.933	106.814	106.606	107.050	106.87
	300	107.517	107.744	107.927	107.386	107.053	107.52
	250	108.685	108.798	109.097	109.083	108.651	108.86
	200	109.423	109.883	109.927	110.276	109.443	109.79
	150	112.635	111.964	112.391	112.891	111.999	112.38
length: 2.510 cm	100	116.529	116.925	116.771	117.305	117.213	116.95
width: 2.521 cm	70	122.204	123.230	122.953	122.782	123.312	122.90
	70	2158.586	2160.634	2150.079	2155.145	2155.342	2155.95
ALV 2608-4-1	100	2117.367	2118.967	2122.166	2118.778	2117.902	2119.04
Pc 2	150	2078.473	2076.012	2078.963	2077.895	2079.105	2078.09
Core A3	200	2058.356	2054.582	2053.041	2057.866	2056.394	2056.05
	250	2033.135	2035.371	2033.287	2035.131	2030.017	2033.39
	300	2018.604	2018.276	2018.204	2011.120	2018.273	2016.89
	350	2008.257	2003.031	2007.057	2005.383	2002.057	2005.16
	400	1998.369	1992.994	1992.567	1996.343	1992.010	1994.46
	350	1995.646	2002.980	1993.761	1996.911	1997.206	1997.30
	300	2004.977	2005.856	2002.877	1998.372	2001.253	2002.67
	250	2011.009	2007.989	2009.560	2008.058	2009.620	2009.25
	200	2016.218	2011.387	2019.708	2018.907	2018.761	2016.99
	150	2032.558	2032.535	2034.127	2037.122	2036.817	2034.63
length: 6.080 cm	100	2052.597	2047.541	2050.089	2053.481	2055.181	2051.78
width: 2.509 cm	70	2068.562	2070.288	2074.816	2073.704	2075.763	2072.62
	70	637.687	637.757	637.307	637.212	638.616	637.72
ALV 2608-4-1	100	617.302	617.913	616.512	616.752	616.063	616.91
Pc 2	150	585.157	584.219	584.435	583.017	582.860	583.94

Core B3	200	562.977	561.826	562.064	560.452	560.423	561.55
	250	549.962	549.006	547.481	549.622	547.318	548.68
	300	539.826	539.616	537.957	537.254	536.649	538.26
	350	531.319	530.001	530.137	529.579	528.636	529.93
	400	523.424	523.514	522.722	522.516	522.860	523.01
	350	523.633	524.508	523.441	523.700	523.315	523.72
	300	525.251	524.845	525.165	525.892	525.743	525.38
	250	529.684	529.349	529.007	529.828	529.732	529.52
	200	534.243	533.983	534.272	533.413	533.591	533.90
	150	542.806	543.046	544.963	544.414	543.595	543.76
length: 2.768 cm	100	557.040	562.183	560.094	563.664	563.511	561.29
width: 2.513 cm	70	577.601	577.669	577.834	577.198	578.211	577.70
	70	6366.8	--	--	--	--	6366.8
ALV 2608-4-1	100	5838.7	--	--	--	--	5838.7
Pc 2	150	5607.6	--	--	--	--	5607.6
Core 1	200	5475.2	--	--	--	--	5475.2
	250	5216.6	--	--	--	--	5216.6
	300	5051.5	--	--	--	--	5051.5
	350	5000.4	--	--	--	--	5000.4
	400	4953.8	--	--	--	--	4953.8
	70	927.5	--	--	--	--	927.5
ALV 2608-4-1	100	862.5	--	--	--	--	862.5
Pc 2	150	768.4	--	--	--	--	768.4
Core 2	200	661.4	--	--	--	--	661.4
	250	620.5	--	--	--	--	620.5
	300	578.5	--	--	--	--	578.5
	350	546.8	--	--	--	--	546.8
	400	519.7	--	--	--	--	519.7
	70	2989.3	--	--	--	--	2989.3
ALV 2608-4-1	100	2522.4	--	--	--	--	2522.4
Pc 2	150	1329.1	--	--	--	--	1329.1
Core 4	200	962.2	--	--	--	--	962.2
	250	824.0	--	--	--	--	824.0
	300	686.7	--	--	--	--	686.7
	350	600.3	--	--	--	--	600.3
	400	516.4	--	--	--	--	516.4
	70	314.626	313.346	312.126	310.303	309.883	312.05
JAS 177-2-1	100	243.739	243.397	243.349	243.099	243.725	243.46
Core A2	150	215.481	214.521	214.077	213.719	213.385	214.24
	200	199.998	198.496	198.091	198.303	197.660	198.51
	250	187.728	186.088	184.883	184.316	184.134	185.42
	300	171.939	170.666	170.140	169.900	169.130	170.35
	350	160.626	159.590	159.027	159.089	157.934	159.25
	400	153.294	152.328	152.055	151.545	151.417	152.13
	350	152.204	152.165	152.138	152.092	151.725	152.06
	300	154.280	154.130	153.832	154.500	153.939	154.14
	250	160.107	160.671	160.192	160.762	160.773	160.50
	200	168.698	170.030	169.869	170.306	170.118	169.80
	150	185.603	187.132	187.371	187.428	187.657	187.04
length: 2.218 cm	100	199.953	200.603	200.621	201.397	200.972	200.71
width: 2.514 cm	70	218.030	218.950	220.015	220.015	220.404	219.48
	70	1970.679	1967.907	1952.082	1946.331	1966.707	1960.72
JAS 177-2-1	100	1938.225	1938.673	1933.839	1934.105	1937.615	1936.49
Core B1	150	1870.491	1868.112	1866.645	1863.640	1864.134	1866.60
	200	1829.610	1826.120	1826.484	1826.328	1829.966	1827.70
	250	1798.435	1794.460	1794.601	1797.557	1793.888	1795.79
	300	1775.321	1774.622	1775.426	1776.324	1772.495	1774.84
	350	1756.224	1755.267	1755.827	1757.025	1759.920	1756.85
	400	1746.502	--	1748.644	1745.181	1743.343	1745.92
	350	1745.179	1751.080	1751.198	1751.386	1752.148	1750.20
	300	1759.851	1754.367	1758.087	1756.928	1754.947	1756.83
	250	1767.359	1765.442	1770.256	1770.705	1768.686	1768.49
	200	1784.591	1789.792	1783.725	1785.145	1790.641	1786.78
	150	1809.819	1811.795	1807.653	1810.306	1808.277	1809.57
length: 4.716 cm	100	1844.081	1850.868	1848.891	1847.695	1850.864	1848.48
width: 2.530 cm	70	1890.155	1892.118	1896.345	1890.910	1895.441	1892.99

	70	3091.102	3084.953	3090.156	3075.858	3079.055	3084.22
JAS 177-2-1 Core B2	100	3061.865	3053.692	3064.990	3061.396	3060.384	3060.46
	150	3025.202	3031.239	3015.798	3036.012	3017.584	3025.16
	200	3009.429	2990.444	2997.535	2998.335	2997.086	2998.56
	250	2972.199	2972.043	2975.953	2970.287	2973.411	2972.78
	300	2963.910	2950.067	2955.262	2949.312	2952.282	2954.16
	350	2946.318	2924.595	2944.733	2941.581	2927.182	2936.87
	400	2895.997	2900.238	2900.880	2898.089	2897.285	2898.50
	350	2895.263	2896.184	2896.945	2900.734	2901.119	2898.05
	300	2890.881	2894.065	2901.886	2895.291	2897.104	2895.84
	250	2900.340	2914.090	2904.944	2903.531	2903.011	2905.18
	200	2900.255	2902.641	2910.156	2904.491	2904.085	2904.32
	150	2910.503	2900.946	2915.379	2908.103	2909.121	2908.81
length: 3.940 cm	100	2908.726	2911.321	2904.708	2910.646	2913.575	2909.79
width: 2.490 cm	70	2915.579	2907.889	2912.434	2912.921	2914.079	2912.58
	70	227.249	226.566	226.662	226.368	226.327	226.63
JAS 177-2-1 Core C2	100	217.294	217.596	217.714	216.642	217.136	217.28
	150	203.239	202.206	202.509	202.303	201.895	202.43
	200	194.519	193.915	194.100	193.986	194.010	194.11
	250	192.707	192.840	192.731	192.418	192.439	192.63
	300	191.615	192.347	192.282	192.324	192.058	192.13
	350	191.594	191.662	191.394	191.861	191.618	191.63
	400	191.821	191.713	191.999	191.959	191.851	191.87
	350	192.400	192.625	192.448	192.009	191.940	192.28
	300	192.295	192.829	192.629	192.629	192.562	192.59
	250	192.588	192.607	192.874	193.428	192.696	192.84
	200	193.275	193.233	193.118	192.832	193.428	193.18
	150	194.036	194.147	194.058	193.834	194.526	194.12
length: 1.684 cm	100	198.135	198.350	198.803	198.659	198.840	198.56
width: 2.494 cm	70	204.538	205.062	205.519	206.114	205.927	205.43
	70	705.981	700.726	699.559	700.027	702.002	701.66
ALV 2179-1-1 Core A1	100	668.923	669.453	667.615	668.482	667.635	668.42
	150	632.466	631.657	628.528	631.155	628.174	630.39
	200	607.264	604.945	604.588	604.883	603.348	605.00
	250	588.086	588.087	589.624	585.678	586.983	587.69
	300	575.528	576.449	575.717	575.843	576.054	575.92
	350	565.491	565.159	566.121	564.705	566.500	565.59
	400	560.223	561.459	560.019	561.083	560.965	560.75
	350	560.110	561.736	561.288	560.340	562.180	561.13
	300	563.446	565.603	566.188	565.287	565.028	565.11
	250	569.144	568.900	569.277	569.405	569.993	569.34
	200	576.223	576.950	576.691	576.831	576.685	576.68
	150	589.704	586.060	588.477	590.419	588.755	588.68
length: 1.227 cm	100	610.599	610.206	610.488	608.705	609.243	609.85
width: 2.500 cm	70	636.543	633.144	637.494	637.501	638.534	636.64
	70	1174.117	1170.142	1168.271	1159.571	1163.192	1167.05
ALV 2179-1-1 Core A2	100	1151.085	1143.705	1144.000	1151.837	1152.335	1148.59
	150	1130.405	1127.753	1126.114	1119.097	1126.485	1125.96
	200	1111.778	1103.340	1104.392	1105.404	1108.562	1106.69
	250	1092.732	1095.101	1091.446	1093.232	1096.337	1093.77
	300	1079.162	1075.249	1080.424	1077.993	1082.638	1079.09
	350	1069.860	1070.511	1070.050	1065.363	1066.531	1068.46
	400	1060.841	1063.095	1064.589	1063.225	1061.767	1062.70
	350	1067.572	1065.166	1063.086	1063.529	1065.070	1064.88
	300	1067.695	1069.764	1071.156	1064.323	1070.163	1068.62
	250	1073.940	1074.398	1079.232	1073.927	1078.135	1075.92
	200	1081.777	1087.969	1085.055	1085.629	1078.521	1083.79
	150	1094.489	1093.103	1096.476	1095.134	1097.036	1095.25
length: 1.512 cm	100	1118.171	1111.254	1116.128	1113.354	1117.432	1115.26
width: 2.477 cm	70	1129.681	1126.553	1127.663	1136.349	1136.837	1131.41
	70	1068.020	1058.076	1045.073	1038.420	1041.216	1050.10
ALV 2179-1-1 Core A3	100	1001.936	1004.255	1003.405	1002.527	1002.657	1002.96
	150	955.274	954.003	961.515	956.513	955.928	956.64
	200	926.327	928.599	930.027	924.891	929.664	927.90
	250	907.391	907.141	904.837	904.037	904.137	905.51
	300	890.551	887.398	888.108	884.158	886.297	887.30

	350	876.486	879.913	874.105	872.965	873.598	875.41
	400	866.835	861.410	860.928	863.097	863.697	863.19
	350	862.285	861.886	862.434	863.646	863.059	862.66
	300	864.469	862.581	861.663	864.585	864.191	863.50
	250	867.398	864.946	869.532	867.521	868.132	867.50
	200	871.760	875.320	873.618	876.510	875.317	874.50
	150	884.081	883.647	881.405	887.031	883.500	883.93
length: 1.575 cm	100	901.256	902.294	905.432	904.437	909.051	904.49
width: 2.464 cm	70	926.343	927.987	927.487	928.065	924.423	926.86
	70	1525.934	1514.922	1517.709	1510.970	1513.303	1516.56
ALV 2179-1-1	100	1514.446	1509.204	1512.182	1510.386	1512.859	1511.81
Core B2	150	1496.321	1496.147	1505.554	1504.492	1502.829	1501.06
	200	1486.043	1486.640	1484.575	1490.167	1489.973	1487.48
	250	1486.181	1487.855	1488.447	1480.940	1481.430	1484.97
	300	1480.368	1469.180	1479.771	1479.525	1473.946	1476.55
	350	1473.449	1474.968	1471.480	1462.585	1465.123	1469.51
	400	1461.807	1465.717	1461.805	1464.275	1459.899	1462.70
	350	1463.376	1465.393	1467.523	1470.742	1464.395	1466.28
	300	1467.562	1468.938	1471.480	1472.988	1465.040	1469.20
	250	1466.576	1475.790	1470.244	1470.892	1475.539	1471.80
	200	1475.733	1480.648	1481.299	1480.353	1475.737	1478.75
	150	1482.246	1492.937	1488.151	1484.985	1492.164	1488.09
length: 1.745 cm	100	1502.738	1500.069	1502.000	1500.531	1507.536	1502.57
width: 2.462 cm	70	1506.464	1504.310	1513.987	1511.296	1507.031	1508.61

A2.3 Zn-Rich Actively Diffusing Spire Data

Sample	**Confining Pressure (psi)**	**Permeability (× 10^{-15} m^2)**					**Mean *k* (× 10^{-15} m^2)**
		1	**2**	**3**	**4**	**5**	
	70	6658.693	6634.198	6647.273	6660.403	6615.598	6643.21
ALV 2187-1-1	100	6418.750	6459.792	6443.477	6407.970	6422.589	6430.49
top	150	6273.470	6294.516	6253.229	6222.046	6250.517	6258.71
Core A2	200	6143.058	6107.700	6089.478	6095.600	6119.273	6110.99
	250	5718.614	5724.019	5704.126	5688.041	5693.868	5705.72
	300	5489.469	5465.859	5448.458	5444.027	5463.568	5462.25
	350	5184.894	5158.181	5164.371	5144.300	5179.085	5166.15
	400	4866.193	4848.855	4827.966	4856.613	4837.185	4847.34
	350	4837.835	4862.168	4844.881	4843.998	4826.165	4843.00
	300	4865.125	4856.500	4828.098	4872.631	4846.817	4853.81
	250	4863.433	4848.015	4874.225	4877.266	4885.175	4869.61
	200	4904.051	4892.868	4894.393	4897.635	4884.070	4894.60
	150	4947.950	4955.104	4960.763	4962.010	4953.864	4955.94
length: 6.651 cm	100	5101.075	5111.217	5113.377	5117.133	5117.612	5112.08
width: 2.432 cm	70	5322.470	5322.604	5332.163	5321.283	5362.200	5332.12
	70	5464.986	5454.037	5454.414	5457.863	5443.817	5455.02
ALV 2187-1-1	100	5089.999	5088.461	5063.909	5090.543	5071.230	5080.82
top	150	4462.106	4436.251	4428.860	4450.549	4426.879	4440.91
Core A4	200	4024.770	4011.834	4016.522	4013.390	4000.665	4013.43
	250	3748.715	3750.129	3724.418	3736.529	3728.493	3737.64
	300	3453.819	3435.185	3427.603	3429.893	3422.233	3433.73
	350	3194.177	3191.114	3191.965	3185.809	3187.799	3190.17
	400	3051.050	3035.666	3034.977	3036.078	3032.541	3038.06
	350	3042.999	3041.468	3046.138	3037.374	3041.231	3041.84
	300	3052.491	3058.457	3052.810	3054.882	3045.474	3052.82
	250	3079.161	3078.357	3081.139	3080.152	3075.068	3078.78
	200	3106.480	3125.637	3114.953	3108.371	3116.355	3114.35
	150	3163.085	3165.285	3173.283	3171.776	3178.269	3170.34
length: 6.024 cm	100	3271.145	3277.183	3271.104	3281.492	3289.930	3278.16
width: 2.495 cm	70	3458.879	3479.281	3475.734	3485.555	3476.950	3475.27

ALV 2187-1-1 top Core B1	70	673.124	673.574	674.065	673.891	673.245	673.58
	100	647.683	648.026	647.596	646.852	647.080	647.45
	150	625.481	627.033	625.168	625.663	626.138	625.90
	200	613.799	612.555	613.447	612.524	613.269	613.12
	250	605.890	603.320	603.405	604.322	602.242	603.84
	300	598.343	595.344	596.529	595.351	595.937	596.30
	350	587.025	587.556	586.550	587.527	586.300	586.99
	400	578.367	579.063	579.034	577.706	578.807	578.60
	350	586.918	584.827	585.416	585.430	586.088	585.74
	300	586.072	586.117	586.576	586.347	586.644	586.35
	250	587.667	588.823	587.651	588.330	588.678	588.23
	200	590.941	590.748	590.349	589.770	589.839	590.33
	150	592.478	592.742	594.068	593.994	592.840	593.22
length: 2.794 cm	100	601.329	600.609	601.416	601.163	600.768	601.06
width: 2.480 cm	70	608.343	609.077	609.515	609.809	609.286	609.21
ALV 2187-1-1 bottom Core A2	70	365.869	365.868	365.202	364.965	365.288	365.44
	100	351.325	351.426	350.591	350.704	350.912	350.99
	150	346.152	344.936	345.713	344.632	345.332	345.35
	200	341.200	339.891	339.690	339.820	340.311	340.18
	250	337.509	337.609	338.225	337.200	336.998	337.51
	300	333.788	332.344	332.836	332.474	333.009	332.89
	350	329.595	327.310	328.439	326.958	327.074	327.87
	400	323.466	322.475	322.592	322.354	322.315	322.64
	350	321.918	321.720	321.483	322.910	322.551	322.12
	300	321.879	322.354	321.920	322.315	322.593	322.21
	250	322.751	322.909	322.908	323.107	322.672	322.87
	200	323.267	323.385	324.062	323.781	323.782	323.66
	150	325.133	324.496	325.333	325.175	324.973	325.02
length: 2.740 cm	100	326.678	326.757	326.999	327.081	327.159	326.94
width: 2.475 cm	70	330.823	330.212	330.663	330.820	330.692	330.64
ALV 2187-1-1 bottom Core B1	70	611.896	610.913	609.773	611.338	611.318	611.05
	100	602.279	601.234	600.740	601.304	600.028	601.12
	150	601.540	600.727	600.296	601.416	601.334	601.06
	200	590.933	590.068	589.403	590.609	590.814	590.37
	250	587.381	587.356	586.569	587.045	587.980	587.27
	300	585.562	581.415	579.607	581.503	580.664	581.75
	350	569.371	569.472	568.369	568.566	568.271	568.81
	400	557.653	558.729	558.322	557.115	556.101	557.58
	350	557.564	558.058	556.591	559.534	557.385	557.83
	300	558.220	557.903	558.217	557.629	558.164	558.03
	250	559.231	559.124	559.488	559.733	559.885	559.49
	200	561.918	561.494	562.017	561.046	561.139	561.52
	150	565.273	565.853	565.031	565.017	564.827	565.20
length: 2.965 cm	100	571.239	571.772	572.116	571.720	573.064	571.98
width: 2.442 cm	70	585.463	587.131	587.116	585.725	586.895	586.47
ALV 2187-1-1 bottom Core C2	70	791.755	786.102	780.691	779.569	777.559	783.12
	100	717.446	715.924	713.050	714.491	712.367	714.65
	150	653.611	652.412	651.068	650.171	651.004	651.65
	200	620.161	620.583	618.088	617.581	617.891	618.86
	250	585.333	585.505	584.412	583.198	583.220	584.33
	300	552.704	551.313	551.195	550.456	549.579	551.05
	350	534.617	533.710	533.415	533.906	531.364	533.40
	400	524.726	524.236	523.658	523.092	523.323	523.81
	350	527.388	527.134	526.865	527.189	526.934	527.10
	300	533.242	532.383	533.746	533.127	532.897	533.08
	250	548.661	549.299	549.998	549.034	550.641	549.53
	200	575.126	575.146	575.378	575.447	576.053	575.43
	150	598.799	597.958	599.635	599.288	599.561	599.05
length: 2.478 cm	100	626.535	627.167	628.327	628.025	628.088	627.63
width: 2.447 cm	70	666.393	668.601	670.173	672.646	673.679	670.29
ALV 2187-1-1 bottom Core C3	70	2390.832	2394.769	2391.943	2391.364	2386.087	2391.00
	100	2229.503	2238.901	2236.241	2230.430	2231.651	2233.34
	150	1920.621	1919.462	1920.579	1919.042	1919.275	1919.80
	200	1716.540	1710.463	1711.330	1704.299	1705.228	1709.57
	250	1585.536	1579.598	1578.021	1580.419	1575.392	1579.79
	300	1472.483	1468.573	1467.364	1468.029	1463.081	1467.90

	350	1374.552	1372.525	1372.810	1372.698	1371.127	1372.74
	400	1310.287	1307.153	1305.305	1303.090	1304.962	1306.16
	350	1313.565	1312.338	1313.761	1315.505	1311.901	1313.41
	300	1330.704	1330.012	1330.236	1331.817	1329.345	1330.42
	250	1353.095	1355.069	1353.224	1352.598	1356.551	1354.12
	200	1389.235	1391.053	1388.257	1391.331	1389.777	1389.93
	150	1462.509	1467.587	1467.341	1466.474	1464.415	1465.66
length: 3.667 cm	100	1575.883	1579.610	1584.316	1582.993	1583.849	1581.34
width: 2.436 cm	70	1709.974	1721.917	1721.646	1722.105	1728.448	1720.81
	70	2053.057	2043.485	2045.464	2038.471	2039.839	2044.06
ALV 2187-1-2	100	1965.943	1965.456	1967.274	1957.973	1960.378	1963.40
Core B2-2	150	1873.752	1870.951	1869.170	1872.658	1868.326	1870.97
	200	1821.789	1817.582	1816.586	1814.126	1819.072	1817.83
	250	1780.053	1777.586	1775.811	1774.120	1770.384	1775.59
	300	1749.693	1749.818	1746.469	1748.199	1749.101	1748.66
	350	1724.736	1722.605	1717.374	1719.834	1719.346	1720.78
	400	1706.849	1700.644	1705.806	1701.737	1704.904	1703.99
	350	1703.419	1709.374	1706.026	1705.268	1708.658	1706.55
	300	1714.077	1712.685	1714.719	1713.653	1712.418	1713.51
	250	1721.502	1725.038	1726.570	1724.646	1723.657	1724.28
	200	1741.544	1741.158	1741.700	1739.671	1740.626	1740.94
	150	1769.830	1768.003	1770.611	1769.227	1773.456	1770.22
length: 5.090 cm	100	1809.971	1812.796	1814.133	1815.299	1812.812	1813.00
width: 2.505 cm	70	1848.943	1851.607	1854.164	1855.480	1857.298	1853.50
	70	2570.160	2564.665	2557.726	2556.054	2556.365	2560.99
ALV 2187-1-2	100	2322.046	2331.406	2321.569	2316.916	2312.604	2320.90
Core C1/C2	150	2036.488	2028.397	2015.765	2013.981	2017.506	2022.41
	200	1825.819	1814.865	1817.392	1805.431	1804.858	1813.66
	250	1714.092	1711.153	1703.415	1702.178	1699.311	1706.02
	300	1631.547	1620.510	1615.895	1615.181	1614.123	1619.44
	350	1535.403	1529.162	1527.549	1525.628	1526.478	1528.84
	400	1481.106	1481.151	1475.803	1473.265	1471.254	1476.51
	350	1478.379	1477.540	1479.896	1478.808	1479.017	1478.73
	300	1486.552	1494.595	1488.903	1488.405	1489.679	1489.62
	250	1504.517	1505.277	1506.644	1505.960	1504.932	1505.47
	200	1529.108	1531.267	1527.378	1527.238	1529.359	1528.87
	150	1572.720	1577.646	1576.818	1579.498	1579.233	1577.18
length: 4.129 cm	100	1668.730	1671.967	1674.676	1681.474	1678.630	1675.09
width: 2.501 cm	70	1802.936	1804.128	1805.008	1810.656	1809.913	1806.53
	70	2873.270	2874.319	2884.616	2875.474	2881.073	2877.75
ALV 2187-1-2	100	2813.558	2795.990	2797.338	2799.622	2800.578	2801.41
Core C3-1	150	2706.760	2702.048	2699.148	2710.673	2697.417	2703.21
	200	2662.886	2656.993	2650.832	2653.075	2662.862	2657.33
	250	2638.885	2641.291	2636.073	2650.564	2639.343	2641.23
	300	2610.208	2604.257	2601.112	2599.350	2595.320	2602.05
	350	2557.019	2560.456	2567.255	2564.812	2559.577	2561.82
	400	2536.088	2534.729	2534.466	2531.511	2535.595	2534.48
	350	2538.812	2537.077	2537.782	2547.550	2542.347	2540.71
	300	2547.013	2546.323	2547.534	2551.807	2550.151	2548.57
	250	2571.911	2570.396	2571.602	2568.317	2572.586	2570.96
	200	2597.356	2600.661	2599.309	2598.509	2593.172	2597.80
	150	2620.329	2632.859	2629.010	2630.108	2630.057	2628.47
length: 3.956 cm	100	2668.538	2677.377	2675.460	2683.174	2684.027	2677.71
width: 2.457 cm	70	2709.951	2710.512	2706.896	2703.079	2708.828	2707.85
	70	3014.635	3021.559	3013.237	3005.625	3008.864	3012.78
ALV 2187-1-2	100	2974.698	2962.377	2965.785	2965.236	2952.757	2964.16
Core C3-2	150	2918.221	2909.659	2907.224	2915.713	2913.263	2912.81
	200	2820.336	2812.317	2808.248	2802.994	2801.067	2808.98
	250	2728.292	2721.864	2729.989	2720.229	2717.634	2723.60
	300	2675.150	2665.897	2671.459	2669.562	2667.936	2670.00
	350	2624.841	2613.295	2621.782	2620.495	2610.187	2618.11
	400	2500.419	2509.405	2497.203	2499.830	2501.657	2501.70
	350	2507.529	2504.235	2506.410	2502.459	2501.885	2504.50
	300	2521.811	2520.099	2516.986	2525.968	2521.227	2521.22
	250	2545.396	2553.080	2547.827	2551.890	2545.883	2548.81
	200	2605.484	2604.343	2614.820	2612.951	2609.584	2609.43

	150	2684.300	2701.210	2678.866	2697.772	2688.202	2690.06
length: 4.577 cm width: 2.476 cm	100	2756.305	2762.373	2764.534	2764.815	2774.963	2764.59
	70	2811.845	2822.047	2816.914	2828.316	2817.335	2819.29
	70	1589.988	1585.115	1581.549	1581.513	1578.061	1583.24
ALV 2187-1-2	100	1547.349	1540.150	1541.063	1544.358	1538.944	1542.37
Core C5	150	1495.414	1493.658	1495.666	1492.305	1490.892	1493.59
	200	1464.224	1463.541	1459.424	1459.242	1458.175	1460.92
	250	1439.789	1439.702	1439.027	1435.324	1436.456	1438.06
	300	1427.848	1425.390	1428.353	1425.437	1424.568	1426.32
	350	1413.576	1410.049	1409.929	1410.628	1409.230	1410.68
	400	1402.651	1400.049	1404.196	1397.953	1398.337	1400.64
	350	1398.547	1401.294	1402.502	1400.428	1400.604	1400.67
	300	1402.060	1401.455	1402.867	1401.282	1403.408	1402.21
	250	1407.559	1405.717	1406.468	1408.343	1406.527	1406.92
	200	1409.308	1411.396	1415.603	1410.661	1412.148	1411.82
	150	1417.571	1418.858	1422.848	1419.707	1422.090	1420.21
length: 4.057 cm width: 2.498 cm	100	1430.934	1434.261	1434.630	1434.222	1437.987	1434.41
	70	1454.303	1456.951	1455.243	1458.775	1456.253	1456.30
	70	2973.918	3021.832	3010.906	2996.012	2991.406	2998.77
ALV 2190-14-1	100	2944.241	2938.886	2929.914	2935.051	2925.511	2934.71
Core A1	150	2856.352	2855.566	2849.235	2857.279	2858.189	2855.32
	200	2818.963	2792.367	2787.270	2808.706	2803.765	2802.19
	250	2761.914	2752.440	2756.411	2749.160	2750.822	2754.15
	300	2731.179	2721.361	2730.844	2721.069	2726.867	2726.26
	350	2702.120	2685.918	2683.075	2686.750	2689.219	2689.41
	400	2663.477	2666.785	2660.228	2656.789	2661.429	2661.74
	350	2660.531	2661.846	2665.738	2668.943	2665.905	2664.59
	300	2668.160	2671.661	2683.255	2668.623	2672.864	2672.91
	250	2680.921	2682.216	2671.167	2687.991	2681.303	2680.71
	200	2683.472	2699.381	2693.063	2695.860	2688.774	2692.10
	150	2712.889	2724.505	2720.169	2720.963	2722.109	2720.12
length: 4.092 cm width: 2.432 cm	100	2767.174	2761.987	2761.942	2752.062	2762.094	2761.05
	70	2806.584	2806.437	2812.775	2818.176	2810.866	2810.96
	70	1326.084	1324.667	1326.91	1324.362	1325.540	1325.51
ALV 2190-14-1	100	1293.923	1290.773	1293.516	1289.618	1291.403	1291.85
Core B1	150	1237.404	1238.509	1236.924	1235.336	1235.081	1236.65
	200	1197.635	1194.282	1195.743	1193.784	1196.212	1195.53
	250	1171.979	1166.251	1165.816	1163.120	1164.991	1166.43
	300	1141.489	1140.943	1139.700	1138.181	1139.682	1140.00
	350	1114.928	1114.051	1112.473	1111.070	1111.640	1112.83
	400	1077.912	1074.650	1072.130	1070.053	1071.944	1073.33
	350	1072.953	1072.714	1073.753	1074.515	1072.920	1073.37
	300	1080.058	1082.967	1082.756	1083.376	1081.254	1082.08
	250	1090.971	1091.904	1092.578	1090.932	1093.518	1092.00
	200	1105.202	1106.044	1104.796	1104.931	1106.889	1105.57
	150	1127.810	1126.441	1127.894	1131.825	1129.328	1128.66
length: 3.465 cm width: 2.424 cm	100	1157.947	1159.935	1158.272	1160.026	1158.969	1159.03
	70	1184.328	1188.537	1189.757	1186.858	1187.240	1187.34
	70	895.474	892.434	893.275	890.610	891.081	892.57
ALV 2190-14-1	100	841.627	840.347	838.936	840.498	839.484	840.18
Core B2	150	814.685	812.604	812.625	812.659	812.664	813.05
	200	800.295	797.031	797.708	797.254	796.089	797.67
	250	785.366	786.430	784.185	785.071	785.463	785.30
	300	777.269	775.055	773.698	775.912	773.809	775.15
	350	764.123	762.296	761.054	760.327	760.587	761.68
	400	761.137	761.409	761.987	761.543	759.557	761.13
	350	762.201	760.668	762.183	763.067	761.894	762.00
	300	762.946	764.798	764.291	763.791	763.240	763.81
	250	766.214	765.716	765.990	766.673	767.524	766.42
	200	768.932	769.642	771.186	771.332	770.700	770.36
	150	777.216	775.979	776.443	777.498	776.055	776.64
length: 2.589 cm width: 2.454 cm	100	789.111	790.522	789.860	791.936	788.725	790.03
	70	815.466	817.521	817.704	818.144	817.476	817.26
	70	48.031	48.061	48.516	48.342	48.260	48.24
J2-128-8-R1	100	42.051	41.772	41.590	41.755	41.249	41.68
Core Ex	150	34.502	34.227	34.327	34.104	33.915	34.21

	200	29.394	29.070	28.955	28.950	28.711	29.02
	250	25.110	25.219	24.952	25.028	24.925	25.05
	300	22.258	22.370	22.078	21.992	22.075	22.15
	350	19.926	19.947	19.838	19.910	19.885	19.90
	400	18.343	18.258	18.178	18.198	18.200	18.24
	350	18.238	18.453	18.302	18.310	18.264	18.31
	300	18.581	18.600	18.651	18.749	18.533	18.62
	250	19.228	19.086	19.111	19.294	19.155	19.18
	200	19.941	19.982	20.093	20.232	20.071	20.06
	150	21.567	21.631	21.832	21.740	21.872	21.73
length: 1.843 cm	100	24.848	24.806	24.917	24.903	24.999	24.89
width: 2.520 cm	70	28.186	28.550	28.403	28.378	28.423	28.39
	70	1404.659	1392.526	1395.073	1396.818	1396.285	1397.07
J2-137-7-R1	100	1342.322	1342.357	1336.218	1343.497	1335.839	1340.04
Core B1	150	1256.634	1256.966	1258.244	1248.551	1248.726	1253.82
	200	1182.514	1185.964	1181.748	1180.107	1177.953	1181.65
	250	1125.367	1115.682	1118.944	1117.250	1111.637	1117.77
	300	1071.498	1068.972	1070.685	1064.678	1066.365	1068.44
	350	1032.527	1033.833	1028.987	1023.033	1027.35	1029.14
	400	995.096	996.518	993.874	992.586	992.962	994.21
	350	989.032	985.626	987.055	985.332	985.554	986.52
	300	980.497	979.734	980.319	974.039	978.648	978.65
length: 1.484 cm	250	1028.438	1026.296	1028.114	1026.824	1027.870	1027.51
width: 2.448 cm	200	1028.818	1025.087	1024.395	1026.143	1023.439	1025.58
	70	539.667	537.693	537.644	537.108	535.084	537.44
J2-222-1-R1	100	477.871	477.220	477.769	477.648	476.834	477.47
Core A1	150	408.553	407.048	406.043	405.557	405.227	406.48
	200	369.819	368.017	367.551	366.957	366.442	367.76
	250	345.400	344.199	344.280	343.686	343.216	344.16
	300	328.027	327.560	327.244	327.182	326.733	327.35
	350	315.619	315.443	315.235	315.048	315.401	315.35
	400	306.789	305.558	305.780	305.321	305.418	305.77
	350	306.676	307.082	306.829	306.652	306.780	306.80
	300	308.676	309.305	308.883	309.058	308.742	308.93
	250	313.248	312.829	313.478	312.773	313.411	313.15
	200	319.856	319.454	319.672	320.050	319.365	319.68
	150	333.889	334.736	335.309	335.276	335.530	334.95
length: 1.950 cm	100	366.068	367.008	367.391	367.739	367.286	367.10
width: 2.464 cm	70	408.872	409.572	410.023	410.930	411.209	410.12
	70	235.586	236.242	236.405	236.890	237.164	236.46
J2-222-1-R1	100	235.479	235.351	235.426	235.760	234.925	235.39
Core A2	150	233.738	233.041	232.963	232.933	233.359	233.21
	200	231.267	231.263	231.408	231.073	231.444	231.29
	250	229.428	228.925	228.878	228.635	228.739	228.92
	300	228.046	227.621	227.514	227.470	227.763	227.68
	350	226.384	226.469	226.845	226.924	226.655	226.66
	400	226.434	225.923	225.873	225.686	225.688	225.92
	350	225.714	226.146	225.658	226.060	226.197	225.95
	300	226.297	226.293	225.654	226.325	226.090	226.13
	250	226.398	226.524	226.387	226.252	226.068	226.33
	200	226.812	226.675	226.816	226.478	227.306	226.82
	150	228.075	228.030	228.339	228.831	228.313	228.32
length: 1.804 cm	100	229.508	229.453	229.909	229.633	229.681	229.64
width: 2.448 cm	70	231.397	230.982	231.367	231.122	231.059	231.19
	70	396.525	395.562	394.641	393.563	392.870	394.63
J2-222-1-R1	100	312.058	310.730	309.699	309.771	309.639	310.38
Core Ex	150	242.285	240.943	240.563	240.235	240.096	240.82
	200	222.076	220.966	220.287	220.716	220.076	220.82
	250	210.763	210.271	210.243	210.367	209.981	210.33
	300	203.528	203.003	202.590	203.000	202.228	202.87
length: 1.596 cm	350	196.499	195.915	195.559	195.651	195.784	195.88
width: 2.448 cm	400	191.425	190.783	190.829	190.506	190.440	190.80
	350	191.086	191.163	190.916	191.078	191.148	191.09
	300	192.145	192.490	192.835	192.119	192.553	192.43
	250	195.059	194.718	194.706	194.841	194.867	194.84
	200	197.803	197.600	197.819	198.049	198.363	197.93

	150	203.855	203.511	203.486	203.662	203.712	203.65
length: 1.596 cm	100	224.762	225.510	225.887	225.821	226.498	225.70
width: 2.448 cm	70	306.431	309.564	311.021	311.245	311.614	309.97
	70	419.268	418.889	418.844	418.151	418.176	418.67
J2-127-1-R2	100	396.462	396.245	394.816	394.644	394.507	395.33
Core B2	150	386.220	385.491	384.394	384.030	384.261	384.88
	200	379.303	379.341	378.888	379.474	379.203	379.24
	250	375.339	374.431	374.877	373.708	374.028	374.48
	300	371.397	371.296	370.883	370.664	371.020	371.05
	350	368.489	367.497	367.715	367.851	368.245	367.96
	400	366.314	366.514	365.369	365.801	366.725	366.14
	350	366.209	366.207	366.324	366.244	366.382	366.27
	300	366.527	367.456	366.700	367.057	366.920	366.93
	250	367.664	368.929	367.666	368.053	368.377	368.14
	200	368.933	369.365	368.761	369.027	369.278	369.07
	150	371.371	371.819	372.181	371.295	371.878	371.71
length: 3.146 cm	100	374.614	375.868	376.007	375.331	375.339	375.43
width: 2.441 cm	70	380.247	380.158	380.752	380.613	382.070	380.77
	70	465.080	464.732	463.596	463.411	462.840	463.93
J2-127-1-R2	100	453.647	454.612	453.384	453.265	453.382	453.66
Core B3	150	447.820	447.184	447.075	447.082	446.502	447.13
	200	445.003	444.491	444.116	443.642	443.488	444.15
	250	440.676	441.406	441.254	440.784	440.522	440.93
	300	438.654	437.923	438.860	437.714	437.818	438.19
	350	434.544	434.647	434.129	433.557	434.129	434.20
	400	433.190	432.157	432.050	431.588	432.465	432.29
	350	432.206	431.646	432.776	431.800	432.831	432.25
	300	432.833	433.247	433.043	433.606	434.075	433.36
	250	434.905	434.033	434.599	434.496	434.856	434.58
	200	435.795	436.781	435.691	435.845	436.573	436.14
	150	438.288	438.755	438.233	439.015	438.599	438.58
length: 3.549 cm	100	441.612	441.976	441.659	442.551	442.176	441.10
width: 2.426 cm	70	446.227	447.814	447.013	447.435	447.055	447.11

A2.4 Black Smoker Chimney Data

Sample	**Confining Pressure (psi)**	**Permeability (× 10^{-15} m^2)**					**Mean *k* (× 10^{-15} m^2)**
		1	**2**	**3**	**4**	**5**	
	70	40.844	40.854	40.801	41.003	40.617	40.82
ALV 1445-3	100	31.284	31.291	31.024	31.201	31.058	31.17
Core C1	150	27.477	27.396	27.460	27.126	27.200	27.33
	200	21.619	21.358	21.560	21.319	21.414	21.45
	250	18.849	18.716	18.852	18.666	18.586	18.73
	300	16.207	16.120	15.992	16.024	16.103	16.09
	350	14.726	14.738	14.642	14.672	14.497	14.66
	400	13.537	13.531	13.429	13.370	13.389	13.45
	350	13.492	13.539	13.514	13.540	13.618	13.54
	300	14.278	14.322	14.305	14.384	14.370	14.33
	250	16.605	16.471	16.632	16.589	16.638	16.59
	200	19.813	19.671	19.807	19.804	19.934	19.81
	150	25.269	25.426	25.462	25.851	25.756	25.55
length: 1.225 cm	100	29.658	29.720	29.725	29.903	29.943	29.79
width: 2.518 cm	70	36.348	36.507	36.620	36.655	36.690	36.56
	70	341.788	341.136	340.158	339.896	339.002	340.30
ALV 2179-4-1	100	266.006	265.297	265.247	265.772	265.353	265.54
Core A1	150	196.477	196.482	196.431	195.968	195.572	196.19
	200	167.941	167.745	167.691	167.426	167.197	167.60
	250	150.613	150.368	150.073	149.944	149.739	150.15
	300	135.588	135.810	135.581	135.560	135.303	135.57
	350	124.352	123.986	123.651	123.573	123.654	123.84

	400	114.003	113.920	113.543	113.630	113.338	113.69
	350	115.283	115.488	115.494	115.338	115.309	115.38
	300	118.579	118.678	118.802	118.541	118.741	118.67
	250	122.887	122.945	122.783	122.968	123.051	122.93
	200	126.767	126.707	126.849	126.985	126.961	126.85
	150	131.458	131.356	131.057	131.340	131.380	131.32
length: 0.801 cm	100	148.808	149.077	149.546	149.544	149.801	149.36
width: 2.520 cm	70	197.296	198.840	199.139	199.719	199.769	198.95
	70	52.166	52.748	52.856	52.655	53.039	52.69
ALV 2179-4-1	100	42.345	42.328	41.695	41.441	41.250	41.81
Core B1	150	33.493	33.483	33.508	33.100	33.188	33.35
	200	27.413	27.349	26.907	26.661	26.822	27.03
	250	22.005	21.895	21.670	21.482	21.552	21.72
	300	17.942	17.835	17.751	17.534	17.395	17.69
	350	15.040	14.886	14.770	14.704	14.555	14.79
	400	13.037	12.973	12.835	12.724	12.904	12.89
	350	13.126	13.063	13.159	13.070	13.043	13.09
	300	13.741	13.702	13.701	13.738	13.806	13.74
	250	14.817	15.097	15.046	14.997	15.043	15.00
	200	17.504	17.529	17.580	17.700	17.862	17.64
	150	21.594	21.654	21.736	22.045	21.990	21.80
length: 1.065 cm	100	27.005	26.996	26.936	27.196	27.253	27.08
width: 2.528 cm	70	31.357	31.356	31.289	31.660	31.650	31.46
	70	215.130	213.951	214.158	213.362	212.929	213.91
ALV 2179-4-1	100	168.140	168.261	167.300	167.650	167.196	167.71
Core C1	150	143.735	143.275	143.603	143.163	143.026	143.36
	200	132.608	132.126	132.191	131.923	131.526	132.07
	250	125.340	125.201	125.205	128.999	128.647	126.67
	300	124.319	124.114	124.107	123.927	124.148	124.12
	350	123.114	122.752	122.770	122.863	122.504	122.80
	400	122.022	122.106	121.982	122.189	122.074	122.08
	350	122.132	121.957	122.028	121.912	121.883	121.98
	300	122.108	122.233	122.012	122.086	122.337	122.16
	250	122.422	122.901	122.633	122.457	122.450	122.57
	200	123.041	122.990	122.792	122.881	122.924	122.93
	150	123.354	123.378	123.436	123.419	123.294	123.38
length: 1.201 cm	100	127.359	127.636	127.386	127.522	127.805	127.54
width: 2.531 cm	70	136.429	136.851	137.348	137.508	137.749	137.18
	70	0.795	0.753	0.757	0.785	0.777	0.77
J2-137-1-R1	100	0.721	0.675	0.703	0.696	0.683	0.70
Core D1	150	0.695	0.671	0.656	0.666	0.669	0.67
	200	0.677	0.663	0.661	0.686	0.660	0.67
	250	0.657	0.623	0.614	0.635	0.634	0.63
	300	0.621	0.636	0.624	0.601	0.604	0.62
	350	0.629	0.623	0.617	0.612	0.618	0.62
	400	0.627	0.619	0.611	0.603	0.600	0.61
	350	0.610	0.611	0.620	0.603	0.639	0.62
	300	0.637	0.612	0.621	0.601	0.621	0.62
	250	0.625	0.637	0.624	0.646	0.640	0.63
	200	0.640	0.655	0.637	0.650	0.664	0.65
	150	0.640	0.643	0.635	0.650	0.653	0.64
length: 2.020 cm	100	0.680	0.665	0.667	0.656	0.654	0.66
width: 2.533 cm	70	0.700	0.667	0.720	0.669	0.692	0.69
	70	0.501	0.483	0.494	0.506	0.506	0.50
J2-137-1-R1	100	0.445	0.427	0.441	0.432	0.434	0.44
Core D2	150	0.415	0.403	0.413	0.412	0.405	0.41
	200	0.406	0.395	0.421	0.416	0.403	0.41
	250	0.411	0.395	0.377	0.413	0.394	0.40
	300	0.394	0.394	0.386	0.393	0.404	0.39
	350	0.405	0.386	0.394	0.386	0.392	0.39
	400	0.387	0.376	0.366	0.375	0.397	0.38
	350	0.388	0.385	0.375	0.384	0.388	0.38
	300	0.397	0.387	0.398	0.390	0.388	0.39
	250	0.408	0.418	0.410	0.427	0.431	0.42
	200	0.451	0.423	0.443	0.450	0.461	0.45
	150	0.483	0.473	0.484	0.474	0.466	0.48

length: 1.889 cm	100	0.494	0.486	0.495	0.503	0.516	0.50
width: 2.534 cm	70	0.573	0.562	0.574	0.549	0.570	0.57
	70	0.970	1.033	0.973	1.011	0.989	1.00
J2-137-1-R1	100	0.941	0.935	0.901	0.934	0.871	0.92
Core D3	150	0.763	0.803	0.783	0.767	0.817	0.79
	200	0.774	0.722	0.775	0.742	0.775	0.76
	250	0.744	0.753	0.764	0.740	0.754	0.75
	300	0.722	0.711	0.722	0.715	0.702	0.71
	350	0.676	0.691	0.696	0.704	0.699	0.69
	400	0.670	0.701	0.684	0.692	0.684	0.69
	350	0.696	0.713	0.683	0.695	0.715	0.70
	300	0.701	0.714	0.736	0.716	0.718	0.72
	250	0.750	0.726	0.727	0.731	0.730	0.73
	200	0.764	0.714	0.724	0.745	0.757	0.74
	150	0.755	0.766	0.788	0.784	0.772	0.77
length: 2.123 cm	100	0.781	0.790	0.778	0.801	0.789	0.79
width: 2.533 cm	70	0.802	0.810	0.835	0.810	0.794	0.81
	70	0.894	0.908	0.869	0.918	0.905	0.90
J2-137-1-R1	100	0.755	0.732	0.758	0.736	0.758	0.75
Core D4	150	0.689	0.667	0.658	0.637	0.661	0.66
	200	0.641	0.611	0.612	0.632	0.622	0.62
	250	0.615	0.663	0.612	0.605	0.641	0.63
	300	0.604	0.613	0.607	0.618	0.593	0.61
	350	0.593	0.593	0.605	0.599	0.604	0.60
	400	0.599	0.607	0.590	0.587	0.600	0.60
	350	0.603	0.578	0.610	0.600	0.622	0.60
	300	0.624	0.612	0.613	0.593	0.615	0.61
	250	0.617	0.614	0.636	0.626	0.615	0.62
	200	0.651	0.617	0.628	0.626	0.636	0.63
	150	0.630	0.652	0.652	0.632	0.657	0.65
length: 2.139 cm	100	0.660	0.665	0.671	0.642	0.654	0.66
width: 2.526 cm	70	0.686	0.697	0.687	0.697	0.679	0.69
	70	29.573	29.698	30.018	29.730	29.741	29.75
J2-213-3-R1	100	25.614	25.203	25.234	25.114	25.153	25.26
Core A1	150	21.951	21.891	21.836	22.030	21.795	21.90
	200	20.371	20.347	20.248	20.217	20.221	20.28
	250	19.196	19.305	19.472	19.242	19.212	19.29
	300	18.536	18.428	18.376	18.471	18.434	18.45
	350	17.922	17.957	17.873	17.813	17.939	17.90
	400	17.537	17.563	17.454	17.359	17.440	17.47
	350	17.447	17.485	17.539	17.439	17.507	17.48
	300	17.575	17.604	17.761	17.672	17.640	17.65
	250	17.956	17.833	17.860	17.907	17.884	17.89
	200	18.251	18.100	18.301	18.219	18.325	18.24
	150	18.864	18.728	18.713	18.744	18.837	18.78
length: 2.287 cm	100	19.674	19.852	19.752	19.930	19.908	19.82
width: 2.492 cm	70	21.015	21.125	21.184	21.142	21.231	21.14
	70	48.768	48.880	48.898	49.026	48.972	48.91
J2-213-3-R1	100	45.986	45.305	45.418	45.442	45.399	45.51
Core B1	150	42.314	42.275	42.364	42.090	42.166	42.24
	200	40.704	40.712	40.296	40.307	40.334	40.47
	250	39.230	38.910	39.001	38.968	39.086	39.04
	300	37.503	37.663	37.684	37.603	37.940	37.68
	350	36.207	36.242	36.348	36.000	36.002	36.16
	400	35.086	35.063	34.779	34.917	34.839	34.94
	350	35.011	35.157	35.150	35.242	35.331	35.18
	300	35.806	35.684	35.989	35.769	35.889	35.83
	250	36.595	36.466	36.581	36.524	36.601	36.55
	200	37.253	37.486	37.189	37.520	37.184	37.33
	150	38.419	38.277	38.343	38.123	38.233	38.28
length: 1.526 cm	100	39.686	39.518	39.546	39.545	39.695	39.60
width: 2.485 cm	70	41.330	41.643	41.507	41.470	41.591	41.51
	70	145.398	144.73	146.158	145.144	144.465	145.18
J2-213-3-R1	100	135.884	135.292	135.557	134.619	136.561	135.58
Core D1	150	123.745	122.970	123.249	121.982	122.768	122.94
	200	115.644	115.183	115.355	114.749	115.242	115.23

	250	106.472	106.354	106.853	106.308	105.595	105.60
	300	99.981	100.422	99.220	99.071	98.800	99.50
	350	92.481	92.160	91.900	92.009	91.986	92.11
	400	87.036	86.522	86.651	86.247	86.657	86.62
	350	87.533	87.292	87.312	87.492	87.623	87.45
	300	89.576	89.806	89.764	90.623	89.867	89.93
	250	94.961	95.042	95.249	95.322	95.471	95.21
	200	101.409	101.525	101.889	102.534	101.938	101.86
	150	110.934	110.159	109.454	110.320	110.540	110.28
length: 2.140 cm width: 2.534 cm	100	118.407	119.333	118.587	118.251	119.122	118.74
	70	125.588	126.324	125.950	124.985	125.134	125.60

A2.5 Relict Spire Data

Sample	Confining Pressure (psi)	Permeability ($\times 10^{-15}$ m^2) 1	2	3	4	5	Mean k ($\times 10^{-15}$ m^2)
	70	808.480	812.160	808.902	804.514	811.802	809.17
J2-129-1-R3 Core B2	100	773.741	773.353	783.880	779.411	785.952	779.25
	150	758.878	765.074	758.214	765.760	764.409	762.46
	200	751.863	749.283	753.089	748.623	755.961	751.76
	250	741.410	742.655	743.596	752.497	747.414	745.50
	300	738.624	742.381	740.495	739.244	741.148	740.38
	350	738.323	735.565	735.238	735.549	742.062	737.34
	400	731.579	730.360	734.040	731.284	731.887	731.83
	350	739.865	740.830	744.306	741.146	736.768	740.58
	300	749.307	747.735	746.747	745.167	748.308	747.45
	250	758.588	755.978	758.882	760.541	760.838	758.96
	200	768.069	764.754	771.376	767.075	763.098	766.87
	150	775.379	782.196	777.117	772.017	775.045	776.34
length: 6.172 cm width: 2.427 cm	100	781.127	778.062	781.131	786.606	776.725	780.72
	70	788.378	793.959	783.856	788.381	784.877	787.88
	70	160.769	162.082	163.694	164.550	165.633	163.34
J2-136-6-R1 Core A1-1	100	155.377	158.668	160.505	161.116	161.883	159.49
	150	154.667	157.081	158.003	157.465	159.148	157.27
	200	154.031	155.825	155.232	154.757	155.111	154.99
	250	145.111	146.171	146.947	146.363	146.888	146.29
	300	139.251	140.414	140.225	140.056	140.544	140.10
	350	136.978	136.840	137.552	137.248	135.974	136.92
	400	134.207	133.482	133.213	132.933	133.802	133.53
	350	133.836	132.993	133.354	133.722	133.085	133.40
	300	134.930	134.833	135.090	134.487	133.992	134.67
	250	136.094	136.217	135.908	136.749	136.631	136.32
	200	138.538	139.021	139.580	139.055	139.402	139.12
	150	143.932	144.538	143.996	143.963	144.522	144.19
length: 1.373 cm width: 2.487 cm	100	159.290	160.987	159.676	159.676	159.677	159.86
	70	162.079	161.668	162.085	162.571	162.641	162.21
	70	210.965	214.467	217.088	215.465	216.380	214.86
J2-136-6-R1 Core A1-2	100	207.103	207.931	208.128	208.412	208.597	208.03
	150	197.464	196.778	198.678	197.903	198.416	197.85
	200	195.350	193.845	194.260	194.932	194.093	194.50
	250	191.956	192.783	191.871	192.360	193.112	192.42
	300	189.774	190.577	190.662	191.307	191.560	190.77
	350	189.376	190.911	189.856	189.138	190.825	190.02
	400	188.033	189.302	188.348	189.952	188.505	188.83
	350	189.296	189.779	189.934	189.936	189.698	189.73
	300	191.141	192.119	192.211	191.061	191.482	191.60
	250	193.272	193.022	192.782	193.363	193.764	193.24
	200	196.031	194.507	195.685	194.339	195.347	195.18
	150	197.376	199.104	199.720	197.207	197.465	198.17
length: 1.688 cm width: 2.514 cm	100	201.832	201.821	202.357	200.847	200.583	201.49
	70	203.792	204.620	205.342	204.802	203.522	204.41

J2-136-6-R1 Core C2	70	33.071	33.470	33.999	34.308	34.242	33.81
	100	30.373	30.246	30.340	30.393	30.269	30.32
	150	25.988	25.812	25.776	25.610	25.415	25.72
	200	22.792	22.704	22.807	22.490	22.404	22.64
	250	20.745	20.758	20.692	20.586	20.625	20.68
	300	19.670	19.319	19.306	19.321	19.258	19.37
	350	18.383	18.357	18.443	18.371	18.155	18.34
	400	17.495	17.435	17.615	17.508	17.423	17.50
	350	17.564	17.446	17.428	17.507	17.514	17.49
	300	17.531	17.639	17.627	17.512	17.444	17.55
	250	17.835	17.803	17.874	17.773	17.678	17.79
	200	18.037	18.267	18.296	18.219	18.214	18.21
	150	18.696	18.862	18.777	18.744	18.983	18.81
length: 2.372 cm width: 2.515 cm	100	19.652	19.869	19.902	19.935	19.978	19.87
	70	20.995	20.961	20.959	21.143	21.232	21.06
ALV 2944-3-S1 Pc 1 Core A1	70	683.843	688.083	686.732	689.698	689.550	687.58
	100	656.516	657.892	658.673	653.463	653.528	656.01
	150	641.700	642.742	638.482	642.989	638.834	640.95
	200	635.832	632.037	632.838	631.474	633.105	633.06
	250	632.394	631.522	626.772	628.521	628.526	629.54
	300	628.841	628.453	626.643	623.299	624.661	626.38
	350	622.733	625.803	624.513	622.251	626.409	624.34
	400	622.875	626.328	625.195	623.707	622.846	624.19
	350	624.921	623.326	625.792	623.472	625.508	624.60
	300	624.610	623.369	622.411	623.317	623.923	623.53
	250	622.550	624.080	625.430	624.537	623.039	623.93
	200	624.665	625.190	626.269	624.139	627.487	625.55
	150	625.269	624.449	628.274	626.723	627.915	626.52
length: 0.819 cm width: 2.477 cm	100	628.189	628.711	630.248	628.215	632.061	629.48
	70	632.862	634.153	638.277	636.996	637.797	636.01
ALV 2944-3-S1 Pc 1 Core A3	70	55.960	55.986	56.164	55.857	55.641	55.92
	100	50.022	49.888	49.649	49.695	49.693	49.79
	150	44.941	44.947	45.044	44.982	44.839	44.95
	200	43.191	43.031	42.843	43.153	42.847	43.01
	250	41.988	41.626	41.753	41.645	41.754	41.75
	300	41.103	40.978	40.955	40.736	40.740	40.90
	350	40.458	40.234	40.128	39.983	40.524	40.26
	400	39.839	39.640	39.593	39.669	39.643	39.68
	350	39.729	39.862	39.758	39.905	39.972	39.85
	300	39.933	40.140	40.166	40.389	40.095	40.14
	250	40.473	40.212	40.304	40.315	40.374	40.34
	200	40.640	40.658	40.693	40.652	40.546	40.64
	150	41.295	41.132	41.203	41.363	41.307	41.26
length: 1.318 cm width: 2.523 cm	100	42.189	42.138	42.208	42.320	42.220	42.21
	70	43.663	43.970	43.980	43.912	43.978	43.90
ALV 2944-3-S1 Pc 1 Core B1	70	860.657	857.078	859.168	856.516	859.167	858.52
	100	858.719	858.650	859.349	863.313	855.340	859.07
	150	859.903	855.803	860.586	859.153	860.407	859.17
	200	858.978	864.317	858.478	856.450	858.833	859.41
	250	848.512	849.385	849.667	845.963	849.373	848.58
	300	831.111	822.824	822.712	829.943	822.098	825.73
	350	779.515	775.456	773.122	773.506	768.774	774.07
	400	718.958	712.928	710.557	711.981	710.062	712.89
	350	711.777	706.391	709.618	711.513	709.384	709.73
	300	715.337	714.565	713.511	713.711	714.259	714.28
	250	740.351	738.415	741.750	743.656	741.980	741.23
	200	768.264	767.953	769.637	772.738	779.223	771.55
	150	845.362	843.716	847.383	840.959	849.064	845.29
length: 0.876 cm width: 2.487 cm	100	863.859	870.794	867.483	866.551	865.437	866.82
	70	867.894	859.497	864.257	867.606	865.470	864.94
ALV 2944-3-S1 Pc 2 Core A1	70	340.804	341.811	341.585	342.683	342.926	341.96
	100	338.986	339.285	340.045	338.723	339.399	339.29
	150	333.117	333.699	332.295	333.385	332.995	333.10
	200	331.026	331.090	331.845	331.259	331.618	331.37
	250	328.601	328.164	329.185	328.644	328.771	328.67
	300	327.818	327.474	327.518	326.848	326.525	327.24

	350	326.357	326.201	325.928	326.293	325.687	326.09
	400	325.600	325.420	325.840	325.619	325.319	325.56
	350	324.709	325.394	326.135	325.048	325.535	325.36
	300	325.383	326.023	326.695	325.566	325.454	325.82
	250	326.134	326.444	326.550	326.467	326.614	326.44
	200	326.796	327.083	327.726	326.964	328.067	327.33
	150	328.039	328.091	328.245	328.693	329.493	328.51
length: 0.767 cm	100	330.975	331.075	331.104	331.346	331.325	331.16
width: 2.506 cm	70	334.299	335.170	335.285	334.342	335.220	334.86
	70	667.838	661.729	662.414	663.098	661.108	663.23
ALV 2944-3-S1	100	659.733	660.785	659.203	660.934	659.267	659.98
Pc 2	150	656.318	656.476	655.422	656.331	655.501	656.01
Core A2	200	651.996	651.245	652.947	651.902	651.618	651.94
	250	650.423	650.281	651.397	650.571	650.281	650.59
	300	647.316	646.075	646.518	644.834	644.299	645.81
	350	646.722	642.272	643.217	640.546	642.857	643.12
	400	640.449	638.994	639.207	640.294	639.148	639.62
	350	640.434	640.093	641.263	641.457	641.835	641.02
	300	640.679	642.580	642.063	641.914	642.124	641.87
	250	642.690	643.267	642.820	643.768	642.170	642.94
	200	645.968	644.062	645.662	643.973	644.703	644.87
	150	644.984	646.539	645.286	646.972	646.680	646.09
length: 1.333 cm	100	653.994	653.833	653.299	653.299	654.132	653.71
width: 2.473 cm	70	654.810	655.028	655.174	654.063	656.236	655.06
	70	594.346	594.370	592.646	593.177	593.059	593.52
ALV 2944-3-S1	100	584.008	585.242	585.127	584.648	585.440	584.89
Pc 2	150	569.732	571.415	571.898	569.849	570.634	570.70
Core A3	200	565.394	568.522	566.674	568.391	565.178	566.83
	250	565.627	565.075	561.702	565.464	563.897	564.35
	300	562.843	563.406	563.259	562.950	561.993	562.89
	350	562.338	560.733	562.103	562.482	561.424	561.82
	400	561.069	561.411	560.209	560.331	560.547	560.71
	350	562.792	559.413	562.250	560.115	561.571	561.23
	300	561.830	562.515	558.905	563.284	563.077	561.92
	250	562.666	563.019	563.151	563.617	563.840	563.26
	200	564.050	563.897	564.562	564.409	565.265	564.44
	150	566.383	565.771	567.068	565.938	566.647	566.36
length: 0.847 cm	100	569.678	568.684	567.717	569.870	568.384	568.87
width: 2.478 cm	70	572.007	574.363	575.778	575.800	575.754	574.74
	70	502.241	500.869	498.663	497.093	497.879	499.35
ALV 2944-3-S1	100	475.937	476.392	476.345	477.158	476.605	476.49
Pc 2	150	447.539	446.704	446.238	445.562	446.547	446.52
Core A4	200	427.767	425.687	426.478	426.245	426.486	426.53
	250	414.955	414.737	414.473	413.696	413.133	414.20
	300	405.082	404.612	404.471	404.330	403.741	404.45
	350	397.623	398.576	398.535	397.421	397.142	397.86
	400	393.220	392.237	392.857	392.564	392.434	392.66
	350	391.324	392.990	392.278	391.352	391.579	391.90
	300	392.564	392.186	393.457	392.695	393.560	392.89
	250	394.958	393.545	393.424	393.439	394.775	394.03
	200	397.198	396.566	397.014	396.270	396.341	396.68
	150	400.453	399.298	401.350	400.615	400.004	400.34
length: 0.903 cm	100	408.594	409.339	410.055	409.413	409.087	409.30
width: 2.464 cm	70	418.643	417.885	419.596	419.184	418.804	418.82
	70	485.113	485.267	483.318	484.576	484.216	484.50
ALV 2941-6-S1	100	373.073	372.785	372.578	372.199	371.600	372.45
Core A1	150	244.321	243.831	243.920	243.551	243.319	243.79
	200	194.730	194.383	194.665	194.259	194.464	194.50
	250	162.702	162.667	162.220	162.400	162.217	162.44
	300	140.896	140.616	140.475	140.598	140.577	140.63
	350	127.420	127.686	127.393	127.470	127.050	127.40
	400	117.482	117.347	117.493	117.402	117.367	117.42
	350	117.721	117.906	117.659	117.614	117.813	117.74
	300	118.879	118.716	118.619	118.681	118.959	118.77
	250	120.250	119.996	120.089	119.947	120.195	120.10
	200	121.999	121.907	121.822	122.478	122.084	122.06

	150	125.708	125.470	125.174	125.618	125.367	125.47
length: 1.022 cm width: 2.533 cm	100	133.688	134.247	133.902	134.008	133.879	133.94
	70	146.664	147.005	146.941	146.979	147.026	146.92
	70	706.984	707.995	706.453	705.814	706.629	706.77
J2-125-3-B1	100	625.010	624.188	622.849	623.088	621.790	623.38
Core B2-1	150	518.801	518.641	517.744	517.880	518.151	518.24
	200	441.591	440.956	440.460	440.805	439.543	440.67
	250	389.552	390.022	389.141	388.756	388.842	389.26
	300	356.855	357.115	356.372	355.107	356.138	356.32
	350	331.274	330.446	330.342	330.383	330.188	330.53
	400	313.348	312.191	311.659	311.778	311.899	312.17
	350	312.551	312.014	311.560	312.064	312.254	312.09
	300	313.721	313.448	313.248	313.846	313.473	313.55
	250	314.896	315.788	315.196	315.012	315.291	315.24
	200	317.318	318.197	317.836	317.818	318.561	317.95
	150	322.036	322.981	323.167	323.396	322.759	322.87
length: 1.384 cm width: 2.515 cm	100	332.425	331.919	332.006	332.436	332.524	332.26
	70	342.049	343.218	343.343	343.660	343.417	343.14
	70	198.179	197.239	197.219	196.262	196.589	197.10
J2-125-3-B1	100	182.530	182.870	182.457	182.411	182.236	182.50
Core B2-2	150	164.525	164.421	164.097	163.982	164.032	164.21
	200	157.089	156.761	156.580	156.212	156.274	156.58
	250	153.088	153.007	152.774	152.859	152.467	152.84
	300	149.334	149.407	149.370	149.443	149.654	149.44
	350	148.417	148.316	147.563	147.901	147.664	147.97
	400	146.844	146.577	146.392	146.642	146.333	146.56
	350	146.584	146.779	146.687	146.757	146.472	146.66
	300	147.208	147.095	147.432	147.018	147.131	147.18
	250	147.866	147.892	148.188	148.149	147.776	147.97
	200	148.976	149.091	148.836	149.053	148.858	148.96
	150	150.811	151.082	150.902	151.187	151.255	151.05
length: 1.105 cm width: 2.529 cm	100	154.730	154.993	155.359	155.316	155.168	155.11
	70	160.349	160.401	160.563	160.389	160.771	160.49
	70	107.029	107.504	107.535	106.91	107.893	107.37
J2-125-3-B1	100	103.506	104.002	104.106	103.528	103.982	103.82
Core B3-1	150	100.650	100.513	99.949	100.047	100.189	100.27
	200	98.198	98.428	98.531	98.780	99.078	98.60
	250	98.021	97.863	98.372	97.264	97.970	97.90
	300	96.853	96.639	97.265	97.397	96.908	97.01
	350	96.415	96.904	96.408	96.665	95.971	96.47
	400	96.144	95.784	96.935	96.517	96.004	96.28
	350	95.914	96.145	96.077	96.054	96.374	96.11
	300	96.460	96.214	96.109	97.298	96.064	96.43
	250	96.905	96.601	97.159	96.843	97.262	96.95
	200	97.100	97.504	97.432	97.584	97.141	97.35
	150	98.296	97.682	98.006	97.949	97.993	97.99
length: 1.539 cm width: 2.514 cm	100	98.646	99.218	99.087	98.464	99.137	98.91
	70	100.096	101.025	100.607	100.604	100.562	100.58
	70	262.591	256.348	259.299	259.664	258.898	259.35
J2-125-3-B1	100	251.857	251.548	251.476	250.678	250.815	251.27
Core B3-2	150	241.873	241.531	241.090	241.228	241.029	241.35
	200	235.784	235.396	235.389	235.639	234.982	235.44
	250	231.588	231.110	231.148	230.351	230.810	231.00
	300	227.772	227.705	227.183	227.666	227.120	227.49
	350	224.862	224.682	224.603	224.403	224.045	224.52
	400	222.058	222.448	221.873	221.325	221.771	221.89
	350	222.159	222.198	222.161	222.068	221.998	222.12
	300	222.999	223.115	223.019	222.906	222.686	222.94
	250	224.322	224.440	224.538	223.991	224.609	224.38
	200	226.369	226.525	226.281	226.815	226.542	226.51
	150	229.822	230.024	230.269	230.190	230.315	230.12
length: 1.240 cm width: 2.515 cm	100	234.513	234.800	234.420	234.518	235.107	234.67
	70	241.482	241.580	241.954	242.350	242.301	241.93
	70	585.330	583.465	583.563	582.459	582.584	583.48
J2-125-3-B1	100	551.472	549.544	547.749	548.252	548.108	549.02
Core Ex B2	150	517.586	518.202	516.991	519.668	516.100	517.71

	200	510.922	508.442	508.073	510.103	510.315	509.57
	250	507.267	505.756	505.553	506.440	504.813	505.97
	300	501.040	503.217	504.353	501.748	502.118	502.49
	350	501.861	501.499	500.422	501.912	500.689	501.28
	400	501.027	499.140	499.184	499.003	498.889	499.45
	350	498.067	500.548	500.416	499.268	499.003	499.46
	300	500.284	500.232	501.805	501.572	501.623	501.10
	250	501.203	502.370	503.758	502.650	503.158	502.63
	200	504.038	505.090	503.636	505.780	504.121	504.53
	150	505.919	506.013	505.622	506.951	507.327	506.37
length: 1.028 cm width: 2.488 cm	100	516.900	517.396	516.319	515.246	515.081	516.19
	70	535.320	534.638	534.859	536.350	535.109	535.25
	70	2472.037	2495.098	2476.376	2481.773	2487.882	2482.62
ALV 2178-4-1 Core 4	100	2429.717	2428.869	2420.147	2425.724	2426.898	2426.27
	150	2366.304	2362.218	2353.314	2356.438	2356.804	2359.01
	200	2302.719	2306.515	2309.169	2306.041	2305.518	2305.99
	250	2261.786	2264.155	2262.585	2260.671	2265.696	2262.98
	300	2223.127	2222.766	2221.824	2231.848	2222.057	2224.32
	350	2176.568	2176.435	2165.645	2157.681	2171.598	2169.57
	400	2135.504	2124.717	2126.187	2128.373	2122.493	2127.45
	350	2127.937	2122.710	2124.698	2125.924	2124.909	2125.23
	300	2129.502	2129.350	2127.262	2135.078	2128.807	2130.00
	250	2134.345	2139.285	2127.687	2143.804	2135.261	2136.07
	200	2145.271	2155.861	2150.125	2142.599	2152.015	2149.17
	150	2159.577	2166.944	2160.775	2162.864	2171.645	2164.36
length: 2.658 cm width: 2.423 cm	100	2191.329	2195.234	2203.287	2194.142	2198.333	2196.46
	70	2204.024	2213.434	2220.444	2202.699	2216.443	2211.40
	70	1712.353	1704.519	1707.223	1700.496	1701.163	1705.15
ALV 2178-4-1 Core 5	100	1658.322	1667.218	1664.201	1660.727	1664.610	1663.01
	150	1629.448	1621.552	1616.074	1626.624	1616.275	1621.99
	200	1594.692	1604.678	1594.781	1590.200	1593.260	1595.51
	250	1577.009	1577.760	1572.692	1575.275	1571.583	1574.86
	300	1555.346	1553.667	1558.424	1559.454	1555.942	1556.57
	350	1542.681	1531.104	1536.788	1544.083	1541.234	1539.17
	400	1525.643	1523.886	1526.888	1531.237	1520.488	1525.62
	350	1527.355	1517.073	1518.324	1523.330	1522.219	1521.66
	300	1524.196	1526.715	1525.447	1518.002	1523.086	1523.49
	250	1522.831	1525.372	1524.618	1526.755	1526.364	1525.19
	200	1526.031	1524.628	1526.665	1530.319	1532.318	1527.99
	150	1533.517	1527.296	1533.022	1530.940	1536.301	1532.21
length: 2.425 cm width: 2.490 cm	100	1536.452	1538.661	1532.047	1541.739	1537.252	1537.23
	70	1547.598	1542.283	1540.844	1546.286	1541.312	1543.66
	70	709.898	708.433	696.656	696.338	695.707	701.38
ALV 2178-4-1 Core A4	100	679.620	679.661	679.934	676.913	681.157	679.46
	150	659.713	659.841	654.472	657.598	656.590	657.64
	200	629.370	627.772	628.468	628.500	629.846	628.79
	250	603.405	604.686	604.875	603.964	604.040	604.19
	300	595.219	595.169	590.342	592.043	591.477	592.85
	350	584.282	586.718	583.156	587.273	587.258	585.73
	400	581.822	582.986	580.382	580.531	581.854	581.51
	350	582.370	581.191	583.543	580.652	581.120	581.77
	300	587.301	586.454	585.236	585.678	584.402	585.81
	250	589.438	587.071	588.160	589.354	589.252	588.65
	200	599.496	596.232	597.649	595.797	596.249	597.08
	150	611.716	615.612	614.588	618.414	616.131	615.29
length: 1.047 cm width: 2.518 cm	100	643.185	644.396	643.631	645.994	649.323	645.30
	70	661.829	659.892	662.235	660.822	660.619	661.08
	70	843.171	840.390	836.936	830.649	832.354	836.69
ALV 2178-4-1 Core A5	100	814.896	815.770	814.750	816.494	816.407	815.66
	150	796.049	791.372	792.180	792.645	791.632	792.77
	200	784.678	782.536	786.419	783.013	784.599	784.25
	250	774.957	771.210	772.192	774.952	774.043	773.47
	300	765.519	765.965	768.707	767.257	766.901	766.87
	350	759.766	760.582	764.082	761.020	763.373	761.76
	400	757.804	755.381	751.881	754.317	754.306	754.74
	350	756.900	755.418	758.484	754.571	756.704	756.41

	300	755.287	757.311	758.474	756.512	755.778	756.67
	250	758.393	755.062	757.295	757.049	761.428	757.84
	200	762.146	759.611	759.975	760.242	760.763	760.55
	150	764.392	764.103	764.915	767.410	767.653	765.69
length: 1.054 cm width: 2.500 cm	100	779.306	777.531	779.514	777.352	777.339	778.21
	70	793.580	789.295	789.103	786.025	791.521	789.90
	70	880.804	880.538	881.58	884.209	886.517	882.73
ALV 2461-R13	100	872.624	871.949	872.991	872.411	874.417	872.88
Core 1-1	150	848.543	850.674	849.943	849.141	849.376	849.54
	200	839.961	836.950	836.832	836.213	837.052	837.40
	250	830.424	828.609	829.343	829.282	827.073	828.95
	300	821.129	823.712	823.574	822.034	821.483	822.39
	350	817.599	817.259	817.158	817.660	818.239	817.58
	400	812.841	815.003	814.030	813.093	813.458	813.68
	350	813.399	814.702	813.665	813.862	815.317	814.19
	300	814.068	816.258	814.360	815.556	814.471	814.94
	250	816.250	815.756	816.226	815.354	816.822	816.08
	200	818.805	818.981	818.533	817.250	819.089	818.53
	150	821.452	821.962	821.503	822.627	821.795	821.87
length: 5.293 cm width: 2.550 cm	100	828.069	828.327	830.270	829.708	829.478	829.17
	70	835.787	836.924	836.771	836.473	838.127	836.82
	70	1245.831	1240.842	1235.190	1233.866	1232.009	1237.54
ALV 2461-R13	100	1213.236	1211.245	1210.812	1211.398	1210.559	1211.45
Core 1-2	150	1182.432	1184.094	1185.790	1183.977	1182.722	1183.80
	200	1168.891	1165.528	1169.335	1168.059	1168.878	1168.14
	250	1152.699	1150.892	1153.037	1153.205	1152.248	1152.42
	300	1142.086	1142.626	1142.197	1142.618	1142.891	1142.48
	350	1133.838	1133.695	1136.227	1131.973	1131.587	1133.46
	400	1118.897	1119.796	1118.887	1117.585	1115.900	1118.21
	350	1120.755	1120.873	1120.610	1121.009	1120.741	1120.80
	300	1125.598	1125.230	1124.822	1125.235	1125.076	1125.19
	250	1130.804	1132.122	1133.164	1131.076	1131.307	1131.69
	200	1136.398	1139.502	1137.059	1137.769	1139.845	1138.11
	150	1150.731	1151.840	1152.026	1149.934	1151.535	1151.21
length: 4.610 cm width: 2.539 cm	100	1169.250	1169.182	1169.068	1169.944	1169.246	1169.34
	70	1183.355	1185.685	1183.782	1185.212	1184.256	1184.46
	70	857.437	858.760	856.627	858.340	857.446	857.72
ALV 2461-R13	100	829.753	829.912	829.624	831.358	830.857	830.30
Core 2	150	765.423	764.435	763.174	765.856	764.958	764.77
	200	739.775	740.555	738.575	741.033	741.591	740.31
	250	734.297	733.296	734.281	734.381	732.956	733.84
	300	733.845	733.138	734.938	732.536	734.488	733.79
	350	734.604	735.574	735.360	734.915	734.122	734.91
	400	730.602	731.303	729.454	732.255	732.011	731.12
	350	733.103	733.702	732.041	733.423	735.387	733.53
	300	738.362	736.963	738.178	737.535	738.319	737.87
	250	736.142	736.206	736.225	737.376	737.532	736.70
	200	734.390	735.204	734.772	734.733	734.891	734.80
	150	733.718	734.228	734.150	733.445	733.700	733.85
length: 5.884 cm width: 2.538 cm	100	735.509	736.826	738.896	739.170	735.102	737.10
	70	744.316	745.105	745.622	744.993	745.523	745.11
	70	0.809	0.796	0.859	0.793	0.816	0.81
ALV 2461-R13	100	0.811	0.817	0.817	0.858	0.821	0.82
Core 3-1	150	0.747	0.861	0.783	0.882	0.844	0.82
	200	0.796	0.797	0.798	0.795	0.782	0.79
	250	0.833	0.812	0.775	0.815	0.732	0.79
	300	0.753	0.767	0.789	0.787	0.786	0.78
	350	0.766	0.765	0.744	0.751	0.765	0.76
	400	0.747	0.767	0.749	0.770	0.753	0.76
	350	0.774	0.771	0.772	0.759	0.760	0.77
	300	0.766	0.782	0.784	0.790	0.768	0.78
	250	0.795	0.797	0.781	0.779	0.779	0.79
	200	0.808	0.807	0.803	0.808	0.815	0.81
	150	0.823	0.836	0.841	0.840	0.815	0.83
length: 3.830 cm width: 2.545 cm	100	0.883	0.887	0.869	0.865	0.889	0.88
	70	0.877	0.874	0.855	0.870	0.890	0.87

	70	0.469	0.458	0.447	0.409	0.424	0.44
ALV 2461-R13	100	0.300	0.294	0.241	0.291	0.287	0.28
Core 3-2 (1-1)	150	0.257	0.268	0.263	0.274	0.267	0.27
	200	0.251	0.245	0.261	0.250	0.211	0.24
	250	0.254	0.251	0.245	0.248	0.244	0.25
	300	0.234	0.245	0.244	0.239	0.250	0.24
	350	0.241	0.233	0.250	0.234	0.234	0.24
	400	0.234	0.223	0.233	0.227	0.240	0.23
	350	0.228	0.234	0.233	0.244	0.228	0.23
	300	0.223	0.239	0.223	0.228	0.227	0.23
	250	0.229	0.234	0.240	0.244	0.239	0.24
	200	0.233	0.218	0.229	0.230	0.240	0.23
length: 1.085 cm	150	0.246	0.230	0.241	0.248	0.244	0.24
width: 2.543 cm	100	0.261	0.261	0.252	0.218	0.279	0.25
	70	0.284	0.276	0.276	0.278	0.272	0.28
	70	0.353	0.392	0.372	0.369	0.358	0.37
ALV 2461-R13	100	0.345	0.342	0.351	0.345	0.319	0.34
Core 3-2 (1-2)	150	0.313	0.326	0.307	0.319	0.330	0.32
	200	0.329	0.323	0.318	0.326	0.326	0.32
	250	0.313	0.319	0.326	0.318	0.306	0.32
	300	0.314	0.325	0.298	0.304	0.323	0.31
	350	0.308	0.305	0.320	0.332	0.318	0.32
	400	0.304	0.324	0.308	0.297	0.285	0.30
	350	0.314	0.302	0.324	0.315	0.329	0.32
	300	0.310	0.320	0.310	0.314	0.308	0.31
	250	0.315	0.319	0.327	0.309	0.314	0.32
	200	0.332	0.328	0.316	0.314	0.326	0.32
length: 1.100 cm	150	0.327	0.316	0.316	0.329	0.310	0.32
width: 2.550 cm	100	0.335	0.328	0.327	0.339	0.339	0.33
	70	0.317	0.364	0.329	0.335	0.322	0.33
	70	11.719	11.812	11.843	11.794	11.773	11.79
ALV 2461-R13	100	10.491	10.431	10.405	10.416	10.479	10.44
Core 3-2 (2)	150	8.656	8.692	8.643	8.641	8.635	8.65
	200	7.682	7.687	7.685	7.701	7.690	7.69
	250	7.026	7.000	6.997	6.973	6.957	6.99
	300	6.337	6.429	6.473	6.465	6.425	6.43
	350	6.183	6.103	6.106	6.112	6.093	6.12
	400	5.897	5.891	5.891	5.865	5.862	5.88
	350	5.933	5.942	5.939	5.993	5.950	5.95
	300	6.084	6.063	6.102	6.040	6.048	6.07
	250	6.254	6.270	6.292	6.277	6.272	6.27
	200	6.559	6.553	6.547	6.578	6.560	6.56
length: 2.263 cm	150	7.250	7.263	7.292	7.309	7.292	7.28
width: 2.546 cm	100	8.221	8.205	8.208	8.225	8.239	8.22
	70	9.291	9.362	9.379	9.382	9.425	9.37
	70	21.39	21.283	21.004	20.901	20.651	21.04
ALV 2461-R13	100	15.937	16.28	16.108	16.233	16.250	16.16
Core 4-1	150	11.979	11.725	11.689	11.607	11.637	11.73
	200	9.720	9.644	9.661	9.706	9.674	9.68
	250	8.189	8.080	8.100	8.132	8.044	8.11
	300	6.703	6.605	6.635	6.580	6.537	6.61
	350	5.496	5.491	5.364	5.388	5.286	5.40
	400	4.188	4.150	4.050	4.004	4.006	4.08
	350	4.441	4.484	4.439	4.453	4.479	4.46
	300	5.146	5.179	5.154	5.251	5.225	5.19
	250	6.081	6.139	6.174	6.215	6.136	6.15
	200	7.400	7.423	7.423	7.403	7.451	7.42
length: 2.245 cm	150	8.582	8.582	8.597	8.564	8.573	8.58
width: 2.548 cm	100	10.315	10.285	10.446	10.277	10.342	10.33
	70	11.964	12.06	12.167	12.087	12.074	12.07
	70	13.658	13.591	13.487	13.468	13.420	13.53
ALV 2461-R13	100	10.474	10.484	10.493	10.513	10.483	10.49
Core 4-2	150	7.431	7.362	7.319	7.283	7.272	7.33
	200	5.963	5.879	5.919	5.839	5.850	5.89
	250	5.143	5.048	5.035	5.007	5.014	5.05
	300	4.437	4.380	4.370	4.346	4.349	4.38

	350	3.974	3.942	3.920	3.927	3.909	3.93
	400	3.660	3.650	3.625	3.599	3.627	3.63
	350	3.676	3.648	3.653	3.701	3.646	3.67
	300	3.773	3.781	3.784	3.776	3.794	3.78
	250	3.991	3.963	3.978	3.940	3.970	3.97
	200	4.172	4.180	4.198	4.189	4.247	4.20
	150	4.602	4.588	4.611	4.605	4.615	4.60
length: 2.224 cm	100	5.424	5.491	5.491	5.527	5.539	5.49
width: 2.558 cm	70	6.359	6.410	6.450	6.437	6.500	6.43
	70	3.787	3.785	3.741	3.732	3.780	3.76
ALV 2461-R13	100	3.142	3.108	3.100	3.126	3.094	3.11
Core 6	150	2.222	2.200	2.197	2.163	2.168	2.19
	200	1.797	1.784	1.777	1.782	1.786	1.79
	250	1.547	1.530	1.514	1.519	1.497	1.52
	300	1.353	1.357	1.343	1.337	1.343	1.35
	350	1.242	1.214	1.228	1.185	1.197	1.21
	400	1.108	1.050	1.085	1.087	1.085	1.08
	350	1.098	1.143	1.106	1.111	1.107	1.11
	300	1.175	1.148	1.158	1.146	1.131	1.15
	250	1.198	1.207	1.219	1.193	1.192	1.20
	200	1.297	1.275	1.286	1.276	1.297	1.29
	150	1.422	1.424	1.402	1.408	1.472	1.43
length: 3.670 cm	100	1.708	1.740	1.747	1.731	1.743	1.73
width: 2.546 cm	70	2.024	2.031	2.047	2.075	2.041	2.04
	70	57.819	58.621	58.644	58.112	57.982	58.23
ALV 2461-R13	100	54.567	54.258	54.644	54.233	54.554	54.45
Core 7	150	51.777	51.449	51.617	51.256	51.335	51.49
	200	49.731	49.595	49.782	49.786	49.497	49.68
	250	49.100	48.911	48.822	48.551	48.880	48.85
	300	48.233	48.668	48.186	48.103	48.228	48.28
	350	47.853	47.379	47.427	47.671	47.285	47.52
	400	46.690	46.791	47.076	47.000	46.536	46.82
	350	47.544	46.779	47.257	47.267	47.079	47.18
	300	47.804	47.829	47.333	47.800	47.687	47.69
	250	48.136	47.901	48.053	48.274	48.275	48.13
	200	48.827	48.848	48.549	48.750	48.931	48.78
	150	49.340	49.374	49.549	49.253	49.670	49.44
length: 3.168 cm	100	50.959	50.549	50.658	51.048	50.520	50.75
width: 2.545 cm	70	51.760	52.226	52.166	52.152	52.514	52.16
	70	128.853	131.433	132.126	131.696	132.454	131.31
ALV 2461-R13	100	128.489	127.266	128.089	126.804	127.003	127.53
Core 8-1	150	121.343	121.390	121.490	121.809	121.563	121.52
	200	118.854	119.259	119.003	118.423	118.461	118.80
	250	116.826	117.533	116.689	116.985	116.409	116.89
	300	115.364	115.163	115.346	115.060	114.959	115.18
	350	114.583	114.522	114.296	114.151	114.137	114.34
	400	113.331	113.486	113.182	113.201	113.090	113.26
	350	113.700	113.626	113.015	113.661	113.791	113.56
	300	112.961	114.035	113.066	113.078	113.852	113.40
	250	113.699	113.676	114.103	113.711	113.867	113.81
	200	114.541	114.132	113.789	114.050	114.629	114.23
	150	114.284	114.619	114.887	115.006	114.575	114.67
length: 3.362 cm	100	116.071	116.263	116.375	116.840	117.349	116.58
width: 2.555 cm	70	119.058	118.945	118.417	118.778	119.064	118.85
	70	138.234	138.874	139.621	139.698	139.124	139.11
ALV 2461-R13	100	130.864	130.625	130.910	130.286	130.154	130.57
Core 8-2	150	124.316	124.367	123.778	124.737	124.093	124.26
	200	119.633	118.911	119.140	119.169	119.109	119.19
	250	116.132	115.368	115.642	115.329	115.043	115.50
	300	112.906	112.135	112.549	112.647	112.799	112.61
	350	109.481	109.466	110.080	109.147	109.332	109.50
	400	107.686	107.448	107.434	107.454	107.804	107.57
	350	107.678	107.785	107.993	108.372	107.541	107.87
	300	108.433	108.715	109.615	108.421	108.057	108.65
	250	109.964	110.243	110.073	109.984	110.112	110.08
	200	111.101	111.574	112.096	111.029	111.216	111.40

length: 3.389 cm width: 2.564 cm	150	113.721	113.565	114.081	114.629	113.879	113.97
	100	116.575	116.777	116.954	116.368	116.928	116.72
	70	120.350	120.522	120.478	120.523	121.252	120.62

Appendix 3: Porosity Data

A3.1 Massive Anhydrite Data

Sample	Confining Pressure (psi)	Porosity (%) 1	2	3	4	5	Mean ϕ (%)
J2-210-8-R2 Core A-1	300	2.964	2.173	1.540	2.426	2.807	2.32
	400	3.315	1.287	3.062	3.062	3.347	2.66
	450	3.570	0.404	2.046	2.299	3.473	1.88
J2-210-8-R2 Core A-2	300	3.125	3.742	2.198	3.125	0.276	1.86
	400	3.051	0.583	2.198	2.508	3.361	2.01
	450	4.288	2.198	3.125	3.125	0.276	1.91
J2-210-8-R2 Core A-3	300	5.945	5.945	0.847	2.537	2.203	2.78
	400	5.737	0.100	3.079	5.527	4.645	2.14
	450	5.527	2.203	3.893	5.465	1.723	3.39
J2-216-5-R1 Core A2	300	9.147	12.644	13.754	9.106	13.933	11.51
	400	13.933	8.795	12.153	13.399	11.445	11.80
	450	13.221	10.383	14.070	10.559	9.063	11.31
J2-216-14-R1 Core A	300	3.643	3.191	1.317	1.194	2.009	2.06
	400	3.316	2.537	3.807	3.480	2.537	3.09
	450	3.519	3.972	1.557	3.846	3.480	3.11
J2-216-14-R1 Core B	300	5.624	5.606	5.684	5.624	5.624	5.63
	400	5.527	5.527	5.389	5.467	5.389	5.46
	450	5.467	5.467	5.389	5.467	5.546	5.47
J301-3 Core A	300	14.795	14.795	14.846	14.846	14.846	14.83
	400	14.757	14.757	14.706	14.757	14.846	14.77
	450	14.757	14.757	14.666	14.666	14.717	14.71
J301-3 Core B	300	8.001	7.861	7.892	7.946	7.892	7.92
	400	7.837	7.752	7.837	7.892	7.783	7.82
	450	7.837	7.892	7.868	7.783	7.892	7.85
ALV 2581-8 Core A	300	12.696	12.734	12.630	12.668	12.630	12.67
	400	12.630	12.601	12.564	12.564	12.601	12.59
	450	12.497	12.535	12.535	12.601	12.535	12.54
MIR 1, 1/74 Sta 2403 Core A-1	300	11.017	11.017	10.876	10.806	10.876	10.92
	400	10.876	10.806	10.806	10.806	10.876	10.83
	450	10.946	10.946	10.876	10.876	10.806	10.89
MIR 1, 1/74 Sta 2403 Core A-2	300	12.322	12.173	12.173	12.130	12.023	12.16
	400	12.023	12.066	12.023	11.949	11.800	11.97
	450	12.023	11.949	11.875	11.875	11.949	11.93
MIR 1, 1/74 Sta 2403 Core B	300	9.073	9.007	8.942	9.045	9.007	9.02
	400	8.942	8.914	8.914	8.914	8.877	8.91
	450	8.914	8.783	8.783	8.783	8.914	8.84
MIR 1, 2/78 Sta 2417 Core A	300	15.105	14.960	14.992	14.919	14.992	14.99
	400	14.774	14.743	14.847	14.774	14.702	14.77
	450	14.670	14.670	14.670	14.630	14.670	14.66
MIR 1, 2/78 Sta 2417 Core B	300	13.497	13.587	13.416	13.416	13.416	13.47
	400	13.358	13.244	13.301	13.301	13.244	13.29
	450	13.188	13.188	13.277	13.188	13.220	13.21
ALV 21837-0 Core 2	300	5.020	--	--	--	--	5.02
	400	3.641	--	--	--	--	3.64
	450	--	--	--	--	--	--
ALV 21837-0 Core 3	300	6.115	--	--	--	--	6.12
	400	2.395	--	--	--	--	2.40
	450	--	--	--	--	--	--
ALV 21837-0 Core B	300	6.633	--	--	--	--	6.63
	400	4.022	--	--	--	--	4.02
	450	--	--	--	--	--	--

A3.2 Flange, Slab and Crust Data

Sample	Confining Pressure (psi)	Porosity (%) 1	2	3	4	5	Mean ϕ (%)
ALV 3517-R1 Core D1	300	25.098	21.125	21.801	21.171	21.664	22.12
	400	24.330	21.486	21.084	21.084	20.409	21.64
	450	24.147	20.768	20.587	20.368	19.295	20.97
ALV 3517-R1 Core D3	300	23.724	18.833	19.017	21.247	18.508	20.17
	400	23.119	19.202	20.318	18.094	18.461	19.76
	450	22.928	18.603	19.387	18.461	19.344	19.68
ALV 3521-R2 Core A2	300	42.067	41.983	41.983	41.983	41.983	42.00
	400	40.570	40.570	40.570	40.570	40.369	40.53
	450	39.968	39.968	40.079	40.079	40.079	40.03
ALV 3521-R2 Core Ex 1	300	45.559	45.470	45.074	45.272	45.272	45.33
	400	44.671	44.671	44.671	44.869	44.869	44.75
	450	44.296	44.160	44.473	44.473	44.269	44.33
ALV 3521-R2 Core Ex 2	300	46.020	45.803	46.239	45.747	45.747	45.91
	400	44.878	44.659	44.659	44.451	44.659	44.66
	450	44.017	43.800	44.396	43.745	43.800	43.95
ALV 2415-1B Core A1	300	19.230	20.608	20.529	19.977	20.667	20.20
	400	20.806	20.390	20.667	20.390	20.390	20.53
	450	20.390	20.943	20.529	20.529	20.667	20.61
ALV 2415-1B Core B1	300	31.238	31.141	31.372	31.105	31.008	31.17
	400	31.105	30.971	30.971	30.971	30.638	30.93
	450	30.807	30.874	30.771	30.673	30.638	30.75
ALV 2415-1B Core 1	300	17.110	--	--	--	--	17.110
	400	15.271	--	--	--	--	15.271
	450	--	--	--	--	--	--
ALV 2415-1B Core 2	300	19.164	--	--	--	--	19.164
	400	17.216	--	--	--	--	17.216
	450	--	--	--	--	--	--
ALV 2927-3 Core B1	300	38.150	38.219	38.219	38.277	38.219	38.22
	400	37.899	37.969	37.969	37.899	37.969	37.94
	450	37.775	37.845	37.845	37.969	37.845	37.86
ALV 2927-3 Core 1	300	41.806	--	--	--	--	41.806
	400	39.623	--	--	--	--	39.623
	450	--	--	--	--	--	--
ALV 2927-3 Core 2	300	32.669	--	--	--	--	32.669
	400	29.474	--	--	--	--	29.474
	450	--	--	--	--	--	--
ALV 2927-3 Core 3	300	40.726	--	--	--	--	40.726
	400	38.191	--	--	--	--	38.191
	450	--	--	--	--	--	--
J2-286 Core A1	300	20.686	20.686	20.686	20.581	20.686	20.66
	400	20.686	20.371	20.371	20.476	20.476	20.48
	450	20.476	20.371	20.371	20.371	20.208	20.36
J2-286 Core A3	300	24.025	25.195	25.225	25.860	26.063	25.26
	400	26.100	25.255	25.023	24.957	25.225	25.31
	450	26.131	25.225	25.121	25.225	25.157	25.37
J2-286 Core C2-1	300	27.407	27.494	26.959	27.043	27.257	27.23
	400	27.494	27.107	27.343	27.193	27.193	27.27
	450	27.193	27.043	27.193	27.127	27.043	27.12
J2-286 Core C2-2	300	24.243	23.990	24.143	24.089	24.143	24.12
	400	24.539	24.143	24.102	24.143	23.947	24.17
	450	24.341	24.200	24.046	24.200	24.200	24.20
J2-286 Core C3-1	300	31.056	28.503	27.191	25.301	26.118	27.56
	400	30.168	28.945	26.879	27.097	25.989	27.77
	450	30.263	27.532	26.443	28.945	29.731	28.55
J2-286 Core C3-2	300	22.005	20.927	20.523	21.466	21.272	21.23
	400	21.677	20.466	19.929	20.122	21.330	20.69
	450	21.523	19.929	21.196	19.854	20.332	20.56
J2-286 Core C4	300	22.267	20.833	20.443	19.152	19.667	20.44
	400	21.688	19.797	20.056	18.951	19.281	19.93
	450	21.484	19.152	19.355	18.839	19.409	19.63

ALV 2608-3-3 Core B2	300	43.155	42.980	42.760	42.760	43.143	42.96
	400	42.599	42.647	42.314	42.426	42.709	42.54
	450	42.426	42.647	41.872	42.154	42.204	42.26
ALV 2608-3-3 Core C1	300	29.401	29.252	28.955	29.103	29.103	29.16
	400	28.870	28.658	28.955	28.870	28.573	28.79
	450	28.807	28.573	28.573	28.510	28.807	28.65
ALV 2608-4-1 Pc 1 Core A1	300	35.109	34.934	34.865	34.934	34.865	34.94
	400	34.971	34.794	34.865	34.587	34.725	34.79
	450	34.832	34.556	34.656	34.794	34.794	34.73
ALV 2608-4-1 Pc 1 Core C1-1	300	37.501	37.326	36.938	37.840	36.538	37.23
	400	37.050	36.650	36.825	36.663	35.370	36.51
	450	37.275	35.816	35.705	34.876	35.147	35.75
ALV 2608-4-1 Pc 1 Core C1-2	300	46.627	46.561	45.672	46.413	46.644	46.38
	400	46.561	46.116	46.495	46.264	46.199	46.33
	450	45.902	45.968	46.199	45.672	45.754	45.90
ALV 2608-4-1 Pc 1 Core C3-1	300	35.624	34.357	34.902	35.093	35.226	35.04
	400	35.093	34.828	34.828	34.638	34.770	34.77
	450	35.035	35.300	34.373	35.300	35.300	35.06
ALV 2608-4-1 Pc 1 Core C3-2	300	37.516	36.459	37.255	37.516	37.182	37.18
	400	37.124	37.573	36.995	36.735	37.124	37.11
	450	37.182	36.662	36.402	35.827	36.995	36.61
ALV 2608-4-1 Pc 2 Core A3	300	39.877	39.660	40.022	39.877	39.733	39.83
	400	39.699	39.626	39.589	39.660	39.555	39.63
	450	39.771	39.660	39.555	39.555	39.555	39.62
ALV 2608-4-1 Pc 2 Core B3	300	43.230	43.159	43.105	43.105	43.105	43.14
	400	42.923	42.727	42.980	42.852	42.727	42.84
	450	42.727	42.478	42.673	42.798	42.798	42.69
ALV 2608-4-1 Pc 2 Core 1	300	45.569	--	--	--	--	45.569
	400	44.132	--	--	--	--	44.132
	450	--	--	--	--	--	--
ALV 2608-4-1 Pc 2 Core 2	300	47.969	--	--	--	--	47.969
	400	46.249	--	--	--	--	46.249
	450	--	--	--	--	--	--
ALV 2608-4-1 Pc 2 Core 4	300	44.009	--	--	--	--	44.009
	400	42.376	--	--	--	--	42.376
	450	--	--	--	--	--	--
JAS 177-2-1 Core A2	300	46.347	46.218	46.071	46.071	45.754	46.09
	400	45.924	45.772	45.543	45.772	45.478	45.70
	450	45.395	45.772	45.327	45.395	45.327	45.44
JAS 177-2-1 Core B1	300	39.921	38.307	38.472	39.337	38.179	38.84
	400	39.383	38.390	38.472	38.472	39.588	38.86
	450	39.217	37.935	38.472	38.263	38.060	38.39
JAS 177-2-1 Core B2	300	42.600	40.598	40.167	41.171	41.267	41.15
	400	42.128	40.547	40.315	41.789	40.453	41.04
	450	41.692	40.505	40.409	40.598	39.789	40.59
JAS 177-2-1 Core C2	300	37.972	41.246	42.354	42.354	42.088	41.17
	400	41.615	41.062	38.781	38.051	38.051	39.48
	450	41.062	38.051	38.051	39.147	36.959	38.63
ALV 2179-4-1 Core A1	300	38.877	38.396	35.518	35.892	36.131	36.94
	400	38.052	34.800	37.090	34.358	32.661	35.34
	450	36.475	32.322	34.358	29.859	32.456	33.02
ALV 2179-4-1 Core A2	300	41.325	36.814	35.705	39.910	36.102	37.91
	400	39.507	35.817	37.014	37.414	39.419	37.81
	450	38.816	37.100	36.216	37.100	36.814	37.20
ALV 2179-4-1 Core A3	300	40.768	39.392	39.981	36.275	35.887	38.41
	400	39.392	36.662	36.468	37.161	36.275	37.17
	450	38.805	36.857	34.837	36.578	37.356	36.86
ALV 2179-4-1 Core B2	300	43.273	43.191	43.191	43.011	43.273	43.19
	400	42.622	42.256	42.256	42.176	42.541	42.37
	450	42.256	42.071	42.071	41.996	42.176	42.11

A3.3 Zn-Rich Actively Diffusing Spire Data

Sample	Confining Pressure (psi)	Porosity (%) 1	2	3	4	5	Mean ϕ (%)
ALV 2187-1-1 top Core A2	300	45.72	45.57	45.41	45.57	45.37	45.53
	400	44.20	44.00	44.01	44.11	44.11	44.08
	450	43.60	43.35	43.30	43.60	43.40	43.45
ALV 2187-1-1 top Core A4	300	36.72	36.51	36.40	36.56	36.51	36.54
	400	35.93	35.93	35.87	35.77	35.72	35.84
	450	35.62	35.56	35.66	35.45	35.66	35.59
ALV 2187-1-1 top Core B1	300	45.93	45.48	45.48	45.02	45.38	45.46
	400	44.80	43.89	44.12	44.12	44.02	44.19
	450	43.89	43.67	43.44	43.67	43.44	43.62
ALV 2187-1-1 bottom Core A2	300	39.15	38.87	38.61	38.79	39.15	38.92
	400	38.44	38.44	38.51	38.16	38.26	38.36
	450	37.98	38.08	38.08	38.08	38.08	38.06
ALV 2187-1-1 bottom Core B1	300	42.28	42.12	42.12	41.95	42.03	42.10
	400	41.63	41.79	41.70	42.03	41.79	41.79
	450	41.21	41.04	41.04	41.21	40.79	41.06
ALV 2187-1-1 bottom Core C2	300	41.04	41.11	40.91	40.98	41.09	41.03
	400	40.80	40.44	40.44	40.44	40.44	40.51
	450	40.34	40.34	40.34	40.44	40.52	40.39
ALV 2187-1-1 bottom Core C3	300	40.81	40.81	40.59	40.59	40.37	40.63
	400	40.25	40.00	40.03	40.03	39.71	40.00
	450	40.09	39.71	40.03	39.15	39.81	39.76
ALV 2187-1-2 Core B2-2	300	41.88	41.63	41.82	41.78	41.78	41.78
	400	41.39	41.39	41.29	41.19	41.19	41.29
	450	41.00	40.90	40.80	40.86	40.96	40.90
ALV 2187-1-2 Core C1/C2	300	39.47	39.33	39.33	39.29	39.42	39.37
	400	38.84	38.66	38.75	38.70	38.66	38.72
	450	38.57	38.48	38.39	38.39	38.34	38.43
ALV 2187-1-2 Core C3-1	300	41.41	41.53	41.21	41.16	41.23	41.31
	400	40.98	40.78	40.85	40.85	40.98	40.89
	450	40.73	40.60	40.48	40.48	40.35	40.53
ALV 2187-1-2 Core C3-2	300	42.59	42.41	42.21	42.34	42.34	42.38
	400	41.66	41.72	41.35	41.17	41.42	41.46
	450	40.61	40.55	40.43	40.68	40.68	40.59
ALV 2187-1-2 Core C5	300	43.03	42.89	42.83	42.89	42.69	42.87
	400	42.30	42.30	42.16	42.20	42.20	42.23
	450	42.10	41.96	41.81	41.96	42.20	42.00
ALV 2190-14-1 Core A1	300	47.52	47.39	47.64	47.45	47.39	47.48
	400	47.02	46.78	46.84	46.90	46.78	46.86
	450	46.65	46.84	46.41	46.60	46.97	46.69
ALV 2190-14-1 Core B1	300	48.06	47.56	47.56	47.76	47.17	47.62
	400	46.59	45.81	45.92	46.00	46.00	46.06
	450	45.42	45.04	45.15	45.34	45.34	45.26
ALV 2190-14-1 Core B2	300	41.54	40.96	41.34	41.34	41.54	41.34
	400	41.34	40.77	40.77	41.26	40.96	41.02
	450	41.15	40.77	40.96	40.96	41.15	41.00
J2-128-8-R1 Core Ex	300	27.98	27.94	28.15	28.11	27.98	28.03
	400	27.52	27.64	27.14	27.48	27.14	27.38
	450	27.31	26.98	27.14	26.68	26.94	27.01
J2-137-7-R1 Core B1	300	48.02	47.42	47.12	48.19	48.32	47.81
	400	44.75	44.16	43.86	44.16	44.45	44.27
	450	43.86	43.99	43.40	43.57	43.40	43.64
J2-222-1-R1 Core A1	300	34.99	34.75	34.99	34.99	35.23	34.99
	400	34.22	34.04	34.22	33.87	34.00	34.07
	450	34.04	33.69	33.33	33.69	33.82	33.72
J2-222-1-R1 Core A2	300	36.35	35.87	35.87	36.01	35.77	35.97
	400	36.25	35.52	35.39	35.63	35.34	35.63
	450	36.15	35.21	35.39	35.39	35.87	35.60
J2-222-1-R1 Core Ex	300	30.01	30.26	29.51	29.76	29.26	29.76
	400	29.76	29.26	29.51	29.26	29.07	29.37
	450	29.76	29.26	29.01	29.07	29.26	29.27

J2-127-1-R2 Core B2	300	37.85	37.53	37.31	37.31	37.19	37.44
	400	37.22	36.87	36.87	37.44	36.87	37.05
	450	37.09	36.43	36.65	36.87	36.78	36.76
J2-127-1-R2 Core B3	300	36.25	36.16	36.09	36.09	36.25	36.16
	400	35.67	35.60	35.50	35.57	35.92	35.65
	450	35.43	35.60	35.50	35.50	35.50	35.51

A3.4 Black Smoker Chimney Data

Sample	Confining Pressure (psi)	Porosity (%)					Mean ϕ (%)
		1	2	3	4	5	
ALV 1445-3 Core C1	300	24.839	24.882	25.223	24.882	24.882	24.94
	400	24.070	24.691	23.537	23.876	23.876	24.01
	450	23.493	22.918	23.494	22.581	23.494	23.19
ALV 2179-4-1 Core A1	300	42.799	43.004	43.336	41.995	42.594	42.74
	400	41.933	41.728	41.256	41.194	41.131	41.45
	450	40.722	41.194	40.722	40.926	41.461	41.00
ALV 2179-4-1 Core B1	300	36.794	36.746	36.488	36.376	36.536	36.59
	400	35.288	34.872	35.080	34.458	35.080	34.95
	450	34.408	34.042	34.042	34.408	34.250	34.23
ALV 2179-4-1 Core C1	300	42.171	42.338	41.902	42.338	42.338	42.22
	400	41.416	41.468	41.685	41.251	41.034	41.37
	450	40.599	40.817	40.217	40.432	40.599	40.53
J2-137-1-R1 Core D1	300	17.085	16.700	16.827	17.085	16.926	16.92
	400	16.926	16.669	16.542	16.926	16.315	16.67
	450	16.542	16.700	16.542	16.444	16.413	16.53
J2-137-1-R1 Core D2	300	14.025	13.871	13.650	13.996	14.150	13.94
	400	14.025	14.120	13.899	13.431	13.775	13.85
	450	13.899	13.526	13.526	13.526	13.526	13.60
J2-137-1-R1 Core D3	300	18.255	18.000	18.127	18.098	17.746	18.04
	400	17.873	17.970	17.619	17.843	17.716	17.80
	450	17.843	17.716	17.619	17.619	17.619	17.68
J2-137-1-R1 Core D4	300	17.749	17.621	17.749	17.621	18.005	17.75
	400	17.877	17.237	17.237	17.364	17.364	17.41
	450	17.621	17.109	17.109	17.335	17.237	17.28
J2-213-3-R1 Core A1	300	29.020	29.337	28.755	28.755	28.797	28.93
	400	29.295	28.396	28.438	28.618	28.438	28.64
	450	28.576	28.618	28.438	28.438	28.438	28.50
J2-213-3-R1 Core B1	300	30.507	30.549	30.507	30.689	30.549	30.56
	400	30.369	30.005	30.005	30.005	30.369	30.15
	450	29.825	30.145	30.145	30.187	30.005	30.06
J2-213-3-R1 Core D1	300	39.484	38.969	38.969	38.713	38.969	39.02
	400	39.117	38.713	38.199	38.199	38.861	38.62
	450	38.713	38.457	38.603	37.942	38.861	38.51

A3.5 Relict Spire Data

Sample	Confining Pressure (psi)	Porosity (%) 1	2	3	4	5	Mean ϕ (%)
J2-129-1-R3 Core B2	300	41.124	41.128	40.946	40.946	40.946	41.02
	400	40.227	40.156	40.227	40.227	40.156	40.20
	450	39.941	39.941	39.903	39.870	40.013	39.93
J2-136-6-R1 Core A1-1	300	34.964	30.802	25.403	31.456	34.744	31.27
	400	33.644	29.065	27.336	29.715	30.802	30.04
	450	33.329	29.621	31.579	28.755	29.498	30.51
J2-136-6-R1 Core A1-2	300	30.960	30.433	30.257	29.480	30.006	30.22
	400	30.359	30.359	29.480	28.858	30.183	29.84
	450	30.006	28.432	29.132	29.308	30.006	29.37
J2-136-6-R1 Core C2	300	27.547	24.719	25.103	24.847	24.975	25.42
	400	26.514	23.827	24.464	24.591	24.791	24.82
	450	26.771	24.663	24.591	25.103	24.719	25.16
ALV 2944-3-S1 Pc 1 Core A1	300	43.153	43.513	33.599	34.720	34.390	37.62
	400	41.929	35.448	34.720	34.982	34.920	36.30
	450	41.570	36.774	30.705	32.544	31.555	34.40
ALV 2944-3-S1 Pc 1 Core A3	300	29.564	34.089	34.089	28.905	28.340	30.89
	400	33.547	33.547	29.439	28.684	30.886	31.16
	450	32.658	30.224	28.684	28.905	29.439	29.95
ALV 2944-3-S1 Pc 1 Core B1	300	40.307	39.444	37.771	31.292	31.978	35.96
	400	36.769	33.338	31.729	37.771	33.775	34.60
	450	36.769	26.120	27.592	27.101	30.493	29.38
ALV 2944-3-S1 Pc 2 Core A1	300	32.519	32.250	38.747	31.981	32.455	33.50
	400	39.836	28.430	32.519	27.895	28.430	31.12
	450	38.138	29.232	30.778	32.519	33.737	32.74
ALV 2944-3-S1 Pc 2 Core A2	300	42.181	42.083	43.220	39.818	45.966	42.61
	400	44.589	42.310	42.439	40.624	40.496	42.07
	450	43.805	38.594	39.495	38.370	40.624	40.13
ALV 2944-3-S1 Pc 2 Core A3	300	39.539	41.847	40.197	45.493	36.588	40.63
	400	47.494	40.384	41.517	40.384	40.384	41.95
	450	47.351	41.517	41.186	44.498	38.882	42.59
ALV 2944-3-S1 Pc 2 Core A4	300	35.785	30.412	31.574	29.891	30.876	31.64
	400	35.025	29.661	27.863	28.732	28.270	29.80
	450	36.278	32.918	30.356	30.589	31.053	32.17
ALV 2941-6-S1 Core A1	300	34.089	29.885	32.331	30.972	35.340	32.46
	400	35.890	32.176	29.208	31.786	34.244	32.58
	450	34.518	31.397	27.992	28.599	28.754	30.16
J2-125-3-B1 Core B2-1	300	36.834	33.842	33.416	36.498	33.295	34.74
	400	35.641	36.069	33.842	35.641	33.628	34.95
	450	36.405	33.508	32.659	35.426	33.203	34.21
J2-125-3-B1 Core B2-2	300	36.501	36.245	31.005	36.612	37.126	35.42
	400	35.843	29.993	29.633	34.964	33.688	32.72
	450	35.074	33.290	35.221	35.221	34.199	34.59
J2-125-3-B1 Core B3-1	300	36.058	31.102	31.405	32.864	31.982	32.64
	400	35.194	31.514	32.092	31.020	33.058	32.54
	450	34.610	34.500	32.755	34.221	35.279	34.26
J2-125-3-B1 Core B3-2	300	35.960	34.149	32.618	35.002	35.583	34.64
	400	34.285	33.808	29.308	30.015	33.569	32.13
	450	34.149	32.144	29.308	30.250	34.659	32.03
J2-125-3-B1 Core Ex B2	300	39.833	36.423	38.571	37.272	36.990	37.80
	400	39.139	38.287	37.151	36.141	34.889	37.09
	450	38.287	36.301	37.841	29.910	34.044	35.14
ALV 2178-4-1 Core 4	300	49.742	49.339	49.206	49.206	49.206	49.34
	400	47.613	47.685	47.480	47.420	47.420	47.52
	450	46.894	46.894	46.762	46.894	46.894	46.87
ALV 2178-4-1 Core 5	300	45.628	45.706	45.706	45.569	45.628	45.65
	400	44.886	44.886	44.749	44.964	44.749	44.85
	450	44.344	44.418	44.208	44.149	44.149	44.25
ALV 2178-4-1 Core A4	300	39.885	39.620	39.620	39.620	39.346	39.62
	400	39.081	38.815	38.665	38.665	39.081	38.86
	450	38.815	39.081	38.392	38.542	38.665	38.70

ALV 2178-4-1 Core A5	300	45.057	44.940	45.057	44.784	44.504	44.87
	400	44.386	44.105	44.105	44.105	44.105	44.16
	450	43.831	44.105	43.831	43.551	43.551	43.77
ALV 2461-R13 Core 1-1	300	26.730	26.664	26.767	26.767	26.700	26.73
	400	26.531	26.700	26.567	26.567	26.634	26.60
	450	26.567	26.737	26.567	26.435	--	26.58
ALV 2461-R13 Core 1-2	300	22.163	22.233	22.233	22.201	22.092	22.18
	400	22.131	22.061	22.061	22.030	21.991	22.06
	450	22.131	21.991	21.921	22.061	22.100	22.04
ALV 2461-R13 Core 2	300	28.991	28.962	28.835	28.801	28.898	28.90
	400	28.835	28.611	28.898	28.582	28.645	28.71
	450	--	--	--	--	--	--
ALV 2461-R13 Core 3-1	300	17.353	17.528	17.403	17.003	17.353	17.33
	400	17.178	16.828	16.916	16.741	17.003	16.93
	450	16.916	16.741	16.878	16.703	16.578	16.76
ALV 2461-R13 Core 3-2(1-1)	300	6.476	4.809	4.484	3.609	6.367	5.03
	400	10.405	4.894	5.999	11.196	10.077	8.08
	450	10.866	8.589	8.961	7.520	6.738	8.42
ALV 2461-R13 Core 3-2(1-2)	300	12.820	9.885	8.243	11.166	9.842	10.23
	400	12.820	11.124	9.294	10.390	8.607	10.35
	450	14.296	11.716	10.068	9.477	8.971	10.75
ALV 2461-R13 Core 3-2(2)	300	12.527	12.404	12.280	12.086	11.755	12.21
	400	12.651	11.940	9.916	10.925	9.732	10.98
	450	12.033	11.571	12.227	10.374	11.848	11.59
ALV 2461-R13 Core 4-1	300	19.582	18.698	17.729	19.526	18.185	18.73
	400	19.471	18.698	17.673	17.418	19.084	18.45
	450	19.212	17.929	18.642	18.827	18.185	18.55
ALV 2461-R13 Core 4-2	300	22.637	22.637	22.445	21.971	20.458	22.01
	400	22.237	20.854	19.668	22.237	22.179	21.41
	450	22.503	21.118	20.326	21.971	22.445	21.66
ALV 2461-R13 Core 6	300	17.543	17.335	17.624	17.497	17.452	17.49
	400	17.497	17.254	17.335	17.254	17.254	17.32
	450	17.579	17.173	17.254	17.497	17.012	17.30
ALV 2461-R13 Core 7	300	23.383	24.596	24.692	24.692	24.692	24.41
	400	24.692	24.692	24.747	24.692	24.596	24.68
	450	24.498	24.692	24.596	24.596	24.498	24.58
ALV 2461-R13 Core 8-1	300	20.783	20.606	20.645	20.783	20.683	20.70
	400	20.556	20.606	20.606	20.645	20.618	20.61
	450	20.783	20.694	20.556	20.694	20.468	20.64
ALV 2461-R13 Core 8-2	300	20.701	20.663	20.663	20.663	20.750	20.69
	400	20.528	20.490	20.528	20.490	20.501	20.51
	450	20.490	20.317	20.403	20.403	20.403	20.40

Appendix 4: Microstructure Tables

Mineral abbreviations used in microstructure tables:

Mineral	Abbreviation
amorphous silica	am Si
anhydrite	anh
barite	brt
calcite	ca
chalcocite	ch
chalcopyrite	cp
clay	cl
covellite	co
plagioclase	pl
palagonatized glass	gl
pyrite	py
pyrrhotite	po
sphalerite	sp
stevensite	st
wurtzite	wz

A4.1 Massive Anhydrite Data

Sample / Section	k ($\times 10^{-15}$ m^2)	ϕ (%)	Minerals Present	Grain Packing & Size	Pore Size	Pore Connectivity	Channel Width min-max (avg)
J2-210-8-R2							
A-1	0.3	2.3	anh (py, cp)	tight; 150-1500 µm (avg: 1000 µm) sized anh crystals; sulfides 20-150 µm	most pores 60-150 µm (avg: 90 µm); sulfide crystals precipitated in pore space	low	10-80 µm (20 µm)
J2-216-14-R1							
A	0.3	2.1	anh, cp (py, sp)	tight; areas of large anh 20-2500 µm (avg: 450µm); patches of small, euhedral anh crystals ~150 µm	pores ranging 10-200 µm (avg: 60 µm)	low	< 40 µm (10 µm)
B (top)	0.3	5.6	anh, cp (py, sp)	tight; areas of large anh 20-1500 µm (avg: 400µm); patches of small euhedral anh crystals ~150 µm	pores ranging 10-200 µm (avg: 60 µm)	low	< 40 µm (10 µm)
B (bottom)	0.3	5.6	anh, cp (py, sp)	tight; areas of large anh 20-1600 µm (avg: 400µm); patches of small euhedral anh crystals ~100 µm	pores ranging 10-250 µm (avg: 80 µm)	low	< 40 µm (10 µm)
J301-3							
A	38.5	14.8	anh (py)	moderate; anh (100-1300 µm) with minor py crystals 20-80 µm; anh crystals highly fragmented	pores ranging 50-500 µm (avg: 200 µm)	moderate	10-80 µm (25 µm)
B	0.7	7.9	anh (py)	tight; anh 100-1400 µm (avg: 400 µm); py crystals 20-150 µm; anh crystals highly fragmented	pores ranging 50-500 µm (avg: 200 µm)	low	10-50 µm (20 µm)
ALV 21837-0							
B	0.3	6.6	anh (py)	tight; anh 50-1400 µm (avg: 900 µm); also patches of small euhedral anh crystals ~50-100 µm	pores range from 30-200 µm (avg: 50 µm); most pores isolated	low	10-60 µm (20 µm)
ALV 2581-8							
A	352.6	12.7	anh (py, cp)	moderate; 200-1300 µm sized anh crystals; sulfide crystals <50 µm	most pores 60-150 µm (avg: 90 µm); small sulfide crystals precipitated in pore space	high	20-120 µm (60 µm)
MIR 1, 1/74, Sta 2403							
A-1	123.2	10.9	anh, py, cp	loose; anh crystals 100-1700 µm (avg: 500 µm); py and cp grains < 100 µm	most pores 50-300 µm (avg: 150 µm); some sulfide clusters in pore space	high	20-100 µm (70 µm)
B	77.1	9.0	anh, py, cp	moderate; anh crystals 100-1400 µm (avg: 400 µm); py and cp < 100 µm	most pores 20-300 µm (avg: 100 µm); some sulfide clusters in pore space	moderate	10-100 µm (40 µm)
MIR 1, 2/78, Sta 2417							
A	477.9	15.0	anh (cp)	loose; anh crystals 100-1200 µm (avg: 500 µm); cp grains < 80 µm	pores ranging 50-300 µm (avg: 150 µm)	high	10-150 µm (60 µm)
B	595.9	13.5	anh (cp)	loose; anh crystals 100-1200 µm (avg: 400 µm); cp < 100 µm	pores ranging 50-300 µm (avg: 150 µm)	high	10-150 µm (60 µm)

A4.2 Flange, Slab and Crust Data

Sample / Section	k ($\times 10^{-15}$ m^2)	ϕ (%)	Minerals Present	Grain Packing & Size	Pore Size	Pore Connectivity	Channel Width min-max (avg)	Section Cut
ALV 3517-R1								
D1	55.1	22.1	ca, st (cp, sp)	tight; patches of large ca crystals (250 µm), but mostly ~50 µm crystals	some ~350 µm pores around smaller crystals; mostly ~60 µm	low	< 20 µm (10 µm)	(2)
D3	29.5	20.2	ca, st (cp, sp)	tight; patches of large ca crystals (250 µm), but mostly ~50 µm crystals	some ~350 µm pores around smaller crystals; mostly ~60 µm	low	< 20 µm (10 µm)	(3)
ALV 3521-R2								
Ex 1	1243.4	45.3	ca, st (brt, cp, sp)	tight; large areas of small (~50µm) ca crystals, few patches of larger ~100µm	most pores 20-150 µm regularly distributed, some larger ~300 µm pores	moderate	< 40 µm (10 µm)	(2)
Ex 2	954.7	45.9	ca, st (brt, cp, sp)	tight; large areas of small (~50µm) ca crystals, few patches of larger ~100µm	most pores 20-150 µm regularly distributed, some larger ~300 µm pores	moderate	< 40 µm (10 µm)	(3)
ALV 2927-3								
B1	1889.1	38.2	py, wz (po, cp, cl)	loose; small (20-125 µm) sulfide crystals with small amounts of clay	irregularly shaped pores ranging 40-350 µm (avg: 150 µm); smaller isolated pores	high	10-75 µm (20 µm)	(1)
3	967.3	40.7	py, wz (po, cp, cl)	moderate; small (20-125 µm) sulfide crystals with small amounts of clay	irregularly shaped pores ranging 40-200 µm (avg: 80 µm); minor isolated pores	high	10-180 µm (40 µm)	(3)
2	148.7	32.7	py, wz (po, cp, cl)	tight-moderate; small (5-130 µm) sulfide crystals with small amounts of clay	irregularly shaped pores ranging 30-250 µm (avg: 50 µm); minor isolated pores	moderate	10-70 µm (20 µm)	(2)
ALV 2415-1B								
B1	1552.3	31.2	py, po (am Si, cp, wz)	moderate; 10-300 µm (avg: 75 µm) sized, poorly sorted sulfide crystals	pores ranging from 30-250 µm (avg: 50 µm); some am Si restricting pore channels	moderate (high in 1 layer)	10-50 µm (20 µm) (20-130 µm (30 µm))	(1)
A1	55.4	20.2	py, po, am Si (cp, wz)	tight; 10-280 µm (avg: 75 µm) sized sulfide crystals; lots of am Si	pores ranging from 30-200 µm (avg: 75 µm); abundant am Si restricting pore channels	low	10-50 µm (20 µm)	(2)
J2-286								
C3-1	146.0	27.6	py, wz, po (am Si)	tight; 10-50 µm sized sulfide crystals; large bladed po crystals (200-3000 µm)	pores ranging from 20-300 µm (avg: 20 µm); remnant worm tubes and possible flange edge	low	10-50 µm (20 µm)	(2)
C3-2	48.7	21.2	py, am Si (wz, cp)	tight; 20-200 µm sized sulfide crystals with lots of am Si around crystals	pores ranging from 10-400 µm (avg: 20 µm); lots of remnant worm tubes	low	10-50 µm (20 µm)	(2)
C2-1	0.8	27.2	py, wz (po)	moderate; 10-175 µm sulfide crystals	pores ranging from 10-250 µm (avg: 75 µm); remnant worm tubes	moderate	10-100 µm (20 µm)	(3)
A1	0.5	20.7	py, po, am Si (wz)	moderate; 20-200 µm (avg: 50 µm) sized sulfide crystals; lots of am Si	pores ranging from 10-300 µm (avg: 75 µm); remnant worm tubes	low	10-100 µm (20 µm)	(2)

ALV 2608-3-3								
B2	2737.1	42.9	gl (pl, am Si, py)	loose but variable packing; poorly sorted gl shards 50-1400 µm (avg: 300 µm)	very porous; pores ranging from 50-800 µm (avg: 175 µm)	high	10-200 µm (40 µm)	(1)
C1	1447.1	29.2	gl, am Si (pl, py)	moderate, but variable; poorly sorted gl shards 30-1000 µm (avg: 200 µm)	very porous, but connectivity lost to am Si; pores range from 50-600 µm (avg: 150 µm)	moderate	10-50 µm (10 µm)	(1)
ALV 2608-4-1, Pc 1								
A1	740.6	34.9	gl, am Si, cl (pl)	tight; poorly sorted, angular gl shards 50-200 µm (avg: 80 µm) and am Si ± cl	pores range from 10-400 µm (avg: 30 µm); some channels blocked by am Si ± cl	low	10-40 µm (15 µm)	(1)
C3-2	111.7	37.2	gl, am Si, cl (pl)	tight; poorly sorted, angular gl shards 50-200 µm (avg: 80 µm) and am Si ± cl	pores range from 20-500 µm (avg: 60 µm); few channels blocked by am Si ± cl	moderate	10-80 µm (20 µm)	(2)
C3-1	24.1	35.0	gl, am Si, cl (pl)	moderate; poorly sorted, angular gl shards 50-300 µm (avg: 100 µm)	pores range from 20-500 µm (avg: 100 µm); few channels blocked by am Si ± cl	moderate (very low in 1 layer)	10-200 µm (50 µm) (<30 µm (5 µm))	(2)
ALV 2608-4-1, Pc 2								
A3	2016.9	39.8	gl (am Si, cl, pl)	moderate; angular gl shards 30-400 µm (avg: 200 µm) with am Si coating	very porous; pores ranging from 50-1000 µm (avg: 175 µm)	high	10-200 µm (40 µm)	(1)
2	574.6	48.0	gl (am Si, cl, pl)	tight; angular gl shards 50-200 µm (avg: 100 µm) with am Si coating	very porous; pores ranging from 50-1000 µm (avg: 175 µm); minor am Si ± cl	high	10-200 µm (40 µm)	(2)
B3	538.3	43.1	gl (am Si, cl, pl)	tight; gl shards 50-200 µm (avg: 100 µm) and 2000-3000 µm in some areas	very porous; pores ranging from 50-1000 µm (avg: 175 µm); minor am Si ± cl	high	10-200 µm (40 µm)	(2)
JAS 177-2-1								
B2	2954.2	41.2	gl (am Si, cl, pl)	loose; angular gl shards 30-900 µm (avg: 200 µm) with am Si coating	very porous; pores ranging from 50-800 µm (avg: 175 µm); minor am Si ± cl	high	10-1000 µm (50 µm)	(1)
B1	1774.8	38.8	gl (am Si, cl, pl)	loose; angular gl shards 30-900 µm (avg: 200 µm) with am Si coating	very porous; pores ranging from 50-800 µm (avg: 175 µm); minor am Si ± cl	high	10-1000 µm (50 µm)	(1)
A2	170.4	46.1	gl, pl (am Si, cl)	loose; angular gl shards 30-900 µm (avg: 200 µm) with am Si coating	very porous; pores ranging from 20-650 µm (avg: 150 µm); areas of high am Si ± cl	high	20-350 µm (40 µm)	(2)
ALV 2179-1-1								
B2	1476.5	43.2	cp, py, sp	moderate; 10-100 µm (avg: 50 µm) sized sulfide crystals	pores ranging from 30-200 µm (avg: 60 µm); remnant worm tubes	high	10-150 µm (60 µm)	(1)
A1	575.9	36.9	cp, py, sp	moderate; <50 µm (avg: 30 µm) sized sulfide crystals; well sorted	pores ranging from 30-200 µm (avg: 60 µm); remnant worm tubes	high	<30 µm (10 µm)	(3)

(1) parallel-to-layering core
thin section cut radially
transects different layers

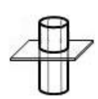

(2) perpendicular-to-layering core
thin section cut axially
transects different layers

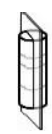

(3) perpendicular-to-layering core
thin section cut radially
consists of a single layer

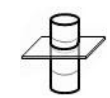

A4.3 Zn-Rich Actively Diffusing Spire Data

Sample / Section	k ($\times 10^{-15}$ m^2)	ϕ (%)	Minerals Present	Grain Packing & Size	Pore Size	Pore Connectivity	Channel Width min-max (avg)
ALV 2187-1-1 (top)							
A2	5462.3	45.5	sp (cp, co)	loose; sulfide crystals 10-300 μm (avg: 120 μm)	pores 10-600 μm (avg: 140 μm)	high	10-300 μm (100 μm)
A4	3433.7	36.5	sp (cp)	loose; sulfide crystals 10-250 μm (avg: 120 μm)	pores 10-600 μm (avg: 140 μm)	high	10-250 μm (100 μm)
B1	596.3	45.5	sp (cp)	loose; sulfide crystals 10-200 μm (avg: 150 μm)	pores 10-600 μm (avg: 200 μm)	high	10-150 μm (80 μm)
ALV 2187-1-2							
C1/C2	1619.4	39.4	sp (cp)	loose; sulfide crystals 10-200 μm (avg: 130 μm)	pores 10-650 μm (avg: 150 μm)	high	10-150 μm (70 μm)
C5	1426.3	42.9	sp (cp)	loose; sulfide crystals 10-200 μm (avg: 130 μm)	pores 10-650 μm (avg: 150 μm)	high	10-150 μm (70 μm)
ALV 2190-14-1							
A1	2726.3	47.5	cp, sp	loose; sulfide crystals 10-120 μm (avg: 75 μm)	pores 10-450 μm (avg: 150 μm)	high	10-140 μm (70 μm)
J2-128-8-R1							
Ex	22.2	28.0	cp, wz, am Si	mod-tight; sulfide crystals 5-300 μm (avg: 100 μm); 1 layer with lots of am Si	pores 10-450 μm (avg: 120 μm)	moderate (low in 1 layer)	10-150 μm (10-40 μm)
J2-222-1-R1							
A2	327.3	35.0	sp, anh, cp, ch (co)	moderate; sulfides 10-300 μm (avg: 100 μm); anh ~ 150 μm	pores 10-550 μm (avg: 150 μm)	moderate	10-120 μm (60 μm)
Ex	202.9	29.8	sp, anh, cp, ch (co)	moderate; sulfides 10-400 μm (avg: 150 μm); anh ~ 200 μm	pores 10-600 μm (avg: 150 μm)	moderate	10-120 μm (60 μm)
J2-127-1-R2							
B3	438.2	36.2	cp, wz	moderate; sulfide crystals 10-300 μm (avg: 150 μm)	pores 10-350 μm (avg: 120 μm)	moderate	10-150 μm (45 μm)

A4.4 Black Smoker Chimney Data

Sample / Section	*k* ($\times 10^{-15}$ m^2)	ϕ (%)	Minerals Present	Grain Packing & Size	Pore Size	Pore Connectivity	Channel Width min-max (avg)
J2-137-1-R1							
D1	0.6	16.9	cp, anh, wz, py	tight; sulfide crystals 10-200 µm (avg: 90 µm); anh 50-300 µm (avg: 120 µm)	pores 10-200 µm (avg: 75 µm)	low	< 20 µm (10 µm)
J2-213-3-R1							
A1	18.4	28.9	cp, anh, wz (py)	tight; sulfide crystals 10-150 µm (avg: 80 µm); anh 50-350 µm (avg: 200 µm)	pores 10-150 µm (avg: 100 µm)	low	10-30 µm (10 µm)
D1	99.5	39.0	cp, anh, wz (co, py)	moderate; sulfides 10-250 µm (avg: 120 µm); anh 50-350 µm (avg: 200 µm)	pores 10-300 µm (avg: 175 µm)	moderate	10-150 µm (40 µm)
ALV 1445-3							
C1	16.1	24.9	cp, anh, py	tight; sulfide crystals 10-150 µm (avg: 80 µm); anh 50-300 µm (avg: 150 µm)	pores 10-200 µm (avg: 75 µm)	low	< 20 µm (10 µm)

A4.5 Relict Spire Data

Sample / Section	k ($\times 10^{-15}$ m^2)	ϕ (%)	Minerals Present	Grain Packing & Size	Pore Size	Pore Connectivity	Channel Width min-max (avg)
J2-129-1-R3							
B2	740.4	41.0	wz, cp, am Si, anh (py)	loose-mod; most sulfide crystals between 5-200 µm (avg: 60 µm)	most pores 10-350 µm (avg: 130 µm); lots of am Si in pore space around smaller grains	moderate	10-120 µm (50 µm)
J2-136-6-R1							
A1-2	190.8	30.2	wz, cp, py	moderate; sulfide crystals 10-125 µm (avg: 70 µm)	pores 10-350 µm (avg: 130 µm)	moderate	10-100 µm (50 µm)
C2	19.4	25.4	wz, cp (py)	mod-tight; sulfide crystals 10-120 µm (avg: 70 µm)	pores 10-240 µm (avg: 60 µm); lots of am Si in pore space around smaller grains	low	10-80 µm (30 µm)
ALV 2944-3-S1, Pc 1							
A1	626.4	37.6	cp, wz, py (am Si)	moderate; sulfide crystals 5-130 µm (avg: 40 µm)	pores 10-400 µm (avg: 150 µm)	high	10-120 µm (50 µm)
A3	40.9	30.9	cp, wz, py, am Si, anh	tight; sulfide crystals 10-100 µm (avg: 50 µm)	pores 10-350 µm (avg: 100 µm)	low	10-100 µm (30 µm)
ALV 2944-3-S1, Pc 2							
A1	327.2	33.5	cp, wz, py	loose; sulfide crystals 10-180 µm (avg: 90 µm)	pores 10-600 µm (avg: 100 µm)	high	10-200 µm (60 µm)
A2	645.8	42.6	cp, wz, py	loose; sulfide crystals 10-130 µm (avg: 80 µm)	pores 10-250 µm (avg: 100 µm)	high	10-80 µm (60 µm)
ALV 2941-6-S1							
A1	140.6	32.5	cp, wz (py)	loose; sulfide crystals 10-275 µm (avg: 125 µm)	pores 10-550 µm (avg: 140 µm)	high	10-150 µm (40 µm)
J2-125-3-B1							
B2-1	356.3	34.7	cp (wz, py)	loose; sulfide crystals 10-175 µm (avg: 80 µm)	pores 10-350 µm (avg: 100 µm)	high	10-175 µm (60 µm)
B3-1	97.0	32.6	cp, wz, py	loose-mod; sulfide crystals 5-150 µm (avg: 70 µm)	pores 10-450 µm (avg: 100 µm)	moderate	10-125 µm (40 µm)
Ex	502.5	37.8	cp, wz, py	loose-mod; sulfide crystals 10-150 µm (avg: 80 µm)	pores 10-500 µm (avg: 100 µm)	mod -high	10-250 µm (40 µm)

ALV 2178-4-1								
4	2224.3	49.3	py, cp (wz)	loose; sulfide crystals 10-250 µm (avg: 120 µm)	pores 10-600 µm (avg: 120 µm)	high	10-250 µm (70 µm)
A5	766.9	44.9	py, cp (wz)	loose; sulfide crystals 10-350 µm (avg: 120 µm)	pores 10-400 µm (avg: 70 µm)	high	10-130 µm (70 µm)
ALV 2461-R13							
C1-1	822.4	26.7	cp, wz, py (am Si)	moderate; sulfide crystals 10-150 µm (avg: 70 µm)	pores 10-350 µm (avg: 120 µm)	moderate	10-160 µm (40 µm)
C1-2	1142.5	22.2	cp, wz, py, po, am Si	moderate; sulfide crystals 10-300 µm (avg: 100 µm)	pores 10-450 µm (avg: 120 µm)	moderate	10-140 µm (50 µm)
C3-2(1-2)	0.3	10.4	cp, wz, py, po, am Si	tight; sulfide crystals 10-320 µm (avg: 100 µm)	pores 10-400 µm (avg: 80 µm)	low	10-50 µm (10 µm)
C3-2(2)	6.4	12.2	cp, wz, po, am Si (py)	tight; sulfide crystals 10-275 µm (avg: 80 µm)	pores 10-400 µm (avg: 80 µm)	low	10-50 µm (10 µm)
C4-1	6.6	18.7	cp, wz, am Si (py, po)	tight; sulfide crystals 10-150 µm (avg: 75 µm)	pores 10-500 µm (avg: 80 µm)	low	10-60 µm (15 µm)
C4-2	4.4	22.0	cp, wz, py, am Si (po)	tight; sulfide crystals 10-120 µm (avg: 70 µm)	pores 10-500 µm (avg: 80 µm)	low	10-60 µm (15 µm)
C8-2	112.6	20.7	cp, wz, po,(py, am Si)	moderate; sulfide crystals 10-175 µm (avg: 100 µm)	pores 10-550 µm (avg: 120 µm)	moderate	10-250 µm (20 µm)

References

Aquilano, D., M. Rubbo, M. Catti, A. Pavese, and P. Ugliengo (1992), Theoretical equilibrium and growth-morphology of anhydrite ($CaSO_4$) crystals, *J. Crystal Growth, 125* (3-4), 519-532.

Bernabé, Y., W. F. Brace, and B. Evans (1982), Permeability, porosity, and pore geometry of hot-pressed calcite, *Mech. Mater., 1* (3), 173-183.

Bernabé , Y. (1991), Pore Geometry and Pressure Dependence of the Transport Properties in Sandstones, *Geophysics, 56*, 436-446.

Bernabé, Y., U. Mok, and B. Evans (2003), Permeability-porosity Relationships in Rocks Subjected to Various Evolution Processes, *Pure Appl. Geophys., 160*, 937-960.

Bourbie, T., and B. Zinszner (1985), Hydraulic and Acoustic Properties as a Function of Porosity in Fontainebleau Sandstone, *J. Geophys. Res., 90* (B13), 524-532.

Cooper, M.J., H. Elderfield, and A. Schultz (2000), Diffuse hydrothermal fluids from Lucky Strike hydrothermal vent field: Evidence for a shallow conductively heated system, *J. Geophys. Res., 105* (B8), 19,369-19,375.

Craddock, P. R., and W. Bach (2010), Insights to Magmatic-Hydrothermal Processes in the Manus back-arc Basin as Recorded by Anhydrite, *Geochim. Cosmochim. Acta*, doi: 10.1016/j.gca.2110.07.004.

David, C., T. F. Wong, W. L. Zhu, J. X. Zhang (1994), Laboratory measurement of compaction-induced permeability change in porous rocks – Implications for the generation and maintenance of pore pressure excess in the crust, *Pure App. Geophys., 143* (1-3), 425-456.

Delaney, J. R., V. Robigou, R. McDuff, and M. K. Tivey (1992), Geology of a Vigorous Hydrothermal System on the Endeavor Segment, Juan de Fuca Ridge, *J. Geophys. Res., 97* (B13), 19663-19682.

deMartin, B., G. Hirth, and B. Evans (2004), Experimental Constraints on Thermal Cracking of Peridotite at Oceanic Spreading Centers, in *Mid-Ocean Ridges: Hydrothermal Interactions Between the Lithosphere and Oceans*, *Geophys. Monogr. Ser., vol. 148,* edited by C. R. German et al., pp. 219-244, AGU, Washington, D.C.

Elderfield, H., and A. Schultz (1996), Mid-ocean ridge hydrothermal fluxes and the chemical composition of the ocean, *Ann. Rev. Earth Planet. Sci., 24,* 191-224.

Embley, R. W., and W. W. Chadwick, Jr. (1994), Volcanic and hydrothermal processes associated with a recent phase of seafloor spreading at the northern Cleft segment: Juan de Fuca Ridge, *J. Geophys. Res., 99* (B3), 4741-4760.

Ferrini, V. L., M. K. Tivey, S. M. Carbotte, F. Martinez, and C. Roman (2008), Variable morphologic expression of volcanic, tectonic, and hydrothermal processes at six hydrothermal vent fields in the Lau back-arc basin, *Geochem. Geophys. Geosyst., 9*, Q07022.

Fontaine, F. J., M. Rabinowicz, and J. Boulégue (2001), Permeability changes due to mineral diagenesis in fractured crust: Implications for hydrothermal circulation at mid-ocean ridges, *Earth Planet. Sci. Lett., 184*, 407-425.

Fredrich, J. T., K. H. Greaves, and J. W. Martin (1993), Pore geometry and transport properties of Fontainebleau Sandstone, *Int. J. Rock Mech. Min. Sci., 30*, 691–697.

Freeze, R. A. and J. A. Cherry (1979), *Groundwater*, Prentice Hall, Inc: Upper Saddle River, NJ, 30-38.

Gallant, R. M., and K. L. Von Damm (2006), Geochemical controls on hydrothermal fluids from the Kairei and Edmond Vent Fields, 23 degrees-25 degrees S, Central Indian Ridge, *Geochem. Geophys. Geosyst., 7*, doi:10.1029/2005GC001067.

German, C. R., and L. M. Parson (1998), Distributions of hydrothermal activity along the Mid-Atlantic Ridge: Interplay of magmatic and tectonic controls, *Earth Plan. Sci. Lett., 160* (3-4), 327-341.

Goldfarb, M. S., D. R. Converse, H. D. Holland, and J. M. Edmond (1983), The genesis of hot spring deposits on the East Pacific Rise, 21°N, in *Econ. Geol. Monogr., 5*, ed. H. Ohmoto and B. J. Skinner, Economic Geology Publishing Co., Lancaster, Penn., 184-197.

Goldfarb, M. S. (1988), Flanges and the formation of hydrothermal edifices, Endeavor segment, Juan de Fuca Ridge (abstract), *Eos Trans. AGU, 69* (44), Fall Meeting Suppl., 1484.

Guéguen, Y. and V. Palciauskas (1994), *Introduction to the Physics of Rocks*, Princeton University Press: Princeton, NJ, 117-134.

Haymon, R. M. (1983), Growth history of hydrothermal black smoker chimneys, *Nature, 301*, 695-698.

Hannington, M. D., M. K. Tivey, A. C. Larocque, S. Petersen, P. A. Rona (1995), The occurrence of gold in sulfide deposits of the TAG Hydrothermal Field, Mid-Atlantic Ridge, *The Canadian Mineralogist, 33*, 1285-1310.

Henderson, N., E. Flores, M. Sampaio, L. Freitas, and G. M. Platt (2005), Supercritical fluid flow in porous media: modeling and simulation, *Chem. Eng. Sci., 60* (7), 1797-1808.

Humphris, S. E., P. M. Herzig, D. J. Miller, J. C. Alt, K. Becker, D. Brown, G. Brügmann, H. Chiba, Y. Fouquet, J. B. Gemmell, et al. (1995), The internal structure of an active sea-floor massive sulphide deposit, *Nature, 377*, 713-716, doi: 10.1038/377713a0.

Juteau, T., and R. Maury (1999), The oceanic crust: from accretion to mantle recycling. Springer, New York, pp. 247-271.

Kerr, R. C. (1997), Heat transfer and hydrothermal fluid flow at flanges on large seafloor sulphide structures, *Earth. Plan. Sci. Lett., 152*, 93-99.

Koski, R. A., P. F. Lonsdale, W. C. Shanks, M. E. Berndt, and S. S. Howe (1985), Mineralogy and Geochemistry of a Sediment-Hosted Hydrothermal Sulfide Deposit From the Southern Trough of Guaymas Basin, Gulf of California, *J. Geophys. Res., 90* (B8), 6695-6707.

Kuhn, T., P. M. Herzig, M. D. Hannington, D. Garbe-Schönberg, and P. Stoffers (2003), Origin of fluids and anhydrite precipitation in the sediment-hosted Grimsey hydrothermal field north of Iceland, *Chem. Geol., 202* (1-2), 5-21.

Kumagai, H., K. Nakamura, T. Toki, T. Morishita, K. Okino, J. Ishibashi, U. Tsunogai, S. Kawagucci, T. Gamo, T. Shibuya, T. Sawaguchi, N. Neo, M. Joshima, T. Sato, and K. Takai (2008), Geological background of the Kairei and Edmond hydrothermal fields along the Central Indian Ridge: Implications of their vent fluids' distinct chemistry, *Geofluids, 8*, 239-251.

Langmuir, C., S. Humphris, D. Fornari, C. Van Dover, K. Von Damm, M. K. Tivey, D. Colodner, J. L. Charlou, D. Desonie, C. Wilson, Y. Fouquet, G. Klinkhammer, and H. Bougault (1997), Hydrothermal vents near a mantle hot spot: The Lucky Strike vent field at 37 degrees N on the Mid-Atlantic Ridge, *Earth Plan. Sci. Lett., 148* (1-2), 69-91.

Le Ravalec, M., M. Darot, T. Reuschlé, and Y. Guéguen (1996), Transport Properties and Microstructural Characteristics of a Thermally Cracked Mylonite, *Pure Appl. Geophys., 146*, 207-227.

Lonsdale, P. and K. Becker (1985), Hydrothermal plumes, hot springs, and conductive heat-flow in the southern trough of Guaymas Basin, *Earth Planet. Sci. Lett., 73* (2-4), 211-225.

Lowell, R. P. (1991), Modeling continental and submarine hydrothermal systems, *Rev. Geophys., 29* (3), 457-476.

Lowell, R. P., and L. N. Germanovich (2004), Hydrothermal Processes at Mid-Ocean Ridges: Results From Scale Analysis and Single-Pass Models, in *Mid-Ocean Ridges: Hydrothermal Interactions Between the Lithosphere and Oceans, Geophys. Monogr. Ser., vol. 148,* edited by C. R. German et al., pp. 219-244, AGU, Washington, D.C.

Lowell, R. P., P. A. Rona, and R. P. Von Herzen (1995), Seafloor hydrothermal systems. *J. Geophys. Res., 100* (B1), 327-352.

Lowell, R. P., Y. Yao, and L. N. Germanovich (2003), Anhydrite precipitation and the relationship between focused and diffuse flow in seafloor hydrothermal systems, *J. Geophys. Res., 108* (B9), 2424, doi:10.1029/2002JB002371.

Luquot, L. and P. Gouze (2009), Experimental determination of porosity and permeability changes induced by injection of CO_2 into carbonate rocks, *Chem. Geol., 265* (1-2), 148-159.

McCune, C. C., H. S. Fogler, and W. E. Kline (1979), An Experimental Technique for Obtaining Permeability-Porosity Relationships in Acidized Porous Media, *Ind. Eng. Chem. Fundam., 18,* 188-191.

Mills, R. A., T. Clayton, and J. C. Alt (1996), Low-temperature fluid flow through sulfidic sediments from TAG: Modification of fluid chemistry and alteration of mineral deposits, *Geophys. Res. Lett., 23* (23), 3495-3498.

Mills, R. A. and M. K. Tivey (1999), Seawater entrainment and fluid evolution within the TAG hydrothermal mound: Evidence from analyses of anhydrite, *In*: Cann, J. H. Elderfield, and A. Laughton (eds.), *Dynamics of Processes Associated with New Ocean Crust*, Cambridge University Press, Cambridge, U. K., 225-248.

Norton, D., and R. Knapp (1977), Transport Phenomena in Hydrothermal Systems: The Nature of Porosity, *Amer. Jour. Sci., 277*, 913-936.

Quispe, J. R., R. E. Rozas, and P. G. Toledo (2005), Permeability-porosity relationship from a geometrical model of shrinking and lattice Boltzmann and

Monte Carlo simulations of flow in two-dimensional pore networks, *Chem. Eng. Jour., 111* (2-3), 225-236.

Pape, H., C. Clauser, J. Iffland, R. Krug, and R. Wagner (2005), Anhydrite cementation and compaction in geothermal reservoirs: Interaction of pore-space with flow, transport, P-T conditions, and chemical reactions, *Int. J. Rock Mech. Mining Sci., 42*, 1056-1069.

Paterson, M. S. (1983), The equivalent channel model for permeability and resistivity in fluid-saturated rock - A re-appraisal, *Mech. Mater.*, 345-352.

Pearson, A., J. S. Seewald, and T. I. Eglinton (2005), Bacterial incorporation of relict carbon in the hydrothermal environment of Guaymas Basin, *Geochim. Cosmochim. Acta*, *69* (23), 5477-5486.

Pester, N. J., D. A. Butterfield, D. I. Foustoukos, K. K. Roe, K. Ding, T. M. Shank, and W. E. Seyfried Jr. (2008), The Chemistry of Diffuse-Flow Vent Fluids on the Galapagos Rift (86°W): Temporal Variability and Subseafloor Phase Equilibria Controls, in *Magma to Microbe: Modeling Hydrothermal Processes at Ocean Spreading Centers, Geophys. Monogr. Ser., vol. 178*, edited by R. P. Lowell et al., pp. 123-144, AGU, Washington, D.C.

Reis, J. C. and A. M. Acock (1994), Permeability Reduction Models for the Precipitation of Inorganic Solids in Berea Sanstone, *J. Geophys. Res., 18*, 347-368.

Rona, P. A., M. D. Hannington, C. V. Raman, G. Thompson, M. K. Tivey, S. E. Humphris, C. Lalou, and S. Petersen (1993), Active and relict sea-floor hydrothermal mineralization at the TAG Hydrothermal Field, Mid-Atlantic Ridge, *Econ. Geol. and the Bull. Soc. Econ. Geol.*, *88* (8), 1989-2017.

Rouxel, O., Y. Fouquet, and J. N. Ludden (2004), Subsurface processes at the lucky strike hydrothermal field, Mid-Atlantic ridge: evidence from sulfur, selenium, and iron isotopes, *Geochim. Cosmochim. Acta, 68*, 2295-2311.

Scheirer, D. S., T. M. Shank, and D. J. Fornari (2006), Termperature variations at diffuse and focused flow hydrothermal vent sites along the northern East Pacific Rise, *Geochem. Geophys. Geosyst.*, *7*, Q03002, doi:10.1029/2005GC001094.

Sleep, N. H. (1991), Hydrothermal circulation, anhydrite precipitation, and thermal structure at ridge axis. *J. Geophys. Res.*, *96* (B2), 2375-2387.

Steefel, C. I., and A. C. Lasaga (1994), A coupled model for transport of multiple chemical-species and kinetic precipitation dissolution reactions with application to reactive flow in single-phase hydrothermal systems, *Amer. Jour. Sci., 294* (5), 529-592.

Thompson, G., M. J. Mottl, and P. A. Rona (1985), Morphology, mineralogy and chemistry of hydrothermal deposits from the TAG area, 26°N Mid-Atlantic ridge, *Chem. Geol., 49*, 243-257.

Tivey, M. K., S. Humphris, G. Thompson, M. Hannington, and P. Rona (1995), Deducing patterns of fluid flow and mixing within the TAG active hydrothermal mound using mineralogical and geochemical data, *J. Geophys. Res., 100* (B7), 12527-12555.

Tivey, M. K., and R. E. McDuff (1990), Mineral Precipitation in the Walls of Black Smoker Chimneys: A Quantitative Model of Transport and Chemical Reaction, *J. Geophys. Res., 95* (B8), 12617-12637.

Tivey, M. K., D. S. Stakes, T. L. Cook, M. D. Hannington, and S. Petersen (1999), A model for growth of steep-sided vent structures on the Endeavor Segment of the Juan de Fuca Ridge: Results of a petrologic and geochemical study, *J. Geophys. Res., 104* (B10), 22859-22883.

Todd, A. C. and M. D. Yuan (1992), Barium and Strontium Sulfate Solid Solution Scale Formation at Elevated Temperatures, *SPE Prod. Eng., 7*, 85-92.

Turcotte, D.L. and G. Schubert (1982), *Geodynamics: Applications of Continuum Physics to Geological Problems*, Cambridge University Press: New York, NY.

Turner, J. S. (1995), Laboratory models of growing flanges, and a comparison with other growth mechanisms of "black smoker" chimneys, *Earth Plan. Sci. Lett., 134* (3-4), 491-499.

Von Damm, K. L., A. M. Bray, L. G. Buttermore, and S. E. Oosting (1998), The geochemical controls on vent fluids from the Lucky Strike vent field, Mid-Atlantic Ridge. *Earth Plan. Sci. Lett., 160* (3-4), 521-536.

Walsh, J. B. (1965), The Effect of Cracks on the Compressibility of Rock, *J. Geophys. Res., 70* (2), 381-389.

Walsh, J. B., and W. F. Brace (1984), The Effect of Pressure on Porosity and the Transport Properties of Rocks, *J. Geophys. Res., 89*, 9425-9431.

Wark, D. A. and E. B. Watson (1998), Grain-scale permeabilities of texturally equilibrated, monomineralic rocks, *Earth Planet. Sci. Lett., 164*, 591–605.

Wilcock, W. S. D., and J. R. Delaney (1996), Mid-ocean ridge sulfide deposits: Evidence for heat extraction from magma chambers or cracking fronts? *Earth Plan. Sci. Lett.*, *145* (1-4), 49-64.

Woods, A. W. and J. R. Delaney (1992), The heat and fluid transfer associated with the flanges on hydrothermal venting structures, *Earth Planet. Sci. Lett.*, *112*, 117-129.

Zhang, S., M. S. Paterson, and S. F. Cox (1994), Porosity and permeability evolution during hot isostatic pressing of calcite aggregates, *J. Geophys. Res.*, *99* (B8), 15741-15760.

Zhang, J. X., T. F. Wong, T. Yanagidani, and D. M. Davis (1990), Pressure-Induced Microcracking and GrainCrushing in Berea and Boise Sandstones – Acoustic-Emission and Quantitative Microscopy Measurements, *Mechanics of Materials, 9* (1), 1-15.

Zhu, W., B. Evans, and Y. Bernabé (1999), Densification and permeability reduction in hot-pressed calcite: A kinetic model, *J. Geophys. Res*., *104*, 25,501-25,511.

Zhu, W., C. David, and T .Wong (1995), Network models of permeability evolution during cementation and hot isostatic pressing, *J. Geophys. Res., 100* (B8), 15451-15464.

Zhu, W., M. K. Tivey, H. Gittings, and P. R. Craddock (2007), Permeability-porosity relationships in seafloor vent deposits: Dependence on pore evolution processes, *J. Geophys. Res., 112,* B05208, doi: 10.1029/2006JB004716.

Zhu, W. and T. F. Wong (1996), Permeability reduction in a dilating rock: Network modeling of damage and tortuosity, *Geophys. Res. Lett*, *23* (22), 3099-3102.